Advanced Monte Carlo Methods for Thermal Radiation Transport

by

Allan B. Wollaber

A dissertation submitted in partial fulfillment
of the requirements for the degree of
Doctor of Philosophy
(Nuclear Engineering and Radiological Sciences and Scientific Computing)
in the University of Michigan
2008

Doctoral Committee:

Professor Edward W. Larsen, Chair
Professor Tamas I. Gombosi
Professor James P. Holloway
Professor William R. Martin

© Allan B. Wollaber 2008
All Rights Reserved

To my family: my wife Carrie and my son Dobi

Acknowledgements

I wish to acknowledge the significant impact that my advisor, Prof. Edward Larsen has had upon my approach to technical problems. Through his continued demand for excellence, he has recognized and brought forth a potential that I did not know that I had. He has also been a wonderful person work with.

I would like to thank my family for their encouragement and assistance. My wife Carrie deserves special recognition for her ability to manage almost everything required to keep me functional and grounded. My parents, Bruce and Debra, have also been supportive of me and my choice of career path.

I would like to thank my fellow students in the NERS department who have provided me with conceptual help, software advice, and stress relief. I would particularly like to thank Troy Becker and Greg Davidson, Troy for his indefatigable assistance in everything from integrating factors to cat-sitting, and Greg for his C++ tutelage and geometry library.

Thanks is due to Todd Urbatsch and Jeff Densmore for providing distance support through Los Alamos National Laboratory during my first summer at the University, which motivated this work. It was also a pleasure working with them locally during my summer practicum.

Bob Hill of Argonne National Laboratory deserves recognition for bringing me to Argonne and providing me with all the resources that I needed, despite the several setbacks that I encountered.

Finally, I would like to thank my fellowship for their invaluable support, without which, none of this would have been possible. This work was performed under appointment by the Department of Energy Computational Science Graduate Fellowship, which is provided under grant number DE-FG0297ER25308.

Table of Contents

List of Figures

Figure

List of Tables

Table

Chapter I

Introduction

This thesis develops, tests, and analyzes new computational methods for the simulation of neutral particle radiation interacting with a material. The field in which the physics of particle-matter interactions are considered is commonly referred to as *radiation transport*. Computational simulations of radiation transport are necessary in many applications, including medical imaging, radiation dose calculations (in a human or other "detector"), radiation shielding, fission and fusion simulations, and radiative heat transport. Radiation transport is not limited to neutral particles, but the methods discussed in this thesis are so restricted, as the mathematical models we shall use do not include terms that represent charge repulsion or attraction. However, neutrons, photons, and more recently, neutrinos in core-collapse supernovae are all believed to be adequately represented by a neutral particle radiation transport equation with differences in how the particles are coupled to the background medium.

The original transport equation, due to Boltzmann [1], describes the nonlinear transport processes of rarefied gas molecules interacting with each other. The radiation transport equations for other neutral particles are similar in form but make assumptions that lead to the deletion and addition of certain physical terms in Boltzmann's transport equation. It is usually assumed that the neutral particles do not interact with each other [2]. The neutral particles instead interact with the atoms of a background material, with which they may (for example) scatter, become absorbed, or cause a fission. The transport equations we shall consider do not account for stochasticities in the material or particle densities, although these are also active areas of research. The particles are considered as points, and Newtonian (non-quantum, non-relativistic) descriptions of the mechanics are employed with minor exceptions. Particle collisions are considered to be instantaneous. Additionally, we only consider particle transport in *isotropic* materials, or materials which "look the same" from all

directions.

There are at least two substantial reasons why simulating radiation transport is a difficult undertaking. The mathematical description of the particle density exists in a high-dimensional phase space, and the equation that describes this density may take substantially different characters in different regions of this phase space. Generally, the particle density is a function of seven independent variables: three for position, two for the direction of flight, one for energy, and one for time. Computationally resolving all of these dimensions on a spatial, temporal, angular, and energy grid requires substantial storage, even without considering the solution methodology. Additionally, even a relatively simple transport equation – the linear, neutron transport equation – is integro-differential, and its character can change widely in different material regimes. For instance, if the material interaction probability is high, absorption is weak, and there are no radiative sources nearby, the equation can be approximated by a time-dependent diffusion equation, which is a parabolic partial differential equation (PDE). If this same problem is in steady-state, then the equations form an elliptic PDE. Finally, if the interaction probabilities are very low and there are nearby sources, the equation is dominated by particle "streaming," which is described by a hyperbolic PDE. Textbooks on numerical methods for the solution of PDEs are typically divided into chapters devoted to particular methods for each of these cases; these three cases alone are difficult enough to substantiate wholly separate numerical solution approaches. Thus, the linear radiation transport equation is rich with physical and mathematical subtlety, and as such, it is probably impossible to create a single computational method that can efficiently capture all its character. Most computational methods must settle for capturing a portion of the equation's character or risk being fraught by complexity or inefficiency.

Broadly speaking, there are two problem classifications that naturally emerge from the physics of particle-material interactions: linear and nonlinear. In a linear particle transport problem, the radiation particles do not affect the background material in such a way that the probabilities of interactions change during a time scale of interest, and the particles do not interact with each other. The latter assumption can be valid when the density of radiation particles is many orders of magnitude less than the density of the background material. Situations like this occur in radiation shields, in source-detector problems, and in nuclear reactors that are in a steady state. These problems are completely specified by equations involving a single unknown for the radiation particle density; an example of which is the neutron transport equation without temperature feedback. By contrast, a nonlinear trans-

port problem has terms that include particle-particle interactions and/or materials that change their interaction probabilities over time scales of interest. Examples of nonlinear models include the neutron transport equation with temperature feedback and the thermal radiative transport (TRT) (or photon transport) equation in high-temperature materials. Most simulation methods particular to the field of nuclear engineering are directly applicable to linear problems. In many cases they are also applied to linearized versions of the nonlinear problems.

1.1 Linear Transport Solution Methodologies

Two fundamentally different computational approaches exist to simulate linear radiation transport equations, each with well-established schools of thought, advantages, and disadvantages. They are deterministic methods and *Monte Carlo*, or stochastic methods. More recently, hybrid deterministic-Monte Carlo methods have combined these approaches to increase the efficiency of Monte Carlo calculations. In this section we present a brief description and history of each of these methods and their applications to linear transport problems.

Deterministic methods entail the discretization of the entire problem domain on phase space grids. The solution is then represented on these subdomains, and a typically large, discrete, linear system of coupled equations is generated and solved. Representing the solution on these subdomains is a topic unto itself. For example, in the spatial variable, one may choose from finite element or finite volume representations; in the angular term, discrete ordinates or spherical harmonics expansions are frequently used. Once a decision has been made as to how to represent the discretized system, the resulting system of equations is "determined," and a numerical solution of this system produces the global estimate of the radiation field. Here, "global" means "over all of phase space." The property that deterministic solutions are inherently global is one of the advantages of deterministic methods. However, truncation errors are introduced in the discretization process, or in any approximation made to reduce the number of equations to a level amenable for computation. Many practitioners of deterministic methods continue to look for ways to quantify these errors [3] [4]. Also, it has not always been known whether a particular deterministic method will maintain its accuracy in all problem regimes. For instance, in thick, diffusive problems it may become impractical to impose spatial grids on the order of a mean free path of particle flight (this imposition is often necessary to maintain accuracy). Now, analysis tools are available to deduce whether or not a particular deterministic method

will be accurate in the limit of thick, diffusive systems [5]. The hope is that if a particular deterministic method is accurate in the thick, diffusive limit and the thin, streaming limit, then it will be accurate elsewhere.

Another limitation of deterministic methods is that direct matrix inversions of the large, linear system are prohibitively inefficient; consequently, iterative procedures must be used. The most straightforward iterative procedures can converge very slowly, hence a host of acceleration schemes have been developed. An excellent overview of modern deterministic methods and some of their acceleration schemes is provided in references [6] and [7].

A further limitation of deterministic methods that has emerged more recently is their weak *parallel scalability*, which refers to the ability of a computational method to require less wall-clock time as the number of computer processors is increased. Currently, any deterministic method that involves a discretization of the angular variable suffers from weak parallel scalability – instead of the wall-clock time decreasing proportionately as the number of processors is increased, after a moderate number of processors are employed, the return from increasing the number of processors becomes marginal. This is significant in that many supercomputers today involve thousands, or even hundreds of thousands of processors. Enhancing the parallel scalability of deterministic methods, even at the expense of serial performance, is another area of active research [8] [9] [10].

Linear radiation transport equations have a well-known Monte Carlo interpretation and a rich history. Several references are available that provide the Monte Carlo method its mathematical foundation and apply it to certain linear, transport problems [11] [12] [13]. Monte Carlo methods exploit pseudo-random number sequences to simulate the discrete interactions of individual radiation particles with the background material. If the interactions of the Monte Carlo particles directly follow the mechanics of physical particles, then the simulation is designated an *analog* Monte Carlo method. Typically, many fewer Monte Carlo particles are simulated than the amount that occur in the physical problem; consequently, each Monte Carlo particle represents some multiple of physical particles. In an analog Monte Carlo method, this multiple is fixed. If a sufficiently large number of particles are simulated with their behaviors tabulated, then one can obtain estimates of their average behavior. It is possible to show via the central limit theorem that the expected error in these estimates – the standard deviation of the sample mean – is reduced by a factor proportional to $1/\sqrt{N}$, where N is the total number of particles simulated. This means that in the limit as $N \rightarrow \infty$, Monte Carlo methods converge to the exact solution

of the linear transport problem, assuming that the underlying system is represented exactly. More practically, if one predetermines an acceptable level of error, it is then possible to probabilistically estimate a number of histories such that the solution is within this error tolerance (this number must be determined during the calculation or after a trial calculation, in which an estimate of the largest coefficient of $1/\sqrt{N}$ is generated throughout the solution region). However, the necessary number of histories may be too large for efficient computation. Monte Carlo methods also have the advantage that if the problem phase space can be represented on a single computer, than the parallelization is trivially and strongly scalable. Even if this is not the case, it is frequently possible to decompose the domain of the problem onto separate computers and maintain some degree of parallel scalability. Monte Carlo methods also suffer no theoretical restrictions in the expression of the underlying problem geometry, whereas deterministic methods may have difficulties adequately representing curved surfaces due to the regularity of the spatial grid. Analogously, energy and angular discretizations are not necessary if the continuum physics are suitably representable.

Monte Carlo methods are frequently applied to *local* problems, or problems in which the solution is desired in a small fraction of the total phase space. A classic example of this is a source-detector problem, in which a single detector sits far away from a radiation source, and the detector's response to the radiation is desired. By contrast, in a *global* problem, the solution is desired throughout the entire problem phase space. For local problems especially, *variance reduction* techniques have been devised in which a more accurate (lower variance) estimate of the problem solution is obtained with fewer particle histories. These techniques introduce more computational overhead per history, but, if employed properly, the overall variance reduction more than compensates for the additional overhead.

Variance reduction techniques for local problems generally exploit the locality of the solution phase space to increase the efficiency of each history. If we consider a source-detector problem, then the detector and the regions containing the flight paths of particles that are most likely to journey to the detector are important, whereas regions far removed from these flight paths are not. In this problem, the variance in the detector response may be reduced by ensuring that Monte Carlo particles follow these flight paths with a high probability, but without biasing the mean of the solution. Methods such as these are termed *nonanalog*, since the Monte Carlo particles are not transported according to the same principles as do the physical particles. This is typically achieved by introducing the concept of particle *weight*, whereby Monte

Carlo particles are allowed to represent a variable fraction of physical particles. It is then possible to attempt to restrict the particle weights to some optimal value by effectively combining low weight particles to become average-weight (*rouletting*) and by *splitting* large weight particles into average-weight particles. Employing the mechanisms of splitting and rouletting in concert is termed *weight windows*. However, determining the proper average weight throughout the problem phase-space requires much trial-and-error and an experienced, patient code user to adjust the parameters to an acceptable level. It is sometimes possible to automatically and dynamically adjust these parameters during the Monte Carlo calculation [14]. We note that variance reduction is not confined to weight windows; many other techniques are available [2] [12] [13].

Variance reduction techniques for global problems that do not rely on a separate, deterministic calculation are meager, and Monte Carlo is not often used in global problems that have a highly varying problem solution; i.e., Monte Carlo is typically only applied to relatively thin global problems. Only the technique of "implicit capture" (also known as absorption weighting or survival biasing) is used. In this technique, particles are not allowed to undergo absorptions, rather, their weight is changed by the fraction that scatters during a collision event. This technique extends the lives and flight paths of the particle histories, but it is frequently not sufficient to generate accurate solutions in regions far away from particle sources.

Within the last 15 years, Monte Carlo methods for local problems have found success by employing a deterministic calculation to automatically set the Monte Carlo biasing parameters. In this thesis we refer to such schemes as *hybrid* deterministic-Monte Carlo methods. For instance, it has been shown that the "important" regions of a source-detector problem are proportional to the inverse of the adjoint solution, in which the detector region is employed as an adjoint source term [15]. Hybrid approaches exploit this fact by employing a deterministic calculation to obtain a global estimate of the adjoint solution, and then setting the inverse of the adjoint solution as the center of a weight window in a Monte Carlo calculation. It is not necessary to obtain a highly accurate adjoint solution, but generally, more accurate deterministic solutions yield more efficient Monte Carlo calculations.

The development of hybrid deterministic-Monte Carlo methods is recent, and with few exceptions [16], limited to local problems. Yet it is easy to conceive of global problems of interest to a Monte Carlo user: a source-multiple-detector problem, a shielding problem requiring internal heating rates, or a radiation dose estimate for a hospital wing, for example. In these problems, the radiation population varies over

regions of phase space by so much that traditional Monte Carlo methods falter: they could take lifetimes to reduce the problem-wide variance to an acceptable level. As of this writing, the only hybrid, global method available remedies this by setting weight windows according to a deterministic estimate of the *forward* solution [16] [17]. This method, developed by Cooper and Larsen, has been shown to potentially be orders of magnitude more efficient than Monte Carlo with implicit capture, which is the only variance reduction method currently available for global problems. In his thesis, Cooper considered steady-state, 2-D, energy-independent, linear neutron transport problems and 1-D, gray, nonlinear *thermal radiative transfer* (TRT) problems. One of the new contributions in this thesis will be an extension and modification of Cooper's method to more complicated problems described by the 1-D, frequency-dependent, nonlinear TRT equations.

1.2 A Nonlinear Transport Problem

The TRT equations describe the heating and cooling of a material through which high-energy photons pass. These equations are nonlinear because the photon radiation is strongly coupled to the temperature of the background material. Physically, it becomes necessary to model radiative transport when material temperatures are so high that the radiative term dominates the convective and conductive heat transfer terms, or else when an external source of radiation dominates the heat transfer. Such situations occur in stellar atmospheres, plasma experiments, and the cooling of certain materials. The physical processes are described by a system of nonlinear equations with two unknowns: the radiative intensity and the material temperature (we assume that the material is well-described by a temperature, i.e., that it is in local thermodynamic equilibrium). The equations are coupled by absorptive and emissive terms – the material cools through the emission of photons in accordance with a Planckian frequency spectrum, and is heated by the absorption of photons. In the limit of small material heat capacities, the nonlinear transport equation reduces to a simpler linear transport equation.

In addition to the nonlinearity complications, the interaction coefficients of TRT can be strong functions of space and frequency. The probability of an absorption, for instance, can vary by many orders of magnitude over the range of photon frequencies, and it is typical to find dense and thin regions in the same problem. Therefore, many problems contain distinct regions in which the equations take hyperbolic and parabolic characters, and it is difficult to construct a comprehensive numerical

method that adequately handles both of these behaviors. Also, TRT problems are inherently global, so solution methods have historically been restricted to deterministic methods and to global Monte Carlo methods that historically have limited variance reduction capabilities. Finally, solution methods for the TRT equations have the added burden of conserving the total system energy. Altogether, this makes the computational simulation of the TRT equations a formidable task.

The state-of-the-art in both deterministic and Monte Carlo methods for solving the nonlinear TRT equations involves linearizing the equations over a time step and solving the resultant, linear system during that time step. Performing this linearization incurs a linearization error during the time step, but it enables the utilization of a large portion of the existing arsenal of linear deterministic and Monte Carlo methods. Nonlinear (or, more precisely, semi-linear) solution schemes do exist [18], but they are not widely employed in practical problems. In this thesis we only consider methods that involve a linearization procedure within each time step.

The design of a deterministic method to solve the frequency- and temperature-dependent TRT equations that (i) considers an angular discretization, (ii) correctly maintains the thick, diffusive limit when the spatial grid near the boundary (the *boundary layer*) and interfaces is not adequately resolved, and (iii) may be efficiently run on a modern computing machine remains an active area of research [19] [20]. Spatially resolving all of the boundary layers in a complex, multidimensional problem generally leads to a system of unknowns that is too large for solution, even on modern supercomputers. Therefore, most deterministic methods make a diffusion approximation, eliminating the angular variable. This is done at the expense of accuracy in thin regions and in regions near sources or interfaces. However, a diffusion version of the TRT equations is considerably easier to solve and to parallelize than the angle-discretized TRT equations.

The classic method of choice for Monte Carlo practitioners is due to Fleck and Cummings, and is known as the Implicit Monte Carlo (IMC) method [21]. The IMC method makes approximations to the TRT equations that create a linear transport equation that is valid over a time step, and for which a Monte Carlo interpretation is well-known. However, TRT problems are usually global, as opposed to local in nature. For instance, a standard test problem is the so-called "Marshak wave," in which an initially cold material is suddenly subjected to a hot, isotropic wave of photons, and the propagation of the wave front is desired. Since the interaction coefficients depend strongly on the temperature, which is itself dependent on the radiation, reducing statistical noise becomes a paramount issue. However, in the

vicinity of the wavefront, the photon population is a rapidly decreasing function; it can fall by several orders of magnitude. Because traditional variance reduction techniques such as particle splitting and Russian roulette have not been readily available to an IMC calculation (as these rely on a suitable estimate of the average particle weight), the result has been that the statistical confidence in solutions near the wavefront can also decrease rapidly in the vicinity of the wavefront. To achieve adequate statistical resolution in spatial regions that contain exponentially small photon populations, it can become necessary to greatly increase the number of IMC particles simulated, which can lead to prohibitively long computation times. Consequently, traditional IMC has been effective only on problems in which other approximations have been made to limit the size of phase space. It is worth noting that alternative Monte Carlo formulations of the TRT equations exist that make fewer approximations than IMC [22] [23] [24]. We shall not consider these in detail, but we remark that these may be expected to encounter the same difficulties that the IMC method faces regarding Monte Carlo calculations for global problems.

Improvements in global variance reduction methods could mitigate the need for vastly-increased costs in computation times for global Monte Carlo problems that contain spatial regions that are sparsely populated by photons. The extension of an existing global method for transport problems [16] will be a topic we consider in this thesis. Historically, this has not been the approach to reduce the computation times in IMC calculations. Most of the performance enhancements to the IMC equations have introduced an approximate, but much more efficient treatment of the spatial regions that are determined to be highly diffusive [25] [26]. Despite the introduction of approximations, these methods have proven to be sufficiently accurate provided that the parameters that "turn them on" during the IMC calculation are properly chosen. We anticipate that these types of enhancements should be compatible with improvements in global variance reduction techniques.

Besides the difficulties that are a characteristic of any Monte Carlo method applied to a global problem, the IMC method is known to produce unphysical solutions when a sufficiently large time step is used [27] [28] [29]. However, little attention has been given to the stability characteristics of the IMC equations. Most of the existing literature has centered upon the accuracy of the IMC equations based upon analyses of physically-limiting conditions of the TRT equations. Larsen and Mercier [27] found an upper limit on the size of the time step that ensures that the IMC equations satisfy a "maximum principle" that the underlying TRT equations satisfy. Larsen and Densmore [28] also established that the IMC equations do not obtain the correct

asymptotic equilibrium diffusion limit. Gentile has observed that the IMC equations applied to a 0-D, nonlinear problem tend to produce temperature solutions that overshoot the equilibrium condition at early times [30]. Martin and Brown [29] analyzed the temporal convergence rate of the IMC equations applied to a 0-D, linear problem, and demonstrated the presence of unphysical, damped oscillations in some of their numerical results. Mosher and Densmore [31] extended the results of Martin and Brown to derive stability and monotonicity conditions on α and the size of the time step for the IMC equations applied to a 0-D, gray, and linear problem. However, there have been no attempts to analyze the stability characteristics of the IMC equations applied to a nonlinear or spatially-dependent problem; Mosher and Densmore's paper is the only contribution to the literature that addresses stability characteristics of the IMC equations.

Two fundamental sources of inaccuracies arise during the derivation of the IMC equations. One concerns the treatment of the nonlinear, temperature-dependent problem data. To avoid solving a system of nonlinear equations or introducing a costly iteration procedure, these data are approximated throughout the time step by freezing their value at the beginning of the time step. This introduces an error into the calculation that is proportional to the size of the step. Another source of inaccuracy necessitates the introduction of a user-defined parameter α. This parameter is a "knob" that may be adjusted between the values 0.5 and 1 with the implication that using $\alpha = 0.5$ should provide more accurate solutions for smaller time steps. However, Fleck and Cumming point out that using $\alpha < 1$ can introduce unphysical temporal oscillations into the temperature solution [21]. Consequently, in modern computational implementations of the IMC equations, α is usually chosen to be unity.

1.3 Proposed Work and its Impact

In this thesis we re-present, analyze, and consider alternative, more accurate, and more efficient treatments of the IMC equations. We begin by presenting an clear derivation of the IMC equations from the TRT equations by pointing out precisely when and why approximations are made. We discuss the effects of these approximations, and we present a new analysis that indicates the conditions under which the IMC equations can guarantee positive temperature solutions. We also explicitly provide the IMC equations with a Monte Carlo interpretation; this is a task that has never been formally implemented. Although these topics occur in a chapter that is introductory in nature, our intent is to provide a better foundation than the current

literature provides. Additionally, a solid understanding of the IMC equations and their derivation is necessary to understand the motivation of the enhancements we propose in later chapters.

We introduce a dimensionless form of the 1-D, gray, nonlinear TRT equations that are scaled about a specified equilibrium condition. This scaling of the TRT equations is an extension of a previous scaling of a linear problem due to Su and Olson [32]. The scaled TRT equations are simpler to analyze than the original equations, and the dimensionless parameters contained in them have physical significance.

Using the dimensionless form of the 1-D, gray, nonlinear TRT equations, we develop a linear stability theory for the IMC equations applied to a nonlinear problem described by physically representative choices of temperature-dependent problem data. As mentioned above, with the exception of a single paper that defines the conditions under which temperature solutions are monotonic with respect to time for 0-D, gray, linear problems [31], there has been no theory to determine when the IMC equations may be expected to produce non-physical, numerically oscillatory temperature solutions. Our theory is not based upon those results, but it does successfully reproduce and verify them. Furthermore, we demonstrate rigorously that the IMC equations are unconditionally stable for gray, nonlinear, 1-D problems, and we further demonstrate the conditions under which the temperature solutions are susceptible to damped temporal oscillations. We use the stability theory to derive monotonicity conditions on the time step size for the temperature solution of the 1-D, gray, nonlinear IMC equations. We numerically test the stability theory on a series of 0-D and 1-D gray, nonlinear problems to demonstrate its range of applicability. These simulations show that our stability theory goes much farther than any previous effort to characterize the numerical properties of IMC solutions.

Using our 1-D stability theory, we demonstrate numerically and analytically that the most oscillatory temperature solutions may be expected for problems that contain very slowly-varying spatial solutions (small Fourier modes). This implies that 0-D problems are representative of the numerical "worst case" scenarios for a given linearization of the TRT equations over a time step (such as the IMC equations). We capitalize on this property by developing a simpler, 0-D version of the linear stability theory and presenting it as a simple-to-use algorithm for rapidly determining the efficacy of a proposed linearization of the TRT equations. This 0-D stability algorithm is one of the more powerful methods presented in this thesis, and it is used extensively in later chapters on both Monte Carlo and deterministic methods. Using it, we prove that the IMC equations applied to a linear problem can also pro-

duce damped, oscillatory temperature solutions. This demonstrates that damped temporal oscillations are a fundamental deficiency of the IMC equations; they are not due to the approximate treatment of the temperature-dependent problem data. We also use the 0-D stability algorithm to assess the validity of a proposed, simplified deterministic treatment of the TRT equations, two modifications of the IMC equations, and we discuss previously proposed alternative linearizations of the TRT equations intended for Monte Carlo solution techniques. In two of these cases (one is described in Chapter VI, one in Appendix A), the 0-D stability theory predicts that the methods are only conditionally stable, which is surprising given that they are both closely related to other, unconditionally stable methods. Because the theory is relatively simple to apply, but can produce results that are unexpected, we believe that it should be of value to anyone interested in proposing new time discretizations and/or linearizations of the TRT equations applied to gray, linear or nonlinear problems. Our 0-D stability theory successfully reproduces, but is not based upon, the monotonicity conditions given by Mosher and Densmore [31]. It is also more general in that it is directly applicable to nonlinear problems and methods other than IMC.

After discussing the stability and accuracy limitations of the traditional form of the IMC equations at length, we introduce two proposed modifications to them to improve their accuracy. The first modification addresses the inaccuracies that arise due to the approximate treatment of the temperature-dependent problem data in the IMC equations, which are frozen at the beginning of the time step $t_n \leq t \leq t_{n+1}$. We argue that a better treatment would be to evaluate these data at a properly-averaged temperature T_* that is internal to the time step (T_* is the temperature evaluated at time t_* where $t_n \leq t_* \leq t_{n+1}$). To generate T_*, however, it is necessary to obtain an estimate of the temperature at the end of the time step, T_{n+1}. To do this, we propose a new, gray, Quasidiffusion method to be solved by a relatively simple and inexpensive deterministic procedure. This Quasidiffusion method is intended to be used in tandem with a more detailed transport calculation in the following manner. During a time step $t_{n-1} \leq t \leq t_n$, a frequency-dependent transport calculation such as IMC is carried out. Throughout the calculation, certain problem data are averaged over frequency and angle. These data are then provided to the new Quasidiffusion method, which uses them to estimate T_{n+1} for the upcoming time step $t_n \leq t \leq t_{n+1}$. The average temperature T_* is generated and passed to the frequency-dependent transport algorithm, which then uses it to evaluate the temperature-dependent problem data. The transport algorithm then produces solutions over the same time step $t_n \leq t \leq t_{n+1}$ using the more accurate problem data, and produces a new solution

of T_{n+1} that supersedes the solution generated by the deterministic Quasidiffusion method. We numerically show that the use of this temperature-estimation method generally leads to much more accurate solutions of the IMC equations for 1-D gray or frequency-dependent, nonlinear problems. Alternatively, we also motivate the use of the temperature-estimation method to obtain an adaptive estimate of the proper time step size, or to potentially accelerate a deterministic transport calculation. The gains in accuracy demonstrated through the numerical solutions of 0-D and 1-D, gray and frequency-dependent Marshak wave problems suggest that the method merits serious further attention and development. Additionally, nothing precludes the use of this method with the other enhancements proposed in this thesis.

The other modification to the IMC equations that we propose removes the necessity of the user-defined parameter α, and it creates a more accurate system of IMC equations that contain a nuance in their implementation: the use of a *time-dependent* "Fleck factor." We call this modification to the IMC equations the IMC-TDF equations (IMC equations with a Time-Dependent Fleck factor). The traditional Fleck factor f_n is a parameter in the IMC equations that satisfies $0 \leq f_n \leq 1$ and is defined by problem data evaluated at time t_n and the user-supplied parameter α. It controls the validity of the IMC linearization with respect to some of the underlying problem physics. For example, in a Monte Carlo procedure to solve the IMC equations, the Fleck factor dictates the time-distribution of photons emitted due to particles held in the radiation at time t_n. Because this term is constant in the IMC equations, the time-distribution of the source particles is uniform over the time step $t_n \leq t \leq t_{n+1}$. However, from physical arguments, it is possible to show that the proper time distribution of these source particles should be an exponential. The time-dependent Fleck factor $f_n(t)$ employed in the IMC-TDF equations remedies this. Also, it is not necessary to introduce any user-defined parameters (such as α) into the IMC-TDF equations. From another perspective, we show that $f_n(t)$ (in a certain sense) provides an adaptive determination of the parameter α. We discuss the differences in computational implementations between the IMC and IMC-TDF equations, and show that they are minor. We numerically demonstrate that solutions of the IMC-TDF equations are generally more accurate than solutions of the IMC equations. However, this increase in accuracy comes at an increase in cost, as the IMC-TDF equations require the evaluation of exponentials and logarithmic terms that do not exist in the IMC calculation. Also, we show that due to certain properties of $f_n(t)$, the cost of the calculation can become relatively prohibitive as compared with a corresponding IMC calculation if sufficiently large time steps are used. However, we also motivate

some possible remedies for the increase in cost which should not substantially affect the increase in accuracy obtained using the IMC-TDF equations. Because the implementational differences between the IMC and IMC-TDF equations are so minor, and because the modification improves the accuracy of the IMC equations, we believe that the method should be further examined.

To increase the efficiency of IMC calculations, we propose a modification and extension of the hybrid global weight window method due to Cooper and Larsen [16] [17]. Cooper's method consists of using a deterministic Quasidiffusion calculation to obtain an estimate of the forward radiation solution. The weight windows in a subsequent Monte Carlo calculation are then chosen to be proportional to the forward solution.[1] In Cooper's thesis, the focus is primarily on 2-D, energy-independent neutron transport problems, for which large gains in efficiency are numerically demonstrated. The latter chapters of his thesis demonstrate an extension of his method to 1-D, gray TRT problems solved using the IMC equations. The numerical results of these chapters are good, but not as compelling. Furthermore, the Quasidiffusion equations that he derives cannot easily be extended to account for frequency-dependence, there is a nuance in how the method described in his thesis should be applied to problems with energy or frequency dependence, and it is not clear that his approach rigorously conserves energy.

We derive a new set of gray Quasidiffusion equations that depend upon the IMC solution of a frequency-dependent problem over the previous time step – the same equations used to generate T_* in the temperature estimation algorithm discussed above and in Chapter V. We argue that the proper choice of weight windows should be frequency-*independent*, not frequency-dependent as is implicated in a straightforward application of Cooper's method. This simplifies the overall calculation and should produce much more efficient solutions. We also define the method such that it rigorously conserves energy when Russian roulette is used. We present a logical enhancement to the weight window that increases its efficiency in Marshak wave problems. In numerical tests on gray and frequency-dependent Marshak wave problems, we demonstrate that our method can be over an order of magnitude more efficient than a corresponding IMC calculation. We note that comparisons of efficiency between differing Monte Carlo methods are performed using a metric called

[1] In steady-state problems, Cooper recommends an iterative refinement scheme that updates the accuracy of the Quasidiffusive parameters. In such a scheme, the Monte Carlo calculation is periodically stopped, the Quasidiffusion solution is recalculated, and the weight windows are updated. In time-dependent problems, we do not consider this enhancement.

the Figure of Merit (FOM), defined by:

$$FOM = \frac{1}{R^2 T_{\text{cpu}}},$$

where R is the (possibly spatially-, angular-, time-, and frequency-dependent) relative statistical error of a quantity of interest, and T_{cpu} is the amount of computational time required by the Monte Carlo method. The FOM includes a combination of the relative error *and* the computational time because the desired properties of a highly efficient Monte Carlo method are small errors in relatively little time. Thus, methods that take the same amount of time but have higher errors, or methods that finish quickly but have large errors, are deemed less efficient. Designers of Monte Carlo and hybrid deterministic-Monte Carlo methods seek methods that produce large FOMs over a variety of problem types. If the FOMs produced by the new hybrid approach are much larger than those of traditional IMC over a sufficiently wide variety of problems, then it becomes possible to solve TRT problems of much higher complexity than is currently viable.

We remark that the methods proposed in this thesis are numerically tested only for systems with 1-D spatial-dependence. However, with the exception of the stability analysis in Chapter IV, none of the methods that we propose are *limited* to 1-D systems. Furthermore, because the problems we consider are nonlinear and already incorporate angle, frequency, and temporal dependencies, generalization to greater dimensions for numerical testing purposes would likely require the use of a supercomputer. Some of the 1-D test problems we shall consider later take several days to run in parallel on 20 3.4 Ghz processors; one might imagine what adding another degree of freedom would require for such a problem. We also believe that, because the new methods we describe are preliminary and never-before tested, exercising them using 4 degrees of freedom (time, space, angle, and frequency) should be sufficient to capture their essential features.

To summarize, IMC has emerged as the dominant methodology to obtain transport solutions of the TRT equations. However, the IMC temperature solutions are unphysical if the desired time step size is too large, and the amount of computation required to achieve acceptable statistics can be excessive. Although the IMC method has existed for over 35 years, it is still computationally implemented with few modifications to what was initially presented by Fleck and Cummings in [21]. In this thesis, we present a stability theory to better understand when the IMC equations will produce unphysical solutions. We also propose two modifications to the IMC

equations that enhance their accuracy. In the first modification, we consider evaluating the temperature-dependent problem data at a more accurate temperature (T_*) than the beginning-of-time-step value (T_n). In the second modification, we eliminate an unnecessary approximation that occurs in the traditional derivation of the IMC equations. This results in the introduction of a time-dependent Fleck factor. Lastly, we provide a global weight-window variance reduction method to improve the overall efficiency of the IMC calculation.

1.4 Thesis Synopsis

The remainder of this thesis is organized as follows:

Chapter II: Thermal Radiative Transfer: Basic Equations and Approximations
In this chapter we present some common mathematical models and approximations for radiative transfer problems. We discuss the relevant problem physics in greater detail, and we present the TRT equations that are used throughout the thesis. Most of the approximations that we consider attempt to reduce the dimensionality of the problem either by eliminating the angular or frequency variables. We also discuss a choice of problem data, previously defined by Su and Olson, that reduces the TRT equations to a linear system.

Chapter III: The Implicit Monte Carlo Method and its Monte Carlo Interpretation
We briefly discuss the motivation, terminology, and implications behind Monte Carlo methods in general. We then derive the IMC equations due to Fleck and Cummings [21], provide them with a rigorous Monte Carlo interpretation, and discuss their computational implementation. We also discuss some of the limitations of the IMC equations with regard to accuracy and stability. We briefly define the variance reduction techniques of implicit capture, Russian roulette, particle splitting, and weight windows, and we introduce a modification of Russian roulette that rigorously conserves energy.

Chapter IV: Stability Analysis of the IMC Method
The IMC method is known to produce unphysical solutions when sufficiently large time steps are used. In particular, they sometimes introduce unphysical temporal oscillations into the temperature solution. In this chapter, we present a new stability theory of the gray, 1-D IMC equations. To develop the theory we derive linearized

near-equilibrium, dimensionless versions of the 1-D IMC equations. We introduce an *amplification factor* ρ that relates the temperature solutions at the beginning and end of the time step. We then demonstrate that $|\rho| < 1$, indicating that the IMC equations are unconditionally stable. We also show that it is possible to find $-1 < \rho < 0$, indicating that the IMC equations can produce damped, temporal oscillations. We derive a monotonicity condition that, when satisfied, ensures that the IMC equations do not produce temporal oscillations. We demonstrate the stability theory numerically using a series of three different gray radiative transport problems, and demonstrate that the worst oscillations occur for problems that contain small Fourier modes (large wavelengths). We then present a generic 0-D stability analysis algorithm that may be used to relatively quickly assess the efficacy of a proposed time-discretization of the TRT equations.

Chapter V: Temperature Estimation and Evaluation

The IMC equations have traditionally been limited to an explicit-in-time treatment of the temperature-dependent problem data. In this chapter, we develop a new, simplified deterministic method that may be used to estimate the temperature at the end of the time step. This deterministic method exploits the IMC calculation of the previous time step in order to generate suitable angle- and frequency-averaged problem data, resulting in a system of gray, Quasidiffusion equations that are reasonably accurate much simpler to solve. We also define a properly time-averaged temperature that may then be used to evaluate the temperature-dependent problem data in the IMC calculation, and we show numerically that its use greatly improves the accuracy of the IMC temperature solutions.

Chapter VI: A Time-Dependent Fleck Factor

During the derivation of the IMC equations, a questionable approximation is introduced in which time-averaged unknowns are replaced by "instantaneous" unknowns. This leads to the introduction of a parameter known as the "Fleck factor", which also contains a user-defined constant α. In this chapter, we derive a more accurate system of IMC equations that incorporates a time-dependent Fleck factor: the IMC-TDF equations. We analyze the introduction of this term from the perspective of stability and accuracy, and we test the system numerically on a series of sample problems.

Chapter VII: A Global Weight Window

In this chapter we propose a frequency-independent weight window that may be used to improve the efficiency and accuracy of an IMC solution. This weight window is proportional to the forward, gray scalar intensity produced by the simplified

deterministic procedure developed in Chapter V. Related work by Cooper [16] has indicated some success for gray radiative transport problems, but we here extend those results to frequency dependence while maintaining energy conservation.

Chapter VIII: Conclusions

Here we review the major ideas and sum up the results presented in the thesis. We also discuss the implications of the work from a broader perspective and consider some promising ideas for future work.

Chapter II

Thermal Radiative Transfer: Basic Equations and Approximations

It is well-known that the radiation energy transferred per unit time is proportional to the *fourth power* of a material's temperature. Physically, it becomes necessary to model radiative transport when material temperatures are so high that the radiative term dominates the convective and conductive heat transfer terms, or else when an external source of radiation dominates the heat transfer. Many applications exist in which radiation transfer becomes important, for example, the modeling of stellar atmospheres, high energy plasmas, and the cooling of certain materials. The physical processes are described by a system of nonlinear equations with two unknowns: the radiative intensity and the material temperature (assuming that the material is well-described by a temperature, i.e., that it is in local thermodynamic equilibrium). The equations are coupled by absorptive and emissive terms – the material cools through the emission of photons in accordance with a Planckian frequency spectrum, and is heated by the absorption of photons. In this chapter we introduce the thermal radiative transfer equations and some of their more common approximations.

2.1 The Thermal Radiative Transfer Equations

The equations of thermal radiative transfer are a mathematical model that describe the physical process of photons scattering through and being absorbed in and emitted by a high-energy background material. Since photons are described equally well using either quantum particles or electromagnetic waves, it is possible to characterize the underlying physics using Maxwell's equations of electromagnetism, but this is almost always avoided in favor of the quantum description [33]. Thus, a depiction of the underlying physics begins by considering a discrete packet of energy

traveling through phase space. The phase space is fully specified via the quantities:

$$\mathbf{x} = \text{particle location (three variables)}\,, \tag{2.1a}$$

$$\mathbf{\Omega} = \text{particle direction of flight (two variables, since } |\mathbf{\Omega}| = 1)\,, \tag{2.1b}$$

$$\nu = \text{particle frequency (one variable)}\,, \tag{2.1c}$$

$$t = \text{time (one variable)}\,. \tag{2.1d}$$

This seven-dimensional phase space description is one of the central reasons that accurate simulations are difficult and expensive. Also, in plasmas, for instance, the photon distribution for a single problem may vary by orders of magnitude in nearly all of these seven dimensions [34].

Let us choose a very small (a *differential*) element of this phase space, and consider its resident photon energy. This packet of photon energy is located in a differential volume dV about position $\mathbf{x}$, traveling in directions $d\Omega$ about $\mathbf{\Omega}$, has frequencies in the range $(\nu, \nu + d\nu)$, and is traveling at the speed of light c. This packet of energy may leave its element of phase space according to two mechanisms: it may either stream out of the differential volume traveling in direction $\mathbf{\Omega}$, or it may collide with an electron located in the same volume. Other photons may enter this unit of phase space by streaming into it, by scattering into it, or by being emitted into it by an excited electron located in dV or another, specified photon source. By carefully accounting for these sinks and sources of the photon energy, one can form a balance equation for the photon energy in this unit of phase space that includes terms accounting for all the physics. For instance, the absorptive and emissive terms may be derived using the quantum mechanical properties of photons and their interactions with free and orbiting electrons [33]. The relevant unknown for a packet of photon energy is referred to as the *specific intensity*, $I(\mathbf{x}, \mathbf{\Omega}, \nu, t)$. I should be understood as an energy density function – that is, integrating this quantity over an element of phase space will reveal the energy in the radiation for that unit of phase space. More specifically,

$$I = ch\nu n(\mathbf{x}, \mathbf{\Omega}, \nu, t) = \text{the } \textit{specific intensity}\,, \tag{2.2a}$$

where

$$n(\mathbf{x}, \mathbf{\Omega}, \nu, t) dV d\Omega d\nu = \text{the mean number of photons} \tag{2.2b}$$
$$\text{in } dV d\Omega d\nu \text{ about } (\mathbf{x}, \mathbf{\Omega}, \nu) \text{ at time } t\,,$$

$$h = 6.6260693 \times 10^{-35} \text{ jk-sh} = \text{Planck's constant}\,, \tag{2.2c}$$

$$c = 299.792458 \text{ cm/sh} = \text{speed of light}\,. \tag{2.2d}$$

In the above units, a jerk (jk) is 10^9 Joules and a shake (sh) is 10^{-8} seconds. The energy released in a ton of TNT – a TNT equivalent – is 4.2 jks, and, during a shake, light travels only 300 cm, which is nearly the height of a standard basketball goal.

Through the processes of absorption and emission, the photon energy is transferred to or from the internal energy of the underlying material. Assuming that the material is in local thermodynamic equilibrium, its energy can be well-described by specifying its temperature. The general equations of heat transfer contains terms that describe convective, conductive, and radiative source and loss terms. Here we assume that the radiative term is sufficient to describe the heat transfer, the net result being that heat energy may only move between the internal energy of the material and the radiative power of the photons. To describe the internal energy of the material, we make the assumption that it is in Local Thermodynamic Equilibrium (LTE). This essentially means that the frequency spectrum of emitted photons follows a Planck distribution, and that the material energy is well-described by a temperature. Thus, our second unknown to consider is $T(\mathbf{x}, t)$, the material temperature at position $\mathbf{x}$ and time t. Temperature is an average measure of the thermal energy in a material; it only depends on the state of a material at a particular location in space and time. The temperature T is most familiarly expressed in kelvins (K), but it is more convenient to convert this to units of kilo-electron-volts (keV) using Boltzmann's constant k:

$$T_{\text{keV}}(\mathbf{x}, t) = kT_{\text{K}}(\mathbf{x}, t)\,, \tag{2.3a}$$

where

$$k = 8.617343 \times 10^{-8} \text{ keV/K}\,. \tag{2.3b}$$

As a general guide to the temperature scale of a keV, the core of the sun is estimated to be about 1.3 keV (15 million K). We will later show how the probabilities of photon absorption and emission are strong, nonlinear functions of T; this is the central source of the nonlinearity in thermal radiative transport.

Other references [33] [34] have ably presented thorough derivations of the relevant source and sink terms for the radiative transport equations, so we shall not repeat those details here. Instead, we shall begin by directly writing a simplified version of the system. This system is described in one spatial dimension ($0 \leq x \leq X$), and correspondingly requires only one angular variable, $\mu = \cos\theta$, where the angle θ is measured from the positive x direction. We further assume no scattering is present

in the system, and that the system is in LTE. The equations that model this system are given by:

$$\frac{1}{c}\frac{\partial I}{\partial t}(x,\mu,\nu,t) + \frac{\partial I}{\partial x}(x,\mu,\nu,t) + \sigma_a(x,\nu,T)I(x,\mu,\nu,t) \\ = 2\pi\sigma_a(x,\nu,T)B(\nu,T) + \frac{Q}{2}(x,\nu,t)\,, \quad (2.4a)$$

$$c_v(x,T)\frac{\partial T}{\partial t}(x,t) = \int_0^\infty \int_{-1}^1 \sigma_a(x,\nu',T)\big[I(x,\mu',\nu',t) - 2\pi B(\nu',T)\big]d\mu' d\nu'\,, \quad (2.4b)$$

for $0 \le x \le X$, $-1 \le \mu \le 1$, $0 < \nu < \infty$, and $0 < t$. We also impose the initial conditions:

$$I(x,\mu,\nu,0) = I^i(x,\mu,\nu)\,, \quad (2.4c)$$

$$T(x,0) = T^i(x)\,, \quad (2.4d)$$

and the boundary conditions:

$$I(0,\mu,\nu,t) = I^\ell(\mu,\nu,t)\,, 0 < \mu \le 1\,, \quad (2.4e)$$

$$I(X,\mu,\nu,t) = I^r(\mu,\nu,t)\,, -1 \le \mu < 0\,. \quad (2.4f)$$

In these equations, we have defined:

$$I = ch\nu n(x,\mu,\nu,t) = \text{the } \textit{specific intensity}\,, \quad (2.5a)$$

$$n(x,\mu,\nu,t) = \text{the mean number of photons per unit of phase space}\,, \quad (2.5b)$$

$$h = 6.6260693 \times 10^{-35} \text{ jk-sh} = \text{Planck's constant}\,, \quad (2.5c)$$

$$c = 299.792458 \text{ cm/sh} = \text{speed of light}\,, \quad (2.5d)$$

$$T = T(x,t) = \text{material temperature (keV)} \quad (2.5e)$$

$$B = B(\nu,T) = \text{Planck's function for radiation}\,, \quad (2.5f)$$

$$= \frac{2h\nu^3}{c^2}\left(e^{h\nu/T} - 1\right)^{-1}\,, \quad (2.5g)$$

$$Q = Q(x,\nu,t) = \text{inhomogeneous photon source} \quad (2.5h)$$

$$c_v = c_v(x,T) = \text{specific heat of material} \quad (2.5i)$$

$$\sigma_a = \sigma_a(x,\nu,T) = \text{the absorption opacity,}$$

$$= \text{(probability of absorption per unit distance)}\,. \quad (2.5j)$$

The quantities I and T are unknown; all of the other quantities are prescribed. In addition, it is useful to define the material energy density U_m and radiation energy density U_r, which are given by the relationships:

$$\frac{\partial U_m}{\partial T}(x,t) = c_v(x,T)\,, \tag{2.6a}$$

$$U_r(x,t) = aT(x,t)^4\,, \tag{2.6b}$$

where

$$a = \text{radiation constant} = \frac{8\pi^5 k^4}{15h^3c^3} = 0.01372\ \frac{\text{jk}}{\text{cm}^3\ \text{keV}^4}\ . \tag{2.6c}$$

Here, U_m is the internal energy density of the material, while cU_r is the total radiative power per unit volume emitted by a material at temperature T (note that cU_r is not the total power in the radiation from all sources).

Eqs. (2.4) are the *thermal radiative transfer* (TRT) equations. It is also useful to identify the physical processes implicit in each of the terms in these equations. The first term in Eq. (2.4a) is a time rate-of-change term. This time derivative is related to several loss terms in phase space on the left side and gain terms on the right hand side. The second term on the left hand side is a loss term due to photons streaming out of an element of phase space. The third term is a loss term due to photons that are absorbed into the background material. In such an event, the photon is removed from its element of phase space and is allocated as a source term in the material temperature equation [Eq. (2.4b)]. The first term on the right hand side is a radiative source due to the background temperature of the material (hence, a corresponding loss term appears on the right hand side of Eq. (2.4b)). The last remaining term on the right hand side of Eq. (2.4b) is due to a prescribed, inhomogeneous source. With these in place, Eq. (2.4b) may be more easily recognized as a conservation of energy in the material – the time rate of change of material energy is proportional to the difference between photons absorbed by the material and Planckian emissions lost to the radiation.

The equation for the specific intensity is integro-differential in nature and non-linearly coupled to the material temperature. Nonlinear systems of equations are notorious for their often-surprising complexity (see *Chaos* [35], for instance), and even a linear (integro-differential) transport equation can take predominantly elliptic, parabolic, or hyperbolic forms in various problem regimes. Yet, the TRT equations in Eqs. (2.4) include several assumptions. We have already made the LTE assumption. Physically, this implies that "the matter is in thermal equilibrium at a

temperature T, emitting photons in a Planckian spectrum (with temperature T), and the radiation field, which may be far from equilibrium, does not affect this thermal equilibrium." [24] Another assumption implicit to these equations is that the material is motionless. However, for situations in which the radiation momentum is comparable to the material momentum, it is already typical for researchers to "split" the fluid and radiation operators to essentially produce (within a time step) a decoupled system of radiation and fluid equations. In this case, Eqs. (2.4) may be considered the radiation "part" of such a system, written in the rest frame of the material. We have also neglected the polarity of the photons, which, if included, would add another independent variable to the equations [33].

The greatest assumption made is to cast the equations in one spatial dimension, which is sometimes referred to as a "slab geometry." Because this is one of the simplest physically interesting geometric models, this geometry is frequently used as a first step in methods development. Appropriately, this will be the central geometry used for the computational studies in this thesis; the most difficult equations we attempt to solve computationally will allow for temporal, 1-D spatial, angular, and frequency variation. These dimensions should capture most of the important complexities from the perspective of methods development without imposing computational runtimes that would require a dedicated supercomputer. We shall also seek to develop the new methods in this thesis in such a way that they are not restricted to slab geometry – this geometry is just the testing ground for the new methods.

The assumption to disregard scattering is made for similar reasons. First, the inclusion of the physical, Compton scattering processes introduces an additional nonlinearity into the equations [34]. Treating the full form of this scattering term is a topic of its own. It is possible to include a weaker (linear) form of scattering that occurs only when photons scatter with nonrelativistic electrons, or Thomson scattering [33]. However, allowing for Thomson scattering does not substantially affect the methods development. Its inclusion might be considered more of an exercise rather than of fundamental significance. The physical process of absorption and reemission is the more important phenomenon and deserves the most attention.

2.1.1 Simple Material Models

In practice, the opacities (or interaction coefficients) are usually either determined experimentally or require relatively complicated quantum-electrodynamic physical models. In this thesis we will use a simple but physically meaningful, analytic model

for the absorption opacity [36]:

$$\sigma_a(\nu, T) = \frac{\gamma_a(x)}{(h\nu)^3} \left(1 - e^{-h\nu/T}\right) , \tag{2.7}$$

where γ_a is specified by the user or a relevant problem description. This model includes a correction for stimulated emission (the exponential term) and assumes a cubic proportionality to the photon energy. There is also a special case, to be discussed below, in which we shall assume a frequency-independent absorption opacity. We will usually assume the specific heat to be temperature-independent and prescribed for each material:

$$c_v(x, T) = c_v(x) . \tag{2.8}$$

This is physically the case if the material is a perfect gas [37].

2.1.2 The Equilibrium Solution

If T_0 is a positive, constant temperature and the inhomogeneous source, initial conditions, and boundary conditions are such that:

$$Q(x, t) = 0 , \tag{2.9a}$$
$$T^i(x) = T_0 , \tag{2.9b}$$
$$I^i(x, \mu, \nu) = 2\pi B(\nu, T_0) , \tag{2.9c}$$
$$I^\ell(\mu, \nu) = I^r(\mu, \nu) = 2\pi B(\nu, T_0) , \tag{2.9d}$$

then Eqs. (2.4) have the exact *equilibrium solution*:

$$I(x, \mu, \nu, t) = 2\pi B(\nu, T_0) , \tag{2.10a}$$
$$T(x, t) = T_0 . \tag{2.10b}$$

Any realistic method should reproduce this solution given the above initial and boundary conditions – it is the first and simplest test to verify that a particular method is working. These equations may also be referred to as the *steady-state, infinite medium* solution, as they satisfy Eqs. (2.4) with the differential terms set to zero.

2.2 Common Approximations to the TRT Equations

Analytical solutions of Eqs. (2.4) are impossible except for the simplest of scenarios. To generate solutions to physically interesting problems, it is necessary to make some approximations. We shall first consider a discretization of the frequency variable, commonly referred to as the "Multigroup" approximation. This approximation is nearly always used in deterministic methods, and is sometimes used in Monte Carlo methods.

2.2.1 The Multigroup Approximation

In this method, we divide the frequency variable into G groups with group boundaries arbitrarily given by $\nu_0 = 0 < \nu_1 < \nu_2 \ldots \nu_G = \infty$. Let us define, for $g = 1, \ldots G$, the frequency-integrated *group specific intensity*:

$$I_g(x, \mu, t) = \int_{\nu_{g-1}}^{\nu_g} I(x, \mu, \nu, t) d\nu \,, \tag{2.11}$$

and group Planck function:

$$B_g(T) = \int_{\nu_{g-1}}^{\nu_g} B(T, \nu) d\nu \,, \tag{2.12}$$

and group source:

$$Q_g(x, t) = \int_{\nu_{g-1}}^{\nu_g} Q(x, \nu, t) d\nu \,. \tag{2.13}$$

Next, we operate on Eq. (2.4a) with $\int_{\nu_{g-1}}^{\nu_g} (\cdot) d\nu$ for $g = 1, \ldots, G$ to obtain the system (suppressing the spatial, temporal, and angular variables for compactness where it is clear):

$$\frac{1}{c}\frac{\partial I_g}{\partial t} + \mu \frac{\partial I_g}{\partial x} + \int_{\nu_{g-1}}^{\nu_g} \sigma_a(\nu) I(\nu) d\nu = 2\pi \int_{\nu_{g-1}}^{\nu_g} \sigma_a(\nu) B(\nu) d\nu + \frac{Q_g}{2} \,, \tag{2.14a}$$

$$c_v \frac{\partial T}{\partial t} = \sum_{g=1}^{G} \int_{\nu_{g-1}}^{\nu_g} \int_{-1}^{1} \sigma_a(\nu') (I(\mu', \nu') - 2\pi B) \, d\mu' d\nu' \,, \tag{2.14b}$$

for $0 \leq x \leq X$, $-1 \leq \mu \leq 1$, $0 < \nu < \infty$, and $0 < t$, with initial conditions:

$$I_g(x, \mu, 0) = I_g^i(x, \mu) \,, \tag{2.14c}$$

$$T(x, 0) = T^i(x) \,. \tag{2.14d}$$

and boundary conditions:

$$I_g(0,\mu,t) = I_g^{\ell}(\mu,t) \quad 0 < \mu \leq 1 \tag{2.14e}$$

$$I_g(X,\mu,t) = I_g^{r}(\mu,t) \quad -1 \leq \mu < 0\,. \tag{2.14f}$$

The above equations are exact, but the integration over the terms involving the opacities have necessarily been left unevaluated. As in Pomraning [34], if we define group mean opacities such that:

$$\sigma_{a,g}(x,\mu,t) = \frac{\int_{\nu_{g-1}}^{\nu_g} \sigma_a(x,\nu,T)(2\pi B(\nu,T) - I(x,\nu,\mu,t))\,d\nu}{\int_{\nu_{g-1}}^{\nu_g} (2\pi B(\nu,T) - I(x,\nu,\mu,t))\,d\nu}\,, \tag{2.15}$$

Then the equations become (again, suppressing variables for compactness where clear):

$$\frac{1}{c}\frac{\partial I_g}{\partial t} + \mu\frac{\partial I_g}{\partial x} = \sigma_{a,g}(x,\mu,t)(2\pi B_g - I_g) + \frac{Q_g}{2}\,, \tag{2.16a}$$

$$c_v\frac{\partial T}{\partial t} = -\sum_{g=1}^{G}\int_{-1}^{1} \sigma_{a,g}(x,\mu',t)(2\pi B_g - I_g(\mu'))d\mu'\,, \tag{2.16b}$$

with the initial and boundary conditions the same as above. These equations are similar in form to the continuous equations and remain exact, but a new difficulty emerges – in order to find the group-averaged opacities we must already know the full form of the specific intensity. As this is completely impractical, it is common to assume a reasonable form of the frequency behavior. The hope is that since these group-average opacities are homogeneous functionals of the specific intensity, a crude estimate will still lead to relatively accurate results [34]. Also, if a very large number of groups are used, the impact of the specific shape of the weighting function on the group-averaged coefficients will diminish.

The formation of the group-averaged absorption opacity requires careful consideration since it is weighted against the difference $B - I$, and since it is a highly varying function of frequency (it is not uncommon to find that it varies by five to ten orders of magnitude). Researchers typically use one of two physically meaningful weighting functions; these produce the group Planck and group Rosseland means. The Planck mean is accurate in the limiting case of an equilibrium solution in an optically thin, emission-dominated system. In this regime, it can be shown that in the optically thin limit [34]

$$B(\nu,T) \gg I(x,\mu,\nu)\,,$$

so that it is reasonable to approximate

$$2\pi B(\nu,T) - I(x,\mu,\nu) \approx 2\pi B(\nu,T)\,,$$

in which case the group average absorption opacity is found by a simple weighting against the Planck function alone:

$$\sigma_{a,g}(x,T) = \frac{\int_{\nu_{g-1}}^{\nu_g} \sigma_a(x,\nu)B(\nu,T)d\nu}{\int_{\nu_{g-1}}^{\nu_g} B(\nu,T)d\nu}\,. \tag{2.17}$$

The group Rosseland mean is found by making the assumption that the specific intensity satisfies a diffusion equation, given by the system:

$$2\pi B(\nu,T) - I(x,\mu,\nu,t) \approx -\frac{2\pi}{\sigma_a}\frac{\partial B(\nu,T)}{\partial T}\mu\frac{\partial}{\partial x}T(x,t)\,. \tag{2.18}$$

This equation may be found by performing an asymptotic equilibrium diffusion analysis of the TRT equations [38]. It may be expected to be accurate in the interior of a thick problem in which the specific heat is small and the speed of light is large. A more precise interpretation of this equation is [28]:

> Physically, this represents a system in which the mean-free path is $O(\epsilon)$ when compared to the length scale over which I and T vary by $O(1)$, the mean-free time is $O(\epsilon^2)$ when compared to the time scale over which I and T vary by $O(1)$, and $O(\epsilon)$ amounts of radiation energy absorbed and emitted by the material correspond to $O(1)$ changes in the material temperature.

The Rosseland mean is therefore given by:

$$\sigma_{a,g}(x,T) = \frac{\int_{\nu_{g-1}}^{\nu_g} \frac{\partial B(\nu,T)}{\partial T}d\nu}{\int_{\nu_{g-1}}^{\nu_g} \frac{1}{\sigma_a(\nu)}\frac{\partial B(\nu,T)}{\partial T}d\nu}\,. \tag{2.19}$$

The Rosseland mean is accurate if the problem is highly diffusive and slowly varying in time. Unfortunately, the Planck mean and the Rosseland mean absorption opacities can easily differ by an order of magnitude [34]. In this thesis, when group-average absorption opacities are required we will use the Rosseland mean to generate them – the Rosseland mean has been shown to be more accurate in the presence of strong temperature gradients, which we expect to find in our problems of interest [39].

2.2.2 The Gray Approximation

If the opacities are not dependent on frequency, then we may integrate Eqs. (2.4) over all frequencies. If we define:

$$I(x,\mu,t) = \int_0^\infty I(x,\mu,\nu,t)d\nu\,, \tag{2.20a}$$

$$Q(x,t) = \int_0^\infty Q(x,\nu,t)d\nu\,, \tag{2.20b}$$

and use

$$\frac{ac}{4\pi}T^4 = \int_0^\infty B(\nu,T)d\nu\,, \tag{2.20c}$$

then we exactly find:

$$\frac{1}{c}\frac{\partial I}{\partial t}(x,\mu,t) + \mu\frac{\partial}{\partial x}I(x,\mu,t) + \sigma_a(x)I(x,\mu,t) = \sigma_a(x)\frac{ac}{2}T^4 + \frac{Q}{2}(x,t)\,, \tag{2.20d}$$

$$c_v(x,T)\frac{\partial T}{\partial t}(x,t) = \int_{-1}^1 \sigma_a(x)\left[I(x,\mu,t) - \frac{ac}{2}T^4(x,t)\right]d\mu'\,, \tag{2.20e}$$

for $x \in V$, $-1 \leq \mu \leq 1$, and $0 < t$, with initial conditions:

$$I(x,\mu,0) = I^i(x,\mu)\,, \tag{2.20f}$$

$$T(x,0) = T^i(x)\,. \tag{2.20g}$$

and boundary conditions:

$$I(0,\mu,t) = I^\ell(\mu,t) \quad 0 < \mu \leq 1 \tag{2.20h}$$

$$I(X,\mu,t) = I^r(\mu,t) \quad -1 \leq \mu < 0\,. \tag{2.20i}$$

Eqs. (2.20) are known as the *Gray Thermal Radiative Transfer* (GTRT) equations, and are another approximation that methods researchers use for testing purposes. Alternatively, this is also what one would find using $G = 1$ in the multigroup approximation, with a slight caveat if the opacities actually do depend upon frequency. In that case, the Planck mean opacity given in Eq. (2.17) may be explicitly calculated as:

$$\begin{aligned}\sigma_p = \sigma_p(x,t) &\equiv \frac{\int_0^\infty B(\nu,T)\sigma_a(x,\nu)\,d\nu}{\int_0^\infty B(\nu,T)\,d\nu}\,,\\ &= \frac{15\gamma h}{(\pi T)^4}\int_0^\infty \frac{1-e^{-h\nu/T}}{e^{h\nu/T}-1}d\nu\,,\end{aligned}$$

$$= \frac{15\gamma h}{(\pi T)^4} \int_0^\infty e^{-h\nu/T} d\nu \,,$$
$$= \frac{15\gamma}{\pi^4 T^3} \,, \tag{2.21}$$

and the Rosseland mean opacity given in Eq. (2.19) as:

$$\sigma_r = \sigma_{a,g}(x,T) \equiv \frac{\int_0^\infty \frac{\partial B(\nu,T)}{\partial T} d\nu}{\int_0^\infty \frac{1}{\sigma_a(\nu)} \frac{\partial B(\nu,T)}{\partial T} d\nu} \,. \tag{2.22}$$

The numerator of this expression may simplified to:

$$\begin{aligned} \int_0^\infty \frac{\partial}{\partial T} B(\nu,T)\, d\nu &= \frac{\partial}{\partial T} \int_0^\infty B(\nu,T)\, d\nu \\ &= \frac{\partial}{\partial T} \frac{acT^4}{4\pi} \\ &= \frac{acT^3}{\pi} \,. \end{aligned} \tag{2.23}$$

To evaluate the denominator, we first consider:

$$\begin{aligned} \frac{\partial}{\partial T} B(\nu,T) &= \frac{\partial}{\partial T} \frac{2h\nu^3}{c^2} (e^{h\nu/kT} - 1)^{-1} \\ &= \frac{2h\nu^3}{c^2} \frac{-1}{(e^{h\nu/kT} - 1)^2} e^{h\nu/kT} \left(\frac{h\nu}{k}\right) \left(\frac{-1}{T^2}\right) \\ &= \frac{2h^2\nu^4}{kc^2T^2} \frac{e^{h\nu/kT}}{(e^{h\nu/kT} - 1)^2} \,, \end{aligned} \tag{2.24}$$

where T, for now, is written in Kelvin (recall that we have been using $T \leftarrow kT$, we are departing from this for the moment). Then the entire denominator is given by:

$$\begin{aligned} \int_0^\infty \frac{1}{\sigma_a(\nu)} \frac{\partial B(\nu,T)}{\partial T} d\nu &= \int_0^\infty \frac{(h\nu)^3}{\gamma(1 - e^{-h\nu/kT})} \frac{2h^2\nu^4}{kc^2T^2} \frac{e^{h\nu/kT}}{(e^{h\nu/kT} - 1)^2}\, d\nu \,, \\ &= \frac{2h^5}{\gamma kc^2T^2} \int_0^\infty \frac{\nu^7 e^{2h\nu/kT}}{(e^{h\nu/kT} - 1)^3}\, d\nu \,, \end{aligned}$$

and if we define $z = h\nu/kT$,

$$= \frac{2k^7T^6}{\gamma h^3c^2} \int_0^\infty \frac{z^7 e^{2z}}{(e^z - 1)^3}\, dz \,,$$

then the denominator reduces to

$$= \frac{2k^7T^6}{\gamma h^3c^2} Z \,, \tag{2.25}$$

where Z is defined as:

$$Z \equiv \int_0^\infty \frac{z^7 e^{2z}}{(e^z-1)^3}\, dz \,, \tag{2.26}$$

the evaluated integral. Dividing the numerator and denominator, we find that

$$\begin{aligned} \sigma_r &= \frac{acT^3}{\pi} \frac{\gamma h^3 c^2}{2Zk^7T^6} \,, \\ &= \frac{ah^3c^3}{2\pi Zk^7} \frac{\gamma}{T^3} \end{aligned}$$

or, using the definition of a, the radiation constant,

$$\begin{aligned} \sigma_r &= \left(\frac{8\pi^5 k^4}{15h^3c^3} \right) \frac{h^3c^3}{\pi 2Zk^7} \frac{\gamma}{T^3} \\ &= \frac{4\pi^4}{15Z} \frac{\gamma}{k^3T^3} \end{aligned}$$

or, returning T to units of keV,

$$\sigma_r = \frac{4\pi^4}{15Z} \frac{\gamma}{T^3} \,. \tag{2.27}$$

We note here that both σ_p and σ_r are inversely proportional to T^3. This is a strong source of nonlinearity in the TRT equations. Additionally, it is possible to numerically estimate Z, which we find to be approximately equal to $5,105$. Therefore, for this particular analytical model of the absorption opacity, we find that

$$\sigma_r \approx 0.033\, \sigma_p \,. \tag{2.28}$$

This confirms the earlier assertion that the Planck and Rosseland mean opacities can easily differ by an order of magnitude, in this case, for $G = 1$.

The GTRT equations also have a simpler equilibrium solution given by (for any $T_0 > 0$):

$$I(x, \mu, t) = \frac{ac}{2} T_0^4 \,, \tag{2.29a}$$

$$T(x, t) = T_0 \,. \tag{2.29b}$$

2.2.3 The Diffusion Approximation

The next method of simplification eliminates the angular variable by finding equations for the first two terms in a spherical harmonics expansion. We first operate on Eq. (2.4a) by $\int_{-1}^{1}(\cdot)d\mu$ to obtain (exactly):

$$\frac{1}{c}\frac{\partial I_0}{\partial t}(x,\nu,t) + \frac{\partial}{\partial x}I_1(x,\nu,t) + \sigma_a(x,\nu,T)I_0(x,\nu,t) = \sigma_a(x,\nu,T)4\pi B(\nu,T) + Q(x,\nu,t)\,, \quad (2.30)$$

where

$$I_0 = I_0(x,\nu,t) \equiv \int_{-1}^{1} I(x,\mu,\nu,t)d\mu \quad (2.31)$$

is the "scalar intensity", or the isotropic term in the angular expansion, and

$$I_1 = I_1(x,\nu,t) \equiv \int_{-1}^{1} \mu I(x,\mu,\nu,t)d\mu \quad (2.32)$$

is the "radiative flux" or "current." This definition implies I_1 is the magnitude of the radiation energy flowing along the x-axis per unit frequency, area, and time. Next we must attempt to find a closure relationship between I_1 and I_0, since we now have one equation with two unknowns. Operating again on Eq. (2.4a), this time by $\int_{-1}^{1}\mu(\cdot)d\mu$, we obtain:

$$\frac{1}{c}\frac{\partial I_1}{\partial t}(x,\nu,t) + \frac{\partial}{\partial x}\int_{-1}^{1}\mu^2 I(x,\mu,\nu,t)d\mu + \sigma_a(x,\nu,T)I_1(x,\nu,t) = 0\,, \quad (2.33)$$

where the streaming term has been left unevaluated. Evaluating this term exactly would lead to a new term of higher-order angular moments, for which we would have to develop yet another system of equations. Here we assume that the angular dependence of the specific intensity is adequately represented by the first two terms of a Legendre polynomial expansion (an isotropic and linear-in-angle term):

$$I(x,\mu,\nu,t) \approx \frac{1}{2}\left(I_0(x,\nu,t) + 3\mu I_1(x,\nu,t)\right)\,. \quad (2.34)$$

Introducing this approximation into the streaming term of Eq. (2.33), we find:

$$\int_{-1}^{1}\mu^2 I(x,\mu,\nu,t)d\mu \approx \frac{1}{2}\int_{-1}^{1}\mu^2\left(I_0(x,\nu,t) + 3\mu I_1(x,\nu,t)\right)\,,$$

$$= \frac{1}{3} I_0(x,\nu,t)\,.$$

Substituting this result back into Eq. (2.33), we obtain the closure relation:

$$\frac{1}{c}\frac{\partial I_1}{\partial t}(x,\nu,t) + \frac{1}{3}\frac{\partial}{\partial x} I_0(x,\nu,t) + \sigma_a(x,\nu,T)\, I_1(x,\nu,t) = 0\,. \tag{2.35}$$

To get this last equation to resemble Fick's law of diffusion [$I_1 = -D\frac{\partial}{\partial x} I_0$], it is also necessary to assume that the radiative flux is constant, thereby removing the time derivative term. The closure relation becomes:

$$I_1(x,\nu,t) = -D(x,\nu,T)\frac{\partial}{\partial x} I_0(x,\nu,t)\,, \tag{2.36}$$

where

$$D(x,\nu,T) \equiv \frac{1}{3\sigma_a(x,\nu,T)} \tag{2.37}$$

is the so-called diffusion coefficient. Inserting this closure equation into Eq. (2.30) we obtain the *diffusion equation*:

$$\frac{1}{c}\frac{\partial I_0}{\partial t}(x,\nu,t) - \frac{\partial}{\partial x} D(x,\nu,T)\frac{\partial}{\partial x} I_0(x,\nu,t) + \sigma_a(x,\nu,T) I_0(x,\nu,t) = \sigma_a(x,\nu,T) 4\pi B(\nu,T) + Q(x,\nu,t)\,, \tag{2.38a}$$

written only in terms of the first moment, I_0. It is coupled to the material temperature via:

$$c_v(x,T)\frac{\partial T}{\partial t}(x,t) = \int_0^\infty \sigma_a(x,\nu',T)\big[I_0(x,\nu',t) - 4\pi B(\nu',T)\big]\,d\nu'\,. \tag{2.38b}$$

Initial conditions for these equations follow simply by integrating the exact initial condition over angle:

$$I_0(x,\nu,0) = \int_{-1}^{1} I^i(x,\mu,\nu)d\mu\,, \tag{2.38c}$$

$$T_0(x,0) = T^i(x)\,. \tag{2.38d}$$

Next we must consider the boundary condition. Unless the specified boundary source is linearly anisotropic or isotropic, it is impossible to represent exactly. We therefore attempt to satisfy it in an integral sense by preserving the normal component of the radiative flux or current. This is known as the *Marshak* boundary condition, given

by (for the left boundary):

$$I_0(0,\nu,t) - 2D(0,\nu,T)\frac{\partial}{\partial x}I_0(0,\nu,t) = 4\int_0^1 \mu I^\ell(\mu,\nu,t)d\mu\,. \tag{2.38e}$$

Because of the two assumptions made above (the angular expansion and a constant radiative flux), we expect these equations to be accurate in problems in which the flux is nearly isotropic. The problem should also be slowly varying – sudden changes in the boundary conditions or materials would not be treated accurately. Although problems of interest may violate these assumptions, the diffusion approximation (or a variant of it) is still frequently used because of the large savings in modeling time and the reduction of other complicating factors that arise in a more accurate treatment of the angular variable.

2.2.4 The Quasidiffusion Approximation

In addition to the diffusion approximation, we shall use a "Quasidiffusion", or Variable Eddington Factor approximation of the solution [40]. The derivation of this method is closely analogous to that of the diffusion approximation, with the exception that the P_1 approximation is not made. That is, instead of truncating an angular expansion as in Eq. (2.34), we define the *Eddington factor*:

$$E(x,\nu,t) \equiv \frac{\int_{-1}^1 \mu^2 I(x,\mu,\mu,t)\; d\mu}{\int_{-1}^1 I(x,\mu,\mu,t)\; d\mu}\,. \tag{2.39}$$

Of course, this Eddington factor depends on the unknown intensity, and is itself unknown. In practice, this is remedied through an iteration process to convergence (in deterministic methods), or one simply makes due with an approximate Eddington factor in the hopes that the overall approximation is better than diffusion alone. Assuming for the moment that E is found exactly, the streaming term in Eq. (2.33) may be rewritten as:

$$\frac{\partial}{\partial x}\int_{-1}^1 \mu^2 I(x,\mu,\nu,t)d\mu = \frac{\partial}{\partial x}E(x,\nu,t)I_0(x,\nu,t)\,,$$

so that Eq. (2.33) then becomes:

$$\frac{1}{c}\frac{\partial I_1}{\partial t}(x,\nu,t) + \frac{\partial}{\partial x}E(x,\nu,t)I_0(x,\nu,t) + \sigma_a(x,\nu,T)I_1(x,\nu,t) = 0\,. \tag{2.40}$$

To obtain a simple (Fick's law-type) closure relation, it is still necessary to assume make the constant flux assumption ($\partial I_1(t)/\partial t = 0$). Doing this, we find a new closure relation:

$$I_1(x,\nu,t) = -\frac{1}{\sigma_a}\frac{\partial}{\partial x}EI_0\,, \tag{2.41}$$

which we substitute into Eq. (2.30) to obtain the *Quasidiffusion equation* in its final form:

$$\frac{1}{c}\frac{\partial I_0}{\partial t}(x,\nu,t) - \frac{\partial}{\partial x}\frac{1}{\sigma_a(x,\nu,T)}\frac{\partial}{\partial x}E(x,\nu,t)I_0(x,\nu,t) + \sigma_a(x,\nu,T)I_0(x,\nu,t) = \sigma_a(x,\nu,T)4\pi B(\nu,T) + Q(x,\nu,t)\,. \tag{2.42}$$

As in the diffusion approximation, the Quasidiffusion equation is written only in terms of the first angular moment I_0. It is coupled to the material temperature equation, and has the same initial conditions as the diffusion equation in the previous section. One may derive Eddington factors on the boundary to obtain a nearly-exact system of equations (the only assumption being the approximation in the time-derivative of the radiative flux). However, in this thesis we shall hedge and use the Marshak boundary condition as stated in Eq. (2.38e). This is because we shall employ the Quasidiffusion approximation only to find *approximate* forward solutions that will subsequently be corrected by a detailed transport calculation.

As the angular intensity becomes isotropic, $E \to 1/3$, which reduces the above to the classical diffusion approximation. We note also that $0 < E \leq 1$. It can also be shown that E depends primarily on the angular shape of I and is relatively insensitive to other variations in phase space. Thus, a Monte Carlo estimator of E should have less variance than an estimator for ϕ.

2.2.5 A Simplifying Linearization

In 1979, Gerald Pomraning discovered a simple choice of material properties for the 1-D Gray Diffusion equations that removed the nonlinear interaction between the specific intensity and material temperature [41]. Some time later, Su and Olson extended the original problem to allow for finite particle speeds and include isotropic scattering, and also found a specific problem that allows for frequency dependence [32] [42] [43]. These references also provide a series of "analytical" benchmark solutions for researchers to test their radiative transfer computational models. We will illustrate their results for the homogeneous, 1-D, gray equations with material

properties carefully chosen such that:

$$\sigma_a(x,T) = \sigma_a \text{ (temperature/space-independent)} \ , \tag{2.43a}$$

$$c_v(T) = vT^3 \, , \tag{2.43b}$$

$$Q(x,t) = \frac{1}{2x_0}\big(H(x+x_0) - H(x-x_0)\big)\big(H(t) - H(t-t_0)\big) \tag{2.43c}$$

where v is a constant. Here, $H(x)$ is a unit Heaviside step function. Thus Q is a constant source between $[-x_0, x_0]$ during time $[0, t_0]$, and is otherwise zero. We also note that, since $U_r = aT^4$,

$$\frac{1}{4a}\frac{\partial U_r}{\partial t} = T^3 \frac{\partial T}{\partial t} \, .$$

Then the 1-D GTRT equations become:

$$\frac{1}{c}\frac{\partial I}{\partial t}(x,\mu,t) + \mu\frac{\partial}{\partial x}I(x,\mu,t) + \sigma_a I(x,\mu,t) = \frac{\sigma_a}{2}U_r(x,t) + \frac{Q}{2}(x,t) \, , \tag{2.44a}$$

$$\frac{\alpha}{4a}\frac{\partial U_r}{\partial t}(x,t) + \sigma_a U_r(x,t) = \int_{-1}^{1} \sigma_a I(x,\mu,t) \, d\mu' \, . \tag{2.44b}$$

Thus, with this choice of material properties, the equations become linear in I and U_r (or T^4), and *almost* analytically solvable (It is necessary to numerically evaluate several integrals; the exact analytic solution is therefore only available to the amount of digits one is willing to work for). It should be noted that these choices of material properties are not physical in nature. However, as Pomraning put it, "We wish to maintain the underlying equations and relax the physical content of the problem to obtain a detailed solution." Yet there is a case in which these assumptions have physical merit. It occurs when the gray, TRT equations are almost in equilibrium, or when the solution can be well-described by a linear perturbation about the constant, equilibrium solution [44]. The above equations therefore emerge either from assuming this "non-physical" material dependence, or they describe first-order linear correction terms to an equilibrium solution.

Although we do not present the results explicitly, we use the benchmark solutions of Su and Olson to verify the accuracy of our computational models. The simpler, linear form of the TRT equations in Eqs. (2.44) is also a convenient testing ground to evaluate the efficacy of numerical approximations to the TRT equations, as numerical methods that do not well-resolve the solutions to the linear problem cannot be expected to adequately perform on more general, nonlinear problems.

Chapter III

The Implicit Monte Carlo Method and its Monte Carlo Interpretation

The first step in most of the commonly-used methods to solve the nonlinear TRT equations is to linearize them over a time step $t_n \leq t \leq t_{n+1}$. This linearization usually incurs a time-discretization error that is proportional to the size of the time step, but it enables the utilization of a large portion of the existing arsenal of linear transport methods. In this chapter, we focus on a well-known and widely-used linearization and its subsequent Monte Carlo interpretation: the Implicit Monte Carlo (IMC) method proposed by Fleck and Cummings [21]. We begin by deriving the IMC equations, making it clear when and how approximations are introduced into the underlying TRT equations. It is important that these approximations be made in such a way that (i) energy is conserved, (ii) stability is maintained, and (iii) accuracy is not largely compromised. We then discuss the implications of the approximations made throughout the derivation on the accuracy, stability, and physicality of the resulting IMC equations, including a critique that has not previously appeared. Next, we describe a generic linear Monte Carlo methodology that is typically used to solve such equations. We provide the IMC equations with a Monte Carlo interpretation, a task that has never been formally implemented in existing literature. The chapter concludes with details necessary to computationally implement a Monte Carlo solver for the IMC equations and a brief introduction to some techniques that can be used to reduce the statistical variance of its solutions.

We begin by rewriting the TRT equations in an equivalent form that is more amenable to a Monte Carlo interpretation. We then derive an equation for the conservation of energy and make some general remarks about its physics.

3.1 Recasting the TRT Equations

The 1-D TRT equations, with their arguments suppressed for clarity, are [from Eqs. (2.4)]:

$$\frac{1}{c}\frac{\partial I}{\partial t} + \mu\frac{\partial I}{\partial x} + \sigma_a I = 2\pi\sigma_a B + \frac{Q}{2}\,, \tag{3.1a}$$

$$\frac{\partial U_m}{\partial t} = \int_0^\infty \int_{-1}^1 \sigma_a (I - 2\pi B)\; d\mu' d\nu'\,. \tag{3.1b}$$

It is useful to make some definitions that will simplify the forthcoming Monte Carlo interpretation of these equations. First, we rewrite the Planck function as:

$$\begin{aligned} B(\nu, T) &= \frac{2h\nu^3}{c^2}\left(e^{h\nu/T} - 1\right)^{-1}\,, \\ &\equiv b(\nu, T)\frac{cU_r(T)}{4\pi}\,, \end{aligned}$$

where b is a frequency-normalized Planck function [see Eq. (2.20c)] given by:

$$\begin{aligned} b = b(\nu, T) &= \frac{B(\nu, T)}{caT^4/4\pi}\,, \\ &= \frac{15h^4\nu^3}{\pi^4 T^4}\left(e^{h\nu/T} - 1\right)^{-1}\,, \end{aligned} \tag{3.2a}$$

which, by its definition, satisfies:

$$\int_0^\infty b(\nu, T)\; d\nu = 1\,.$$

We also define an exact relationship between the material and radiation energy densities:

$$\beta = \beta(x, t) = \frac{\partial U_r}{\partial U_m}\,, \tag{3.2b}$$

and note that

$$\beta = \frac{\partial U_r}{\partial U_m} = \frac{dU_r}{dT}\frac{\partial T}{\partial U_m} = \frac{4aT^3}{c_v(T)}\,. \tag{3.2c}$$

Finally, we rewrite Eqs. (3.1) using these definitions and the definition of the Planck mean in Eq. (2.17). The intensity equation becomes:

$$\frac{1}{c}\frac{\partial I}{\partial t} + \mu\frac{\partial I}{\partial x} + \sigma_a I = \frac{1}{2}\sigma_a bcU_r + \frac{Q}{2}\,, \tag{3.3a}$$

with the material energy equation given by

$$\frac{1}{\beta}\frac{\partial U_r}{\partial t} + \sigma_p c U_r = \iint \sigma_a I \; d\mu' d\nu' \,, \tag{3.3b}$$

or

$$\frac{\partial U_m}{\partial t} + \sigma_p c U_r = \iint \sigma_a I \; d\mu' d\nu' \,, \tag{3.3c}$$

where the double integral integrates over all frequencies and angles, and we have made a substitution in Eq. (3.3b) using Eq. (3.2c):

$$\frac{\partial U_m}{\partial t} = \frac{\partial U_m}{\partial U_r}\frac{\partial U_r}{\partial t} = \frac{1}{\beta}\frac{\partial U_r}{\partial t} \,.$$

Although it may seem redundant to write Eq. (3.3b) and Eq. (3.3c) in different but mathematically equivalent forms, approximations are typically made to one or the other equation in such a way that they lose their equivalency. Eqs. (3.3) are an exact recasting of the original TRT equations, and they serve as a starting point for subsequent derivations.

It is desirable to create methods that conserve energy. To this end, we here derive the exact energy conservation equation. First, we operate on Eq. (3.3a) by integrating over all angles and frequencies:

$$\frac{1}{c}\frac{\partial I_0}{\partial t} + \frac{\partial I_1}{\partial x} + \iint \sigma_a I \; d\mu d\nu = c\sigma_p U_r + Q \,, \tag{3.4}$$

where $I_0(x,t) = \iint I(x,\mu,\nu,t) d\mu d\nu$ and $I_1(x,t) = \iint \mu I(x,\mu,\nu,t) d\mu d\nu$, as in Chapter 2. We add this result to Eq. (3.3c) to obtain

$$\frac{1}{c}\frac{\partial I_0}{\partial t} + \frac{\partial I_1}{\partial x} + \frac{\partial U_m}{\partial t} = Q \,,$$

or:

$$\frac{\partial}{\partial t}\left(\frac{I_0}{c} + U_m\right) = Q - \frac{\partial I_1}{\partial x} \,. \tag{3.5}$$

Eq. (3.5) is an exact statement of energy conservation at any time t. The two terms inside the time derivative represent the total energy in the radiation and the material; their time derivative depends only on gains from a source Q or losses due to leakage. It is important to observe that two cancellations occur when the equations are added, namely, the absorption $[\iint \sigma_a I d\mu d\nu]$ and emission $[c\sigma_p U_r]$ terms that

couple the two equations necessarily drop out. We shall later make approximations to Eqs. (3.3), but it these approximations will not affect the conservation of energy given by Eq. (3.5). To accomplish this, approximations applied to the absorption and emission terms in Eq. (3.3a) must be performed alongside consistent approximations to the corresponding terms in Eq. (3.3c). [Eq. (3.3b) is rarely used to estimate the temperature at the end of the time step in Monte Carlo methods.] If this is done, then any approximate rendering of the absorption and emission processes will have no effect on the conservation of energy.

3.2 Time Discretization and Linearization

In 1971, Fleck and Cummings published a seminal paper describing a particular time-discretization and linearization of the TRT equations: the IMC method [21]. This method approximates the TRT equations in such a way that the resulting equations become similar in character to that of a linear neutron transport problem. Fleck and Cummings went on to discuss a Monte Carlo interpretation of the equations, whose details we shall consider later. The essential feature of the linearization is to approximate photon absorption and reemission in a special way through an "effective scattering" process. This approximation essentially allows for much larger time steps than the mean absorption-reemission duration – a very short interval – without a great expense in accuracy. This advantage is characteristic of most time implicit methods, although the quantifier "implicit" is a misnomer since the problem parameters must be (explicitly) evaluated at the beginning of the time step. The IMC method has emerged as the standard for solving radiative transfer problems, and has even been adapted for deterministic methods [45].

The introduction of effective scattering is born from an attempt to reduce the complexity of the coupling between the material temperature T and the radiation I. The central observation is that if the radiation source term $\sigma_a B$ could be approximated by the current intensity and other quantities known at the beginning of the time step, then the equations "would be coupled in a simpler lower-triangular manner" [22]. Specifically, Eq. (3.3a) could then be solved *independently* of Eq. (3.3c), with the result used to solve Eq. (3.3c).

We begin the derivation by making an approximation of necessity. Many of the parameters in Eqs. (3.1) are temperature- or otherwise time-dependent. In general, information is known at the beginning of a time step $t = t_n$ from a previous calculation or initial conditions, and the solution is then desired at the end of the time

step $t_{n+1} = t_n + \Delta_{t,n}$. We therefore approximate most of these parameters with their values at the beginning of the time step. Where this is done, the new quantity will have the subscript n:

$$\sigma_{a,n} = \sigma_a(x, \nu, T(t_n)) \approx \sigma_a(x, \nu, T(t)) \,, \tag{3.6a}$$

$$b_n = b(\nu, T(t_n)) \approx b(\nu, T(t)) \,, \tag{3.6b}$$

$$\sigma_{p,n} = \int \sigma_{a,n} b_n(\nu)\, d\nu \approx \int \sigma_a(x, \nu, T(t))\, b(\nu, T(t))\, d\nu \tag{3.6c}$$

Naturally, these approximations lose validity if the solution rapidly changes during a time step, although energy conservation is unaffected (none of the above terms appear in Eq. (3.5)). Next, we make the fundamental approximation to reduce the complexity of the coupling between the intensity equation Eq. (3.3a) and the material equation Eq. (3.3b):

$$\frac{c_v}{4aT^3}\frac{\partial U_r}{\partial t} \approx \frac{c_{v,n}}{4aT_n^3}\frac{\partial U_r}{\partial t} = \frac{1}{\beta_n}\frac{\partial U_r}{\partial t} \,, \tag{3.7}$$

and we introduce this result into Eq. (3.3b) to obtain a *linear* equation for U_r:

$$\frac{1}{\beta_n}\frac{\partial U_r}{\partial t} + \sigma_{p,n} c U_r = \iint \sigma_{a,n} I \; d\mu' d\nu' \,. \tag{3.8}$$

We pause here to note that when the approximation ($\beta \approx \beta_n$) is made, the two material update equations given by Eq. (3.3b) and Eq. (3.3c) are no longer equivalent. The next step is to discretize Eq. (3.8) in time. If we define a time-average nomenclature by:

$$\overline{f} = \frac{1}{\Delta_{t,n}} \int_{t_n}^{t_{n+1}} f(t)\, dt \,, \tag{3.9}$$

and we operate with it on Eq. (3.8), we obtain (exactly):

$$\frac{U_{r,n+1} - U_{r,n}}{\Delta_{t,n}\beta_n} + \sigma_{p,n} c \overline{U_r} = \iint \sigma_{a,n} \overline{I}\, d\mu' d\nu' \,. \tag{3.10}$$

Our next goal is to eliminate $U_{r,n+1}$ from this equation so that it only contains time-average and beginning-of time step information. To do this, Fleck and Cummings make the approximation

$$\overline{U_r} \approx \alpha U_{r,n+1} + (1-\alpha) U_{r,n} \,,$$

which may also be written as:

$$U_{r,n+1} - U_{r,n} = \frac{\overline{U_r} - U_{r,n}}{\alpha}\,, \tag{3.11}$$

where α is a user-defined parameter such that $\frac{1}{2} \leq \alpha \leq 1$. This parameter controls, to some extent, the degree of "implicitness" of the method, with $\alpha = 1$ being the most implicit and commonly-used choice. Using this result, Eq. (3.10) becomes:

$$\frac{\overline{U_r} - U_{r,n}}{\alpha\Delta_{t,n}\beta_n} + \sigma_{p,n}c\overline{U_r} = \iint \sigma_{a,n}\overline{I}\, d\Omega' d\nu'\,. \tag{3.12}$$

Grouping terms and solving for $\overline{U_r}$, we get:

$$\overline{U_r} = \frac{1}{1+\alpha\Delta_{t,n}\beta_n c\sigma_{p,n}} U_{r,n} + \frac{\alpha\Delta_{t,n}\beta_n}{1+\alpha\Delta_{t,n}\beta_n c\sigma_{p,n}} \iint \sigma_{a,n}\overline{I}\, d\mu' d\nu'\,. \tag{3.13}$$

We next define the *Fleck factor*, f, given by

$$f_n = \frac{1}{1+\alpha\Delta_{t,n}\beta_n c\sigma_{p,n}}\,, \tag{3.14}$$

and we rewrite Eq. (3.13) as:

$$\overline{U_r} = f_n U_{r,n} + \frac{(1-f_n)}{c\sigma_{p,n}} \iint \sigma_{a,n}\overline{I}\, d\mu' d\nu'\,. \tag{3.15}$$

The final (and most dubious) approximation is to replace the time-average values in Eq. (3.15) by their "instantaneous" counterparts, $\overline{U_r} \approx U_r(t)$, and $\overline{I} \approx I(t)$, to obtain:

$$U_r(t) \approx f_n U_{r,n} + \frac{(1-f_n)}{c\sigma_{p,n}} \iint \sigma_{a,n} I(x,\mu',\nu',t)\, d\mu' d\nu'\,. \tag{3.16}$$

This is the result we are after: $U_r(t)$ now depends explicitly on "old" data and current intensity data only; i.e., the system is now lower triangular. However, we remark here that Eq. (3.16) is only true in a time-average sense. That is, averaging Eq. (3.16) over the time step will reproduce Eq. (3.15), but Eq. (3.16) is not exact at $t = t_n$. In Chapter VI we consider replacing this approximation with a more accurate one.

We continue by substituting Eq. (3.16) into Eq. (3.3a):

$$\frac{1}{c}\frac{\partial I}{\partial t} + \mu\frac{\partial I}{\partial x} + \sigma_{a,n} I = \frac{1}{2}\sigma_{a,n} b_n c f_n U_{r,n} + \frac{1}{2}\frac{\sigma_{a,n} b_n}{\sigma_{p,n}} \iint (1 - f_n)\sigma_{a,n} I(x, \mu', \nu', t)\, d\mu' d\nu' + \frac{Q}{2}\,, \quad (3.17)$$

and we define effective absorption and scattering opacities:

$$\sigma_{ea,n} = \frac{\sigma_{a,n}}{1 + \alpha\Delta_{t,n}\beta_n c\sigma_{p,n}} = f_n \sigma_{a,n}\,, \quad (3.18a)$$

$$\sigma_{es,n} = \frac{\sigma_{a,n}\alpha\Delta_{t,n}\beta_n c\sigma_{p,n}}{1 + \alpha\Delta_{t,n}\beta_n c\sigma_{p,n}} = (1 - f_n)\sigma_{a,n}\,. \quad (3.18b)$$

It should be remarked that f_n – and the scattering ratio $(1 - f_n)$ – are independent of frequency. Additionally, the sum of the effective opacities is the true absorption opacity:

$$\sigma_{a,n} = \sigma_{es,n} + \sigma_{ea,n}\,. \quad (3.18c)$$

We also define a local "reemission spectrum" $\chi_n(x, \nu)$: [1]

$$\chi_n = \chi_n(x, \nu) \equiv \frac{\sigma_{a,n} b_n}{\int \sigma_{a,n} b_n\, d\nu'} = \frac{\sigma_{a,n} b_n}{\sigma_{p,n}} = \frac{1}{T_n} e^{-\nu/T_n}\,, \quad (3.19a)$$

which satisfies

$$\int_0^\infty \chi_n(x, \nu)\, d\nu = 1\,. \quad (3.19b)$$

The definitions given by Eqs. (3.18) and Eq. (3.19a) allow us to write Eq. (3.17) as a linear transport equation similar in character to that of neutron transport:

$$\frac{1}{c}\frac{\partial I}{\partial t} + \mu\frac{\partial I}{\partial x} + \sigma_{a,n} I = \frac{1}{2}\sigma_{ea,n} b_n c U_{r,n} + \frac{1}{2}\chi_n \iint \sigma_{es,n} I\, d\mu' d\nu' + \frac{Q}{2}\,. \quad (3.20)$$

This equation, together with the boundary conditions for I and the "initial" conditions for I at $t = t_n$, determine I during the time step $t_n \le t \le t_{n+1}$.

The next task is to derive an equation that allows for a calculation of the temperature at the end of the time step $t = t_{n+1}$, assuming that some procedure has been used to solve Eq. (3.20). We next perform the time-averaging integral on Eq. (3.3c)

[1] Note that the rightmost form of $\chi_n(x, \nu)$ in Eq. (3.19a) contains a scaled frequency ν in units of $h\nu'$ and a scaled temperature T in units of kT', where ν' (s^{-1}) and T' (K) are the original quantities. If desired, one can replace these with the original terms $h\nu$ and kT, but the definition in Eq. (3.19a) avoids the introduction of h and k into a computational implementation.

to obtain:

$$\frac{U_{m,n+1} - U_{m,n}}{\Delta_{t,n}} = \iint \sigma_{a,n} \overline{I} \; d\mu' d\nu' - \sigma_{p,n} c \overline{U_r} \, . \tag{3.21}$$

To conserve energy, we must approximate this equation in precisely the same way we performed the approximations that led us to Eq. (3.20). We therefore substitute Eq. (3.15) into Eq. (3.21) to find:

$$\frac{U_{m,n+1} - U_{m,n}}{\Delta_{t,n}} = \iint \sigma_{a,n} \overline{I} \; d\mu' d\nu' - \sigma_{p,n} c \left(f_n U_{r,n} + \frac{1-f}{c\sigma_{p,n}} \iint \sigma_{a,n} \overline{I} \; d\mu' d\nu' \right) . \tag{3.22}$$

and solve for $U_{m,n+1}$ to obtain:

$$U_{m,n+1} = U_{m,n} - c f_n \sigma_{p,n} \Delta_{t,n} U_{r,n} + \iint f_n \sigma_{a,n} \Delta_{t,n} \overline{I} \; d\mu' d\nu' \, . \tag{3.23}$$

Once $U_{m,n+1}$ is calculated, the temperature T_{n+1} can be updated by solving:

$$U_{m,n+1} = \int_0^{T_{n+1}} c_v(T') \; dT' \, . \tag{3.24}$$

In the case of a perfect gas, this reduces to $T_{n+1} = U_{m,n+1}/c_v$.

Throughout this derivation it has been asserted that none of the approximations has violated the conservation of energy given by Eq. (3.5). We next demonstrate this explicitly by rederiving the conservation of energy from Eq. (3.20) and Eq. (3.22). Recalling the definitions of the effective absorption and scattering opacities [Eqs. (3.18)] and the definition of the Planck mean opacity [Eq. (2.17)], Eq. (3.20) may be integrated over all frequencies and angles to obtain:

$$\frac{1}{c} \frac{\partial I_0}{\partial t} + \frac{\partial I_1}{\partial x} + \iint \sigma_{a,n} I \, d\mu d\nu = f_n \sigma_{p,n} c U_{r,n} + \iint (1 - f_n) \sigma_{a,n} I \; d\mu' d\nu' + Q \, , \tag{3.25}$$

and, replacing the "dummy variables" in the effective scattering integral with μ and ν, this simplifies to

$$\frac{1}{c} \frac{\partial I_0}{\partial t} + \frac{\partial I_1}{\partial x} + \iint f_n \sigma_{a,n} I \, d\mu d\nu = f_n \sigma_{p,n} c U_{r,n} + Q \, . \tag{3.26}$$

We next integrate this equation over the time step using the time-averaging operator and notation defined in Eq. (3.9):

$$\frac{1}{c\Delta_{t,n}}(I_{0,n+1} - I_{0,n}) + \frac{\partial \overline{I}_1}{\partial x} + \iint f_n \sigma_{a,n} \overline{I}\, d\mu d\nu = f_n \sigma_{p,n} c U_{r,n} + \overline{Q}\,. \tag{3.27}$$

Adding this result to Eq. (3.22), we correctly reproduce a time-averaged version of the conservation of energy in Eq. (3.5):

$$\frac{1}{\Delta_{t,n}} \left(\frac{1}{c}(I_{0,n+1} - I_{0,n}) + U_{m,n+1} - U_{m,n} \right) = \overline{Q} - \frac{\partial \overline{I}_1}{\partial x}\,. \tag{3.28}$$

Note that the approximated absorption and reemission terms – as well as the problem data that was frozen at the beginning of the time step – vanish as was claimed earlier.

To bring this all together, in the IMC method, we first solve the following radiation transport equation for I:

$$\frac{1}{c}\frac{\partial I}{\partial t} + \mu \frac{\partial I}{\partial x} + \sigma_{a,n} I = \frac{1}{2}\sigma_{ea,n} b_n c U_{r,n} + \frac{\chi_n}{2} \iint \sigma_{es,n} I \; d\mu' d\nu' + \frac{Q}{2}\,, \tag{3.29a}$$

after which, we calculate the material energy density at the end of the time step using:

$$U_{m,n+1} = U_{m,n} - c f_n \sigma_{p,n} U_{r,n} \Delta_{t,n} + \int_{t_n}^{t_{n+1}} \iint \sigma_{ea,n} I \; d\mu d\nu dt\,, \tag{3.29b}$$

and the temperature T_{n+1} from:

$$U_{m,n+1} = \int_0^{T_{n+1}} c_v(T') \; dT'\,. \tag{3.29c}$$

Eq. (3.29b) has the interpretation that, during a time step, the change in material energy is due to a loss term to the radiation and a gain term due to effective absorptions. This latter quantity must be found from a detailed solution of Eq. (3.29a). The initial and boundary conditions are given by:

$$I(x, \mu, \nu, 0) = I^i(x, \mu, \nu)\,, \tag{3.29d}$$

$$T(x, 0) = T^i(x)\,, \tag{3.29e}$$

$$I(0, \mu, \nu, t) = I^\ell(\mu, \nu, t)\,, 0 < \mu \leq 1\,, \tag{3.29f}$$

$$I(X, \mu, \nu, t) = I^r(\mu, \nu, t)\,, -1 \leq \mu < 0\,. \tag{3.29g}$$

3.2.1 Discussion

The introduction of effective scattering into a system that previously had no scattering is worth some attention. The phenomenon is an approximation "in that only the current collision time t is used for modeling the absorption-reemission process, rather than the collective collisions from t_n through t, and the particle is emitted immediately" [24]. In Eqs. (3.29), the Fleck factor f dictates the degree to which the absorption-reemission process is approximated by effective scattering; in fact, $(1-f) = \sigma_{es}/\sigma_a$ is the probability of effective scatter. Since $f \to 0$ as Δ_t becomes large, the probability of effective scattering increases for large time steps. Physically, this means that during long time steps, it is much more likely that absorbed particles will become re-emitted. This behavior was designed to occur in order to reduce the computational requirements of simulating a photon; instead of simulating many absorptions and reemissions, several scattering events are simulated. In many realistic problems, it is typical to find values of f that are nearly equal to 1.

It should be stated that Eqs. (3.29), as they are written, are not analytically solvable except for in the simplest of situations. Therefore, additional approximations in space – and perhaps frequency and angle – are generally required before they may be provided with a Monte Carlo or deterministic solution methodology. However, several questions may be raised at this stage, such as, are Eqs. (3.29) stable? Are they physically meaningful and accurate?

We first consider the question of whether or not Eqs. (3.29) produce physically meaningful solutions. It has already been demonstrated that they satisfy the conservation of energy. And, by inspection, Eqs. (3.29) obtain the correct equilibrium solutions when $\Delta_t \to \infty$. Both of these issues are addressed in Fleck and Cummings paper [21]. However, it is not clear whether or not solutions of Eqs. (3.29) are always positive. We claim that Eqs. (3.29) generally should not produce negative solutions given physically meaningful inputs. In Eq. (3.29a), this is readily apparent since all of its source terms and coefficients are positive. However, in Eq. (3.29b) a negative term appears, which warrants a further analysis that, to this author's knowledge, has not appeared previously. Ignoring the ameliorating effect of the positive effective absorption term in Eq. (3.29b), we question whether

$$U_{m,n} - cf_n\sigma_{p,n}U_{r,n}\Delta_{t,n} > 0\,? \tag{3.30}$$

Using the definition of β from Eq. (3.2b), we write

$$\beta_n = \frac{4aT_n^3}{c_{v,n}} = 4\frac{U_{r,n}}{c_{v,n}T_n}\,, \tag{3.31}$$

which may be solved for $U_{r,n}$ to produce:

$$U_{r,n} = \frac{1}{4}\beta_n c_{v,n} T_n\,. \tag{3.32}$$

We therefore rewrite the inequality as:

$$U_{m,n} - \frac{1}{4}cf_n\sigma_{p,n}\Delta_{t,n}\beta_n c_{v,n}T_n \overset{?}{>} 0\,. \tag{3.33}$$

Next, we employ the definition of the Fleck factor in Eq. (3.14) to obtain:

$$U_{m,n} - \frac{1-f_n}{4\alpha}c_{v,n}T_n \overset{?}{>} 0\,, \tag{3.34}$$

and, since f_n is bounded below by 0, the following condition is sufficient for positivity:

$$U_{m,n} \overset{?}{>} \frac{1}{4\alpha}c_{v,n}T_n\,. \tag{3.35}$$

Since $\alpha \geq 1/2$ (and usually $\alpha = 1$), the question of whether this equation is satisfied primarily depends upon the definition of the specific heat $c_v(T)$. It is possible to find functional forms of the specific heat for which this inequality fails to hold. For instance, let us assume that the vast majority of physically meaningful specific heats may be adequately described by a function of the form:

$$c_v(T) = vT^z\,, \tag{3.36}$$

where v is a constant and $z > 0$ (note that for a perfect gas, $z = 0$, and for the linear "Su-Olson" problem described in Section 2.2.5, $z = 3$). Then Eq. (3.35) becomes

$$\begin{aligned} v\frac{T_n^{z+1}}{z+1} &\overset{?}{>} \frac{1}{4\alpha}vT_n^{z+1}\,, \\ 1 &\overset{?}{>} \frac{z+1}{4\alpha}\,. \end{aligned} \tag{3.37}$$

In practice, the choice $\alpha = 1$ is almost always made. In that case, the inequality in Eq. (3.37) is true when $z \leq 3$. Since $z = 0$ for an ideal gas, and it is unlikely that $z > 3$ describes any physically meaningful material, in most practical situations

Eq. (3.29b) produces positive temperatures. It is possible that Fleck and Cummings anticipated this and declined to remark upon it. However, for the linear Su-Olson problem (in which $z = 3$), the choice $\alpha = 1/2$ violates the inequality in Eq. (3.37). This means that it *is* possible to find a value of $\Delta_{t,n}$ for which Eq. (3.29b) produces a negative temperature, at least for this commonly-used benchmarking problem.

As for stability, Fleck and Cummings claim that it should be sufficient to enforce the inequality [21]:

$$(1 - \alpha)\beta_n c\Delta_{t,n}\sigma_{p,n} \leq 1\,, \tag{3.38}$$

otherwise, unphysical temporal oscillations may occur in the material temperature. They then implore the reader to choose $\alpha = 1$ if "large" time steps are to be used, which means that this inequality is always satisfied. However, this is not the end of the story, as even when $\alpha = 1$, it is possible for the IMC equations to produce damped temporal oscillations. This latter "stability" issue is discussed in depth in Chapter IV of this thesis. Finally, Fleck and Cummings assert that, "α should in general vary between $\frac{1}{2}$ and 1." In Chapter IV we shall rigorously demonstrate that for a typical analytic form of the specific heat and opacities, $\alpha \geq \frac{1}{2}$ is a necessary condition for Eqs. (3.29) to be unconditionally stable.

Concerning accuracy, of foremost importance are the approximations introduced in Eqs. (3.6) and Eq. (3.7), namely, when the problem data is frozen at the *beginning* of the time step. If these data could be estimated using some form of temporal averaging, the equations should become more accurate. In their paper, Fleck and Cummings allude to using a form of time-extrapolation to guess a more accurate temperature based upon the temperatures from previous time steps. However, experience has shown that these temperature extrapolations can introduce undesirable properties into the calculations. Specifically, they can affect the stability and accuracy of the result, especially if the underlying solution method is prone to errors (such as statistical noise in a Monte Carlo calculation). Hence, temperature extrapolation is usually avoided in practice, and the problem data is frozen at the beginning of the time step. In Chapter V of this theses, we discuss an alternative way of estimating the temperature at the end of a time step that relies on a relatively inexpensive, additional deterministic calculation.

Another inaccuracy is created when α is introduced into the system of equations, followed by the approximation in Eq. (3.16), in which time-averaged unknowns are replaced by "instantaneous" unknowns. Since α is user-defined, it cannot accurately relate $U_r(t)$ to $U_{r,n}$ and $U_{r,n+1}$. Eliminating the user parameter α and obtaining a

more accurate approximation of $U_r(t)$ – that still retains the form of Eqs. (3.29) – is the subject of Chapter VI of this thesis. A more rigorous error analysis of Eqs. (3.29) is also presented there for a simplified, but representative class of problems. Yet, the conventional wisdom is that the error in Eqs. (3.29) may be reduced linearly in proportion to the size of the time step. In the parlance of numerical analysis, Eqs. (3.29) are "first-order accurate" in $\Delta_{t,n}$. Additionally, for sufficiently simple problems[2] [46], it is possible to obtain second-order accuracy (implying a quadratic reduction in error) when $\alpha = 1/2$ is chosen.

Additionally, it has been shown that the IMC method is inaccurate (physically impermissibly so) during transients if too-large time steps are used, and it is difficult to determine a priori how small the time steps should be [27]. When one considers the assumptions made in deriving these equations – especially the evaluation of opacities and an emission spectrum using an old (or forward extrapolated) temperature, this is not completely surprising. It has also been shown that the IMC method does not preserve an equilibrium diffusion limit [28]. However, the inaccuracies that do occur in the equations have not been prohibitive.

Despite these difficulties, IMC has been widely-used by the radiative transfer community, and it is a surprisingly robust method when knowledgeably employed. We next motivate a Monte Carlo interpretation of Eqs. (3.29) by discussing the characteristics of a generic, linear transport Monte Carlo algorithm.

3.3 Monte Carlo

A *Monte Carlo* method uses stochastic techniques to estimate the solution of a problem. In general, such problems are simulated on a computer using a large number of random or pseudorandom numbers combined with probability density functions (pdfs) to generate an average result. Monte Carlo transport methods are also more closely linked to the transport processes of physical particles, which implies that the underlying functions and terms in their computational implementation usually retain clear, physical interpretations. By contrast, deterministic transport methods often require careful calculation and attribution of a multitude of terms that make up the coefficients of the underlying large, algebraic system, making them more tedious to implement correctly. Monte Carlo methods also require fewer approximations than deterministic methods; in linear Monte Carlo transport methods, for instance, there is no need to discretize the problem, provided that continuous problem parameters

[2] In [46], a 0-D problem with constant opacities and specific heat is considered.

are known.

Generating a Monte Carlo method for a transport problem involves careful construction of pdfs based on the physical events a particle could undergo in its lifetime (sometimes referred to as a particle *history*). A generic particle history employs random numbers to create a particle inside the simulated problem geometry, choose where the particle travels, choose a collision or leakage event, etc., until the particle loses relevance (by leaking outside the problem, for instance). Typically, many such particles are simulated, and events of interest are tallied and averaged. At the method's conclusion, the average result is reported with some confidence estimate, usually the standard deviation of the average. It can easily be shown using the Central Limit Theorem that the standard deviation of the average decreases at a rate that is inversely proportional to the square root of the number of histories. That is, to improve the confidence in an estimate by a factor of two, one must on average simulate four times as many particles. Correspondingly, Monte Carlo methods have the disadvantage of generally being quite computationally expensive – it may take an astronomical number of histories to obtain a solution estimate with appreciable confidence. The full transport problem addressed in this thesis, for example, generally cannot produce global solutions with adequately resolved statistical errors even on today's massive, parallel supercomputers due to prohibitively long runtimes. It is worth noting that Monte Carlo methods are so-called "embarrassingly parallel" algorithms (provided that the underlying problem fits into a single processor's memory). It is almost trivial to convert a single-processor algorithm to run on very large, distributed computing systems. Monte Carlo methods are widely-used, often giving researchers the powerful ability to use two wholly different methods (stochastic and deterministic) to estimate a problem solution.

Even if continuous problem data is available, it is not possible to exactly solve Eqs. (3.29) using a Monte Carlo method. This is fundamentally due to the nonlinearity in the material temperature, i.e., the effect that the material temperature has on the underlying problem data. The simplest remedy for this problem is to impose a spatial grid in which the temperature is defined to be a constant or some other spatially fitted, functional expansion. No matter how this is done, the imposition of some sort of spatial discretization introduces another source of error into the problem. For instance, if one assumes the simplest solution, which is to use a constant temperature in each spatial zone, then a large number of spatial zones is required to resolve sharp temperature gradients, which is typically too computationally burdensome. Additionally, the numerical treatment of the absorption-reemission

approximation can introduce an unphysical conduction in the problem. Although it is possible to store the locations of each absorbed Monte Carlo photon and construct a spatial temperature distribution within each cell, it is customary to assume either a histogram or linear temperature distribution. Thus, absorbed photons generally lose their identities in a spatial zone, and are reemitted uniformly or linearly in space during the subsequent time step. If the spatial zone is large, then it is possible for a photon to be absorbed on one side of the cell and be released at the other side faster than an underlying radiation wavefront. In subsequent analyses, we shall assume that a spatial grid has been imposed in which the temperature and material data are assumed to be constant, with the understanding that this will introduce an additional source of error.

In general, one has to represent many physical photons with relatively few Monte Carlo photons; Monte Carlo photons therefore represent large packets of physical photons. This is because the maximum number of simulated particles is constrained by computer memory requirements. This limiting factor is generally used as a guide to determine the amount of physical energy each Monte Carlo photon represents. In TRT calculations, there is a slight, additional subtlety that arises – the Monte Carlo particle density is not exactly proportional to the number density of the photons. However, this subtlety may be exploited to develop a compelling solution to the problem of local (per-Monte Carlo particle) energy conservation. Central to these ideas is the concept of a Monte Carlo particle *weight*.

To the reader more familiar with linear, neutron-transport Monte Carlo problems, a particle weight is a dimensionless quantity that represents the relative number of neutrons represented by a Monte Carlo particle. The particle weight is therefore a new independent variable that is controlled by the user and by the Monte Carlo tracking algorithm. In an *analog* neutron transport calculation, in which the particle weight is fixed, the Monte Carlo number density is directly proportional to the neutron number density. This is not the case in a frequency-dependent TRT calculation. The contrast between these two types of problems merits discussion, since we will extend the experience from the linear, neutron-transport Monte Carlo community to create a Monte Carlo interpretation of the IMC equations.

The central reason for the different treatments of the Monte Carlo particle weights is that the unknown for the radiation in a TRT problem, $I(\nu)$, is proportional to the frequency ν times the photon number density $N(\nu)$ (with the arguments x, μ, t suppressed for clarity):

$$I(\nu) = h\nu c N(\nu) \,.$$

The most straightforward Monte Carlo interpretation of Eq. (3.29a), solves directly for a quantity that is proportional[3] to $I(\nu)$, not $N(\nu) = I(\nu)/hc\nu$. By comparison, let us artificially group the terms according to "neutronics" terminology:

$$I(\nu) = (h\nu)[cN(\nu)]\,,$$
$$I(\nu) = \text{energy} \times \text{"angular flux"}.$$

In a neutronics problem, the "angular flux", which is the product of the neutron speed and number density, is the central unknown. Thus, any neutronics-like Monte Carlo interpretation of Eqs. (3.29) would introduce an "energy" term that depends upon the photon frequency. For reasons that will become clear later, this is undesirable. To aid this discussion, let us define

$$M(x,\mu,\nu,t,w)\;dxd\mu d\nu dw = \begin{array}{l}\text{The expected number density of Monte}\\ \text{Carlo particles at location } (x,\mu,\nu)\\ \text{in } (dx,d\mu,d\nu) \text{ with weight } w \text{ in } dw\\ \text{traveling at time } t.\end{array} \tag{3.39}$$

In general, we would like to construct the intensity I from the Monte Carlo density M using the relationship:

$$I(x,\mu,\nu,t) = ch\nu N(x,\mu,\nu,t) \equiv \int_0^\infty cwM(x,\mu,\nu,t,w)\;dw\,, \tag{3.40}$$

which is to say,

$$h\nu N(x,\mu,\nu,t) = \int_0^\infty wM(x,\mu,\nu,t,w)\;dw\,. \tag{3.41}$$

The left side of this expression has units of energy per volume-angle-frequency. Since M is a number density, w cannot be dimensionless – w must have units of energy. As an example of how this weight is treated, let us stipulate that $w = w_0$, a constant. That is, we may write M explicitly as

$$M_{w_0}(x,\mu,\nu,t,w) = M(x,\mu,\nu,t)\delta(w-w_0)\,, \tag{3.42}$$

[3]For instance, in equilibrium, we should find the solution $I(\nu) = 2\pi B(\nu)$. Every existing Monte Carlo algorithm for TRT would treat this problem by sampling from $B(\nu)$ directly, not by sampling $B(\nu)/\nu$.

in which case we have:

$$\begin{aligned} h\nu N(x,\mu,\nu,t) &= \int_0^\infty wM(x,\mu,\nu,t)\delta(w-w_0)\,dw\,, \\ &= w_0 M(x,\mu,\nu,t)\,, \\ \int_0^\infty \int_0^X \int_{-1}^1 h\nu N(x,\mu,\nu,t)\,d\mu dx d\nu &= w_0 \int_0^\infty \int_0^X \int_{-1}^1 M(x,\mu,\nu,t)\,d\mu dx d\nu\,, \\ \text{total system energy at time } t &= w_0 \times \text{total number of Monte Carlo particles}\,, \\ w_0 &= \frac{\text{energy}}{\text{Monte Carlo particle}}\,. \end{aligned}$$

In other words, w_0 is the amount of energy that is represented by a single Monte Carlo particle. This type of Monte Carlo particle weight is sometimes distinguished from its linear, neutron-transport counterpart by terming it an *energy-weight*. In a typical IMC calculation, w_0 is specified at the beginning of the calculation, and the number of Monte Carlo particles injected during each time step is adjusted depending on the amount of particle energy that must be represented during the time step. This ensures that each time step is treated "fairly" in regard to the total amount of energy injected. By contrast, in a steady-state, analog, neutron transport problem, it is typical to specify the total number of particle histories ahead of time and to then impose that w be inversely proportional to that number. This allows the user to set a practical limit upon the calculation time, assuming that each history takes roughly the same amount of time. However, in an IMC calculation, one cannot know the amount of energy injected during a time step for every time step a priori; the variability of of this quantity over disparate time steps means that either the number of histories injected *or* the particle weight must vary.

It is worthwhile to provide IMC equations in which w – the amount of energy represented by a Monte Carlo particle – is an independent variable. If we define:

$$\tilde{I}(x,\mu,\nu,t,w) \equiv cwM(x,\mu,\nu,t,w)\,, \tag{3.43}$$

so that

$$I(x,\mu,\nu,t) = \int_0^\infty \tilde{I}\,dw\,, \tag{3.44}$$

the following Eqs. (3.45) are consistent with Eqs. (3.29):

$$\frac{1}{c}\frac{\partial \tilde{I}}{\partial t} + \mu\frac{\partial \tilde{I}}{\partial x} + \sigma_{a,n}\tilde{I} = \frac{1}{2}\sigma_{ea,n}b_n c U_{r,n}\delta(w - w_0) + \frac{\chi_n}{2}\iiint p(w' \to w)\sigma_{es,n}\tilde{I}\, d\mu' d\nu' dw' + \frac{Q}{2}\delta(w - w_0)\,, \quad (3.45a)$$

$$U_{m,n+1} = U_{m,n} - c f_n \sigma_{p,n} U_{r,n}\Delta_{t,n} + \int_{t_n}^{t_{n+1}} \iiint \sigma_{ea,n}\tilde{I}\, d\mu\, d\nu\, dw\, dt\,. \quad (3.45b)$$

Here the triple integral denotes an integral over all directions, frequencies, and non-negative weights. As discussed above, the quantity w_0 is provided by the user; this and a calculation of the energy that must be represented in the radiation dictate the number of Monte Carlo particles injected during the time step. The quantity $p(w' \to w)$ is the probability that a Monte Carlo particle with weight w' emerges with weight w after an effective scattering event. In the simplest scenario, in which constant particle weights are employed[4], this probability is given by:

$$p_{\text{constant}}(w' \to w) = \delta(w' - w)\,, \quad (3.45c)$$

but other interpretations of p may be formulated. Boundary and initial conditions to these equations are given by:

$$\tilde{I}(x, \mu, \nu, 0, w) = I^i(x, \mu, \nu)\delta(w - w_0)\,, \quad (3.45d)$$

$$T(x, 0) = T^i(x)\,, \quad (3.45e)$$

$$\tilde{I}(0, \mu, \nu, t, w) = I^\ell(\mu, \nu, t)\delta(w - w_0)\,, 0 < \mu \leq 1\,, \quad (3.45f)$$

$$\tilde{I}(X, \mu, \nu, t, w) = I^r(\mu, \nu, t)\delta(w - w_0)\,, -1 \leq \mu < 0\,. \quad (3.45g)$$

These equations, when operated upon by $\int_0^\infty(\cdot)dw$, reduce to the traditional form of the IMC equations given by Eqs. (3.29). However, Eqs. (3.29) by themselves do not have a straightforward Monte Carlo interpretation, whereas Eqs. (3.45) do. It should be noted that Eqs. (3.45) are not unique; one may define alternative Monte Carlo interpretations of Eqs. (3.29) (for instance, one might attempt to define a Monte Carlo scheme that is completely analogous to the physics of photon transport). Yet, Eqs. (3.45) are typical of what one encounters in existing implementations. An

[4]If the term "analog" is defined to mean "a numerical process that is completely analogous to the underlying physics", then using constant particle weights is not strictly an analog procedure, since Monte Carlo photons used to solve Eqs. (3.45) have energies that do not depend on their frequency. We shall attempt to avoid the use of this term to minimize confusion.

additional advantage of Eqs. (3.45) is that energy conservation on a per-particle basis becomes trivial. From these equations, we see that if *Eq.* (3.45c) is used, the energy-weight of a particle never changes, *even if the particle frequency changes*. That is, a particle's energy-weight is *not* related to its frequency, even though $h\nu$ is the traditional photon energy. Let it be made clear: energy-weight (independent of ν) is different from photon energy (linearly dependent on ν). In Eqs. (3.45), ν is simply treated as a parameter, and a Monte Carlo procedure used to solve these equations is not analogous to the physics of photon transport.

Thus, particle energy is introduced into the problem and travels through the system until it is either absorbed in the material, leaks out of the system, or goes to census; it can never be lost. Certain transport schemes in which the energy-weight is allowed to fluctuate may also be developed to contain this property, and will be discussed later. Finally, we note that if we had developed a Monte Carlo interpretation of the gray version of the IMC equations, it would not have been necessary to introduce the concept of energy-weights. However, had we done so, we would have had to perform a separate analysis for the frequency-dependent problem and introduce the concept there. Also, if one later desired to create a non-constant energy-weight kernel $p(w' \rightarrow w)$ to reduce the variance of the Monte Carlo process, it would again be necessary to introduce some type of weight to the gray equations.

3.4 Implicit Monte Carlo Implementation

In this section we describe details that are necessary to computationally implement a constant energy-weight version of Eqs. (3.45), the simplest numerical scenario possible. Readers who are already acquainted with such concepts may proceed to Chapter IV.

To solve Eqs. (3.45) using a Monte Carlo method, it helps to pause and consider the possible energy sources and sinks of physical photons. For instance, in the first time step, Monte Carlo photons may be "born" from the initial condition (existing radiation), the boundary condition, the inhomogeneous source Q, or the material if $T > 0$. At the end of the time step, some of these photons may continue to exist in the radiation – these are generally stored in a *census* to preserve their state in preparation for the next time step. Other photons may have been absorbed in the material during the time step – their energy is subsequently removed from the radiation and attributed to the temperature. At the beginning of the next time step, photons may then emerge from the census (which is like an initial condition), the

boundary condition, Q, or be emitted from the material. Using this as a guide, a natural algorithm emerges to begin the sampling procedures – for instance, a random number may be used to choose from which source a particular photon should begin; if it is the initial condition, it must have $t = 0$ and so forth. This process is delineated explicitly below.

First, we discuss the various particle-energy sources in an IMC calculation. The total energy emitted by an isotropic, inhomogeneous source Q is:

$$E_Q = \int_{t_n}^{t_{n+1}} \int_0^X \int_0^\infty Q(x, \nu, t)\, d\nu\, dx\, dt\,. \tag{3.46}$$

Here, the particle time and frequency are chosen according to the functional form of Q. The particle angle is uniformly chosen in the unit sphere – in practice this is typically done by choosing μ (the cosine of the polar angle) uniformly on $[-1, 1]$, or

$$\mu = 2\xi - 1 \tag{3.47}$$

where ξ is a *uniform random variate* on $(0, 1]$. A uniform random variate is a particular number chosen from a uniform distribution of pseudorandom numbers. Modern computers typically allow one to obtain large streams of ξ with great efficiency. In what follows, choosing μ using Eq. (3.47) is what is meant by "sampling isotropically in angle." To choose a particle location, one first observes that typical geometry models of transport problems consist of many non-overlapping, connected spatial zones. In general, the problem data is decreed to be constant over each spatial zone. Therefore, particle location is chosen by first determining a spatial zone based on its relative contribution to the energy (via a normalization to a pdf), and by then sampling within that spatial zone uniformly. That is, if Q_j is the total energy emitted due to Q in zone j, then that zone is chosen with probability Q_j/E_Q. As an example of choosing a spatial location within a zone uniformly, consider a zone given by $[x_{\text{left}}, x_{\text{right}}]$. In this case, a location is selected according to $x = x_{\text{left}} + \xi\Delta_x$. The particle's initial energy-weight is set to the user-specified value of w_0 for this energy source and for each of the following energy sources.

The total energy due to the boundary source is obtained by integrating the boundary condition over the time step, boundary surface, and angle:

$$E_B = \int_{t_n}^{t_{n+1}} \int_0^\infty \left(\int_0^1 \mu I^\ell(\mu, \nu, t)\, d\mu + \int_{-1}^0 |\mu|\, I^r(\mu, \nu, t)\, d\mu \right) d\nu dt \tag{3.48a}$$

Hence, one chooses particle location (on the boundary), direction, frequency, and time according to the functional forms of I^ℓ and I^r. However, the boundary source is frequently specified as a blackbody at a fixed temperature, in which case the total energy may be written more simply as:

$$E_B = \frac{ac}{4}\left(T_\ell^4 + T_r^4\right)\Delta_t\,, \tag{3.48b}$$

in which case the particle frequency is chosen from a Planckian spectrum[5] at the boundary temperature, the time is chosen uniformly over the time step, and the direction is isotropic in the incoming directions. [For the left boundary, we choose μ according to $\mu = \sqrt{\xi}$, which corresponds to the pdf $f(\mu) = 2\mu$.]

During the first time step, energy may be included due to the initial condition on I (in subsequent time steps, one simply "follows" the existing census particles):

$$E_{IC} = \int_{-1}^{1}\int_0^X\int_0^\infty I^i(x,\mu,\nu)\,d\nu dx d\mu\,. \tag{3.49}$$

Here, particle location is chosen cell-wise and then within the cell as is done for Q, while direction and frequency depend on the form of the initial condition. The initial condition is also frequently given as a blackbody at a certain temperature, in which case the particle direction is isotropically sampled and particle frequency is chosen from a Planckian spectrum. The particle time is specified at $t = 0$.

Finally, we turn to particles emitted from the material during the time step, which is represented by the first term on the right side of Eq. (3.20). This time-independent term represents radiative energy held by the material at the beginning of the time step and radiated uniformly in t during the time step. We rewrite it here to analyze its features:

$$\frac{1}{2}\sigma_{ea,n}b_n c U_{r,n} = \frac{1}{2}\chi_n c f_n \sigma_{p,n} U_{r,n} \tag{3.50}$$

The factor 1/2 tells us that this is an isotropic photon source. The factor $\chi_n(\nu)$ may be thought of as the frequency distribution term, similar to a fission spectrum $\chi(E)$ in neutron transport. The remaining term is what is left after integrating over frequency and angle – the source strength in units of energy per volume-time. The

[5]The details of how to computationally sample a Planckian using only uniform random variates may be found in reference [21].

total particle energy injected during the time step due to this term is therefore:

$$E_R = \int_{t_n}^{t_{n+1}} \int_0^X \int_0^\infty \int_{-1}^1 \frac{1}{2} \chi_n(\nu) c f_n \sigma_{p,n}(x) U_{r,n}(x) \, d\mu \, d\nu \, dx \, dt \,,$$
$$= c\Delta_{t,n} \int_0^X f_n \sigma_{p,n}(x) U_{r,n}(x) \, dx \,. \tag{3.51}$$

If this energy source is selected, the particle's location is determined in a similar manner as was done for Q, and it is emitted uniformly during the time step since E_R has no temporal or angular dependence.

The total energy introduced into the problem during a time step is therefore given by:

$$E_{TOT} = E_Q + E_B + E_{IC} + E_R \,, \tag{3.52}$$

where E_{IC} may be due to a census or the initial condition. A particle is born in one of these energy sources with probability E_X/E_{TOT}, where X may be one of Q, B, or R in a general time step.

After a Monte Carlo particle energy source is selected and the particle is introduced into the problem geometry, the next task is to track it through the problem, updating the independent variables along the way. There are essentially three events that must be considered that affect the nature of a particle's flight through the system: (i) the particle could collide with an atom, (ii) the particle could exit the current region (and enter a region with different opacities), or (iii) the particle time could reach the end of time step value t_{n+1}. Associated with these three possibilities are three distances – a distance to collision, distance to the spatial boundary, and the distance that would be traveled until $t = t_{n+1}$. The calculation of these second two quantities is non-stochastic and straightforward. The distance to the next spatial boundary d_G will satisfy:

$$x_B - x = \mu d_G \,, \tag{3.53a}$$

where x_B is the boundary location in direction μ. The distance to the next time boundary, d_T is simply:

$$d_t = c(t_{n+1} - t) \,. \tag{3.53b}$$

The distance to next collision, d_C, is determined in the following way. Assume that at location s we have a density of photons given by $N(s)$. We then consider the

incremental removal due to collisions along flight path at a location $s + \delta s$. Using the definition of total opacity, this is just:

$$N(s + \delta s) = N(s) - \sigma_a \delta s N(s) + O(\delta_s^2)\,.$$

That is, to first order, the amount removed in a differential distance δs is the probability of interaction per distance, times the distance, times the original density. Rearranging and allowing $\delta s \to 0$, this is:

$$\frac{dN}{ds}(s) = -\sigma_a N(s)\,.$$

This ordinary differential equation has the solution

$$N(s) = Ce^{-\sigma_a s}\,,$$

where C is an unspecified constant. We next normalize this solution on $[0, \infty)$ to construct the pdf for removals due to collisions:

$$N(s) = \sigma_a e^{-\sigma_a s}\,. \tag{3.53c}$$

This is the pdf that we must sample to determine d_C. Being exponential, it has the important property that it is a *memoryless* distribution [47]. This essentially means that the probability of removal during flight over a given interval does not change if that interval is moved. This has the following Monte Carlo implication. Let us imagine that d_C is sampled and determined to be some large distance, many spatial zones away. Then it is equivalent to move particles to the zone boundaries, halt, and sample for d_C repeatedly, rather than attempt to move particles through a multitude of boundaries to the collision location. We next observe that since all cumulative distribution functions (cdfs) are monotonically increasing on $[0, 1]$, and since our URVs are uniformly distributed on $[0, 1]$, we may construct a relationship between the URV ξ and the cdf:

$$\begin{aligned}
\int_0^{\xi} 1\; d\xi' &= \int_0^{d_C} \sigma_a e^{-\sigma_a s} ds\,, \\
\xi &= -e^{-\sigma_a d_C} + 1\,, \\
d_C &= \frac{-\ln(1-\xi)}{\sigma_a}\,,
\end{aligned}$$

$$d_C = \frac{-\ln(\xi)}{\sigma_a}\,, \tag{3.53d}$$

where the last equality results from the probabilistic equivalence of $1-\xi$ and ξ. The next step in the Monte Carlo method, then, is to calculate d_C, d_G, and d_t according to Eqs. (3.53), determine the minimum quantity, and either move the particle to the collision location, spatial boundary, or time boundary respectively. We next consider what to do for each of these events.

If the minimum distance d is to either of the spatial or time boundaries, the particle direction, energy[6], weight, and frequency remain unchanged. The particle location and time is simply updated to those of the boundary using:

$$x' = x + \mu d\,, \tag{3.54a}$$

$$t' = t + d/c\,. \tag{3.54b}$$

If d_G was used, then we check to see whether the particle has leaked out of the boundary. If it has not, the sampling process begins again in the new spatial zone with appropriately updated material properties. If d_t was selected, then the particle "goes to census," where it is stored in computer memory for the calculation of the next time step.

If the minimum distance is to collision, the particle data are also updated according to Eqs. (3.54), but the collision event must then be decided. To see how this is done, let us break up the collision removal term into its component pieces:

$$\sigma_{a,n} I = \left[\frac{\sigma_{ea,n} + \sigma_{es,n}}{\sigma_{a,n}}\right] \sigma_{a,n} I \tag{3.55}$$

We can interpret the bracketed term as a discrete probability distribution for two separate collision events: effective absorptions and effective scatters. Therefore, with probability $\sigma_{ea}/\sigma_a = f$, the particle undergoes an effective absorption – the particle's energy is deposited at the collision location and no longer followed (Note that there is no source term in Eq. (3.29) due to effective absorptions at the instantaneous time). With probability $\sigma_{es}/\sigma_a = 1 - f$, the particle undergoes an effective scatter. The reemission process is mathematically represented by the in-scatter source term of

[6] In [21], a continuous energy deposition model is used. Essentially, in Eq. (3.53d), $\sigma_{a,n}$ is replaced with the scattering opacity σ_{es}. The energy update equation is then adjusted to $E' = Ee^{\sigma_{ea,n}(\nu)d}$, with the energy difference due to absorptions continuously deposited along the particle flight path. This is a *variance reduction* mechanism that is typically used in modern implementations of IMC. The interested reader may refer to [21].

Eq. (3.45a). We rewrite it here:

$$\text{in-scatter source} = \frac{1}{2}\chi_n(\nu) \iiint p(w' \to w)(1-f)\sigma_{a,n}\tilde{I}\, d\mu' d\nu' dw' \tag{3.56}$$

In this term, the triple integral over $\sigma_{a,n}I$ is the collision rate due to all absorptions at location x and time t. The factor $(1-f)$ is the (frequency-independent) probability that such an event may be interpreted as an effective scatter. As above, the factor $1/2$ is an isotropic, angular redistribution term, and the factor χ_n is the emerging photon frequency spectrum. A new particle weight may be chosen according to $p(w' \to w)$; in the constant energy-weight case, the weight remains unchanged. After either an effective absorption or scatter has been selected, the particle is said to have collided, and, if the particle was not absorbed, the process of choosing a new distance is repeated.

Particle tracking ends when the particle has leaked out of the system or gone to census. Alternatively, one can also end the tracking if the energy falls to a user-supplied cutoff criterion and deposit the particle energy directly into the material. The entire process (birth, tracking, death) is generally repeated a large number of times to generate meaningful statistics. These statistics are generated via a "tallying" mechanism. Upon different particle events (collision, boundary-crossing, etc.), one updates a computer memory structure, or *tally* using information about the current particle. This information can be used to ensure energy conservation for verification purposes, to update the material properties to end-of-time-step values in preparation for the next time step, and to provide users with the problem solutions.

The first several tallies we will examine are related to the radiation intensity. In most of the below tallies, we will consider events that occur in a single geometric zone with volume $V_{zone} = \Delta_{x,zone}$ over a range of particle histories $i \in [1, 2, \ldots N_{\text{hist}}]$. From the material update Equation [Eq. (3.45b)], we immediately see that we need an estimate of the energy deposited in a zone due to the effective absorptions. We first note that:

$$f_n\sigma_{a,n}(x,\nu)cwM(x,\mu,\nu,t,w)\, d\mu\, d\nu\, dx\, dw = \begin{array}{l}\text{absorption energy deposition rate} \\ \text{in } d\mu\, d\nu\, dx\, dw \text{ about } (x,\mu,\nu,w) \\ \text{at time } t.\end{array}$$

We would like to accumulate this differential quantity over all frequencies, angles,

and the time step; and average it over a zone volume to find:

$$\begin{aligned}\text{mean energy deposited due to all effective absorptions in } V_{\text{zone}} \\ = \frac{1}{V_{\text{zone}}} \int_{V_{\text{zone}}} \int_{t_n}^{t_{n+1}} \iiint f_n \sigma_{a,n}(x,\nu) cwM(x,\mu,\nu,t,w)\, d\mu\, d\nu\, dt\, dx\, dw\,, \\ \approx \frac{1}{N_{\text{hist}} V_{\text{zone}}} \sum_{i=1}^{N_{\text{hist}}} w_i \equiv T_A \quad (3.57)\end{aligned}$$

where w_i is the total Monte Carlo particle energy deposited in V_{zone} due to *all* effective absorption collisions in history i during time step n. In other words, when a particle undergoes an effective absorption according to Eq. (3.55), we deposit its entire energy w_i into the current zone's material[7]. We will use T_A as shorthand for the "effective absorption tally."

We next turn to an estimate of the scalar intensity during a particular point in time, or at a "snapshot." This essentially follows immediately from the definition of the intensity:

$$\begin{aligned}\text{volume-averaged scalar intensity at time } t \\ = \frac{1}{V_{\text{zone}}} \int_{V_{\text{zone}}} \iiint cwM(x,\mu,\nu,t,w)\, d\mu\, d\nu\, dx \approx \frac{1}{N_{\text{hist}} V_{\text{zone}}} \sum_{i=1}^{N_{\text{hist}}} cw_i\,, \quad (3.58)\end{aligned}$$

where c is the speed of light and w_i is the energy of a Monte Carlo particle in the radiation at time t. Another quantity of interest is the amount (or rate) of energy flowing at position x. Such a quantity might be used in energy conservation on a local or global scale or to obtain a net leakage in the problem boundary. We have:

$$\begin{aligned}\text{rate of energy traveling to the right at position } x \ = J^+(x) \\ = \frac{1}{\Delta_{t,n}} \int_{t_n}^{t_{n+1}} \int_0^1 \iint \mu w M(x,\mu,\nu,t,w)\, d\nu\, dw\, d\mu\, dt \\ \approx \frac{1}{N_{\text{hist}} \Delta_{t,n}} \sum_{i=1}^{N_{\text{hist}}} w_i, \qquad \mu > 0\,, \quad (3.59)\end{aligned}$$

where w_i^+ is the total Monte Carlo particle energy that exits crosses location x during the time step (in the positive direction). If desired, we may combine this with

[7]This procedure assumes that a constant energy-weight is being used. It is also possible to employ a technique known as *absorption weighting* or *survival biasing*, in which a fraction of the particle energy is deposited and the remaining fraction is retained in the radiation.

another tally for J^-, the average energy going the opposite direction, and calculate an estimate of the net energy current $J(x)$:

$$J(x) \approx \frac{1}{N_{\text{hist}}\Delta_{t,n}} \left(\sum_{i=1}^{N_{\text{hist}}} w_i^+ - \sum_{i=1}^{M} w_i^- \right) \tag{3.60}$$

where w_i^- is the total Monte Carlo particle energy that crosses location x during the time step (in any negative direction, dictated by $-1 \leq \mu < 0$). Note that all of the above quantities may also broken up into different frequencies – that is, instead of accumulating all of the particles into a single tally regardless of frequency, we may choose to segregate the particles into a multigroup structure.

It is now possible to rewrite the material update equation [Eq. (3.45b)] in terms of Monte Carlo tallies. Using Eq. (3.57) in Eq. (3.45b), it is simply:

$$U_{m,n+1} = U_{m,n} - cf_n\sigma_{p,n}U_{r,n}\Delta_{t,n} + T_A \,. \tag{3.61}$$

Once $U_{m,n+1}$ is known, the temperature T_{n+1} may be calculated through the relation $\partial U_m/\partial T = c_v$. Finally, given T_{n+1} it is simple to calculate $U_{r,n+1} = aT_{n+1}^4$.

We next turn to the problem of local energy conservation. We begin by integrating Eq. (3.5) over a spatial zone, frequency, and the time step to find (exactly):

$$\begin{aligned} &\frac{1}{c}\left[I_0(t_{n+1}) - I_0(t_n)\right] + U_m(t_{n+1}) - U_m(t_n) \\ &\qquad = \int_{t_n}^{t_{n+1}} \iint Q(x,\nu,t)\; dx\, d\nu\, dt - \int_{t_n}^{t_{n+1}} \iint \frac{\partial}{\partial x} I_1(x,\nu,t)\; dx\, d\nu\, dt \,. \end{aligned} \tag{3.62}$$

This equation may be broken up into several terms. The first term concerns the scalar intensity at the "snapshot" time $t = t_{n+1}$, for which we may use Eq. (3.58) with the slight modification of dividing by c. The second term is assumed known from the initial condition (or census). The third term and fourth terms we may calculate using Eq. (3.29b); that is:

$$U_{m,n+1} - U_{m,n} = T_A - cf_n\sigma_{p,n}U_{r,n}\Delta_{t,n} \,.$$

The first term on the right hand side is just $E_{Q,\text{zone}}$, the energy due to an inhomogeneous source in a single zone. Finally, the last term may be rewritten using the

current tallies defined by Eq. (3.59):

$$\int_{t_n}^{t_{n+1}} \int_0^{\infty} \int_{x_{\text{left}}}^{x_{\text{right}}} \frac{\partial}{\partial x} I_1(x,\nu,t)\, dx\, d\nu\, dt = J(x_{\text{right}}) - J(x_{\text{left}})\,.$$

Putting these results together, we see that energy is conserved if:

$$\frac{1}{c}\left[I_0(t_{n+1}) - I_0(t_n)\right] = c f_n \sigma_{p,n} U_{r,n} \Delta_{t,n} + E_{Q,\text{zone}} - T_A - \left[J(x_{\text{right}}) - J(x_{\text{left}})\right]. \quad (3.63)$$

That is, the difference in the zonal radiation energy at the beginning and end of the time step is due to the gain terms from the material radiation, inhomogeneous source, and incoming partial currents, and the loss terms resulting from effective absorptions and leakages. All of the incoming quantities are explicitly controlled by the algorithm, and all of the energy-loss quantities can be accounted for via tallying.

We conclude our discussion of IMC by providing the gray version of the IMC equations. If one can assume that the opacities are frequency-independent, then it is possible to integrate Eqs. (3.45) over all frequencies to obtain a gray version of the IMC equations. In that case, the equations become:

$$\frac{1}{c}\frac{\partial \tilde{I}}{\partial t} + \mu \frac{\partial \tilde{I}}{\partial x} + \sigma_{a,n}\tilde{I} = \frac{1}{2} f_n \sigma_{a,n} c U_{r,n} \delta(w - w_0) + \frac{1}{2}\int_{-1}^{1}\int_0^{\infty} p(w' \to w)(1-f)\sigma_{a,n}\tilde{I}\, dw' d\mu' + \frac{Q}{2}\delta(w - w_0)\,, \quad (3.64a)$$

with the material update equation:

$$U_{m,n+1} = U_{m,n} - c f_n \sigma_{a,n} U_{r,n} \Delta_{t,n} + \int_{t_n}^{t_{n+1}} \int_{-1}^{1} \int_0^{\infty} f_n \sigma_{a,n} I\, dw\, d\mu\, dt\,, \quad (3.64b)$$

and initial and boundary conditions given by:

$$\tilde{I}(x,\mu,0) = \tilde{I}^i(x,\mu)\delta(w - w_0)\,, \quad (3.64c)$$

$$T(x,0) = T^i(x)\,, \quad (3.64d)$$

$$\tilde{I}(0,\mu,t,w) = I^{\ell}(\mu,t)\delta(w - w_0)\,, 0 < \mu \leq 1\,, \quad (3.64e)$$

$$\tilde{I}(X,\mu,t,w) = I^{r}(\mu,t)\delta(w - w_0)\,, -1 \leq \mu < 0\,. \quad (3.64f)$$

The same mechanisms can then be used to generate Monte Carlo particles, track them, and tally them, but frequency information becomes superfluous. As noted earlier, it is not strictly necessary that Eqs. (3.64) contain an energy-weight parame-

ter, however, it is expedient to provide it in the likely event that the user would like to employ a non-constant energy-weight procedure in order to reduce the variance of the Monte Carlo calculation.

3.4.1 Summary of the IMC Procedure

In this chapter we have presented the derivation of the IMC equations and its implementation details as carefully and precisely as possible to provide the reader with an unambiguous reference. We did this with the intention of allowing the reader to more rapidly understand the central issues of the IMC approach than is presently possible from the current literature. The overall process can be summarized briefly as follows. First, the IMC equations [Eqs. (3.29)] should be understood as a time-discretization of the TRT equations in which the TRT equations have been linearized over a time step. This approximation process has implications upon the problem's accuracy and stability, but it should generally produce reasonable results if one uses physically reasonable materials and sufficiently small time steps. Next, to model Eqs. (3.29) using a Monte Carlo procedure that conserves energy, it is expedient to employ the concept of an energy-weight. This energy-weight is different from the photon energy, and the photon frequency ν becomes simply another parameter. The energy-weight can then be explicitly included as a parameter in the IMC equations [see Eqs. (3.45)] in order to provide them with a straightforward Monte Carlo interpretation. To solve these equations using a Monte Carlo procedure, we first calculate the amount of energy that must be represented by the radiation. This energy may come from the material emissions, an inhomogeneous source Q, the boundary condition, or the previous time step in the form of a census or the initial condition. We then allocate this energy to particles of equal energy-weight w_0. Each particle is introduced into the problem by sampling its direction, position, frequency, and time from pertinent probability density functions. The particles then either travel to a zone boundary, undergo a collision, or enter the next census. If a collision occurs, the particle's energy-weight is either absorbed into the material or it scatters into a new direction and frequency. Energy is automatically conserved since a particle's energy-weight does not change, regardless of its frequency; the particle is either absorbed, leaks out of the system, or goes to census. Each particle is followed until its history has terminated, and the results are tallied and averaged. The tallies and "new" census then provide the algorithm with the necessary ingredients to update the temperatures and begin the calculation for the next time step.

3.5 A Brief Introduction to Variance Reduction

Throughout the previous section we have assumed that the Monte Carlo calculation employs a constant energy-weight procedure. In this procedure, when a particle undergoes a collision, it is either absorbed in the material with probability f_n – at which point its entire energy-weight is deposited into the material – or scattered with probability $(1-f_n)$. Therefore, once a particle has undergone i collisions, its probability of survival is $(1-f_n)^i$ (assuming the problem materials are homogeneous). Since particles usually undergo many collisions as they traverse the problem domain from highly-populated to lightly-populated regions, the probability of finding any given particle in a lightly-populated region can become geometrically small. If obtaining good statistics in these regions is important, one must either geometrically increase the number of particles simulated, or modify the Monte Carlo procedure in such a way that (i) the probability of particle survival is increased in these regions and (ii) the mean solutions do not become biased. In general, techniques that attempt to modify the Monte Carlo procedure in order to increase the confidence in the solution are referred to as *variance reduction* methods. In this section, we briefly introduce four of the most widely-used variance reduction techniques and discuss how they affect the implementation of Eqs. (3.45). This section is *not* intended to fully explicate these methods; the interested reader should refer to one of several textbooks that discuss these topics [11] [12] [13].

3.5.1 Absorption Weighting

The first technique is one of the most widely-used methods in global Monte Carlo particle transport problems, and has been referred to alternately as *survival biasing*, *implicit capture*, or *absorption weighting*. In this technique, instead of depositing all of the particle's energy-weight with probability f_n upon a collision event, we deposit the fraction f_n of its energy-weight into the material and continue to follow the fraction $(1-f_n)$ of its energy-weight in the radiation. The weight update kernel for this procedure is therefore

$$p_{\text{a.w.}}(w' \to w) = \delta[w - (1-f_n)w'] \,, \tag{3.65}$$

where "a.w." stands for absorption weighting. If Eq. (3.65) is used instead of Eq. (3.45c) in Eq. (3.45a) (or Eq. (3.64a)), then particle histories can no longer be terminated due to collision events. This means that each particle history will become longer,

increasing the overall cost of simulating each particle. Also, instead of finding particles with weight w_0 in lightly-populated regions with probability $(1 - f_n)^i$, one may expect to find particles in these regions with *weights* given by $(1-f_n)^i w_0$, on average, where i is the number of collisions and w_0 is the initial energy-weight.

Although absorption weighting successfully provides a means for Monte Carlo particles to move from highly-populated to lightly-populated regions of the problem, it comes at the cost of longer particle histories. Also, because each particle can be expected to undergo a variable number of collisions i before it arrives in a lightly-populated region of the problem, the variance in its weight can become large in these regions. The upshot is that, although the statistics in the lightly-populated regions are improved, the cost of the calculation is increased in the highly-populated regions (where the solution is already satisfactory) and there is room for improvement in the lightly-populated regions. The next three variance reduction methods attempt to remedy these issues by restricting the particle weights in such a way that the efficiency of the calculation is improved and their variance is diminished.

3.5.2 Russian Roulette

If the correct average particle weight could be obtained through some procedure (and such a procedure will be introduced in Chapter VII of this thesis), then one would be able to identify particles whose weights are so small as to not significantly contribute to the solution. The calculation time could be decreased if one could effectively "combine" these low-energy-weight particles into a single, average-energy-weight particle. The technique known as *Russian roulette* does something like this. We next outline the "traditional" version of Russian roulette, in which energy is not conserved, and then modify it to conserve energy.

In the traditional version of Russian roulette, we define w_{low} to be a lower energy-weight cutoff and w_{avg} to be the desired average energy-weight. Then if a particle with energy-weight w undergoes a collision and $w < w_{\text{low}}$, with probability $p = w/w_{\text{avg}}$ (a relatively low probability) we increase the particle's energy weight to w_{avg}, and with probability $(1 - p)$ (a relatively high probability), we terminate the particle history. This technique does not conserve energy since, with probability p, the energy $w_{\text{avg}} - w$ is created "from nowhere", and with probability $(1-p)$ the energy w is lost. To conserve energy, we modify this procedure by introducing a position-dependent "bank" of rouletted energy. In this scheme, when a particle is terminated, its energy-weight is deposited into the energy bank. If a particle's energy is to be increased, its increase is restricted to the amount available in the energy bank. At the end of the

calculation, if excess energy remains in the bank (and this quantity should be small), then it may either be deposited in the material as an effective absorption or attributed to a new census particle. If this modified form of Russian roulette is employed, then both the IMC calculation time and variance in its solution are reduced, all while maintaining a zone-wise conservation of energy. If too-few particles are used, then it is possible that this technique may introduce an inaccuracy into the problem, since the energy bank does not account for the location or time at which energy becomes available. However, if too-few particles are used, one might expect the solution to be inaccurate anyway. In the limit of a large number of histories, it can be shown the Russian roulette technique does not bias the solution.

3.5.3 Splitting

We next turn our attention to particles whose energy-weights are much higher than average. Such particles should occur relatively rarely, but their effect on the overall variance is significant.[8] Additionally, high energy-weight particles have a large effect on the estimate of the mean, so if one is found in a lightly-populated region it would be desirable to more uniformly distribute its contribution among neighboring zones. This may be accomplished through a technique known as particle *splitting*. If we define w_{high} to be a high energy-weight cutoff, and a particle with energy-weight w is found such that $w > w_{\text{high}}$, then we split the particle into j identical "daughter" particles with energy-weight w/j, where

$$j = \text{round}\left(\frac{w}{w_{\text{avg}}}\right). \tag{3.66}$$

It should be clear that such a technique successfully reduces the overall particle weight without affecting the conservation of energy. However, splitting tends to increase the overall calculation time of the Monte Carlo calculation. Additionally, if w_{high} is improperly chosen (for instance, if $w_{\text{high}} < w_{\text{avg}}$), it is possible to have a Monte Carlo algorithm that is "super-critical", meaning that the calculation will never finish.[9] Thus, one must choose the upper cutoff w_{high} with care.

[8] For instance, if the exact particle density in a particular region is small, but the Monte Carlo particle weights are restricted to be a much larger constant, then, to preserve the mean density, this must be simulated by rarely transporting particles to this region.

[9] Splitting is a producer of Monte Carlo particles. If the production rate (splitting plus particle births) exceeds the destruction rate (absorptions and leakage events), the calculation will never finish.

3.5.4 Weight Windows

The final variance reduction technique is known as *weight windows*. This technique combines Russian roulette and splitting so that any given particle's energy-weight is restricted to reside in a possibly parameter-dependent window of interest, defined by w_{low} and w_{high}. Thus, low energy-weights *and* high energy-weights are not permitted in the problem. Since Russian roulette tends to increase – and splitting tends to decrease – the calculation time, there is no way of stating a priori whether or not weight windows will reduce the total calculation time. Assuming that the weight window is well-chosen, the net effect should be to reduce the variance in the problem solution. We reiterate that in Chapter VII of this thesis we shall introduce a means of estimating w_{avg}.

3.6 Summary

In this chapter, we have derived and explicated most of the important features of the IMC method. The majority of what has been presented is foundational and has appeared previously with the exceptions of (i) the positivity condition for T_{n+1} in Eq. (3.35), (ii) the energy-weight interpretation of the IMC equations in Eqs. (3.45), and (iii) the energy-conserving Russian roulette variance reduction mechanism. From this point forward we consider new material. In Chapter IV, we provide a stability theory to better understand when the IMC equations produce unphysical temperature solutions. We also present three enhancements to the IMC method in Chapters V, VI, and VII. Two of the enhancements (in Chapters V and VI) are based on reductions in the impact or number of approximations that lead to the final form of the IMC equations in Eqs. (3.29). In Chapter VII, we present a variance reduction mechanism that controls the Monte Carlo particle energy-weights. In each of the following chapters, an understanding of the fundamentals discussed in this chapter should assist the motivation and understanding of the new material.

Chapter IV

Stability Analysis of the IMC Method

In Chapter III we asserted that the IMC linearization and time discretization depicted in Eqs. (3.29) can produce unphysical, damped oscillations even if $\alpha = 1$. In this chapter, we demonstrate this phenomenon mathematically and numerically for the gray version of these equations in which the opacities are inversely proportional to T^3, and the specific heat is constant. (These are commonly-used and representative choices for the physical parameters.)

It is known that the IMC equations can produce unphysical solutions when a sufficiently large time step is used [27] [28] [29], but little attention has been given to the stability characteristics of the IMC equations. Most of the existing literature has centered upon the accuracy of the IMC equations based upon physical arguments. Larsen and Mercier [27] found an upper limit on the size of the time step that ensures that the IMC equations satisfy a "maximum principle" that the underlying TRT equations satisfy. Larsen and Densmore [28] also established that the IMC equations do not obtain the correct asymptotic equilibrium diffusion limit. Martin and Brown [29] analyzed the temporal convergence rate of the IMC equations applied to a 0-D, linear problem, and demonstrated the presence of unphysical, damped oscillations in some of their numerical results. Mosher and Densmore [31] extended the results of Martin and Brown to derive stability and monotonicity conditions on α and the size of the time step for the IMC equations applied to a 0-D, gray, and linear problem. However, there have been no attempts to analyze the stability characteristics of the IMC equations applied to a nonlinear or spatially-dependent problem; Mosher and Densmore's paper is the only contribution to the literature that addresses stability characteristics of the IMC equations.

This solitary contribution to the topic of stability is presumably because, as we shall demonstrate, the IMC equations are unconditionally stable in most practical

scenarios. However, the conventional wisdom is that unphysical, damped oscillations can exist in the solution of the IMC equations, but that these may be qualitatively lessened by setting $\alpha = 1$ and by reducing the size of the time step. Here we present a new quantitative theory that predicts when and to what extent one may expect these oscillations for a 1-D, gray, nonlinear class of problems. This work is not based upon the analysis given by Mosher and Densmore in [31], but it does verify their monotonicity condition for a linear, 0-D problem. The analysis presented here goes further in that it is applicable to nonlinear and spatially-dependent problems.

We begin by deriving an exact, dimensionless form of the gray TRT equations by scaling the TRT equations about their equilibrium solutions. The IMC approximations are then developed for the scaled equations. Next, linear equations are formed for an additive perturbation to the converged equilibrium solution. These perturbation equations are subsequently solved using an infinite-medium Fourier analysis, and an *amplification factor* ρ is calculated that governs the behavior of the temperature at each time step. We then demonstrate that for $\alpha = 1$, and for certain choices of the dimensionless parameters and time step, the amplification factor can be negative, indicating that unphysical temperature oscillations may occur from step to step. We then test the 1-D theory by numerically demonstrating this phenomenon for different Fourier modes and "realistic" problems. Finally, after recognizing that the damped oscillations are greatest in magnitude for problems that contain small (low-frequency) Fourier modes, we re-present a simpler version of the stability analysis applied to a 0-D problem. We then demonstrate that the IMC equations produce unphysical, damped oscillations even for a linear problem, implying that damped oscillations are a fundamental deficiency of the IMC equations.

The strategy of (i) deriving a 0-D, dimensionless form of the underlying equations, (ii) exactly solving them, (iii) applying linear perturbation theory to the solutions of these equations about their equilibrium solutions, (iv) obtaining an amplification factor that relates the perturbations at the beginning and end of the time step, and (v) analyzing the amplification factor to determine whether it permits divergent or oscillatory solution modes is a relatively simple and useful methodology that a methods-designer may use to quickly assess the efficacy of a proposed time-discretization of the TRT equations. This methodology has the potential of being a valuable tool that may spare researchers a substantial amount of numerical testing effort, as it is very difficult to determine a priori whether a particular time-discretization (or a proposed modification to it) is stable, or if it permits damped oscillations.

Note that during the development of the stability analysis, the IMC approxima-

tion is treated as a time-discretization only; none of the spatial grid effects that occur in a Monte Carlo calculation are considered. Nonetheless, the results of the analysis agree with later numerical experiments where the theory is applicable [specifically, during the derivation, we make a separability assumption on the intensity that limits the applicability of the theory to sufficiently small Fourier modes (long wavelengths)].

Also, throughout this chapter the use of the term "stability" implies that the amplification factor ρ satisfies $|\rho| < 1$, where, for example, the temperature solution may be described by:

$$T(x, t_n) = \rho^n f(x) \,. \tag{4.1}$$

This implies that the solution does not grow in magnitude without bound as the calculation proceeds from step to step. Two types of stable solutions are possible. A solution of the form in Eq. (4.1) has monotonic decay if $0 < \rho < 1$. A solution of the form in Eq. (4.1) has oscillatory decay if $-1 < \rho < 0$. We refer to such solutions as containing "damped, temporal oscillations." Later, we shall implicate that such solutions are unphysical in the absence of an inhomogeneous source, but will avoid the use of the term "unstable" for such systems.

4.1 The Scaled, 1-D, Nonlinear TRT Equations

For convenience, we rewrite the nonlinear, gray, 1-D, TRT equations with no scattering. The transport equation is:

$$\frac{1}{c}\frac{\partial I}{\partial t} + \mu\frac{\partial I}{\partial x} + \sigma I = \frac{1}{2}c\sigma U_r \,, \tag{4.2a}$$

with a material energy equation:

$$\frac{\partial U_m}{\partial t} = \int_{-1}^{1} \sigma I \; d\mu - c\sigma U_r \,. \tag{4.2b}$$

In these equations, the unknowns are the specific intensity $I = I(x, \mu, t)$, the material energy density $U_m = U_m(x, t)$, and the radiative energy density $U_r = U_r(x, t)$. In this chapter we assume that the material temperature is related to the material energy density by a constant specific heat c_v:

$$U_m(x, t) = c_v T(x, t) \,, \tag{4.2c}$$

In practice, the specific heat is only truly constant for an ideal, monatomic gas [37], but it is frequently the case that c_v is only weakly dependent on temperature. The radiative energy density is related to the material temperature by:

$$U_r(x,t) = aT^4(x,t)\,. \tag{4.2d}$$

We also assume that the opacity σ is proportional to the inverse of the temperature cubed:

$$\sigma = \frac{\gamma}{T^3}\,, \tag{4.3}$$

where $\gamma =$ constant. This assumption is strictly true for the analytical model of the opacity given in Eq. (2.7) when it is used to generate either a Planck or Rosseland mean opacity [provided as Eq. (2.17) and Eq. (2.19), respectively]. It is also approximately true in general. With these assumptions, we may write β from Eq. (3.2b) as:

$$\beta(x,t) = \frac{\partial U_r}{\partial U_m} = \frac{dU_r}{dT}\frac{dT}{dU_m} = \frac{4aT^3}{c_v}\,, \tag{4.4}$$

and we note that Eqs. (4.2) have the equilibrium solutions:

$$I = \frac{1}{2}acT_0^4\,, \tag{4.5a}$$

$$U_m = c_v T_0\,, \tag{4.5b}$$

$$U_r = aT_0^4\,, \tag{4.5c}$$

where T_0 is any spatially and temporally constant equilibrium temperature. Later, we shall consider T_0 to be a specified equilibrium temperature around which we will use perturbation theory to expand the solution.

We next consider a scaled version of these equations[1], with scaled spatial and temporal variables given by:

$$z = \sigma_0 x\,, \tag{4.6a}$$

$$\tau = q\sigma_0 ct\ , \tag{4.6b}$$

where

$$q = \frac{aT_0^3}{c_v}\,, \tag{4.6c}$$

[1]This scaling is inspired by and generalizes the scaling used by Su and Olson for a linear problem [42].

$$\sigma_0 = \frac{\gamma}{T_0^3}\,. \tag{4.6d}$$

We define the scaled unknowns by

$$\psi(z,\mu,\tau) \equiv \frac{I(x,\mu,t)}{acT_0^4}\,, \tag{4.6e}$$

$$M(z,\tau) \equiv \frac{U_m(x,t)}{c_v T_0}\,, \tag{4.6f}$$

$$R(z,\tau) \equiv \frac{U_r(x,t)}{aT_0^4}\,, \tag{4.6g}$$

At equilibrium, $\psi = \frac{1}{2}$, and $M = R = 1$. Noting that

$$\frac{\partial}{\partial x} = \frac{dz}{dx}\frac{\partial}{\partial z} = \sigma_0 \frac{\partial}{\partial z}\,, \tag{4.6h}$$

$$\frac{\partial}{\partial \tau} = \frac{d\tau}{dt}\frac{\partial}{\partial \tau} = q\sigma_0 c \frac{\partial}{\partial t}\,, \tag{4.6i}$$

Eq. (4.2a) may be rewritten using Eqs. (4.6) as:

$$\begin{aligned} q\sigma_0\frac{\partial\psi}{\partial\tau} + \mu\sigma_0\frac{\partial\psi}{\partial z} + \sigma\psi &= \frac{1}{2}c\sigma\frac{1}{acT_0^4}(aT_0^4)R\,, \\ &= \frac{1}{2}\sigma R\,, \\ q\frac{\partial\psi}{\partial\tau} + \mu\frac{\partial\psi}{\partial z} + \frac{\sigma}{\sigma_0}\psi &= \frac{\sigma}{2\sigma_0}R\,, \end{aligned} \tag{4.7a}$$

and Eq. (4.2b) as:

$$\begin{aligned} q\sigma_0 c(c_v T_0)\frac{\partial M}{\partial\tau} + c\sigma(aT_0^4)R &= \int_{-1}^{1}\sigma(acT_0^4)\psi\; d\mu\,, \\ \frac{\partial M}{\partial\tau} + \frac{\sigma}{\sigma_0}R &= \frac{\sigma}{\sigma_0}\phi. \end{aligned} \tag{4.7b}$$

where

$$\phi = \phi(z,\tau) = \int_{-1}^{1}\psi(z,\mu,\tau)\,d\mu\,. \tag{4.7c}$$

Eq. (4.7b) may also be written using β so that M is replaced by R. First, we note that:

$$\beta = \frac{\partial U_r}{\partial U_m} = \frac{\frac{d}{dT}aT_0^4 R}{\frac{d}{dT}c_v T_0 M} = \frac{aT_0^3}{c_v}\frac{dR}{dT}\frac{dT}{dM} = q\frac{\partial R}{\partial M}\,,$$

or:

$$\frac{\partial R}{\partial M} = \frac{\beta}{q} = \frac{4aT^3/c_v}{aT_0^3/c_v} = 4M^3 \,.$$

Then, the scaled material energy equation may be written as:

$$\frac{1}{4M^3}\frac{\partial R}{\partial \tau} + \frac{\sigma}{\sigma_0}R = \frac{\sigma}{\sigma_0}\phi \,. \tag{4.7d}$$

Finally, noting that

$$\frac{\sigma}{\sigma_0} = \frac{\gamma}{T^3}\frac{T_0^3}{\gamma} = \left(\frac{T_0}{T}\right)^3 = \frac{1}{M^3}, \tag{4.8}$$

we can simplify the scaled equations given by Eq. (4.7a), Eq. (4.7b), and Eq. (4.7d) to obtain:

$$q\frac{\partial \psi}{\partial \tau} + \mu\frac{\partial \psi}{\partial z} + \frac{1}{M^3}\psi = \frac{1}{2M^3}R \,, \tag{4.9a}$$

with the material energy equation written exactly in either of the following two equivalent forms:

$$\frac{\partial M}{\partial \tau} + \frac{1}{M^3}R = \frac{1}{M^3}\phi, \tag{4.9b}$$

$$\frac{\partial R}{\partial \tau} + 4R = 4\phi \,. \tag{4.9c}$$

Eqs. (4.9) are an exact version of the 1-D, TRT equations, written in dimensionless form, and scaled around their equilibrium condition. The constants that appear in these equations have physical interpretations. First, we note that:

$$q = \frac{aT_0^3}{c_v} = \frac{U_{r,0}}{U_{m,0}} \,.$$

Thus, q is the ratio of the equilibrium radiative and material energy densities. Next, $z = 1 = \sigma_0$ is the average distance a photon travels between collisions under equilibrium conditions, commonly known as a *mean free path*, implying that z is the scaled distance in units of mean free paths. Also, τ may be written as:

$$\tau = q\sigma_0 ct = \frac{a\gamma c}{c_v}t \,,$$

so that when $\tau = 1$, t is the *mean free time* that photons are held in the material

between an absorption and a reemission[2]. To see this, we rewrite Eq. (4.2b) as:

$$\begin{aligned}\frac{\partial U_m}{\partial t} + c\sigma U_r &= \int_{-1}^{1} \sigma I \; d\mu \,, \\ \frac{\partial U_m}{\partial t} + c\left(\frac{\gamma}{T^3}\right) aT^4 &= \int_{-1}^{1} \sigma I \; d\mu \,, \\ \frac{\partial U_m}{\partial t} + \frac{ca\gamma}{c_v} U_m &= \int_{-1}^{1} \sigma I \; d\mu \,.\end{aligned}$$

This first-order differential equation can be "solved" using the following integrating factor:

$$e^{\frac{ca\gamma}{c_v}t} = e^{\tau} \,,$$

and the solution will have an $e^{-\tau}$ behavior. Thus, τ is the duration in units of mean free times *for emission*. This is a different quantity from the more common usage of the term "mean free time", which is the time elapsed for a photon to travel one mean free path. If we define this latter time as t_{coll}, then,

$$t_{\text{coll}} = \frac{1}{c\sigma} = \frac{T_0^3}{c\gamma} \,. \tag{4.10}$$

With $\tau = 1$, the mean free time for emission is t_{e}, given by:

$$t_{\text{e}} = \frac{c_v}{ca\gamma} \,, \tag{4.11}$$

and we find that the two mean free times are related by:

$$t_{\text{e}} = \frac{c_v a}{T_0^3} t_{\text{coll}} \,. \tag{4.12}$$

4.2 The Scaled IMC Equations

Next, we shall explicitly derive IMC equations from Eqs. (4.9)[3]. As in Chapter III, the first approximation is that the parameters $\beta(\tau)$ and $\sigma(\tau)$ are frozen to their

[2]For the reader concerned with units: c_v is typically in jk/cc-keV, γ is in keV^3/cm, and a is in jk/cm^3-keV^4, which means that q, τ, and z are dimensionless.

[3]It is mathematically equivalent to first derive the IMC equations and perform the scaling, or to first perform the scaling and then derive the scaled IMC equations. The latter approach is more general, as the scaled TRT equations provide a good starting point for other analyses, and the scalings are not tied to any property of the linearization.

beginning of time step values, where $\tau_n < \tau < \tau_{n+1}$:

$$\sigma(\tau) \approx \sigma(\tau_n) = \sigma_n, \tag{4.13a}$$

$$\beta(\tau) \approx \beta(\tau_n) = \beta_n\,. \tag{4.13b}$$

However, no approximation is made to the product $\sigma\beta$ due to a cancellation:

$$\sigma(\tau)\beta(\tau) = \frac{\gamma 4a}{c_v} = \sigma_n\beta_n\,. \tag{4.13c}$$

These approximations have the following effects: Eq. (4.9a) and Eq. (4.9b) will have their coefficients replaced by:

$$\frac{1}{M^3} \approx \frac{1}{M_n^3}\,, \tag{4.14}$$

and β=β_n implies that:

$$\frac{\partial R}{\partial M} = 4M^3 \approx 4M_n^3\,. \tag{4.15}$$

However, Eq. (4.9c) does not undergo any approximations.

An additional approximation is made to Eq. (4.9c). We define a time-averaging nomenclature by:

$$\overline{f} = \frac{1}{\Delta_\tau}\int_{\tau_n}^{\tau_{n+1}} f(\tau)\; d\tau\,, \tag{4.16}$$

and we perform this operation on Eq. (4.9c), to obtain:

$$\frac{R_{n+1} - R_n}{\Delta_\tau} + 4\overline{R} = 4\overline{\phi}\,.$$

The first approximation relates $\overline{R}$ to its beginning- and end-of-time-step values:

$$\overline{R} = \alpha R_n + (1-\alpha)R_{n+1}\,, \tag{4.17}$$

in order to eliminate R_{n+1}. Here, as before, $\frac{1}{2} \le \alpha \le 1$ is a user-defined parameter that controls, to some extent, the "implicitness" of the method (when $\alpha = 1$, the method is as implicit as possible). This gives

$$\frac{\overline{R} - R_n}{\alpha\Delta_\tau} + 4\overline{R} = 4\overline{\phi}\,,$$

$$\left(\frac{1}{4\alpha\Delta_\tau} + 1\right)\overline{R} = \overline{\phi} + \frac{1}{4\alpha\Delta_\tau}R_n\,,$$

$$\overline{R} = \frac{4\alpha\Delta_\tau}{1+4\alpha\Delta_\tau}\overline{\phi} + \frac{1}{1+4\alpha\Delta_\tau}R_n\,. \tag{4.18}$$

Next, we define the Fleck factor f as

$$f = \frac{1}{1+4\alpha\Delta_\tau}\,, \tag{4.19}$$

to rewrite Eq. (4.18) as:

$$\overline{R} = (1-f)\overline{\phi} + fR_n\,. \tag{4.20}$$

We now perform the final (and perhaps most dubious) approximation. We replace the average terms in Eq. (4.20) with their "instantaneous" counterparts by setting $\overline{R} = R(\tau)$ and $\overline{\phi} = \phi(\tau)$ and write:

$$R(\tau) \approx (1-f)\phi(\tau) + fR_n\,. \tag{4.21}$$

Although Eq. (4.21) satisfies Eq. (4.20) in a time-average sense, it is not exact at $t = t_n$. In Chapter VI we consider a more accurate approximation at this stage of the derivation.

Next, Eq. (4.21) is substituted into Eq. (4.9a) and Eq. (4.9b). Eq. (4.9a) becomes:

$$\begin{aligned} q\frac{\partial\psi}{\partial\tau} + \mu\frac{\partial\psi}{\partial z} + \frac{1}{M_n^3}\psi &= \frac{1}{2M_n^3}\left[(1-f)\phi + fR_n\right]\,, \\ q\frac{\partial\psi}{\partial\tau} + \mu\frac{\partial\psi}{\partial z} + \frac{1}{M_n^3}\psi &= \frac{f}{2M_n^3}R_n + \frac{1-f}{2M_n^3}\phi\,. \end{aligned} \tag{4.22a}$$

Eq. (4.21) is also substituted into the material energy update equation [Eq. (4.9b)] to ensure energy conservation:

$$\begin{aligned} \frac{\partial M}{\partial\tau} + \frac{1}{M_n^3}\left[(1-f)\phi + fR_n\right] &= \frac{1}{M_n^3}\phi\,, \\ \frac{\partial M}{\partial\tau} + \frac{f}{M_n^3}R_n &= \frac{f}{M_n^3}\phi\,. \end{aligned} \tag{4.22b}$$

Finally, we use the initial condition $R_n = M_n^4$ in Eqs. (4.22) to obtain the scaled IMC equations (in terms of ψ and M only):

$$q\frac{\partial\psi}{\partial\tau} + \mu\frac{\partial\psi}{\partial z} + \frac{1}{M_n^3}\psi = \frac{f}{2}M_n + \frac{1-f}{2M_n^3}\phi\,, \tag{4.23a}$$

$$\frac{\partial M}{\partial \tau} = \frac{f}{M_n^3}\phi - fM_n \,. \tag{4.23b}$$

In the IMC method, a Monte Carlo algorithm is used to solve Eq. (4.23a), which can be interpreted as a linear transport equation with "effective" absorptions and scattering, as discussed in Chapter III. The absorptions are tallied as energy deposited into the material, which corresponds to the first term on the right side of Eq. (4.23b), and the scattering events correspond to the final term in Eq. (4.23a).

To perform a stability analysis on these equations that holds for a general time step n, some concessions must be made. Eqs. (4.23) are linear within a single time step, but they remain nonlinear from step to step. Therefore, they would be extremely difficult to analytically solve. We shall proceed by linearizing these equations about their equilibrium solutions. The equations for the perturbed part of the solution will be linear, and more amenable to analysis, although still difficult to solve.

4.3 The Linearized, Near-Equilibrium IMC Equations

Since Eqs. (4.23) are scaled and conserve energy, we may perturb the system about its equilibrium solutions [$\psi = \frac{1}{2}$, $M = R = 1$] by setting:

$$M(z,\tau) = 1 + \epsilon M_1(z,\tau)\,, \tag{4.24a}$$

$$\psi(z,\mu,\tau) = \frac{1}{2} + \epsilon\psi_1(z,\mu,\tau)\,, \tag{4.24b}$$

$$\phi(z,\tau) = 1 + \epsilon\phi_1(z,\tau) = 1 + \epsilon\int_{-1}^{1}\psi_1(z,\mu,\tau)\,d\mu\,. \tag{4.24c}$$

Using Eqs. (4.24) in Eqs. (4.23), we find, to $O(\epsilon^2)$:

$$q\epsilon\frac{\partial\psi_1}{\partial\tau} + \mu\epsilon\frac{\partial\psi_1}{\partial z} + (1 - 3\epsilon M_{n,1})\left(\frac{1}{2} + \epsilon\psi_1\right) = \frac{f}{2}(1 + \epsilon M_{n,1}) + \frac{1-f}{2}(1 - 3\epsilon M_{n,1})(1 + \epsilon\phi_1)\,, \tag{4.25a}$$

and

$$\epsilon\frac{\partial M}{\partial\tau} = f(1 - 3\epsilon M_{n,1})(1 + \epsilon\phi_1) - f(1 + \epsilon M_{n,1})\,, \tag{4.25b}$$

The $O(1)$ terms of these equations are automatically satisfied (they cancel). The $O(\epsilon)$ terms of these equations are:

$$q\frac{\partial \psi_1}{\partial \tau} + \mu\frac{\partial \psi_1}{\partial z} + \psi_1 = 2fM_{n,1} + \frac{1-f}{2}\phi_1\,, \tag{4.26a}$$

$$\frac{\partial M}{\partial \tau} = f\phi_1 - 4fM_{n,1}\,. \tag{4.26b}$$

Eqs. (4.26) are still too difficult to solve over an arbitrary spatial domain with general boundary and initial conditions. Instead, we shall consider an infinite system that is initially perturbed by a single Fourier mode $e^{i\xi z}$. Because Eqs. (4.26) are linear, the Fourier modes do not interact, so a single Fourier mode will not, as time evolves, produce other Fourier modes. Also, the solution of a single Fourier mode can be combined linearly with other Fourier modes to obtain more general solutions. Moreover, because the equations are for the additive perturbation, there is no difficulty regarding negative intensities or temperatures. We begin by assuming:

$$\psi_1(z,\mu,\tau) = \hat{\psi}(\mu,\tau)e^{i\xi z}\,, \tag{4.27a}$$

$$\phi_1(z,\tau) = \hat{\phi}(\tau)e^{i\xi z} = e^{i\xi z}\int_{-1}^{1}\hat{\psi}(\mu,\tau)\,d\mu \tag{4.27b}$$

$$M(z,\tau) = \hat{M}(\tau)e^{i\xi z}\,, \tag{4.27c}$$

$$M_n(z) = \hat{M}_n e^{i\xi z} = \hat{M}(\tau_n)e^{i\xi z}\,. \tag{4.27d}$$

Substituting these into Eqs. (4.26), we obtain

$$q\frac{\partial \hat{\psi}}{\partial \tau} + \mu i\xi\hat{\psi} + \hat{\psi} = 2f\hat{M}_n + \frac{1-f}{2}\hat{\phi}\,, \tag{4.28a}$$

$$\frac{\partial \hat{M}}{\partial \tau} = f\hat{\phi} - 4f\hat{M}_n\,, \tag{4.28b}$$

which are valid over the time-interval $\tau_n \le \tau \le \tau_{n+1}$. To eliminate the dependence of these equations on n, and to write the solutions in terms of an *amplification factor* ρ, we hypothesize a solution of the following form for each time step $\tau_n \le \tau \le \tau_{n+1}$:

$$\hat{M}_n = \rho^n\hat{M}_0\,, \tag{4.29a}$$

$$\hat{\psi}(\mu,\tau) = \left[\hat{\psi}_p(\mu) + \hat{\psi}_h(\mu,\tau)\right]\rho^n\,, \tag{4.29b}$$

$$\hat{M}(\tau) = \left[\hat{M}_p(\tau-\tau_n) + \hat{M}_h(\tau)\right]\rho^n\,. \tag{4.29c}$$

Here $\hat{M}_0$ is the amplitude of the initial temperature perturbation. We stipulate that $\hat{\psi}_h(\mu,\tau)$ and $\hat{M}_h(\tau)$ are periodic on $0 \leq \tau \leq \infty$ with period Δ_τ. The forms of these solutions are not arbitrary – the h subscript refers to the "homogeneous" parts of the solutions, and the p refers to the "particular" parts. Also, writing the solution in terms of ρ allows for a simple means of analyzing the system's stability. If $|\rho| < 1$, the system is unconditionally stable. If $|\rho| > 1$, the system may have an exponentially diverging solution, and if $\rho < 0$, the system may be prone to oscillations.

We proceed by substituting Eqs. (4.29) into Eqs. (4.28), to obtain:

$$q\frac{\partial\hat{\psi}_h}{\partial\tau}(\mu,\tau) + (\mu i\xi + 1)(\hat{\psi}_h(\mu,\tau) + \hat{\psi}_p(\mu)) = 2f\hat{M}_0 + \frac{1-f}{2}(\hat{\phi}_h(\tau) + \hat{\phi}_p)\,, \tag{4.30}$$

and

$$\frac{\partial\hat{M}_h}{\partial\tau}(\tau) + \hat{M}_p = f(\hat{\phi}_h(\tau) + \hat{\phi}_p) - 4f\hat{M}_0\,, \tag{4.31}$$

where we have divided through by ρ^n. Separating these equations into their time-dependent and time-independent parts, we obtain:

$$q\frac{\partial\hat{\psi}_h}{\partial\tau}(\mu,\tau) + (\mu i\xi + 1)\hat{\psi}_h(\mu,\tau) = \frac{1-f}{2}\hat{\phi}_h(\tau)\,, \tag{4.32a}$$

$$(\mu i\xi + 1)\hat{\psi}_p(\mu) = 2f\hat{M}_0 + \frac{1-f}{2}\hat{\phi}_p\,. \tag{4.32b}$$

$$\frac{\partial\hat{M}_h}{\partial\tau}(\tau) = f\hat{\phi}_h(\tau)\,, \tag{4.32c}$$

$$\hat{M}_p = f\hat{\phi}_p - 4f\hat{M}_0\,. \tag{4.32d}$$

Eqs. (4.32) successfully eliminate the dependence on n – they are defined on $0 \leq \tau \leq \Delta_\tau$. However, it is necessary to stipulate continuity (or boundary) conditions at the interface between steps n and $n+1$. To satisfy the hypotheses given in Eqs. (4.29), the following continuity conditions are imposed:

$$\hat{\psi}_p(\mu) + \hat{\psi}_h^-(\mu,\Delta_\tau) = \left[\hat{\psi}_p(\mu) + \hat{\psi}_h^+(\mu,0)\right]\rho\,, \tag{4.33a}$$

$$\hat{M}_p\Delta_\tau + \hat{M}_h^-(\Delta_\tau) = \hat{M}_0\rho\,. \tag{4.33b}$$

Here, the superscripts "$-$" and "$+$" indicate limits from the left and right in time, respectively. Eqs. (4.32) and Eqs. (4.33) together form a system of equations whose solution contains an explicit dependence on the amplification factor ρ.

The next task is to solve this linear system of coupled equations for ρ. The first step will be to solve Eq. (4.32b) for $\hat{\phi}_p$, which we may use to solve Eq. (4.32d) for $\hat{M}_p$,

thereby eliminating two of the unknowns.

We proceed by solving Eq. (4.32b) for $\hat{\phi}_p$. Rearranging and then integrating over angle, we find:

$$\begin{aligned}\hat{\psi}_p(\mu) &= \left[2f\hat{M}_0 + \frac{1-f}{2}\hat{\phi}_p\right]\frac{1}{1+\mu i\xi}\,,\\ \hat{\phi}_p &= \left[2f\hat{M}_0 + \frac{1-f}{2}\hat{\phi}_p\right]\int_{-1}^{1}\frac{d\mu}{1+\mu i\xi}\,.\end{aligned}$$

The integral on the right side may be written as:

$$\begin{aligned}\int_{-1}^{1}\frac{d\mu}{1+\mu i\xi} &= \int_{-1}^{1}\frac{1-i\xi\mu}{1+\mu^2\xi^2}d\mu\,,\\ &= \int_{-1}^{1}\frac{1}{1+\mu^2\xi^2}d\mu\,,\\ &= \frac{1}{\xi}\int_{-\xi}^{\xi}\frac{1}{1+u^2}du\,,\\ &= \frac{2}{\xi}\tan^{-1}(\xi)\,,\\ &\equiv 2h_1(\xi)\,.\end{aligned}$$

Here

$$h_1(\xi) = \frac{\tan^{-1}(\xi)}{\xi}\,, \tag{4.34}$$

is a shorthand for this monotonically decreasing function on $\xi \in [0,\infty)$. We find that:

$$\begin{aligned}\hat{\phi}_p &= \left[2f\hat{M}_0 + \frac{1-f}{2}\hat{\phi}_p\right]2h_1(\xi)\,,\\ \hat{\phi}_p(1-(1-f)h_1(\xi)) &= 4f\hat{M}_0h_1(\xi)\,,\\ \hat{\phi}_p &= \frac{4fh_1(\xi)}{1-(1-f)h_1(\xi)}M_0\,.\end{aligned} \tag{4.35}$$

We may use this result to write $\hat{\psi}_p(\mu)$ from Eq. (4.32b):

$$\hat{\psi}_p(\mu) = \frac{1}{1+\mu i\xi}\frac{4fh_1(\xi)}{1-(1-f)h_1(\xi)}\hat{M}_0\,. \tag{4.36}$$

Next, the form of $\hat{\phi}_p$ automatically provides $\hat{M}_p$ via Eq. (4.32d):

$$\begin{aligned}\hat{M}_p &= 4f\hat{M}_0\left(\frac{h_1(\xi)}{1-(1-f)h_1(\xi)}-1\right), \\ &= 4f\hat{M}_0\left(\frac{h_1(\xi)-1+(1-f)h_1(\xi)}{1-(1-f)h_1(\xi)}\right), \\ &= -4f\hat{M}_0\left(\frac{1-h_1(\xi)}{1-(1-f)h_1(\xi)}\right). \end{aligned} \tag{4.37}$$

Thus, Eq. (4.36) and Eq. (4.37) provide the forms of the particular solutions ψ_p and M_p. So far, no approximations have been introduced during the solution procedure.

The next task is to solve Eq. (4.32a) for $\hat{\psi}_h(\mu)$ and use that result to find $\hat{M}_h$ from Eq. (4.32c), thereby eliminating two more of the unknowns in the effort to solve for ρ. However, obtaining the exact solution to Eq. (4.32a) is complicated. Although the spatial variable has been suppressed due to the Fourier analysis, it is essentially a time-dependent transport equation in three dimensions: space, angle, and time. Instead of attempting to obtain the entire solution, we shall content ourselves to look only for a subset of the solutions, specifically, separable solutions of the form:

$$\hat{\psi}_h(\mu,\tau) = \hat{M}_0\, a(\mu)\, e^{\lambda\tau}, \tag{4.38}$$

and hope that this form is sufficient to describe the fundamental behavior of Eqs. (4.32). Later, we shall revisit this assumption by testing the theory using numerical experiments. The factor $\hat{M}_0$ appears since it is reasonable to expect that the solutions are proportional to the magnitude of the initial perturbation. We proceed by substituting Eq. (4.38) into Eq. (4.32a). This gives:

$$\begin{aligned}(\lambda q + i\xi\mu + 1)\hat{M}_0 a(\mu)e^{\lambda\tau} &= \frac{1-f}{2}\int_{-1}^{1}\hat{M}_0 a(\mu')e^{\lambda\tau}\,d\mu', \\ \int_{-1}^{1} a(\mu)\,d\mu &= \frac{1-f}{2}\int_{-1}^{1} a(\mu')\,d\mu'\int_{-1}^{1}\frac{d\mu}{\lambda q + i\xi\mu + 1}, \\ 1 &= \frac{1-f}{2}\int_{-1}^{1}\frac{d\mu}{\lambda q + i\xi\mu + 1}, \\ 1 &= \frac{1-f}{2}\frac{1}{1+\lambda q}\int_{-1}^{1}\frac{d\mu}{1+i\frac{\xi\mu}{1+\lambda q}}, \\ 1 &= (1-f)\left(\frac{1}{1+\lambda q}\right)\int_{0}^{1}\frac{d\mu}{1+\left(\frac{\xi\mu}{1+\lambda q}\right)^2}. \end{aligned}$$

This last equality defines λ and requires some discussion. First, the quantity $(1-f)$ is clearly positive and between 0 and 1. Next, the integral must also be positive and between 0 and 1. Therefore, for this equality to hold, the middle quantity must be positive and *greater* than 1. In other words, for this equality to have a real solution, λ must satisfy

$$0 < 1 + \lambda q < 1\,,$$

or

$$\frac{-1}{q} < \lambda < 0\,. \tag{4.39}$$

Assuming that this relationship is satisfied, we now proceed to evaluate the integral and solve for λ.

$$\begin{aligned}
1 &= (1-f)\left(\frac{1}{1+\lambda q}\right)\int_0^1 \frac{d\mu}{1+\left(\frac{\xi\mu}{1+\lambda q}\right)^2}\,,\\
1 &= \frac{1-f}{1+\lambda q}\frac{1+\lambda q}{\xi}\int_0^{\xi/(1+\lambda q)} \frac{du}{1+u^2}\,,\\
1 &= \frac{1-f}{\xi}\tan^{-1}\left(\frac{\xi}{1+\lambda q}\right)\,,\\
\tan\frac{\xi}{1-f} &= \frac{\xi}{1+\lambda q}\,,\\
1+\lambda q &= \frac{\xi}{\tan\frac{\xi}{1-f}}\\
\lambda &= \frac{1}{q}\left(\frac{\xi}{\tan\frac{\xi}{1-f}} - 1\right)\,.
\end{aligned} \tag{4.40}$$

The appearance of the tangent term in the final expression is undesirable – it seems to say that one can find certain Fourier modes that cause λ to approach 0 or to increase in magnitude without bound. However, Eq. (4.39) essentially restricts the physically meaningful Fourier modes to a subdomain that satisfies:

$$\begin{aligned}
\frac{-1}{q} < \lambda &= \frac{1}{q}\left(\frac{\xi}{\tan\frac{\xi}{1-f}} - 1\right)\,,\\
0 &< \frac{\xi}{\tan\frac{\xi}{1-f}},\\
0 &< \frac{\frac{\xi}{1-f}}{\tan\frac{\xi}{1-f}},
\end{aligned}$$

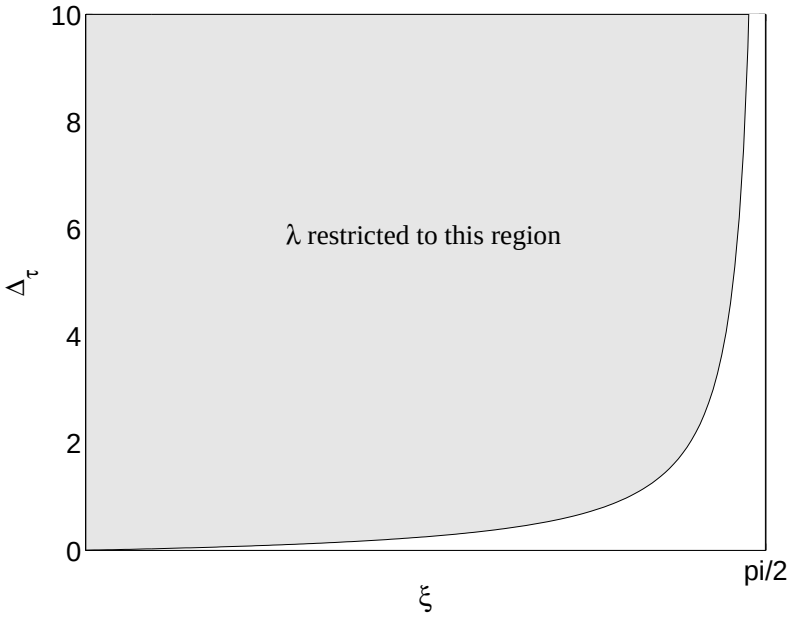

Figure 4.1: The region in which λ is physically permissible.

$$\left|\frac{\xi}{1-f}\right| < \frac{\pi}{2},$$
$$|\xi| < (1-f)\frac{\pi}{2}\,. \tag{4.41}$$

Using the definition of the Fleck factor, this limit may be rewritten as:

$$|\xi| < \left(\frac{4\Delta_\tau}{1+4\Delta_\tau}\right)\frac{\pi}{2}\,. \tag{4.42}$$

The physically meaningful Fourier modes, therefore, are restricted to low frequencies (large spatial waves). Also, this inequality limits the predictive ability of the theory for small time steps. Essentially, the theory may be expected to be valid for small ξ, for large time steps, or both, and may be expected to break down for small time steps and high frequencies (short spatial wavelengths). Figure 4.1 illustrates the region (shaded) where λ satisfies Eq. (4.41).

In conjunction with the separable hypothesis made for $\hat{\psi}_h(\mu,\tau)$, we may also assume that $\hat{M}_h(\tau)$ is proportional to $\hat{M}_0$, the magnitude of the initial perturbation, or that:

$$\hat{M}_h(\tau) = \hat{M}_0 g(\tau)\,, \tag{4.43}$$

where the form of $g(\tau)$ will be determined from Eq. (4.32c), although evaluation of Eq. (4.29c) with $\tau = \tau_n$ stipulates that $g(0) = 1$.

At this point, it is useful to regroup by rewriting the original system of equations for ρ using the solutions and assumptions that have been made thus far. Essentially, Eq. (4.32a) becomes an equation for $a(\mu)$ under the separability assumption in Eq. (4.38):

$$a(\mu) = \frac{1}{1+\lambda q + i\xi\mu}\frac{1-f}{2}\int_{-1}^{1} a(\mu')\,d\mu'\,. \tag{4.44a}$$

Also, Eq. (4.32c) becomes [using Eq. (4.43) and Eq. (4.38)]:

$$\frac{dg}{d\tau} = f\int_{-1}^{1} a(\mu)\,d\mu\,e^{\lambda\tau}\,, \tag{4.44b}$$

$$g(0) = 1\,, \tag{4.44c}$$

with the continuity conditions Eqs. (4.33) rewritten using Eq. (4.36) and Eq. (4.37) as:

$$\frac{1-\rho}{1+i\xi\mu}\frac{2f}{1-(1-f)h(\xi)} = a(\mu)\left(\rho - e^{\lambda\Delta_\tau}\right) \tag{4.44d}$$

$$-4f\frac{1-h(\xi)}{1-(1-f)h(\xi)}\Delta_\tau + g(\Delta_\tau) = \rho\,. \tag{4.44e}$$

The next task is to eliminate $g(\tau)$ from this system, which would leave only $a(\mu)$ and ρ as the remaining unknowns. The solution of the ordinary differential equation Eq. (4.44b) with initial condition Eq. (4.44c) is:

$$g(\tau) = 1 + f\int_{-1}^{1} a(\mu)\,d\mu\frac{e^{\lambda\tau}-1}{\lambda}\,, \tag{4.45}$$

so that

$$g(\Delta_\tau) = 1 + f\int_{-1}^{1} a(\mu)\,d\mu\frac{e^{\lambda\Delta_\tau}-1}{\lambda}\,. \tag{4.46}$$

Defining

$$A \equiv \int_{-1}^{1} a(\mu)\,d\mu\,, \tag{4.47}$$

the continuity condition in Eq. (4.44e) becomes:

$$-4f\frac{1-h(\xi)}{1-(1-f)h(\xi)}\Delta_\tau + 1 + fA\frac{e^{\lambda\Delta_\tau}-1}{\lambda} = \rho\,, \tag{4.48a}$$

and, using Eq. (4.44a) in Eq. (4.44d), the other continuity condition is:

$$\frac{1-\rho}{1+i\xi\mu}\frac{2f}{1-(1-f)h(\xi)} = \frac{1}{1+\lambda q+i\xi\mu}\frac{1-f}{2}A\left(\rho - e^{\lambda\Delta_\tau}\right) . \tag{4.48b}$$

Thus, we have reduced the original system to one with two equations relating ρ and A. Unfortunately, inspection of the angular dependence in Eq. (4.48b) reveals that it can never be satisfied. This is fundamentally due to the separability assumption that was made in Eq. (4.38), since separable solutions do not describe *all* of the solutions of $\hat{\psi}_h(\mu)$. Instead, we shall attempt to satisfy a weaker, angularly-integrated form of Eq. (4.48b). This is similar to the inability of diffusion theory to exactly satisfy an arbitrary angularly-dependent boundary condition [see Eq. (2.38e)]. Instead, diffusion theory satisfies an angularly-integrated (Marshak) boundary condition, which is exact only if the true boundary condition is a weak (isotropic or linear) function of angle. From previous angular integrals, we note that:

$$\frac{1}{2}\int_{-1}^{1}\frac{d\mu}{1+i\xi\mu} = \frac{\tan^{-1}\xi}{\xi} \equiv h_1(\xi) , \tag{4.49}$$

and we define

$$\frac{1}{2}\int_{-1}^{1}\frac{d\mu}{1+\lambda q+i\xi\mu} = \frac{\tan^{-1}\left(\frac{\xi}{1+\lambda q}\right)}{\xi} \equiv h_2(\xi) , \tag{4.50}$$

so that Eq. (4.48b) becomes, upon angular integration:

$$h_1(\xi)(1-\rho)\frac{2f}{1-(1-f)h(\xi)} = h_2(\xi)\frac{1-f}{2}A\left(\rho - e^{\lambda\Delta_\tau}\right) . \tag{4.51}$$

We next solve this result for A:

$$A = \frac{h_1(\xi)}{h_2(\xi)}\frac{1-\rho}{\rho - e^{\lambda\Delta_\tau}}\frac{4f}{[1-(1-f)h_1(\xi)](1-f)} , \tag{4.52}$$

and we introduce this result into Eq. (4.48a) to find that ρ satisfies:

$$\rho + 4f\frac{1-h(\xi)}{1-(1-f)h(\xi)}\Delta_\tau - 1 = f\frac{e^{\lambda\Delta_\tau}-1}{\lambda}\frac{h_1(\xi)}{h_2(\xi)}\frac{1-\rho}{\rho - e^{\lambda\Delta_\tau}}\frac{4f}{[1-(1-f)h_1(\xi)](1-f)} . \tag{4.53}$$

Eq. (4.53) is a quadratic equation for ρ. The solutions of this equation are given by:

$$\rho = \rho(q, \Delta_\tau, \xi) = 1 - \frac{1}{2}\left[(\Theta_1 + \Theta_2 - \Theta_3) \pm \sqrt{(\Theta_1 + \Theta_2 - \Theta_3)^2 - 4\Theta_1\Theta_2}\right] , \quad (4.54)$$

where:

$$\Theta_1 \equiv 1 - e^{\lambda\Delta_\tau} , \quad (4.55a)$$

$$\Theta_2 \equiv \frac{4f(1 - h_1(\xi))}{1 - (1-f)h_1(\xi)} , \quad (4.55b)$$

$$\Theta_3 \equiv f\frac{1 - e^{\lambda\Delta_\tau}}{\lambda}\frac{h_1(\xi)}{h_2(\xi)}\frac{4f}{[1 - (1-f)h_1(\xi)](1-f)} . \quad (4.55c)$$

Thus, under the restriction stated earlier in Eq. (4.39), Eq. (4.54) provides the amplification factors of the perturbed part of the IMC equations for a single Fourier mode. Next we analyze this result to determine whether $|\rho| < 1$ or if $\rho < 0$ for any permissible values of q, Δ_τ, and ξ.

4.4 Analysis

Since the solutions of ρ in Eq. (4.54) are somewhat complicated functions of their arguments, it is useful to first consider the simpler condition of an infinite medium with a spatially flat mode for which $\xi = 0$. In the limit as $\xi \to 0$, we find that:

$$\begin{aligned}\lim_{\xi\to 0}\lambda &= \lim_{\xi\to 0}\frac{1}{q}\left(\frac{\xi}{\tan\frac{\xi}{1-f}} - 1\right) , \\ &= \frac{1}{q}(1 - f - 1) , \\ &= -\frac{f}{q} , \end{aligned} \quad (4.56)$$

and that

$$\lim_{\xi\to 0} h_1(\xi) = \lim_{\xi\to 0}\frac{\tan^{-1}\xi}{\xi} = 1 , \quad (4.57)$$

$$\begin{aligned}\lim_{\xi\to 0} h_2(\xi) &= \lim_{\xi\to 0}\frac{\tan^{-1}\left(\frac{\xi}{1+\lambda q}\right)}{\xi} , \\ &= \frac{1}{1+\lambda q} = \frac{1}{1-f} . \end{aligned} \quad (4.58)$$

Thus, the limits of Eqs. (4.55) give:

$$\lim_{\xi\to 0}\Theta_1 \equiv 1 - e^{-f\Delta_\tau/q}\,, \tag{4.59a}$$

$$\lim_{\xi\to 0}\Theta_2 \equiv 0\,, \tag{4.59b}$$

$$\begin{aligned}\lim_{\xi\to 0}\Theta_3 &\equiv -q\left(1-e^{-f\Delta_\tau/q}\right)\frac{1-f}{1}\frac{4f}{[1-(1-f)](1-f)}\,,\\ &= -4q(1-e^{-f\Delta_\tau/q})\,,\end{aligned} \tag{4.59c}$$

and, by Eq. (4.54), the two values of ρ for $\xi = 0$ are:

$$\begin{aligned}\lim_{\xi\to 0}\rho_1 \equiv \rho_{1,0} &= 1 - \left((1-e^{-f\Delta_\tau/q}) - 4q(1-e^{-f\Delta_\tau/q})\right)\,,\\ &= (1+4q)e^{-f\Delta_\tau/q} - 4q\,,\end{aligned} \tag{4.60a}$$

$$\lim_{\xi\to 0}\rho_2 \equiv \rho_{2,0} = 1\,, \tag{4.60b}$$

where $\rho_{1,0}$ is the root that uses the "plus" sign in the expression involving $\pm$. The "other" root, $\rho_{2,0}$, is extraneous at $\xi = 0$, and does not contribute to the solution. Numerically we have found that for $\xi \neq 0$, ρ_2 is slightly less than unity.

4.4.1 Unconditional Stability

The fundamental question is if $|\rho_{1,0}| < 1$, indicating that the IMC method is unconditionally stable in an infinite medium with no spatial dependence. First, we have:

$$\rho_{1,0} = (1+4q)e^{-f\Delta_\tau/q} - 4q < 1\,,$$

since, by rearranging, this is merely

$$e^{-f\Delta_\tau/q} < 1\,. \tag{4.61}$$

That is, $\rho_{1,0} < 1$, so monotonic, exponential divergence should never occur. Next, we would like to consider if an instability could be caused from $\rho_{1,0} < -1$. Stability is guaranteed when:

$$(1+4q)e^{-f\Delta_\tau/q} - 4q > -1\,,$$

and, if $0 < q < 1/4$, then the equivalent expression

$$(1 + 4q)e^{-f\Delta_\tau/q} > 0 > 4q - 1\,,$$

is always true. Therefore, stability is assured (for all Δ_τ and $0 \leq \alpha \leq 1$) if $q < 1/4$. We next consider the domain $1/4 < q < \infty$. Stability is assured if:

$$\begin{aligned}
(1 + 4q)e^{-f\Delta_\tau/q} - 4q &> -1\,, \\
e^{-f\Delta_\tau/q} &> \frac{4q-1}{4q+1}\,, \\
\frac{-f\Delta_\tau}{q} &> \ln\frac{4q-1}{4q+1}\,, \\
-f\Delta_\tau &> q\ln\frac{4q-1}{4q+1}\,,
\end{aligned}$$

and using the definition of the Fleck factor, this can be written:

$$-\frac{\Delta_\tau}{1 + 4\alpha\Delta_\tau} > q\ln\frac{4q-1}{4q+1}\,. \tag{4.62}$$

We notice that the left hand side of this equation depends only on α and Δ_τ, while the right hand side depends only on q. These functions are also both monotonic on $\Delta_\tau \in [0, \infty)$ and $q \in (1/4, \infty)$. The function on the left side is minimized when $\Delta_\tau \to \infty$, so:

$$-\frac{\Delta_\tau}{1 + 4\alpha\Delta_\tau} > -\frac{1}{4\alpha}\,. \tag{4.63}$$

The function on the right side is maximized when $q \to \infty$, in which case:

$$\lim_{q\to\infty} q\ln\frac{4q-1}{4q+1} = -\frac{1}{2}\,, \tag{4.64}$$

Using Eq. (4.63) and Eq. (4.64) in Eq. (4.62), stability is assured if

$$\begin{aligned}
-\frac{1}{4\alpha} &\geq -\frac{1}{2}\,, \\
\alpha &\geq \frac{1}{2}\,.
\end{aligned} \tag{4.65}$$

Thus, the infinite-medium IMC equations are unconditionally stable for all q and all Δ_τ provided that $0.5 \leq \alpha \leq 1.0$. This result is in agreement with the recommendation provided by Fleck and Cummings in [21], but it provides the recommendation with a firmer foundation. This conclusion does not address spatial effects, which

could further restrict α to values closer to unity. However, we shall see later that ρ_1 is not a strong function of the Fourier mode ξ, so that $\rho_{1,0} \approx \rho_1$ over the range of ξ for which Eq. (4.54) is valid.

We next consider whether it is possible for $\rho_1 < 0$ under the assumption that the most implicit value of α ($\alpha = 1$) is chosen. If so, then the infinite-medium IMC equations permit damped oscillations. In practice, it is known that the IMC equations permit such oscillations, and they are believed to be unphysical, as sufficiently reducing the size of the time step eliminates them. However, until now, their character has not been well-understood, and there has been no quantitative theory to predict their existence for anything but a 0-D, gray, linear problem [31].

4.4.2 Damped Oscillations

As in the previous section, we first consider the spatially flat mode $\xi = 0$ in order to generate some insight as to whether q and Δ_τ may be found such that $\rho_{1,0} < 0$. We begin by finding the minimum value of $\rho_{1,0}$ – if it is negative, then other values of q and Δ_τ in its neighborhood should also cause $\rho_{1,0} < 0$. First, one may take the partial derivative of $\rho_{1,0}$ with respect to Δ_τ to find that $\rho_{1,0}$ is monotonically decreasing in τ, so that

$$\lim_{\Delta_\tau \to \infty} \rho_{1,0}(q, \Delta_\tau) = (1 + 4q)e^{-1/4q} - 4q \,, \tag{4.66}$$

minimizes $\rho_{1,0}$ over all time step values. This resulting function of q has a single minimum value at which its derivative is zero. That is, $\rho_{1,0}$ is minimized when $\Delta_\tau \to \infty$ and when q satisfies:

$$\begin{aligned}
\frac{d}{dq}\left[(1 + 4q)e^{-1/4q} - 4q\right] &= 0 \,, \\
e^{-1/4q}\left(\frac{1}{4q^2}\right) + \left(4qe^{-1/4q}\frac{1}{4q^2} + 4e^{-1/4q}\right) - 4 &= 0 \,, \\
e^{-1/4q} &= \frac{16q^2}{1 + 4q + 16q^2} \,, \\
1 &= -4q \ln\left(\frac{16q^2}{1 + 4q + 16q^2}\right) \,.
\end{aligned}$$

This last equality is satisfied when $q \approx 0.1394$. Using this value of q in Eq. (4.66), we find that:

$$\rho_{1,0}(q = 0.1394, \Delta_\tau = \infty) \approx -0.2984 < 0 \,.$$

In other words, it *is* possible to find q and Δ_τ such that $\rho_1 < 0$. This means that even when $\alpha = 1$, it is possible for the infinite-medium IMC equations to exhibit damped temporal oscillations.

Next, we derive the monotonicity condition for the 0-D, gray IMC equations applied to a nonlinear problem, defined by $\rho_{1,0}(q, \Delta_\tau) > 0$. When this condition is met, the IMC procedure produces time-dependent temperature solutions that are monotonic functions of time. We require:

$$\begin{aligned}
\rho_{1,0}(q, \Delta_\tau) = (1 + 4q)e^{-f\Delta_\tau/q} - 4q > 0\,, \\
e^{-f\Delta_\tau/q} > \frac{4q}{1 + 4q}\,, \\
-f\Delta_\tau > q \ln\left(\frac{4q}{1 + 4q}\right)\,.
\end{aligned}$$

By Eq. (4.19), this is:

$$\begin{aligned}
-\frac{\Delta_\tau}{1 + 4\alpha\Delta_\tau} > q \ln\left(\frac{4q}{1 + 4q}\right)\,, \\
-\Delta_\tau > q \ln\left(\frac{4q}{1 + 4q}\right)(1 + 4\alpha\Delta_\tau)\,,
\end{aligned}$$

or, solving for Δ_τ,

$$\Delta_\tau < \frac{-q \ln\left(\frac{4q}{1+4q}\right)}{4\alpha q \ln\left(\frac{4q}{1+4q}\right) + 1}\,. \tag{4.67}$$

Eq. (4.67) is the monotonicity condition for the 0-D, nonlinear, gray IMC equations. Writing this in terms of the unscaled time step Δ_t, we get:

$$\Delta_t \sigma_0 c < \frac{-\ln\left(\frac{4q}{1+4q}\right)}{4\alpha q \ln\left(\frac{4q}{1+4q}\right) + 1}\,. \tag{4.68}$$

Eqs. (4.67) and (4.68) provide the first quantitative arguments that damped oscillations are unphysical, since, in the limit as $\Delta_\tau \to 0$, one expects to recover the solution of the TRT equations. This is in agreement with what has been seen in practice, which is that decreasing the size of the time step tends to suppress damped oscillations. Eq. (4.68) is similar in form to the condition obtained by Mosher and Densmore for the linear problem [31], and one may draw similar conclusions from it. For instance, one may analytically demonstrate that only by choosing $\alpha = 1$ is it

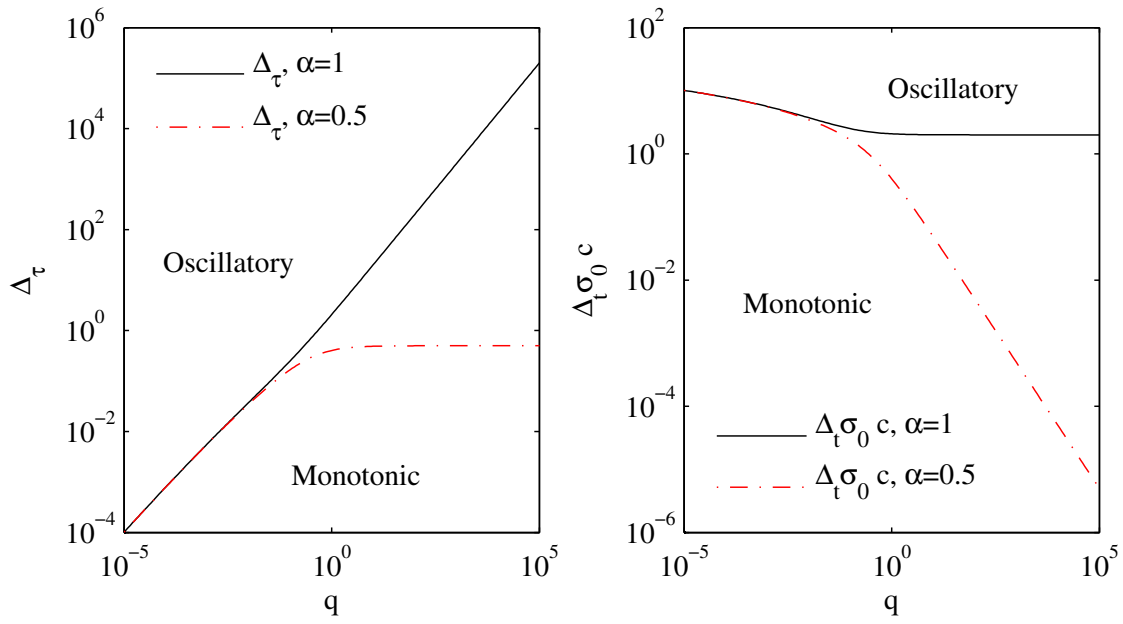

Figure 4.2: Monotonicity conditions on Δ_τ and $\Delta_t \sigma_0 c$ for the 0-D, nonlinear, gray IMC equations.

possible to satisfy Eq. (4.68) for all q [although this could also be argued directly from Eq. (3.38)]. Figure 4.2 provides log-log plots of the monotonicity conditions given by Eq. (4.67) and Eq. (4.68). From Figure 4.2, we see that as $q \to 0$, the scaled time step Δ_τ that satisfies Eq. (4.67) also goes to zero. However, the unscaled time step Δ_t does not; it is increasing. As $q \to \infty$ with $\alpha = 1/2$, the limiting Δ_τ that satisfies Eq. (4.67) approaches the constant value $1/2$. This corresponds to a $1/2q$ behavior for Δ_t, which implies that one cannot find a Δ_t that satisfies the monotonicity condition in Eq. (4.68) for all q. As $q \to \infty$ with $\alpha = 1/2$, the limiting Δ_τ that satisfies Eq. (4.67) goes to infinity, and the corresponding unscaled time step Δ_t goes to the constant 2. This implies that a sufficient condition to eliminate damped oscillations in the IMC solutions applied to this nonlinear, 0-D, gray problem is to choose $\alpha = 1$ and an unscaled time step that satisfies:

$$\Delta_t \leq \frac{2}{\sigma_0 c} = 2t_{\text{coll}}\,, \tag{4.69}$$

where t_{coll}, the time required for a photon to travel one mean free path (here, at the equilibrium temperature), is defined in Eq. (4.10). In practice σ_0 can be very large, so a näive application of Eq. (4.69) over all spatial regions of a generic problem may require impractically small time steps. Next, we shall examine the general shape of

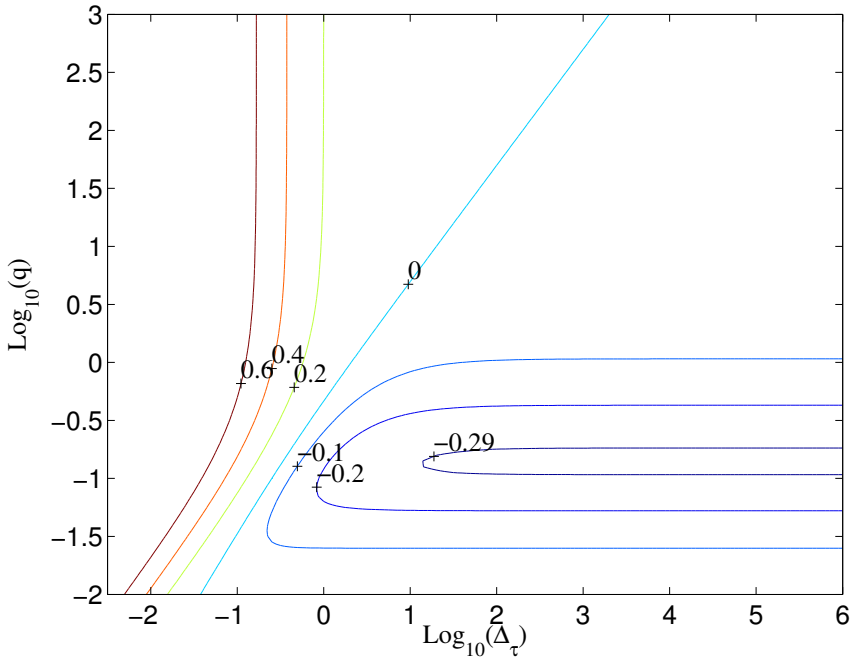

Figure 4.3: A contour plot of the 0-D amplification factor $\rho_{1,0}$.

$\rho_{1,0}$ as a function of Δ_τ and q, assuming that $\alpha = 1$.

Figure 4.3 is a contour plot of $\rho_{1,0}$ for $\xi = 0$, given by Eq. (4.60a). We note that the domain of this figure is large, as it is on a log-log scale, and the axes are rotated relative to Figure 4.2. In Figure 4.3, the contour $\rho_{1,0} = 0$ is the monotonicity condition in Eq. (4.67) that divides the domain between positive, non-oscillatory amplification factors for small Δ_τ and negative, oscillatory amplification factors for large Δ_τ. We also note that the region for which $\rho_{1,0} < -0.1$ is restricted to relatively small q. Since the sufficient condition in Eq. (4.69) was obtained by allowing $q \to \infty$, it is an overly-restrictive limit in problems for which one may expect q to be relatively large.

The next question is whether these results can be extended to Fourier modes other than $\xi = 0$. Figure 4.4 is a contour plot of ρ_1 for a fixed Fourier mode with $\xi = 0.001$. This figure is intended to provide the general shape of ρ_1 as a function of its arguments, especially the region where the minimum occurs. There are two key differences between Figure 4.4 and Figure 4.3 (for which $\xi = 0$). The first difference involves the contours for the negative amplification factors. In Figure 4.3, these contours are not closed; they extend to infinite Δ_τ. In Figure 4.4, the contours are closed, encapsulating the region in which the minimum value of ρ_1 occurs. The second difference is that in Figure 4.4, the contour for which $\rho_1 = 0$ is no longer a

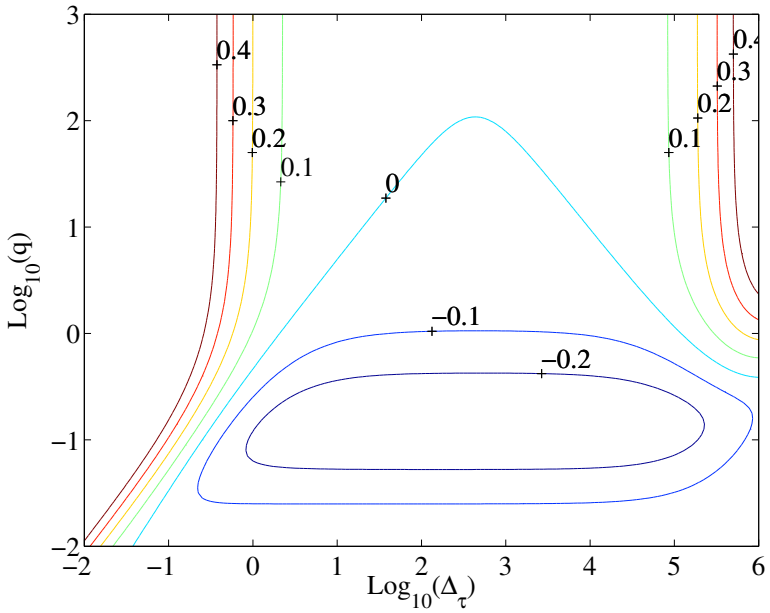

Figure 4.4: A contour plot of the amplification factor ρ_1 for $\xi = 0.001$.

line that neatly divides the non-oscillatory amplification factors for small Δ_τ from the oscillatory amplification factors for large Δ_τ. Instead, the line has become a curve that "folds over" as Δ_τ is increased. For q large enough in the domain of this figure, ρ_1 is always positive. The differences between these two figures are enhanced by increasing the value of ξ; we explore this further in Figure 4.5.

Figure 4.5 depicts the level curves for which $\rho_1 = 0$ for fixed values of ξ on a domain described by q and Δ_τ on a log-log scale. In this figure, $\rho > 0$ throughout the regions above and to the left of a given curve; these regions correspond with monotonic decay. Regions below and to the right of the curves correspond to damped oscillations, for which $-1 < \rho < 0$. From Figure 4.5 we observe that it is possible to guarantee monotonic behavior for any q and Fourier mode ξ by reducing the size of the time step. One surprising aspect of the theory is that, for certain values of q and ξ, it is possible to traverse regions of monotonic and oscillatory behavior more than once by *increasing* the size of the time step. As an alternate reference, this may be seen more readily in Figure 4.6, which depicts the values of $\rho_1(\Delta_\tau)$ along a horizontal slice corresponding to $q = 1$ in Figure 4.5. This behavior seems to indicate that it may be possible to suppress oscillations, by increasing the time step size in a problem. However, such a conclusion would be misguided, as this figure says nothing about the *accuracy* of a given solution. A transition from monotonic to oscillatory behavior should be warning enough that the time step size is too large; further increases in

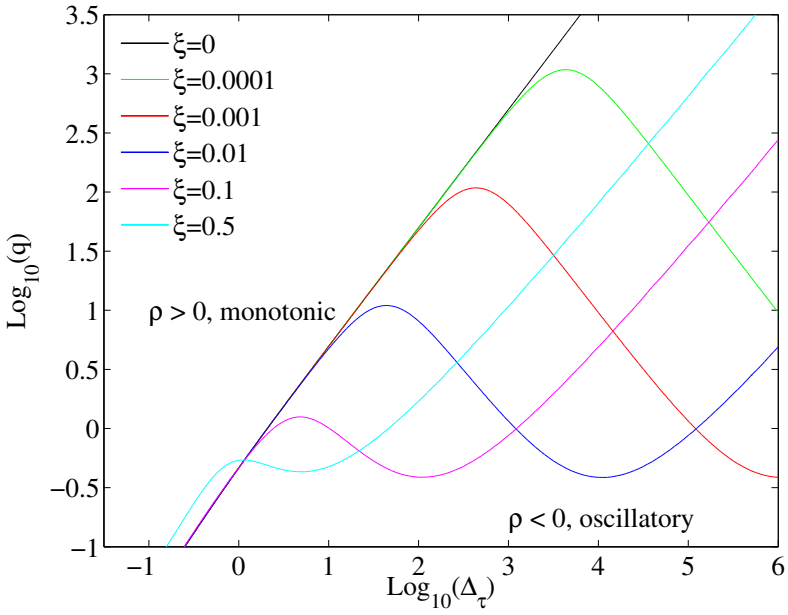

Figure 4.5: The values of q, Δ_τ, and ξ for which $\rho_1 = 0$.

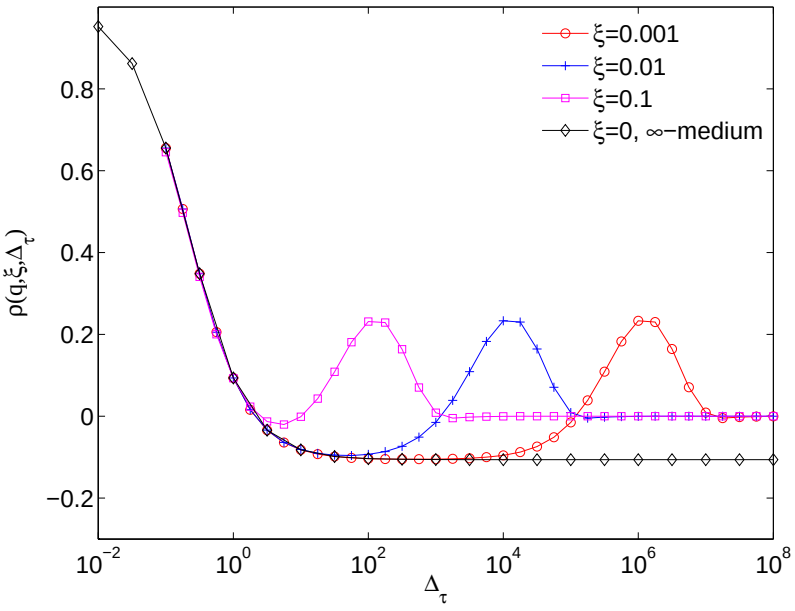

Figure 4.6: The amplification factor ρ_1 as a function of Δ_τ for $q = 1$ and several fixed Fourier modes ξ.

Table 4.1: The location and minimum values of ρ_1 for fixed modes ξ

ξ	q	Δ_τ	ρ
0	0.1394	∞	-0.2984
0.001	0.1392	433.0	-0.2979
0.01	0.1374	43.30	-0.2932
0.1	0.1241	4.320	-0.2538
0.5	0.1121	0.805	-0.1809
1.0	0.1833	0.438	-0.1969

its size would certainly worsen accuracy at the expense of suppressing oscillations. Therefore, disregarding this aspect of the theory, for a fixed q and ξ, it is possible to find a "critical" time step size $\Delta_{\tau,c}$ such that $\rho_1 > 0$ for $\Delta_\tau < \Delta_{\tau,c}$ and $\rho_1 < 0$ for $\Delta_{\tau,c} < \Delta_\tau$. This result satisfies physical intuition and experience in that damped oscillations may be eliminated by reducing the size of the time step. However, it is a little surprising that the predicted critical time step sizes may become less than a mean free time for emission. Returning to Figure 4.5, it is apparent that for $\xi < 0.1$, Eq. (4.67) is a sufficient condition to ensure monotonicity in the IMC solution, as it describes the contour for $\xi = 0$. For $\xi = 0.5$ this condition appears to be violated for $\Delta_\tau < 1$, but this disagreement occurs in a region for which the linear stability theory begins to break down [ξ is relatively large and Δ_τ is small; see Eq. (4.41)]. Thus, we expect that the monotonicity condition given in Eq. (4.67) for $\xi = 0$ is likely sufficient to eliminate damped temporal oscillations for any near-equilibrium problem.

We next consider the second major difference between Figures 4.3 and 4.4, the encapsulation and locations of the minima. Table 4.1 depicts the numerically estimated minimum values of ρ_1 from Eq. (4.54) for a fixed ξ over all combinations of q and Δ_τ. Inspection of this table reveals several important characteristics of this theory. First, the absolute minimum value of ρ_1 occurs for the spatially flat mode $\xi = 0$ for which $q = 0.1394$ and $\rho \approx -0.3$. The time step at this point is listed as ∞, but, more practically, ρ becomes negative when $\Delta_\tau > 0.34$, and rapidly decreases to its near-minimum value, as $\rho < -0.28$ for $\Delta_\tau > 6.3$. Regardless, the magnitude of the damped oscillations is maximized when $\xi = 0$, corresponding to a 0-D, infinite-medium solution. Therefore, we may consider the much simpler-to-solve 0-D, infinite-medium problem as a "worst-case" for potential stability issues. Later we shall consider modifications to the IMC equations and analyze their stability for this simpler 0-D problem based on this conclusion.

Next, as ξ is increased by several orders of magnitude, the minimum value of ρ_1

is relatively unaffected until $\xi \approx 0.1$ (this may be observed by descending along the right-most column of Table 4.1). Thus, the magnitude of the damped oscillations is relatively insensitive to ξ until $\xi \geq 0.1$, at which point the minimum value of ρ_1 jumps from -0.25 to -0.18. Larger ξ corresponds to spatial modes that are increasingly oscillatory. We conjecture that this sudden weakening of the damped temporal oscillations is due to spatial transport effects, which effectually "smear out" the spatial oscillations between time steps. It should also be reiterated that the general solution of a problem for which ξ is large is likely not separable in space and angle, so that the applicability of this theory diminishes as ξ is increased [see Eq. (4.41)]. Separable solutions are "good enough" up to the point that non-separable transport effects begin to dominate. Thus, from this last column we conclude that in a general problem containing many Fourier modes, one may expect the contribution of damped temporal oscillations to be most significant from the largest spatial modes (small ξ), whereas the small modes (large ξ) will have little or no contribution.

Finally, Table 4.1 also provides the *location* of the minimum values of ρ_1 with respect to q and Δ_τ. In the second column, we observe that q is relatively insensitive to the magnitude of ξ, hovering between 0.1394 for $\xi = 0$ and 0.1241 for $\xi = 0.1$. Returning to the differences between Figures 4.3 and 4.4, this means that the "vertical" location of the minimum is relatively unaffected by changes in ξ. From this we conclude that problems for which q (the ratio of $U_{r,0}$ to $U_{m,0}$) is small will tend to be more problematic with respect to the presence of damped, temporal oscillations. In the third column, we see that Δ_τ is highly sensitive to the value of ξ. Returning to the differences between Figures 4.3 and 4.4, this means that the "horizontal" location of the minimum moves to the left somewhat rapidly as ξ is increased. The magnitude of Δ_τ also becomes quite small – less than one mean free time for emission – although, one must remember that as ξ is increased and Δ_τ is decreased, the theory loses its applicability. Later, we shall perform numerical experiments to test the efficacy of the theory in this region.

It was stated earlier that ρ_2, the "other" amplification factor generated by the theory that corresponds to the negative square root in Eq. (4.54), is nearly always equal to, but slightly less than unity. Figure 4.7 depicts a contour plot of ρ_2 for $\xi = 0.1$ over the same range as is shown for ρ_1 in Figure 4.4. This figure confirms that $\rho_2 \approx 1.0$ for a large range of q and Δ_τ, and it should be noted that for smaller ξ there is even less variation. Additionally, the most important region of this figure is for small q and small Δ_τ, which is precisely the region where the theory begins to break down. From this, it is difficult to conclude the precise effects that ρ_2 contributes

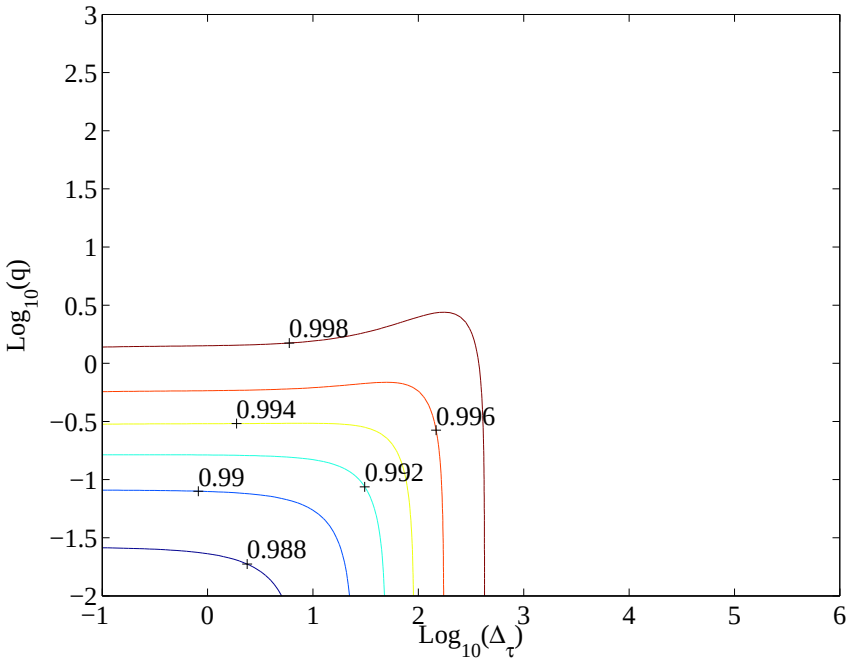

Figure 4.7: A contour plot of the amplification factor ρ_2 for $\xi = 0.1$.

to the solution.

We have found that the IMC equations are unconditionally stable in that they produce amplification factors ρ that are less than unity in magnitude. However, we have also shown that it is possible for the IMC equations to exhibit damped oscillations, and we have quantitatively predicted when these oscillations should occur. In the next section we will test the validity of this stability theory with a series of computational experiments.

4.5 Numerical Results

In this section, we consider three categories of numerical experiments, each of which assumes a gray approximation. The first category directly tests the theory by constructing problems whose initial conditions are equilibrium solutions perturbed by a single Fourier mode. The second category of problems is more physical. These consider an inhomogeneous source that injects energy into an initially low-temperature system until the system has enough energy to reach a specified equilibrium temperature. The third category represents the archetypal problems of interest to the TRT community. In these problems, an initially cold slab is subjected to a burst of relatively hot radiation on one of its boundaries, and a "Marshak" (temperature)

wave emerges that propagates through the geometry. These problems are listed in order increasing difficulty with regard to the incorporation of nonlinear effects and the applicability of the linear stability theory.

Throughout this section it is important to remember that the theory described above does *not* incorporate a spatial grid. However, to perform each of the following numerical experiments using the IMC method, it is necessary to impose a spatial grid. Additionally, it is impossible to avoid the introduction of statistical noise into the calculation, since a finite number of particle history must be used. Together, these have the effect of introducing spatial truncation errors and "extra" Fourier modes that are not directly accounted for by our stability theory.

In each of the experiments, the simulations were performed using the scaled variables. This is done by setting $a = c = 1$, ensuring that $\sigma_0 = 1$, setting $c_v = 1/q$, setting $\Delta_t = \Delta_\tau/q$, and controlling the problem energy so that in equilibrium the scaled temperature $M(t) \to 1$, all to ensure that Eqs. (4.6) are satisfied.

4.5.1 Single Fourier Modes

The first set of experiments is contrived to exactly match the assumptions made in deriving Eq. (4.54). Namely, each problem is a slight perturbation away from equilibrium and contains a single Fourier mode. Although these problems are contrived, if the stability theory fails in this regime, it cannot be expected to perform in more realistic ones. The initial conditions for these problems are given by:

$$M(z) = 1 + M_1 \cos(\xi z)\,, \tag{4.70a}$$

$$\phi(z) = 1 - \frac{M_1}{q} \cos(\xi z)\,, \tag{4.70b}$$

where z is the scaled spatial variable, ξ is a single Fourier mode, and M_1 is the amplitude of the perturbation away from equilibrium. The system is represented by a single period with reflective boundary conditions, which corresponds to an infinite periodic medium. The perturbations in the temperature and intensity are intentionally mismatched. The maximum temperature corresponds with a minimum intensity, and the amplitude is chosen to satisfy the infinite medium energy conservation:

$$q\phi_1 + M_1 = 0\,, \Rightarrow \phi_1 = -\frac{M_1}{q}\,.$$

This is because from experiments it was found that the damped oscillations are most pronounced when this mismatch occurs between the energies in the intensity and the

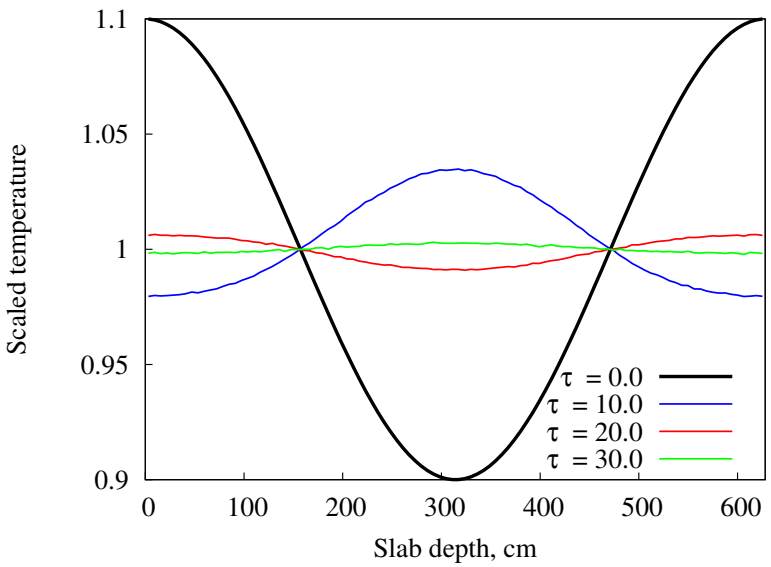

Figure 4.8: Experimentally-obtained damped oscillations in temperature profiles for $\xi = 0.01$, $q = 0.14$, $\Delta_\tau = 10$, for which the theory predicts $\rho_1 = -0.2862$.

material. In other words, the damped oscillations occur from a nonphysical energy exchange between the material and the radiation; the theory is most applicable when temperatures are slightly above (or below) equilibrium while the intensities are slightly below (or above) equilibrium. From another perspective, these problems are initialized such that they maximize the contribution of ρ_1 (which may be negative) and its associated eigenfunction while minimizing the contribution of ρ_2 (which is usually ≈ 1) to the solution. We note that for each of these problems we use 20 spatial zones. We have found from experiments that the stability characteristics are not affected by the spatial grid size, provided that the grid adequately resolves each problem's spatial variation.

In the first experiment, $\xi = 0.01$, $q = 0.14$, and $\Delta_\tau = 10$, for which the theory predicts $\rho_1 = -0.2862$. Figure 4.8 depicts the temperature profiles for the initial condition and three time steps. For these values of ξ and Δ_τ, the theory is extremely accurate: the temperature perturbations retain their cosine shape, invert, and reduce in magnitude at each step almost exactly as the theory predicts that it should. We estimate the reduction in magnitude r_n from step n to $n+1$ quantitatively by computing:

$$r_n = \frac{||M_{n+1} - 1||}{||M_n - 1||} = \frac{\left(\sum_{j=1}^{J} |M_{n+1}(x_j) - 1|^2\right)^{1/2}}{\left(\sum_{j=1}^{J} |M_n(x_j) - 1|^2\right)^{1/2}}, \tag{4.71}$$

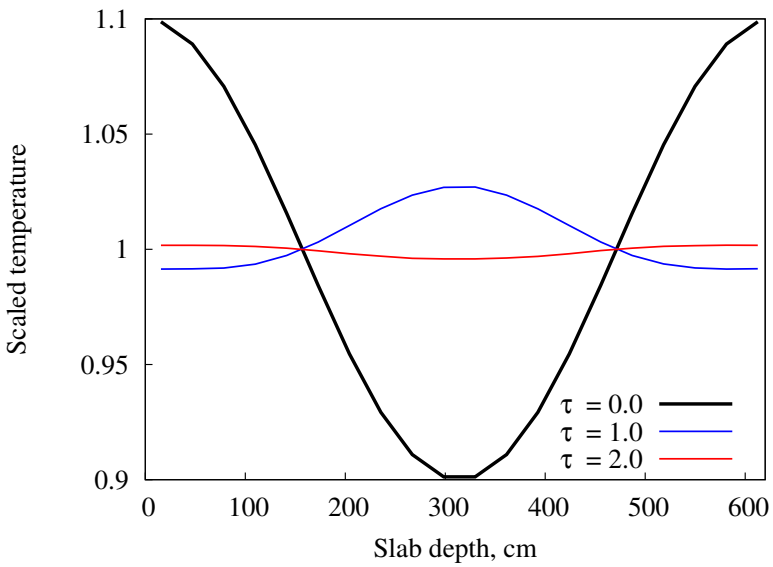

Figure 4.9: Experimentally-obtained damped oscillations in temperature profiles for $\xi = 0.01$, $q = 0.14$, $\Delta_\tau = 1$, for which the theory predicts $\rho_1 = -0.1861$.

for each spatial value centered upon x_j, for cells $1 \leq j \leq J$. The average geometric reduction in amplitude between the first two steps (r_1) is 0.2846, $r_2 = 0.2744$, and $r_3 = 0.2922$, all of which are in excellent agreement with the predicted value of -0.2862.

Next, we test the quantitative predictive ability of this theory by reducing the time step to $\Delta_\tau = 1$ (one mean free time between absorption and reemission), for which $\rho_1 = -0.1861$. The values of q and ξ remain at 0.14 and 0.01 respectively. As may be seen in Figure 4.9, the damped oscillations remain, but their magnitude diminishes more quickly. The average geometric reduction in amplitude for the first time step in this problem is $r_1 = 0.1982$, and $r_2 = 0.1689$, both of which are nearly the value predicted by the theory. The slight deviations occur because the cosine temperature shape is a little skewed – for the time step $\tau = 1.0$, the maximum is approximately 1.027 and the minimum is 0.992.

If we further reduce the time step to $\Delta_\tau = 0.35$, the theory predicts that $\rho_1 = -0.0096$. In other words, the perturbations should almost entirely disappear in a single time step. Figure 4.10 depicts the temperature profiles for this case. While the temperature does not reach equilibrium in a single step, it does in two steps. A slight oscillation remains in the center of the temperature after the first step, although monotonic decay occurs in the outside regions, indicating at least that $\Delta_\tau \approx 0.35$ is at the transition between monotonic decay and oscillatory behavior. The cosine

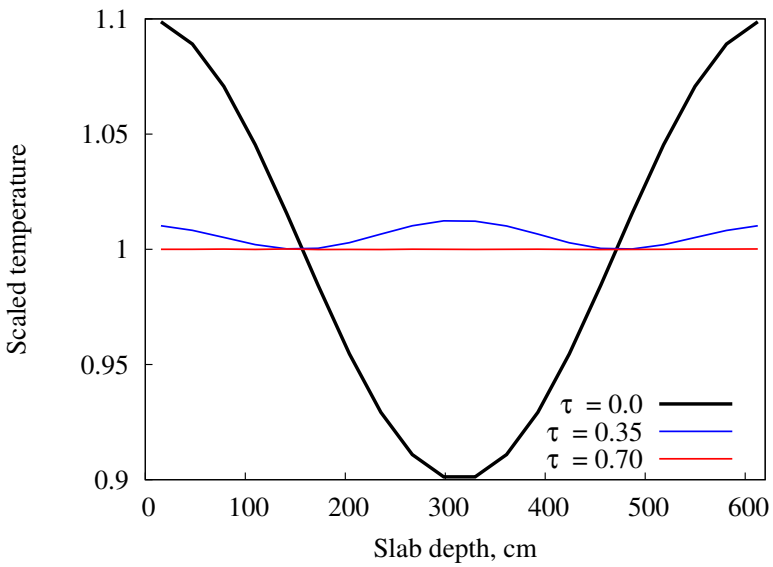

Figure 4.10: Experimentally-obtained temperature profiles for $\xi = 0.01$, $q = 0.14$, $\Delta_\tau = 0.35$ for which the theory predicts $\rho_1 = -0.0096$.

temperature shape has also become distorted at this transitional value of Δ_τ. For this experiment, $r_1 = 0.1007$ and $r_2 = 0.0105$.

Reducing the time step further to $\Delta_\tau = 0.2$, the theory predicts that $\rho_1 = 0.1454$, which implies that the perturbations should monotonically diminish to the equilibrium value. This behavior is verified by experiment and depicted in Figure 4.11. Also, for this problem $r_1 = 0.1747$ and $r_2 = 0.1714$, which are in satisfactory agreement with the prediction of 0.1454, although (again), the cosine temperature shape is distorted for this extremely small time step.

We have seen that as the time step is reduced such that $\Delta_\tau < 1.0$, the cosine shape becomes increasingly distorted. However, the stability theory does adequately predict the transition from oscillatory to monotonic behavior for $\xi = 0.01$, and the numerically calculated amplifications factors remain in reasonable agreement. From further experiments, we can affirm that this accuracy in the theory is retained for smaller Fourier modes ($|\xi| < 0.01$) and for $\xi = 0$.

The next experiment considers $\xi = 0.1$ with $q = 0.1241$ and $\Delta_\tau = 4.32$, for which the theory predicts $\rho_1 = -0.2538$. The results are shown in Figure 4.12. For this Fourier mode the damped oscillations again appear as predicted, but at the last time step they begin to lose their cosine shape, although this is difficult to see. The magnitude of the reduction in amplitude is approximately correct for the first time step at $r_1 = 0.2529$, but loses accuracy at the second step with a value

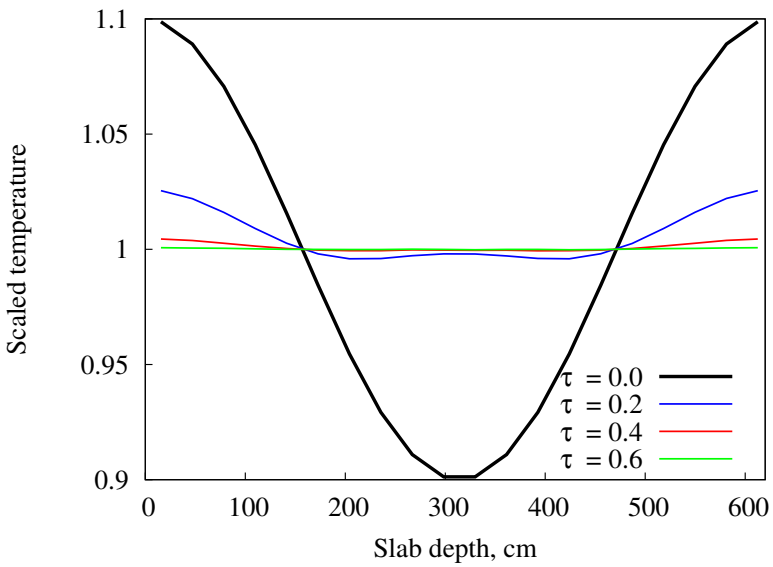

Figure 4.11: Experimentally-obtained temperature profiles for $\xi = 0.01$, $q = 0.14$, $\Delta_\tau = 0.2$ for which the theory predicts $\rho_1 = 0.1454$.

of $r_2 = 0.3087$. From further experiments we found that for several other Δ_τ, the theory is quantitatively correct for the first time step, but is slightly less accurate for the remaining time steps than that obtained for the smaller Fourier mode $\xi = 0.01$.

The last experiment of this type is for $\xi = 0.5$, $q = 0.1121$, and $\Delta_\tau = 0.805$, for which the theory predicts $\rho_1 = -0.1809$. The numerical results are shown in Figure 4.13. A clear distortion in the cosine shape emerges and develops as the time steps proceed, and, from experience, for $\xi > 0.5$ this distortion worsens and the theory loses its quantitative accuracy. For this problem, $r_1 = 0.1220$ and further values of r are less meaningful due to the distortion of the cosine shape (for instance, $r_2 = 0.7427$).

This gradual degradation in accuracy as ξ increases is not surprising – fundamentally, it comes from encroachment upon the limit in Eq. (4.41). From another perspective, this limit emerges from the assumption that the intensity is well-described by separable solutions in space and angle [see Eq. (4.38)]. While separable solutions well-describe the slowly-varying spatial modes (small ξ), non-separable solutions become more important for larger ξ. However, the theory does predict that the magnitude of the damped oscillations decreases for larger ξ, so it may not be that important to accurately represent these non-separable solutions. Physically, this is likely because spatial transport effects suppress high-frequency perturbations in the temperature and intensity, so that the magnitude of any damped oscillations that might occur should be small. In general, we can conclude that the theory successfully quantita-

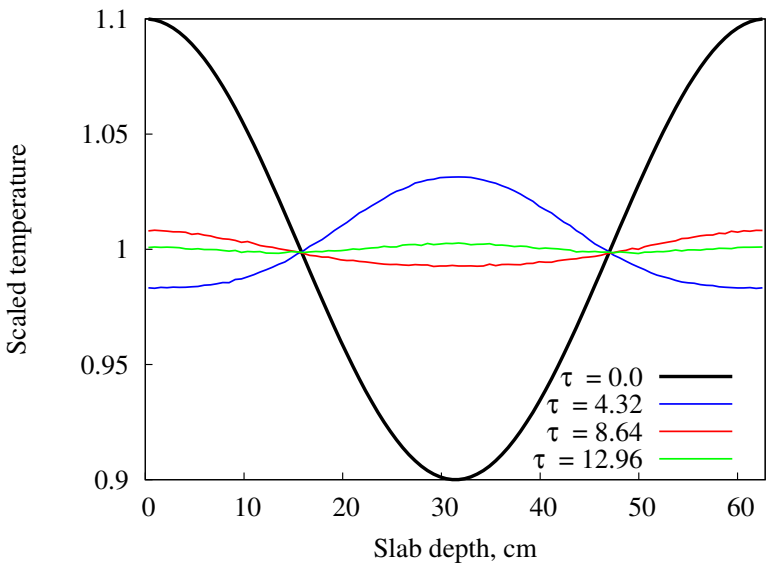

Figure 4.12: Experimentally-obtained temperature profiles for $\xi = 0.1$, $q = 0.1241$, $\Delta_\tau = 4.32$ for which the theory predicts $\rho_1 = -0.2538$.

tively predicts the existence and magnitude of the damped oscillations for this special class of problems that contain a single Fourier mode.

4.5.2 Source Problems

The next class of problems that we consider is more realistic. They begin with a system that is initially at equilibrium at a low temperature. At $\tau = 0$ a photon source is suddenly turned on. This source is left on until it has injected enough energy for the system to reach an equilibrium at $M = 1$, at which point it is shut off. Physically, one should expect to see a monotonic increase in the problem temperature, but we shall attempt to use the theory to predict a time step at which damped oscillations may occur. The stability theory derived above did not incorporate a photon source and was applied to problems that are near equilibrium. Therefore, the theory only becomes directly applicable once the source has been shut off and the solution is near equilibrium.

The first experiment considers a 0-D problem, numerically implemented by assuming a finite slab with a flat source and reflective boundary conditions. We set $q = 0.14$, the initial temperature to 0.1, and the shutoff time to $\tau = 4$. For this value of q, the critical time step value (using $T_0 = 1$) is $\Delta_{\tau,c} \approx 0.35$, and the minimum value of ρ_1 is approximately -0.29 for $\xi = 0$. Figure 4.14 depicts the temperature rise as a function of time over a range of time steps. From this figure it is roughly apparent

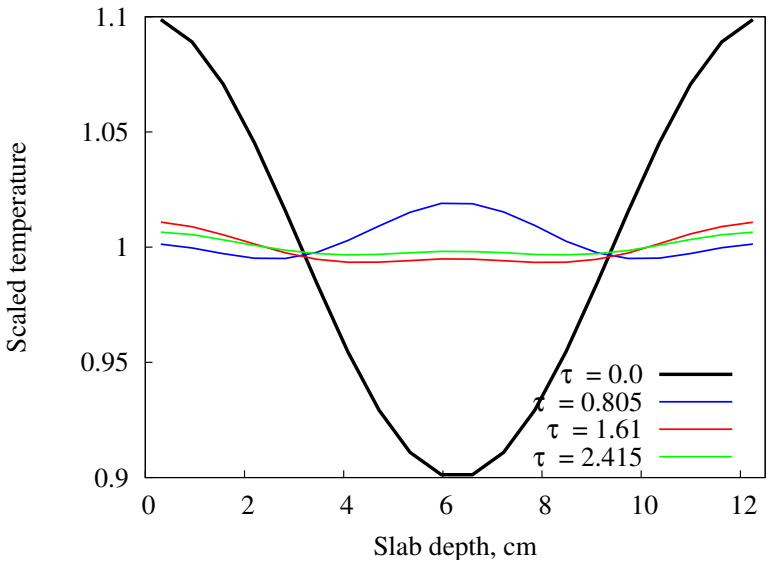

Figure 4.13: Temperature profiles for $\xi = 0.5$, $q = 0.1121$, $\Delta_\tau = 0.805$ for which $\rho_1 = -0.1809$.

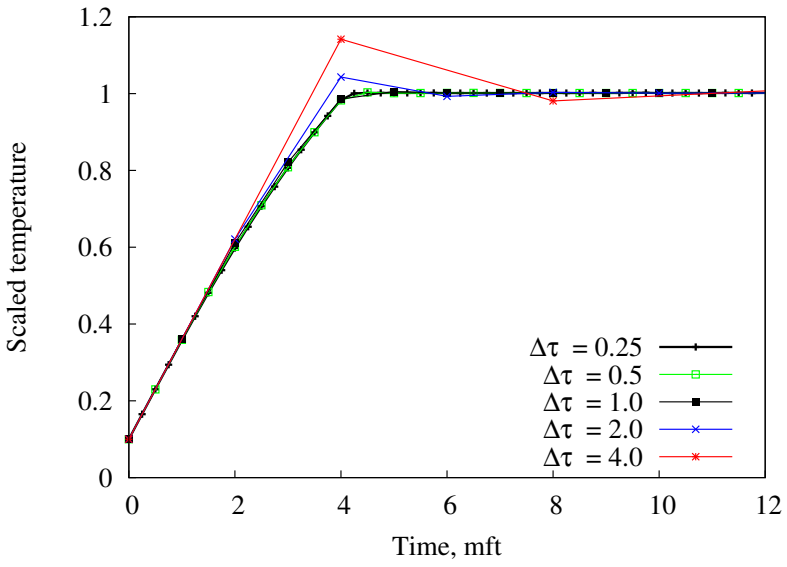

Figure 4.14: Experimentally-obtained temperature rise for an inhomogeneous source shut off at $\tau = 4$ for a range of Δ_τ.

that, although the temperature rise should be monotonic, it is not for the larger time steps. To help discern this behavior, Table 4.2 depicts the temperature values at the shutoff time T^0 and for the first two time steps immediately following the shutoff time (T^{+1} and T^{+2}). In this table, we see that damped oscillatory behavior occurs for $\Delta_\tau \geq 0.35$, although not to the extent expected. For $\Delta_\tau = 4$, one may calculate an "experimental" amplification factor r_1 using

$$r_1 = \frac{0.981 - 1.0}{1.142 - 1.0} = -0.134\,,$$

which is half the theoretical prediction of $\rho_{1,0}(0.14, 4) = -0.2695$. Thus, for this problem, the stability theory appears to be only qualitatively correct, as the oscillations reduce in magnitude faster than predicted. When $\Delta_\tau = 0.25$, the stability theory does successfully predict that the solution is completely monotonic. However, had we chosen to inject *all* of the energy in this short interval, the solution would still have overshot in the first step, so this is a limited success. The apparent quantitative disagreement in the amplitude is likely because, as Δ_τ is reduced in this problem, the likelihood of a "mismatch" occurring between the energy in the material and radiation is also reduced. For a sufficiently fine time step, the source drives the solution to equilibrium, where it essentially rests after it is shut off. From another perspective, by Eq. (4.54), the temperature solution consists of the superposition of two eigenvalues (ρ_1 and ρ_2) and two associated eigenfunctions. Our theory does not predict the relative magnitude of these two solutions, but does indicate when we can expect ρ_1 to be negative, whereas ρ_2 is generally near unity. The contribution of the solution due to ρ_2 is likely more significant for these problems than the "contrived" cosine perturbation problems we considered earlier. Although damped oscillations are difficult to see in this regime (the regime in which the theory predicts the presence of damped oscillations but they are not easily observable), their existence likely contributes to subtle inaccuracies in the IMC solution.

For the second set of numerical experiments involving a photon source, we introduce a space-dependence and material heterogeneity into the problem. The geometry is composed of two spatial regions, and is depicted in Figure 4.15. The description of the inside region, "Region 1", is entirely analogous to the problem just examined. In this region we set $q_1 = 0.14$, which corresponds with $c_{v,1} \approx 7.14$. In the outside regions, "Region 2", we set $q_2 = 0.01$, which corresponds with $c_{v,2} = 100$. The system has reflective boundary conditions. The photon source strength is adjusted in each region such that, at the shutoff time, the system contains sufficient energy to go to

Table 4.2: Temperatures when the source is turned off (T^0) and two steps after the source is turned off (T^{+1} and T^{+2}).

Δ_τ	T^0	T^{+1}	T^{+2}
0.25	0.984	1.001	1.001
0.5	0.982	1.003	1.001
1.0	0.986	1.005	1.001
2.0	1.043	0.993	1.003
4.0	1.142	0.981	1.007

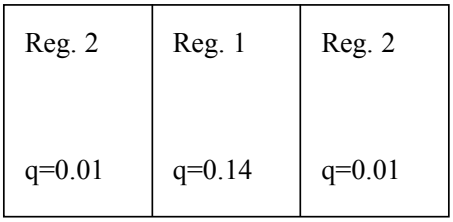

Figure 4.15: The geometry for a two-region source problem.

the specified uniform equilibrium temperature $T_0 = 1$. To numerically implement this problem in an IMC calculation, we set $a = c = 1$ and $\sigma = 1/T^3$. The initial temperature in both regions is 0.1. The source shutoff time is at $\Delta_t = 57.14$ sh, which corresponds to $\Delta_{\tau,1} = 8$ mean free times for emission in region 1, and $\Delta_{\tau,2} = 0.5714$ mean free times for emission in region 2. The primary region of interest in this problem is region 1, in which we expect damped oscillations to occur if the time step is too large, but there should also be some interaction at the boundaries between regions 1 and 2. The slab is 50 cm wide, and discretized into 40 zones, which is sufficient to resolve the spatial variation in the problem. From experiments, we found that the stability characteristics of this problem are not tied to the spatial grid size (assuming the solution is adequately resolved).

Figure 4.16 depicts the scaled temperature results of the numerical experiment using a time step of $\Delta_{\tau,1} = 8$ mean free times for emission ($\Delta_{\tau,2} = 0.5714$) [the mean free times reported in this figure correspond only to region 1]. Thus, all of the energy is injected in a single step. After the first time step ($\tau_1 = 8$), the solution is overshot in both regions, although the magnitude of the overshoot is greater in region 1 where the specific heat is smaller. At the second time step ($\tau_1 = 16$), the temperature oscillates below the equilibrium solution in the interior of region 1. At the interface of regions 1 and 2, there is a jump in the temperature solution – in region 2, the

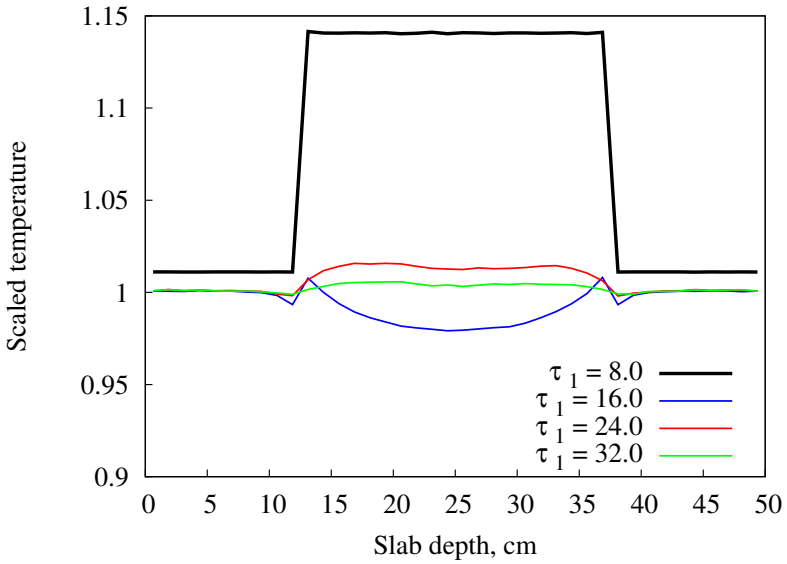

Figure 4.16: Experimentally-obtained temperature profiles for a two-region source problem in which $\Delta_{\tau,1} = 8$ mean free times for emission (in region 1).

temperature is below unity, and in region 1 the temperature is slightly above unity. This likely due to the difference in source strengths in each region. In region 2, the specific heat is large, which means that the photon source must also be large to obtain the proper equilibrium temperature. At the interface, then, some of the energy in region 2 leaks into region 1, causing a depression in the temperature in region 2 and an increase in region 1. In the third time step ($\tau_1 = 24$), the solution in the interior of region 1 oscillates above unity, and in the fourth time step ($\tau = 32$), the temperature has decreased, but not below unity. Although this problem type is not conducive to a straightforward application of the stability theory, in region 1, Eq. (4.60a) predicts the 0-D amplification factor -0.2839 (using $q_1 = 0.14$, and $\Delta_{\tau,1} = 8$). In region 2, we predict an amplification factor of -0.04 (using $q_2 = 0.01$, and $\Delta_{\tau,1} = 0.5714$). While we make no attempt to calculate an "amplification factor" from the numerical results for this heterogeneous problem, the theory does successfully predict that temporal oscillations should occur in region 1, and that they may occur in region 2 but to a much lesser extent.

Figure 4.17 depicts the temperature profiles when $\Delta_{\tau,1} = 4$ mean free times for emission ($\Delta_{\tau,2} = 0.2857$). We note that the limits on the ordinate axis are smaller than those of Figure 4.16. In this figure, damped temporal oscillations still occur in the interior of region 1 after the source is shut off, but to a lesser degree than in Figure 4.16. A similar boundary effect between regions 1 and 2 occurs during the

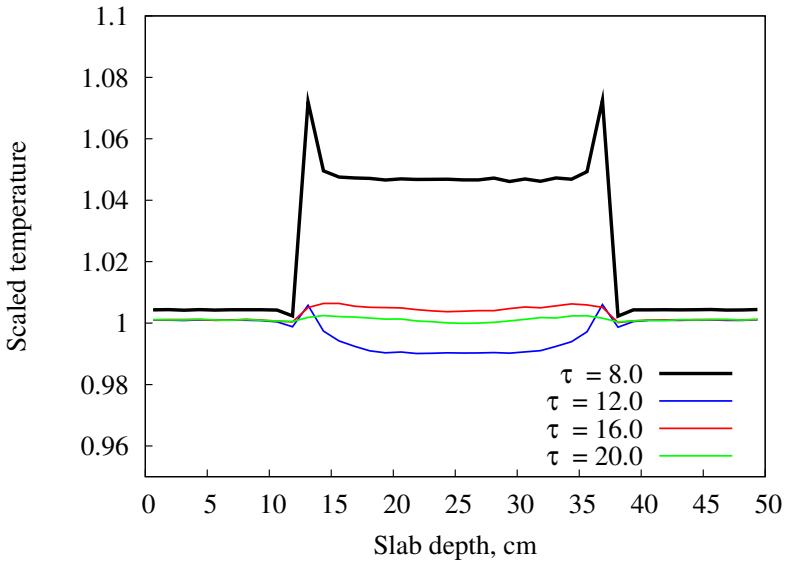

Figure 4.17: Experimentally-obtained temperature profiles for a two-region source problem in which $\Delta_{\tau,1} = 4$ mean free times for emission (in region 1).

first several time steps – the stronger source in region 2 leaks photons into region 1, causing the "horns" of higher temperature at the boundary of region 1. For this problem, the 0-D theory predicts an amplification factor of -0.2695 in region 1 and -0.04 in region 2. These successfully predict the existence and relative magnitude of damped oscillations in region 1 as compared to region 2, although the stability theory alone does not adequately explain the reduction in magnitude from the case in which $\Delta_{\tau,1} = 8$ [it does not provide the relative contributions of the solutions due to ρ_1 and ρ_2 in Eq. (4.54)].

Figure 4.18 depicts the temperature profiles when $\Delta_{\tau,1} = 2$ mean free times for emission ($\Delta_{\tau,2} = 0.1429$). We note that the limits on the ordinate axis are smaller than those of Figures 4.16 and 4.17. There is a small, but discernible amount of statistical noise in the numerical solutions for this problem. This is because the number of histories that would be needed to fully resolve the slight spatial variation in these solutions is cost-prohibitive. As was the case with the 0-D source problem, once the time step is sufficiently fine to begin resolving the photon source, any contribution from damped oscillations (excepting the initial overshoot in the solution) is difficult to perceive. The boundary effect is more pronounced in Figure 4.18 than in previous figures since using a smaller time step provides more opportunities for transport effects to smear out the source contributions. For this problem, the 0-D theory predicts an amplification factor of -0.2410 in region 1 and -0.04 in region 2. The

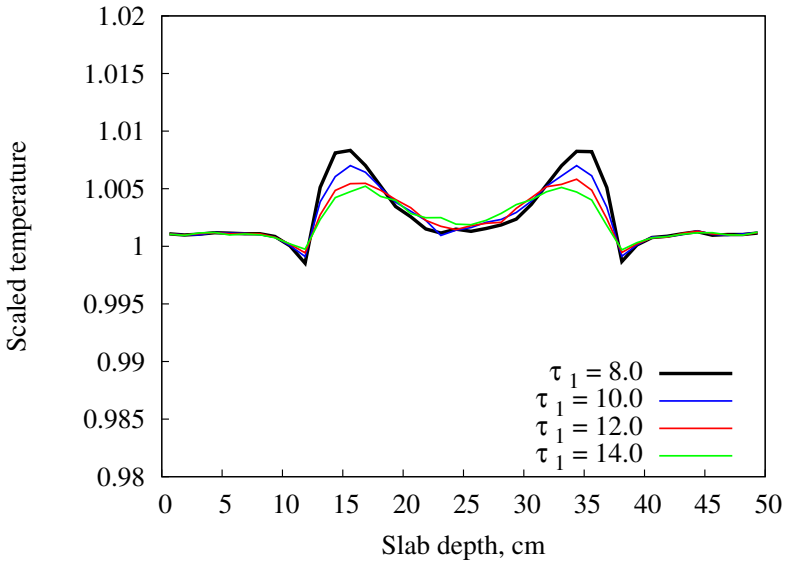

Figure 4.18: Experimentally-obtained temperature profiles for a two-region source problem in which $\Delta_{\tau,1} = 2$ mean free times for emission (in region 1).

apparent lack of damped temporal oscillations in region 1 after the source is shut off seems to indicate a defect in the theory, but can be explained from the above physical arguments concerning the temporal resolution of the photon source and the superposition of the solutions due to ρ_1 and ρ_2. For time steps less than $\Delta_{\tau,1} = 2$, one obtains similar temperature profiles. When $\Delta_{\tau,1} < 0.35$, the theory successfully predicts the solution to be completely monotonic, although, again, if the photon source were to be completely injected during this short of a time interval, it would still overshoot in the initial step.

4.5.3 Marshak Waves

Our last series of numerical experiments concerns a problem that is far-removed from the assumptions used to derive the stability theory, but is of primary interest to the TRT community. These problems are characterized by a slab that is initially cold, and is suddenly subjected to a blast of relatively hot, isotropic photons on one side. The photons propagate into and warm up the system, creating a temperature wave that moves across the system. These radiation and temperature waves are commonly referred to as *Marshak waves* [48] [33]. Marshak wave problems are strongly nonlinear in that the cold material ahead of the wavefront is much more optically thick than the hot material behind the wavefront. The wavefronts can therefore be very steep, and obtaining an accurate estimate of their location – where most of the relevant

physics is taking place – is paramount. Larsen and Mercier [27] found an upper limit on the size of the time step that ensures that the IMC equations satisfy a "maximum principle" that the underlying TRT equations satisfy. When the maximum principle is violated, the IMC solution contains temperatures that are *larger* than the boundary temperature. For Marshak wave problems, this affects the accuracy of the solution in that the temperature becomes too high at the wavefront. It also slows the numerical wave speed since the radiation becomes artificially trapped behind the wavefront. Marshak wave problems are the archetypal problems for the TRT community. In this section, we examine whether the stability theory is able to predict a maximum time step such that the estimate of the wavefront location is guaranteed to be accurate.

For our first numerical experiment, we set $q = 0.14$ and the initial temperature to 0.1. We impose an isotropic right boundary condition equal to the initial temperature and an isotropic left boundary condition at a unit temperature. We consider a slab that is four cm wide. This implies that the slab is initially 4,000 mean free paths thick, but only 4 mean free paths thick once equilibrium is reached. We track the wavefront up to $\Delta_\tau = 40$ mean free times to emission. Under these conditions, the 0-D amplification factor predicts that the maximum time step size for a monotonic solution (for which $\rho_{1,0} = 0$) is $\Delta_\tau \approx 0.35$. By comparison, the upper limit on the time step that ensures that the IMC equations do not violate the maximum principle is $\Delta_\tau = 0.00025$. This is an extremely small time step, and Larsen and Mercier acknowledge that it is likely an overly conservative estimate of when the maximum principle will be violated [27].

We begin by setting $\Delta_\tau = 0.1$ and $\Delta_x = 0.05$ cm. Figure 4.19 depicts the temperature wave at four intermediate times spaced 10 mean free times for emission apart. In this figure we see the temperature wave proceeding to the right, as anticipated. We also observe that there is little spatial variation in the temperature "behind" the wavefront and that the wavefront is relatively steep.

For the next series of tests, we leave the spatial grid size fixed at $\Delta_x = 0.05$ cm and increase the time step beyond $\Delta_\tau = 0.35$. Figure 4.20 depicts the resulting temperature profiles at the fixed time $\tau = 8$ but for the differing time steps. One can immediately spot the two-fold problem that occurs if large time steps are used: the maximum principle is violated in that the wavefront temperature can become *much* greater than the boundary temperature, and the corresponding wave speed is much too slow. Interestingly, these problems begin to occur once $\Delta_\tau \geq 0.5$, which seems to indicate that the stability theory does an adequate job anticipating when these problems begin to emerge. However, our theory does not account for the effect of

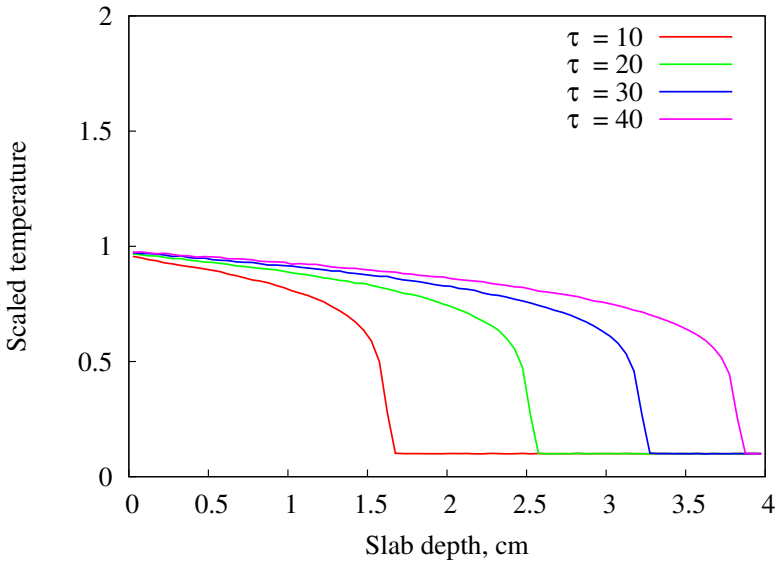

Figure 4.19: Time-dependent temperature profiles for a Marshak wave problem in which $\Delta_\tau = 0.1$ and $\Delta_x = 0.05$.

varying the spatial grid size.

We next consider the effect of fixing the time step at $\Delta_\tau = 0.5$ and varying the spatial grid size. Figure 4.21 depicts the temperature profiles at time $\tau = 8$ for these differing spatial grid sizes. One can see that precisely the same problems emerge as were found when the time step was varied, except here the maximum principle is increasingly violated as Δ_x is *decreased*. These results indicate that the employment of a maximum time step criterion independent of the spatial grid size (either from the stability theory or from [27]) is likely an inadequate indicator of when the maximum principle will be violated. We further explore this relationship by running a larger series of tests in which both the time step and the spatial grid size are varied.

There are two primary characteristics in either of Figures 4.20 and 4.21 that indicate an inaccurate solution: a too-large temperature near the wavefront, and an inaccurate wavefront location. We shall employ these two characteristics as simple metrics to characterize and compare the accuracy of the temperature solution at a particular point in time among several spatial and temporal grid values. Table 4.3 addresses the first of these characteristics. It depicts the maximum temperature obtained over the entire spatial domain at the fixed time $\tau = 8$ for variable spatial and temporal grid sizes. This table provides a simple means to compare the results of a fairly large underlying data set generated with substantial computational effort. Picking any column of this table and tracing downward, one can see the effect of

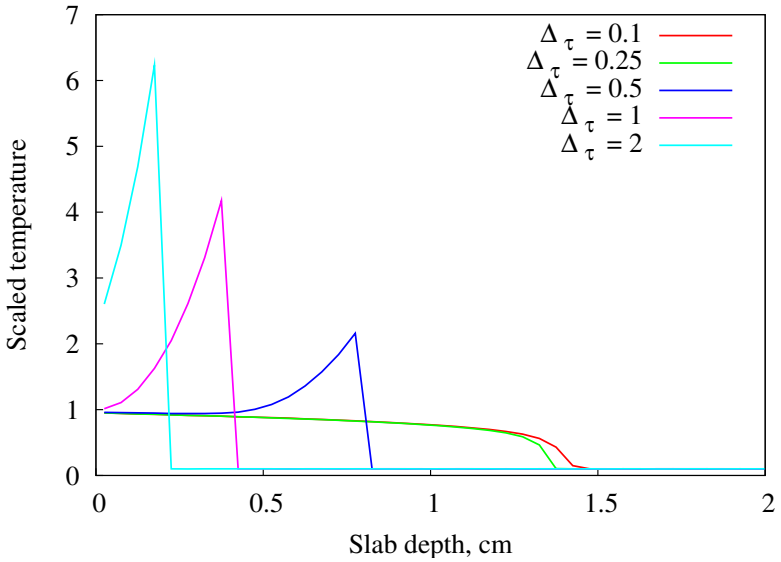

Figure 4.20: Temperature profiles at $\tau = 8$ for a Marshak wave problem in which the *time step* is varied using $\Delta_\tau = 0.1$, 0.25, 0.5, 1, and 2 mean free times for emission.

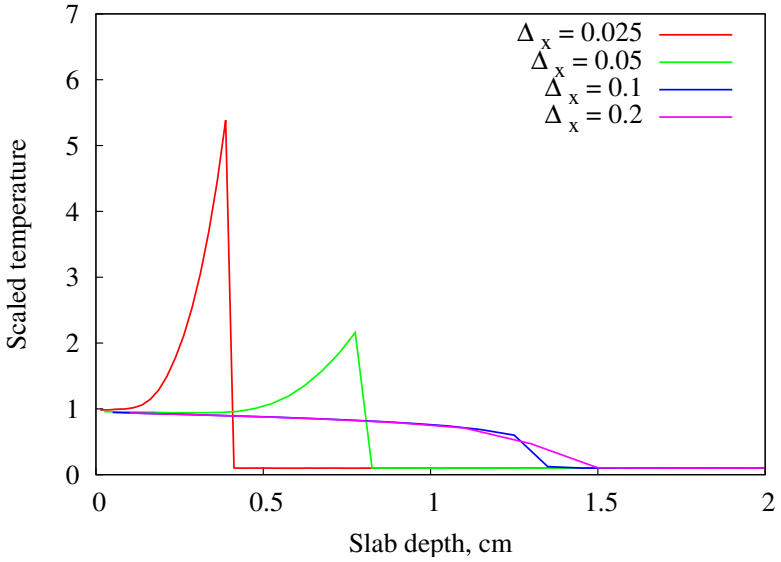

Figure 4.21: Temperature profiles at $\tau = 8$ for a Marshak wave problem in which the *grid size* is varied using $\Delta_x = 0.025$, 0.05, 0.1, and 0.2 cm.

Table 4.3: Maximum temperatures in Marshak wave at $\tau = 8$. Bold numbers indicate violation of the maximum principle.

$\Delta_\tau \backslash \Delta_x$	0.025	0.05	0.1	0.2
0.10	0.953	0.951	0.947	0.937
0.25	**2.551**	0.949	0.946	0.939
0.50	**5.383**	**2.159**	0.946	0.938
1.00	**8.541**	**4.175**	**1.756**	0.937
2.00	**12.412**	**6.233**	**3.122**	**1.386**

Table 4.4: Estimated wavefront location at $\tau = 38$

$\Delta_\tau \backslash \Delta_x$	0.025	0.05	0.1	0.2
0.10	3.688	3.675	3.75	3.7
0.25	3.438	3.675	3.65	3.7
0.50	1.887	3.425	3.65	3.7
1.00	0.938	1.875	3.35	3.5
2.00	0.463	0.925	1.85	3.3

fixing the spatial grid size and increasing Δ_τ. For each Δ_x, a different threshold Δ_τ may be found after which the maximum principle [$T > 1$] is violated. Also, picking any row of this table and tracing from right to left, one can see that similar effects are produced by fixing Δ_τ and decreasing the spatial grid size. In this table there is a diagonal running from the top left to the bottom right that separates inaccurate spatio-temporal grid choices (bottom left) from more accurate ones (top right). From this one may form a rough inequality that indicates when the solution of this problem will be accurate:

$$\Delta_\tau \leq 5\Delta_x \,. \tag{4.72}$$

We may make similar conclusions by using the other metric: the estimate of the wavefront location. To estimate the location of the wavefront at a fixed time, we search the temperature profile from the right for the first occurrence of $T \geq 0.2$, which is twice the temperature at the initial condition. The results are shown in Table 4.4 for time $\tau = 38$. The most accurate estimate of the wavefront location produced in this table (the one employing the finest spatio-temporal grid size) is $x = 3.688$ cm. Because the spatial resolution in this table is variable, the "actual" wavefront location can be smeared inside of the larger spatial grid sizes. However, the general trend to inaccuracy for larger time steps and smaller spatial grids is still clearly observable, and one could employ this metric to arrive at Eq. (4.72).

Thus, we conclude that the stability theory does *not* accurately predict a maximum time step size that guarantees the IMC solution to be accurate. One reason for this is that Marshak wave problems are strongly nonlinear, and therefore are far-removed from the assumptions of the linear stability theory. Another is that Eq. (4.72) demonstrates that the numerical accuracy of a Marshak wave problem must account for the spatial grid size. This last result is not entirely surprising, as it is typical to find stability criteria for related wave problems that have the same form as Eq. (4.72). These criteria are commonly referred to as "CFL" (Courant, Friedrichs, Lewy) conditions [49] [50]. The CFL condition is a necessary condition for the convergence of numerical schemes for wave equations. Using $\alpha = 1$ in the IMC solutions guarantees that the CFL condition is satisfied in the sense that the solution should always converge (which we have also confirmed using the stability theory). We speculate that a stricter, but related condition may be theoretically obtainable to guarantee that the maximum principle is not violated. To our knowledge, no attempt has been made to provide a theoretical means of estimating an inequality like Eq. (4.72), although this would be of great interest to the TRT community.

So far in this chapter we have demonstrated that the IMC equations have the potential to exhibit unphysical, damped oscillations where monotonic behavior should instead be seen. We have also seen that the oscillations tend to be worse for slowly-varying Fourier modes (small ξ), for small q, and for large time steps. Unfortunately, it is likely that a generic TRT problem will contain regions for which the theory predicts damped oscillations. Although these oscillations may be masked in a generic problem, their presence is undesirable. In the next section, we demonstrate how the stability theory can be methodically applied for a simpler 0-D problem. This allows one to quickly generate an amplification factor for a near-equilibrium system using fewer assumptions than those that led to Eq. (4.60a).

4.6 A 0-D Testbed

The 0-D, infinite medium IMC equations are advantageous for demonstration purposes, as they are simpler, exactly solvable, and the above stability theory predicts the worst oscillations occur for $\xi = 0$. In an infinite medium, Eqs. (4.23) reduce (upon elimination of the spatial variable and integration over angle) to:

$$q\frac{d\phi}{d\tau} + \frac{f}{M_n^3}\phi = fM_n\,, \tag{4.73a}$$

$$\frac{dM}{d\tau} = \frac{f}{M_n^3}\phi - fM_n \,. \tag{4.73b}$$

Adding these equations yields the conservation of energy equation in an infinite medium:

$$\frac{d}{d\tau}\left(q\phi + M\right) = 0 \,, \tag{4.74}$$

which implies:

$$q\phi(\tau) + M(\tau) = \text{constant} = q + 1 \,, \tag{4.75}$$

where the final equality comes from the recognition that, at equilibrium, $\phi = M = 1$. Next, we use Eq. (4.75) to eliminate ϕ from Eq. (4.73b):

$$\begin{aligned} \frac{dM}{d\tau} + fM_n &= \frac{f}{M_n^3}\left(\frac{q+1-M}{q}\right) \,, \\ \frac{dM}{d\tau} + \frac{f}{qM_n^3}M &= \frac{f}{qM_n^3}\left((q+1) - qM_n^4\right) \,. \end{aligned} \tag{4.76}$$

This first-order, ordinary differential equation for $M(\tau)$ may be solved with an integrating factor:

$$\begin{aligned} \frac{d}{d\tau}e^{f(\tau-\tau_n)/qM_n^3}M(\tau) &= \frac{f}{qM_n^3}\left((q+1) - qM_n^4\right)e^{f(\tau-\tau_n)/qM_n^3} \,. \\ M(\tau)e^{f(\tau-\tau_n)/qM_n^3} - M_n &= \left((q+1) - qM_n^4\right)\left(e^{f(\tau-\tau_n)/qM_n^3} - 1\right) \,, \\ M(\tau) &= M_n e^{-f(\tau-\tau_n)/qM_n^3} + \left((q+1) - qM_n^4\right)\left(1 - e^{-f(\tau-\tau_n)/qM_n^3}\right) \,, \end{aligned}$$

and thus the temperature at the end of the time step is:

$$M_{n+1} = M_n e^{-f\Delta_\tau/qM_n^3} + \left((q+1) - qM_n^4\right)\left(1 - e^{-f\Delta_\tau/qM_n^3}\right) \,, \tag{4.77}$$

or, rearranging,

$$M_{n+1} = q + 1 - qM_n^4 + \left(M_n - q - 1 + qM_n^4\right)e^{-f\Delta_\tau/qM_n^3} \,. \tag{4.78}$$

Eq. (4.78) is the *exact* solution of the 0-D scaled IMC equations. However, it is not possible to simply rearrange this solution in the form $M_{n+1} = \rho M_n$ in order to determine the amplification factor. Thus, we consider a first-order perturbation in M_n:

$$M_n = 1 + \epsilon P_n \,,$$

and we look for a recursion relationship for P_{n+1}. Noting that:

$$M_n^4 = (1 + \epsilon P_n)^4 = 1 + 4\epsilon P_n + O(\epsilon^2),$$

so that

$$\begin{aligned} M_n - q - 1 + qM_n^4 &= 1 + \epsilon P_n - q - 1 + q(1 + 4\epsilon P_n) \\ &= \epsilon P_n(1 + 4q)\,, \end{aligned}$$

Eq. (4.78) becomes, to first order:

$$\begin{aligned} 1 + \epsilon P_{n+1} &= (q+1) - q(1 + 4\epsilon P_n) + \epsilon P_n(1+4q)e^{-f\Delta_\tau/q}\,, \\ \epsilon P_{n+1} &= -4q\epsilon P_n + \epsilon P_n(1+4q)e^{-f\Delta_\tau/q}\,, \\ P_{n+1} &= \left[(1+4q)e^{-f\Delta_\tau/q} - 4q\right] P_n\,. \end{aligned}$$

Finally, we identify the amplification factor for the infinite homogeneous medium problem that was earlier derived by taking the limit as $\xi \to 0$:

$$\rho_{1,0} = (1+4q)e^{-f\Delta_\tau/q} - 4q\,. \tag{4.79}$$

This result confirms the earlier Fourier analysis, is much easier to obtain, and requires fewer assumptions. From this we found that if $0.5 \leq \alpha \leq 1$, then $|\rho_{1,0}| < 1$, but that it is possible to find values of q and Δ_τ – even when $\alpha = 1$ – for which $\rho_{1,0} < 0$. We also point out that in an infinite medium, a single amplification factor ρ is sufficient to describe the solution.

Throughout this chapter we have assumed special forms of the opacities and specific heat that are intended to be representative of the commonly-used materials that one might find in an IMC calculation. We next question what effect this choice of material temperature-dependence has on the results of the stability theory. Specifically, we would like to know if the unphysical, damped oscillations are a fundamental property of the IMC equations or if they are tied to this particular form of the problem data. To answer this question, we perform the 0-D stability analysis on the IMC equations applied to the *linear* problem defined in Section 2.2.5. The motivation is that if linear IMC equations permit damped oscillations – in which the material data are exactly represented – then there is likely no simple remedy to remove this behavior from the more difficult, nonlinear problem[4].

[4]For instance, one might conjecture that using a middle- or end-of-time-step temperature to

4.6.1 Analysis of a Linear Problem

Because we assumed a special form of the opacities and specific heat in the previous section, it is not possible to begin from the dimensionless form of the TRT equations given in Eqs. (4.9). However, this is an ideal place to demonstrate the simplified, 0-D form of the stability analysis in its entirety. This method is substantially different from that used by Mosher and Densmore [31] on this problem, but it leads to similar results. We proceed by performing the following algorithm:

1. Dimensionalize the 0-D form of the TRT equations under the problem assumptions (here, we use data given in Section 2.2.5).
2. Apply the IMC approximations.
3. Use the conservation of energy to solve the resulting system exactly for the scaled material energy density M.
4. Use perturbation analysis to obtain an amplification factor for the resulting system.
5. Analyze the amplification factor to assess the system's stability.

We begin by rewriting the 0-D TRT equations:

$$\frac{1}{c}\frac{\partial I}{\partial t} + \sigma I = \frac{1}{2} c\sigma U_r \,, \tag{4.80a}$$

$$\frac{\partial U_m}{\partial t} = \int_{-1}^{1} \sigma I \; d\mu - c\sigma U_r \,. \tag{4.80b}$$

For this linear problem, the specific heat is a cubic function of temperature:

$$c_v(T) = vT^3 \,, \tag{4.81}$$

and the opacity is constant:

$$\sigma = \text{constant} \,. \tag{4.82}$$

With these assumptions, we may write β from Eq. (3.2b) as:

$$\beta(x,t) = \frac{\partial U_r}{\partial U_m} = \frac{dU_r}{dT}\frac{dT}{dU_m} = \frac{4aT^3}{vT^3} = \frac{4a}{v} = \text{constant} \,. \tag{4.83}$$

evaluate the opacities may remove or lessen the magnitude of the damped oscillations. This is not the case.

Because β and σ are constant, they do not require any approximation. Next, we define the scaled time variable τ:

$$\tau = q\sigma ct\,, \tag{4.84a}$$

where

$$q = \beta = \frac{4a}{v}\,. \tag{4.84b}$$

Thus, for the linear problem, $q = \beta$, a constant at all times. Additionally, q is is the ratio U_r/U_m (at equilibrium and for all times):

$$q = \frac{4a}{v} = \frac{aT^4}{vT^4/4} = \frac{U_r}{U_m}\,. \tag{4.84c}$$

The scaled material energy density M is:

$$M(\tau) = \frac{U_m[T(t)]}{U_m(T_0)} = \frac{\int_0^T v(T')^3\,dT'}{\int_0^{T_0} v(T')^3\,dT'} = \left(\frac{T}{T_0}\right)^4\,. \tag{4.84d}$$

We note that for the linear problem, M is different – it is a quartic function of temperature. We also find that scaled radiative energy density R is superfluous:

$$R(\tau) = \frac{U_r[T(t)]}{U_r(T_0)} = \frac{aT^4}{aT_0^4} == \left(\frac{T}{T_0}\right)^4 = M(\tau)\,. \tag{4.84e}$$

We also define

$$\phi(\tau) = \frac{\int_{-1}^1 I(\mu,t)\,d\mu}{acT_0^4}\,. \tag{4.84f}$$

Noting that

$$\frac{\partial}{\partial\tau} = \frac{dt}{d\tau}\frac{\partial}{\partial t} = q\sigma c\frac{\partial}{\partial t}\,, \tag{4.84g}$$

Eq. (4.80a) can be rewritten using Eqs. (4.84):

$$q\sigma\frac{d}{d\tau}(\phi acT_0^4) + \sigma(\phi acT_0^4) = c(MaT_0^4)\,,$$

$$q\frac{d\phi}{d\tau} + \phi = M\,, \tag{4.85}$$

and Eq. (4.80b) becomes:

$$q\sigma c\frac{d}{d\tau}\left(\frac{vT_0^4}{4}M\right) + c\sigma(MaT_0^4) = \sigma(\phi acT_0^4)\,,$$

$$\frac{dM}{d\tau} + M = \phi \,. \tag{4.86}$$

To bring this together, the dimensionless form of the 0-D TRT equations applied to this linear problem is:

$$q\frac{d\phi}{d\tau} + \phi = M \,, \tag{4.87a}$$

$$\frac{dM}{d\tau} + M = \phi \,, \tag{4.87b}$$

and we reiterate that $q = \beta = U_r/U_m$ is independent of the equilibrium solution and $M = T^4/T_0^4$; these are different from the results obtained for the nonlinear problem.

The second step is to apply the IMC approximations to these equations. We begin by operating on Eq. (4.87b) using the time-averaging operator in Eq. (4.16):

$$\frac{1}{\Delta_\tau}(M_{n+1} - M_n) + \overline{M} = \overline{\phi} \,, \tag{4.88}$$

and approximating $\overline{M}$ by

$$\overline{M} = \alpha M_{n+1} + (1-\alpha)M_n \,, \tag{4.89}$$

where (again), α is user-defined such that $\frac{1}{2} \leq \alpha \leq 1$. Upon substitution of Eq. (4.89), Eq. (4.88) becomes:

$$\begin{aligned} \frac{1}{\alpha\Delta_\tau}(\overline{M} - M_n) + \overline{M} &= \overline{\phi} \,, \\ \overline{M} + \alpha\Delta_\tau\overline{M} &= M_n + \alpha\Delta_\tau\overline{\phi} \,, \\ \overline{M} &= \frac{1}{1+\alpha\Delta_\tau}M_n + \frac{\alpha\Delta_\tau}{1+\alpha\Delta_\tau}M_n \,. \end{aligned} \tag{4.90}$$

Defining the Fleck factor as

$$f = \frac{1}{1+\alpha\Delta_\tau} \,, \tag{4.91}$$

we rewrite Eq. (4.90):

$$\overline{M} = fM_n + (1-f)\overline{\phi} \,. \tag{4.92}$$

The final (and again, most dubious) approximation is to replace the time-averaged values with "instantaneous" values:

$$M(\tau) \approx fM_n + (1-f)\phi(\tau) \,. \tag{4.93}$$

Introducing Eq. (4.93) into Eq. (4.87a), we obtain:

$$q\frac{d\phi}{d\tau} + \phi = fM_n + (1-f)\phi\,,$$
$$q\frac{d\phi}{d\tau} + f\phi = fM_n\,. \tag{4.94}$$

Introducing Eq. (4.93) into the non-derivative term of Eq. (4.87b), we obtain:

$$\frac{dM}{d\tau} + fM_n + (1-f)\phi = \phi\,,$$
$$\frac{dM}{d\tau} + fM_n = f\phi\,. \tag{4.95}$$

Thus, the dimensionless IMC equations for the linear problem are [by Eq. (4.94) and Eq. (4.95)]:

$$q\frac{d\phi}{d\tau} + f\phi = fM_n\,, \tag{4.96a}$$
$$\frac{dM}{d\tau} + fM_n = f\phi\,. \tag{4.96b}$$

For the third step, we solve Eqs. (4.96) exactly for $M(\tau)$. We first eliminate ϕ from Eq. (4.96b) using the conservation of energy from Eq. (4.75) [$q\phi + M = q + 1$]:

$$\frac{dM}{d\tau} + fM_n = f\frac{q+1-M}{q}\,,$$
$$\frac{dM}{d\tau} + \frac{f}{q}M = \frac{f}{q}(q+1-qM_n)\,. \tag{4.97}$$

The solution procedure for this equation is analogous to that of Eq. (4.76). Its solution is:

$$M(\tau) = M_n e^{\frac{-f(\tau-\tau_n)}{q}} + (q+1-qM_n)\left(1 - e^{-\frac{f(\tau-\tau_n)}{q}}\right)\,. \tag{4.98}$$

At the end of the time step $\tau_n \leq \tau \leq \tau_{n+1}$ with $\Delta_\tau = \tau_{n+1} - \tau_n$, the solution is:

$$M_{n+1} = q + 1 - qM_n + e^{-\frac{f\Delta_\tau}{q}}(M_n + qM_n - q - 1)\,. \tag{4.99}$$

In step four, we apply perturbation theory to Eq. (4.99) to obtain an amplification factor that relates the first-order perturbations at the beginning and end of the time step. Letting ϵ be small, we set:

$$M_n = 1 + \epsilon P_n\,, \tag{4.100a}$$

$$M_{n+1} = 1 + \epsilon P_{n+1} \,. \tag{4.100b}$$

Substitution of Eqs. (4.100) into Eq. (4.99) yields, to first order:

$$1 + \epsilon P_{n+1} = q + 1 - q(1 + \epsilon P_n) + e^{-\frac{f\Delta_\tau}{q}} \left[(1+q)(q + \epsilon P_n) - q - 1\right] \,,$$

$$P_{n+1} = \left[(1+q)e^{-\frac{f\Delta_\tau}{q}} - q\right] P_n \,, \tag{4.101}$$

and we define the amplification factor for the 0-D IMC equations applied to a linear problem as ρ_ℓ:

$$\rho_\ell = (1+q)e^{-\frac{f\Delta_\tau}{q}} - q \,. \tag{4.102}$$

In the final step, we analyze Eq. (4.102) to assess its stability implications. First, we show that $\rho_\ell < 1$, disallowing monotonic, exponential divergence. That is,

$$\rho_\ell = (1+q)e^{-\frac{f\Delta_\tau}{q}} - q < 1 \,, \tag{4.103}$$

since

$$e^{-\frac{f\Delta_\tau}{q}} < 1 \,. \tag{4.104}$$

Next, we examine whether $\rho_\ell < -1$, which would indicate oscillatory and exponential divergence:

$$\rho_\ell = (1+q)e^{-\frac{f\Delta_\tau}{q}} - q > -1 \,,$$
$$e^{-\frac{f\Delta_\tau}{q}} > \frac{q-1}{q+1} \,,$$

and, assuming $q > 1$ since this is trivially satisfied for $q < 1$:

$$-f\Delta_\tau > q \ln\left(\frac{q-1}{q+1}\right) \,, \tag{4.105}$$

$$\frac{-\Delta_\tau}{1+\alpha\Delta_\tau} > q \ln\left(\frac{q-1}{q+1}\right) \,. \tag{4.106}$$

Similar to what occurred in Section 4.4.1, the functions on the left and right side of the equation are independent of each other and monotonic. The function on the left side is minimized when $\Delta_\tau \to \infty$, so

$$\frac{\Delta_\tau}{1+\alpha\Delta_\tau} > -\frac{1}{\alpha} \,, \tag{4.107}$$

while the function on the right is maximized when $q \to \infty$, or:

$$-2 > q \ln\left(\frac{q-1}{q+1}\right) . \tag{4.108}$$

Substitution of Eq. (4.107) and Eq. (4.108) into Eq. (4.106) reveals that $-1 \leq \rho_\ell$ when:

$$\begin{aligned} -\frac{1}{\alpha} &\geq -2 , \\ \alpha &\geq \frac{1}{2} . \end{aligned} \tag{4.109}$$

Thus, the IMC equations applied to a linear problem produce an unconditionally stable method (it has already been stipulated that $1/2 \leq \alpha$). This conclusion is identical to that found for the earlier-analyzed nonlinear problem [see Eq. (4.65)]. However, it is noteworthy in that we previously demonstrated that using $\alpha = 1/2$ can produce a temperature update equation that permits negative temperatures [see Eq. (3.37)]. These two results are not contradictory; they highlight that this stability analysis does not address issues of the underlying equation's physicality. In fact, in [46] it is numerically demonstrated that using $\alpha = 1/2$ for a nearly-linear problem produces a system that is second-order accurate in Δ_τ, and that using $\alpha = 1$ produces a first-order accurate system. This transition from first-order to second-order accuracy when $\alpha = 1$ ("backward Euler") is replaced by $\alpha = 1/2$ ("Crank-Nicholson") is a common phenomenon in numerical methods. It is also well-known that one usually has to "pay a price" to obtain increased accuracy, and that price usually involves the introduction of damped, numerical oscillations (although not the loss of unconditional stability).

Next, we examine whether damped oscillations are permitted in the IMC solution to the linear problem. A contour plot of ρ_ℓ is provided in Figure 4.22. Comparison of Figures 4.22 and 4.3 indicates that applying the IMC approximation to a linear problem versus the earlier-defined nonlinear problem does not qualitatively affect its stability characteristics. The absolute minimum of ρ_ℓ remains the same at -0.2984. This minimum is obtained when $q = 0.5576$, which is exactly four times the value of the nonlinear result; this factor is likely related to the difference in the scaled material energy density M, which is T^4/T_0 for the linear problem, and T/T_0 in the nonlinear problem.

Following an algebraic procedure analogous to that done to obtain the monotonicity conditions in Eq. (4.67) and Eq. (4.68), we find that the linear problem has

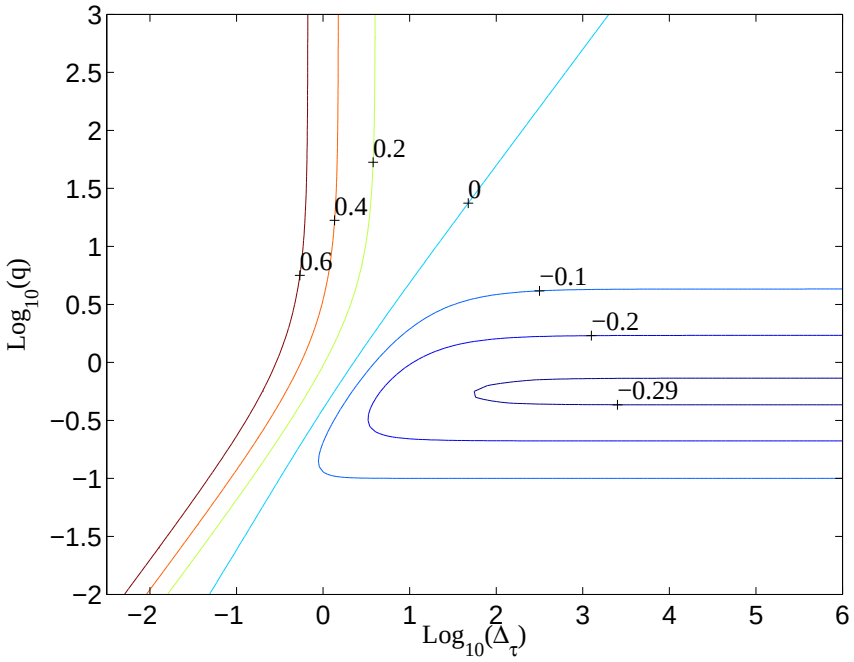

Figure 4.22: A contour plot of the 0-D amplification factor ρ_ℓ of the IMC equations applied to a linear problem.

the following monotonicity condition:

$$\Delta_\tau < \frac{-q \ln\left(\frac{q}{1+q}\right)}{\alpha q \ln\left(\frac{q}{1+q}\right) + 1}\,. \tag{4.110}$$

This inequality (with $\alpha = 1$) exactly reproduces the contour $\rho_\ell = 0$ in Figure 4.22. For the unscaled time step, this is:

$$\Delta_t \sigma c < \frac{-\ln\left(\frac{q}{1+q}\right)}{\alpha q \ln\left(\frac{q}{1+q}\right) + 1}\,, \tag{4.111}$$

Eq. (4.111) is mathematically equivalent to that obtained by Mosher and Densmore (see Eq. (23) of [31]). Thus, we have successfully verified and extended the stability results due to Mosher and Densmore.

To validate the predictions of this theory for a linear problem, we return to the single Fourier mode problem definition that was used in Section 4.5.1. We are using a problem with weak spatial dependence, even though we did not explicitly derive ρ_ℓ to account for it for the following reason. We remarked earlier that for ξ small

enough, the predictions of the stability analysis are only weakly dependent on ξ [see the discussion after Table 4.1], and implicated that one should be able to apply the 0-D version of this theory to other problems to generate characteristic results. If the 0-D theory can produce an amplification factor for $\xi \neq 0$ on a wholly different problem, then this strengthens the argument that one may employ this theory on the IMC equations applied to other problems, or on other approximations of the TRT equations.

To perform the numerical experiment on the linear problem using an IMC algorithm, we set $a = c = \sigma = 1$, $v = 4/q$, $\Delta_t = \Delta_\tau/q$, and perturb the initial conditions using:

$$T(z) = [1 + M_1 \cos(\xi z)]^{(1/4)} \,, \tag{4.112a}$$

$$\phi(z) = 1 - \frac{M_1}{q} \cos(\xi z) \,, \tag{4.112b}$$

so that the scaled energy density M is perturbed according to a cosine shape, not the temperature.

For this experiment, we set $M_1 = 0.4$, use the "worst-case" value of q ($q = 0.5576$), and set $\Delta_\tau = 10$ mean free times for emission. From these we calculate $\rho_\ell = -0.2525$ using Eq. (4.102). We also set $\xi = 0.01$, which produces a slowly-varying spatial wave. Together, these data roughly correspond with the data used to produce Figure 4.8, in which the temperature was perturbed with an amplitude of 0.1.

The experimentally-obtained material energy density profiles M are depicted in Figure 4.23. This figure illustrates an initial cosine shape that is neatly inverting and reducing in magnitude with each time step almost exactly as the theory predicts. Using Eq. (4.71), we calculate $r_1 = 0.2514$ and $r_2 = 0.2551$, which compare extremely well with the predicted value of -0.2525. For brevity, we shall not reproduce linear versions of the other numerical experiments that tested the nonlinear theory here; they are expected to produce similar results.

From these results we conclude that the presence of damped oscillations is not fundamentally tied to how the problem data is handled, rather, it results from the approximate treatment of the unknowns M and ϕ. Thus, there is no simple remedy for the IMC approximations that can remove the presence of damped oscillations. However, other approximations to the TRT equations exist. A method by Carter and Forest [23] can be demonstrated to be unconditionally stable for the same problems that were used in this chapter [see Appendix A]. As a counterpoint, a seemingly-similar method due to Ahrens and Larsen [22] can be shown to be only conditionally

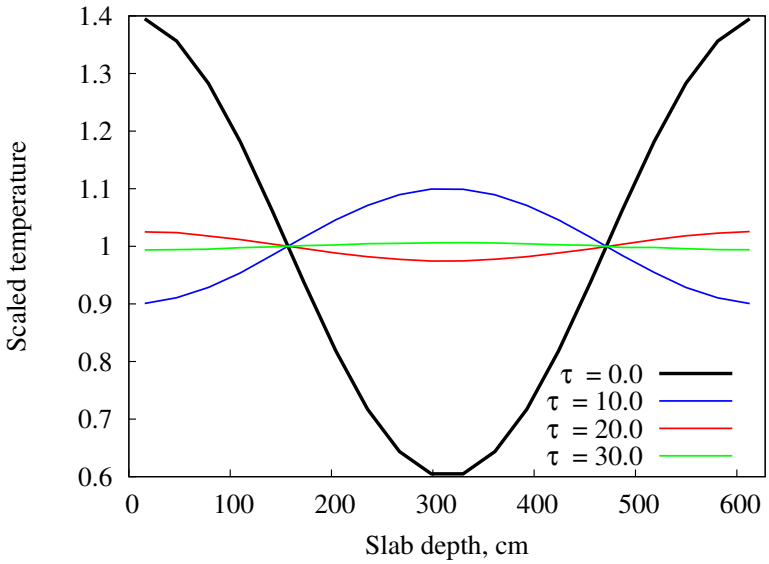

Figure 4.23: Experimentally-obtained damped oscillations in energy density profiles for $\xi = 0.01$, $q = 0.14$, $\Delta_\tau = 10$ in a *linear* problem, for which the theory predicts $\rho_\ell \approx -0.2525$.

stable for the nonlinear, 0-D problem. We plan to expand upon these assertions in a future publication.

4.7 Summary

In this chapter, we have presented a new linear stability theory for TRT problems that are near equilibrium and we have applied it the IMC equations. We found that the IMC equations are unconditionally stable, but their solution can exhibit damped temporal oscillations. These oscillations are unphysical since they are not a feature of the TRT equations; they can always be removed by setting $\alpha = 1$ and reducing the size of the time step. While it has been reported that the IMC equations can produce unphysical solutions if sufficiently large time steps are used [21] [27] [28] [29], before now there has been no theory to predict the magnitude or existence of damped oscillations (except for a 0-D, linear, gray problem [31]).

For most of this chapter, we considered a characteristic gray, 1-D TRT problem in which the opacities are inversely proportional to the temperature cubed and the specific heat is constant. We derived a dimensionless form of the TRT equations applied to this problem, Eqs. (4.9), by scaling the equations about a specified equilibrium condition. In this form, the TRT equations are described by a scaled spatial variable z that is in mean free paths at equilibrium, a scaled temporal variable τ

that is in mean free times to photon emission, and a dimensionless factor q that is the ratio of the equilibrium radiative and material energy densities, as well as the original angular variable μ. After this, the dimensionless form of the IMC equations was derived. Next, linear equations were formed for an additive perturbation to the scaled equations. Finally, we considered spatially-dependent versions of these equations that are described by a single Fourier mode $e^{i\xi z}$. We then solved these equations – assuming that the radiation is a separable function of space and angle – for an amplification factor ρ that relates the perturbations at the beginning and end of the time step.

Analysis of ρ indicates that the IMC equations are unconditionally stable when $\alpha \geq 0.5$, but that it is possible to find conditions under which $\rho < 0$ even when $\alpha = 1$. These nonphysical, damped, temporal oscillations are largest in magnitude when ξ is small, $q \approx 0.13$, and the time step is relatively large. Since q and ξ are parameters that are defined by the underlying problem, damped oscillations can only be eliminated by decreasing the size of the time step. It is possible to employ the theory to obtain a critical time step size under which no oscillations should occur: a monotonicity condition. We argued that meeting the $\xi = 0$ condition given in Eq. (4.67) should be sufficient to ensure monotonicity for all ξ. Additionally, meeting the more restrictive condition provided as Eq. (4.69) should be sufficient for all q and ξ, but is likely overly-restrictive.

The linear stability theory is directly applicable to problems that are near equilibrium and that use large time steps or have slowly-varying spatial Fourier modes. Fortunately, these limitations are not overly restrictive, as we have theoretically implicated and numerically demonstrated that problems that use small time steps or have highly-oscillatory spatial modes are less likely to suffer from damped temporal oscillations. Additionally, many TRT problems of interest contain regions that are relatively thick and use large time steps, and are therefore more likely to contain damped temporal oscillations. We experimentally demonstrated that the stability theory successfully predicts both the existence and magnitude of damped temporal oscillations for a class of problems containing initial conditions that are perturbed by a single Fourier mode, assuming that the Fourier mode is not too oscillatory. When the magnitude of the Fourier mode is near the limit of the theory's reliability, the quantitative predictive capabilities of the theory begin to break down.

The stability theory is somewhat successful at predicting the existence, but not the magnitude, of damped temporal oscillations for problems containing a time-dependent photon source. In these problems, the system begins at a low tempera-

ture, and a photon source injects radiation until the system contains enough energy to obtain a specified equilibrium condition, at which point the source is shut off. When the employed time step was larger than the critical time step size, the theory successfully predicted that the solution would not be monotonic, but not the degree to which an overshoot and subsequent oscillations would occur. The quantitative disagreement is likely because as the time step is reduced, the likelihood of a "mismatch" occurring between the energies in the material and radiation is also reduced. For a sufficiently fine time step, the source drives the solution to equilibrium, where it essentially rests after it is shut off. Although damped oscillations are difficult to see in this regime (the regime in which the theory predicts the presence of damped oscillations but they are not easily observable), their existence likely contributes to subtle inaccuracies in the IMC solution.

The stability theory does not accurately predict a maximum time step size under which the IMC solution of a Marshak wave problem is guaranteed to be accurate. One reason for this is that Marshak wave problems are strongly nonlinear, and therefore are far-removed from the assumptions of the linear stability theory. Another is that we found that the numerical accuracy of a Marshak wave problem must account for the spatial grid size [see Eq. (4.72)]. We conjecture that it may be possible to develop such a theory by extending the concept of a CFL condition, and that the theory should be of the form $\Delta_t \leq k\Delta_x$, where k is a to-be-determined, problem dependent parameter.

Because the analysis on the spatially-dependent problem indicated that the oscillations are greatest in magnitude when $\xi = 0$, we demonstrated that the same conclusions may be reached with less steps and with fewer assumptions by considering the 0-D problem. We then considered the question of whether the results of this stability theory are tied to the initial choice of problem data. To do this, we re-performed the stability analysis on a completely linear, 0-D TRT problem described in Section 2.2.5. The generic methodology can be described by the following algorithm.

1. Dimensionalize the 0-D form of the TRT equations under the specified problem assumptions.

2. Apply time-discretization approximations that correspond to the numerical method in question.

3. Use the conservation of energy to solve the resulting system exactly for the scaled material energy density M.

4. Use perturbation analysis to obtain an amplification factor for the resulting system.

5. Analyze the amplification factor to assess the system's stability.

The analysis of the linear problem indicated that the stability characteristics of the IMC equations are relatively insensitive to the temperature-dependence of the problem data. The absolute minimum amplification factors are the same, and the monotonicity condition is similar. We also numerically reproduced and verified the monotonicity condition due to Mosher and Densmore [31], which is the only previous work that is directly relevant in this subject area. We concluded that damped oscillations are an inherent feature of the IMC method.

The stability analysis algorithm is a relatively simple undertaking that can produce surprising conclusions for seemingly-innocuous looking time discretizations. We commented that other time-discretizations exist that can be found to be unconditionally stable [23] (see Appendix A) or only conditionally stable [22]. The stability algorithm is not restricted to time-discretizations for Monte Carlo calculations; it applies to time-discretizations for deterministic methods also. We shall return to this algorithm in later chapters to assess the stability characteristics of several new time-discretizations of the TRT equations.

As future work, it may be possible to extend the stability analysis presented in this chapter to frequency-dependent problems. Such an analysis would require dimensionless equations that are scaled about an equilibrium condition that includes a frequency-dependent Planck function. However, such a task would be considerably involved, even for relatively simple analytical forms of the opacity.

Chapter V

Temperature Estimation and Evaluation

During the derivation of the IMC equations [Eqs. (3.29)], some of the continuous-in-time problem data that depend on the material temperature – the opacities, specific heat, and the Planckian – are evaluated at the temperature at the beginning of the time step, T_n. The explicit-in-time treatment of these data introduces an error into Eqs. (3.29) that worsens with increasing time intervals. Performing a time-extrapolation of the temperature using data from previous time steps was historically used to try to lessen this error [21] [23]. However, such extrapolations are now deemed unreliable, as they can introduce new instabilities and additional errors into the calculation.

By contrast, in deterministic solvers for the TRT equations, the temperature at which the normalized Planckian is evaluated is iterated upon until it converges to T_{n+1}, the temperature at the end of the time step [51]. The conventional wisdom is that this implicit treatment of the Planck temperature improves the accuracy of the time-discretization without introducing any stability issues. However, the temperature at which the opacities are evaluated is not iterated upon. This is presumably done because it is not believed that the associated increase in accuracy is worth the additional computational expense. However, it would be difficult to argue against incorporating the temperature-dependence of the opacities if T_{n+1} could be calculated without increasing the computational cost. Overall, without greatly increasing the computational cost, the inability of Monte Carlo methods to employ a more accurate Planck temperature has been viewed as an Achilles heel.

Another difficulty that both deterministic and Monte Carlo methods encounter is the designation of the time step size. Currently, the proper time step must be selected either by trial-and-error or by some means of adaptive resizing. Often, if the time step is determined to be too large, it is not computationally feasible to return to

an earlier solution and repeat the calculation. Thus, a reasonably accurate estimate of T_{n+1} could be used to select an appropriate time step size *before* an involved transport calculation is carried out.

In this chapter we present a new frequency-collapsed, deterministic Quasidiffusion method to estimate – before the IMC calculation is performed – the temperature at the end of the time step. We also define a characteristic average temperature T_* which properly interpolates the temperatures at the beginning and end of the time step, and which also can be used to evaluate the problem data. Using T_* should be more accurate than the traditional approach of using T_n to evaluate the problem data. This Quasidiffusion method is intended to be used in tandem with the more detailed transport calculation in the following manner. During a time step $t_{n-1} \leq t \leq t_n$, a frequency-dependent transport calculation such as IMC is carried out. Throughout the calculation, certain problem data are averaged over frequency and angle. These data are then provided to the new Quasidiffusion method, which uses them to estimate T_{n+1} for the upcoming time step $t_n \leq t \leq t_{n+1}$. The average temperature T_* is generated and passed to the frequency-dependent transport algorithm, which then uses it to evaluate the temperature-dependent problem data. The transport algorithm then produces solutions over the same time step $t_n \leq t \leq t_{n+1}$ using the more accurate problem data; these solutions supersede the Quasidiffusion solutions. The method is derived assuming the 1-D form of the frequency-dependent, nonlinear TRT equations, although generalization to full spatial-dependence should be straightforward.

Ideally, any method used to estimate T_{n+1} should be much less computationally expensive than solving Eqs. (3.29) using a Monte Carlo procedure. To satisfy this requirement, we have designed a Quasidiffusion method that capitalizes on the Monte Carlo (or deterministic transport) solution from the previous time step. Specifically, two angle- and frequency-averaged opacities and an Eddington factor are defined that use data from the previous time step. These averaged quantities are then employed in a fully implicit, frequency-collapsed, deterministic Quasidiffusion calculation to obtain an estimate of T_{n+1}. The removal of the frequency and angular variables substantially reduces the cost of generating an estimate of T_{n+1}, and, because the data are based on the detailed transport solution of the previous time step, the solution remains accurate.

It is also desirable that the method to estimate T_{n+1} be "robust" in the sense that solutions should be non-negative and numerically stable under all problem conditions. To satisfy this requirement, we analyze the method to obtain its positivity condition,

and we perform the 0-D stability analysis described in Chapter IV.

After deriving the Quasidiffusion method and analyzing it for robustness and stability, we numerically investigate its employment as a means to generate T_* for the evaluation of temperature-dependent data in IMC calculations. We do not investigate its use in deterministic transport methods or employ it as a method to limit the time step size; these shall be left as future work. Used in this manner, the method increases the accuracy of the IMC calculation, although it should not be expected to increase its order of accuracy [it will remain $O(\Delta_t)$].

To assess the numerical order of accuracy of using T_* to evaluate the temperature-dependent data in IMC, a 0-D, gray, nonlinear problem is considered. Time-dependent temperature solutions are generated for a series of different time-step sizes, and the results are compared to a fine-grid solution. For these problems, we also compare the effects of using T_n, (the traditional approach) and T_{n+1} to evaluate the problem data, and show that T_* is the superior choice. These problems demonstrate that IMC temperature solutions tend to overshoot the equilibrium condition at early times, a problem that is identified and discussed by Gentile in [30], but that using T_* to evaluate the problem data ameliorates this condition. We also numerically test the procedure on a series of more difficult, Marshak wave problems, and demonstrate the accuracy gained by using T_* instead of T_n or T_{n+1} to evaluate the temperature-dependent problem data.

Deterministic transport and Monte Carlo methods both may benefit from the temperature estimation algorithm proposed here. Deterministic methods could use the estimated temperature as a means to reduce the required number of iterations or to use larger time steps. Monte Carlo methods may use the estimated temperature to improve accuracy and enhance their position relative to deterministic methods. Both may use the estimate to select a proper time step size and/or to evaluate temperature-dependent problem data.

To our knowledge, the method proposed here is the first of its kind. Certainly diffusion and Quasidiffusion deterministic methods have been previously developed to solve the TRT equations, but these have never before been designed to capitalize on a more detailed transport algorithm in order to estimate T_{n+1}.

5.1 A New Quasidiffusion Method

We begin from the exact TRT equations with the mindset of performing the fewest number of approximations necessary to arrive at a relatively simple – but

hopefully accurate – algebraic system of equations for the temperature T. The 1-D, purely-absorbing, frequency-dependent TRT equations, suppressing the independent variables where it is clear, are:

$$\frac{1}{c}\frac{\partial I}{\partial t} + \mu\frac{\partial I}{\partial x} + \sigma I = 2\pi\sigma B\,, \tag{5.1a}$$

$$c_v\frac{\partial T}{\partial t} = \int_0^\infty\int_{-1}^1 \sigma(I - 2\pi B)\,d\mu\,d\nu\,. \tag{5.1b}$$

Let us define a frequency and angular integral nomenclature by:

$$\langle f\rangle = \int_0^\infty\int_{-1}^1 f(\mu,\nu)\,d\mu\,d\nu\,, \tag{5.2}$$

operate on Eq. (5.1a) with $\langle\cdot\rangle$, and rewrite Eq. (5.1b) as:

$$\frac{1}{c}\frac{\partial}{\partial t}\langle I\rangle + \frac{\partial}{\partial x}\langle\mu I\rangle + \langle\sigma I\rangle = 2\pi\langle\sigma B\rangle\,, \tag{5.3a}$$

$$c_v\frac{\partial T}{\partial t} = \langle\sigma I\rangle - 2\pi\langle\sigma B\rangle\,. \tag{5.3b}$$

We have previously defined the Planck opacity as:

$$\sigma_p(x) = \frac{\langle\sigma B\rangle}{\langle B\rangle}, \tag{5.4}$$

and we now define the intensity-weighted opacity σ_I:

$$\sigma_I(x) = \frac{\langle\sigma I\rangle}{\langle I\rangle}\,. \tag{5.5}$$

Then Eqs. (5.3) become, using Eq. (5.5) and Eq. (5.4):

$$\frac{1}{c}\frac{\partial}{\partial t}\langle I\rangle + \frac{\partial}{\partial x}\langle\mu I\rangle + \sigma_I\langle I\rangle = \sigma_p caT^4\,, \tag{5.6a}$$

$$c_v\frac{\partial T}{\partial t} = \sigma_I\langle I\rangle - \sigma_p caT^4\,. \tag{5.6b}$$

Next, we multiply Eq. (5.1a) by μ/σ:

$$\frac{\mu}{c\sigma}\frac{\partial I}{\partial t} + \frac{\mu^2}{\sigma}\frac{\partial I}{\partial x} + \mu I = \mu 2\pi B\,, \tag{5.7}$$

and operate on the result with $\langle\cdot\rangle$:

$$\frac{1}{c}\left\langle\frac{1}{\sigma}\frac{\partial}{\partial t}\mu I\right\rangle+\left\langle\frac{\mu^2}{\sigma}\frac{\partial I}{\partial x}\right\rangle+\langle\mu I\rangle=0\,. \tag{5.8}$$

Here we make our first approximation – as is commonly done in diffusion approximations – and discard the time derivative of the first angular moment to find:

$$\langle\mu I\rangle\approx-\left\langle\frac{\mu^2}{\sigma}\frac{\partial I}{\partial x}\right\rangle\,. \tag{5.9}$$

We use this relationship to eliminate the derivative of the first angular moment in Eq. (5.6a) by creating a frequency-averaged Eddington factor and a special, frequency-averaged opacity. From the above we may write

$$\begin{aligned}\frac{\partial}{\partial x}\langle\mu I\rangle&\approx-\frac{\partial}{\partial x}\left\langle\frac{\mu^2}{\sigma}\frac{\partial I}{\partial x}\right\rangle\,,\\&=-\frac{\partial}{\partial x}\left\langle\frac{1}{\sigma}\frac{\partial}{\partial x}\frac{\mu^2 I}{\langle\mu^2 I\rangle}\langle\mu^2 I\rangle\right\rangle\,,\end{aligned}$$

but we make a further approximation that:

$$\frac{\partial}{\partial x}\frac{\mu^2 I}{\langle\mu^2 I\rangle}\approx 0\,, \tag{5.10}$$

which is valid if I is nearly a separable function of space and angle or if I is a slowly-varying spatial function. Then,

$$\begin{aligned}\frac{\partial}{\partial x}\langle\mu I\rangle&\approx-\frac{\partial}{\partial x}\left\langle\frac{1}{\sigma}\frac{\mu^2 I}{\langle\mu^2 I\rangle}\right\rangle\frac{\partial}{\partial x}\langle\mu^2 I\rangle\,,\\&=-\frac{\partial}{\partial x}\frac{\left\langle\frac{1}{\sigma}\mu^2 I\right\rangle}{\langle\mu^2 I\rangle}\frac{\partial}{\partial x}\frac{\langle\mu^2 I\rangle}{\langle I\rangle}\langle I\rangle\,,\\&\equiv-\frac{\partial}{\partial x}\frac{1}{\sigma_\rho}\frac{\partial}{\partial x}E\langle I\rangle\,,\end{aligned} \tag{5.11}$$

where we have defined:

$$E(x)=\frac{\langle\mu^2 I\rangle}{\langle I\rangle}\,, \tag{5.12}$$

$$\sigma_\rho(x)=\frac{\langle\mu^2 I\rangle}{\left\langle\frac{\mu^2}{\sigma}I\right\rangle}\,. \tag{5.13}$$

Here, E is a frequency-averaged Eddington factor. Also, σ_ρ is a specially-weighted opacity that, in the limit as I resembles a Planck function, almost produces the Rosseland mean opacity.

Thus, we have derived a much simpler Quasidiffusive version of the TRT equations in which the frequency and angular variables have been eliminated. This system is given by:

$$\frac{1}{c}\frac{\partial}{\partial t}\langle I\rangle - \frac{\partial}{\partial x}\frac{1}{\sigma_\rho}\frac{\partial}{\partial x}E\langle I\rangle + \sigma_I\langle I\rangle = \frac{1}{2}\sigma_p c U_r\,, \tag{5.14a}$$

and the following equivalent material energy equations:

$$\frac{1}{\beta}\frac{\partial U_r}{\partial t} + \sigma_p c U_r = \sigma_I\langle I\rangle\,, \tag{5.14b}$$

$$\frac{\partial U_m}{\partial t} + \sigma_p c U_r = \sigma_I\langle I\rangle\,, \tag{5.14c}$$

where β has been previously defined in Eq. (3.2b).

5.1.1 Discussion

Eqs. (5.14) are the basis for a to-be-defined deterministic procedure that estimates T_{n+1}. They should be accurate under the assumptions that $\partial/\partial t\,\langle\mu I\rangle$ is small and that Eq. (5.10) is valid. However, it is well-known that the presence of the time-derivative of the first angular moment I_1 allows the TRT equations to be *flux-limited* [33] [17]. Flux-limiting is defined by the following relationship between the first and zeroth angular moments of the radiation intensity:

$$|I_1(x,\mu,\nu,t)| \le I_0(x,\mu,\nu,t)\,. \tag{5.15}$$

This relationship follows directly from Eqs. (5.1), but may be violated due to the approximations made to derive Eqs. (5.14). This is because: "The raw Eddington approximation can give a flux that is arbitrarily large compared with $[I_0]$ if the gradient of $[I_0]$ is large enough; this is something that can never happen if $[\partial I_1/\partial t]$ is retained." [33] The assumption that the time-derivative of I_1 is small changes the form of the intensity equations from a hyperbolic, wave character containing a finite wave speed to a parabolic character in which the wave speed is infinite. In optically thin problems, the temperature wave travels too quickly. In optically thick problems, the material may heat too rapidly. It is likely possible to derive and artificially

introduce numerical remedies known as *flux-limiters* into Eqs. (5.14) that will ensure that Eq. (5.15) is satisfied [33] [52], but we will not do so here (this will be left as future work).

After Eq. (5.13), we asserted that σ_ρ limits to the Rosseland mean opacity when the frequency-dependence of the specific intensity resembles a Planckian. Here we explore this in more detail. When I may be approximately represented as a Planckian, σ_ρ is:

$$\sigma_\rho(x) \approx \frac{\langle \mu^2 B \rangle}{\left\langle \frac{\mu^2}{\sigma} B \right\rangle} . \tag{5.16}$$

It can be shown that the temperature derivative of the Planckian has nearly the same frequency shape as the Planckian itself; i.e., there is a function $g(T)$ such that:

$$B(\nu, T) \approx g(T) \frac{\partial}{\partial T} B(\nu, T) . \tag{5.17}$$

Substituting Eq. (5.17) into Eq. (5.16) produces:

$$\sigma_\rho(x) \approx \frac{\left\langle \mu^2 \frac{\partial B}{\partial T} \right\rangle}{\left\langle \frac{\mu^2}{\sigma} \frac{\partial B}{\partial T} \right\rangle} = \sigma_r(x) \quad [\text{from Eq. (2.19)}] . \tag{5.18}$$

That is, in the limit as I resembles B, σ_ρ resembles the Rosseland mean opacity σ_r.

To deterministically solve Eqs. (5.14), these equations must still be discretized in time and space, and a procedure must be developed to provide estimates of σ_I, σ_ρ, and E.

5.1.2 Time Discretization

The new Quasidiffusion method is intended to be used in tandem with a more detailed transport calculation – in this chapter, IMC. We intend to exploit the IMC calculation by using tallies generated during the previous time step $t_{n-1} \leq t \leq t_n$ in order to approximate the quantities σ_I, σ_ρ, and E during $t_n \leq t \leq t_{n+1}$. The tallies for σ_I, σ_ρ, and E may be performed by averaging them over the time step via path-length estimators, or they may instead be created from the census particles at the end of the time step. The latter approach should be more accurate, as the data will be more recent, but if the system is highly absorbing then the census may not hold enough particles to generate adequate statistics for these quantities. Also, during the initial time step, it is not possible to estimate these data, in which case this method is not applicable. No matter what method is used to generate the approximations

to these quantities, to time-discretize the above equations over a time step, we shall consider them to be frozen "at" the initial time t_n:

$$\sigma_I \approx \sigma_{I,n} \tag{5.19a}$$

$$\sigma_\rho \approx \sigma_{\rho,n} \tag{5.19b}$$

$$E \approx E_n \,. \tag{5.19c}$$

This introduces an inaccuracy into the calculation, although it may be possible to "extrapolate" the opacities by assuming they have a known temperature-dependence (such as proportionality to T^{-3}), and updating them via an iterative procedure.

The strategy to develop time-discretized versions of Eqs. (5.14) is similar to the derivation of the IMC equations and proceeds as follows. First, we perform implicit time discretizations on each of Eqs. (5.14). We then eliminate U_r from the subsequent system and form a triangular system for $\langle I \rangle_{n+1}$ and $U_{m,n+1}$ only. These equations can then first be solved for $\langle I \rangle_{n+1}$, and then for $U_{m,n+1}$. With $U_{m,n+1}$ known, the new temperature may be calculated from the relationship between c_v and U_m [Eq. (2.6a)]. If desired, the newly-calculated value of T_{n+1} could then be used to repeat the entire process, assuming that the opacities (σ_ρ, σ_I, σ_p) have a known temperature-dependence.

We begin by performing implicit time-discretizations on the unknowns in Eqs. (5.14):

$$\frac{1}{c\Delta_{t,n}} \left(\langle I \rangle_{n+1} - \langle I \rangle_n \right) - \frac{\partial}{\partial x} \frac{1}{\sigma_{\rho,n}} \frac{\partial}{\partial x} E_n \langle I \rangle_{n+1} + \sigma_{I,n} \langle I \rangle_{n+1} = \frac{1}{2} \sigma_{p,n} c U_{r,n+1} \,, \tag{5.20a}$$

$$\frac{1}{\beta_n \Delta_{t,n}} \left(U_{r,n+1} - U_{r,n} \right) + \sigma_{p,n} c U_{r,n+1} = \sigma_{I,n} \langle I \rangle_{n+1} \,, \tag{5.20b}$$

$$\frac{1}{\Delta_{t,n}} \left(U_{m,n+1} - U_{m,n} \right) + \sigma_{p,n} c U_{r,n+1} = \sigma_{I,n} \langle I \rangle_{n+1} \,. \tag{5.20c}$$

In Eq. (5.20b) we have made the additional approximation $\beta \approx \beta_n$. Because of this, Eq. (5.20b) and Eq. (5.20c) are not equivalent. Next, we solve Eq. (5.20b) for $U_{r,n+1}$:

$$U_{r,n+1} = \frac{1}{1 + \beta_n \sigma_{p,n} c \Delta_{t,n}} U_{r,n} + \frac{\beta_n \Delta_{t,n}}{1 + \beta_n \sigma_{p,n} c \Delta_{t,n}} \sigma_{I,n} \langle I \rangle_{n+1} \,. \tag{5.21}$$

Recognizing the Fleck factor f_n from Eq. (3.14) (with $\alpha = 1$), the previous equation

may be written more simply as:

$$U_{r,n+1} = f_n U_{r,n} + \frac{1-f_n}{\sigma_{p,n}c}\sigma_{I,n}\left\langle I\right\rangle_{n+1} \ . \tag{5.22}$$

Next, we substitute Eq. (5.22) into Eq. (5.20a):

$$\frac{1}{c\Delta_{t,n}}\left(\left\langle I\right\rangle_{n+1} - \left\langle I\right\rangle_{n}\right) - \frac{\partial}{\partial x}\frac{1}{\sigma_{\rho,n}}\frac{\partial}{\partial x}E_n\left\langle I\right\rangle_{n+1} + \sigma_{I,n}\left\langle I\right\rangle_{n+1} = f_n\sigma_{p,n}cU_{r,n} + (1-f_n)\sigma_{I,n}\left\langle I\right\rangle_{n+1} \ , \tag{5.23}$$

and rearrange terms to obtain:

$$-\frac{\partial}{\partial x}\frac{1}{\sigma_{\rho,n}}\frac{\partial}{\partial x}E_n\left\langle I\right\rangle_{n+1} + \left(\frac{1}{c\Delta_{t,n}} + f_n\sigma_{I,n}\right)\left\langle I\right\rangle_{n+1} = f_n\sigma_{p,n}cU_{r,n} + \frac{1}{c\Delta_{t,n}}\left\langle I\right\rangle_{n} \ . \tag{5.24}$$

We continue by defining

$$D_n = \frac{1}{\sigma_{\rho,n}} \, , \tag{5.25a}$$

$$\Sigma_n = \frac{1}{c\Delta_{t,n}} + f_n\sigma_{I,n} \, , \tag{5.25b}$$

$$S_n = f_n\sigma_{p,n}cU_{r,n} + \frac{1}{c\Delta_{t,n}}\left\langle I\right\rangle_{n} \ , \tag{5.25c}$$

and rewriting Eq. (5.24) as:

$$-\frac{\partial}{\partial x}D_n\frac{\partial}{\partial x}E_n\left\langle I\right\rangle_{n+1} + \Sigma_n\left\langle I\right\rangle_{n+1} = S_n \, . \tag{5.26a}$$

Eq. (5.26a) is a "steady-state", gray, and slightly modified Quasidiffusion equation. Next, we derive an equation for T_{n+1} that depends on $\left\langle I\right\rangle_{n+1}$. Substituting Eq. (5.22) into Eq. (5.20c), we find:

$$\frac{1}{\Delta_{t,n}}\left(U_{m,n+1} - U_{m,n}\right) - \sigma_{p,n}cf_nU_{r,n} + (1-f_n)\sigma_{I,n}\left\langle I\right\rangle_{n+1} = \sigma_{I,n}\left\langle I\right\rangle_{n+1} \ ,$$

$$U_{m,n+1} = U_{m,n} - \Delta_{t,n}f_n\sigma_{p,n}cU_{r,n} + \Delta_{t,n}f_n\sigma_{I,n}\left\langle I\right\rangle_{n+1} \ . \tag{5.26b}$$

This final expression is comparable to the IMC material update equation [Eq. (3.29b)]. The temperatures T_{n+1} are updated by solving:

$$U_{m,n+1} = \int_0^{T_{n+1}} c_v(T')\,dT' \, . \tag{5.26c}$$

The initial conditions for this method are provided from the IMC calculation. Although it is possible to derive boundary conditions that involve a special surface Eddington factor, we shall use a Marshak boundary condition.[1] This may be found by operating on Eq. (2.38e) with an integral over all frequencies and the time step. For the left boundary we find:

$$\langle I\rangle^{n+1}(0) - 2D_{n,n+1}(0)\frac{\partial}{\partial x}\langle I\rangle^{n+1}(0) = \frac{4}{\Delta_{t,n}}\int_{t_n}^{t_{n+1}}\int_0^\infty\int_0^1 \mu I^\ell(\mu,\nu,t)\,d\mu\,d\nu\,dt\,, \quad (5.27a)$$

and for the right boundary,

$$\langle I\rangle^{n+1}(X) + 2D_{n,n+1}(X)\frac{\partial}{\partial x}\langle I\rangle^{n+1}(X) = \frac{4}{\Delta_{t,n}}\int_{t_n}^{t_{n+1}}\int_0^\infty\int_{-1}^0 |\mu|\, I^r(\mu,\nu,t)\,d\mu\,d\nu\,dt\,, \quad (5.27b)$$

where the implicit-in-time approximation has been made for $\langle I\rangle$, and the spatial variable has been made explicit to designate the left and right sides of the slab ($x = 0$ or X, respectively). Note that the spatial derivative term is to be evaluated *at* these locations; it is not zero.

The arguments for positivity in $\langle I\rangle$ and $U_{m,n+1}$ are analogous to those made in Section 3.2.1. Because Eq. (5.26a) is a diffusion equation with positive coefficients and sources, it cannot produce a negative solution. In fact, since the "wave speed" of this system is infinite, it is possible to show that solutions of $\langle I\rangle_{n+1}$ must be positive. In Eq. (5.26b), however, there is a negative term – the same negative term that appeared in Eq. (3.29b). In Chapter III, we analyzed the conditions under which this term may be expected to produce negative solutions [see Eq. (3.35) and Eq. (3.37)]. That analysis applies here with $\alpha = 1$. We may therefore conclude that Eq. (5.26b) will produce positive solutions when the specific heat is constant, and should produce positive solutions when the specific heat is an n^{th} order polynomial in temperature with $n \leq 3$.

To summarize, the general procedure to estimate T_{n+1} is to first solve Eq. (5.26a) for $\langle I\rangle_{n+1}$, and then to solve Eq. (5.26b) for $U_{m,n+1}$, from which T_{n+1} may be calculated via Eq. (5.26c). This value of T_{n+1} is used in the definition of the time-average

[1]For consistency, all of the averaged problem data [E, σ_I, σ_ρ] are generated from "snapshot" tallies, and it is not possible to generate an estimator for instantaneous surface-crossings.

temperature T_* to evaluate the temperature-dependent problem data in a subsequent IMC calculation over $t_n \leq t \leq t_{n+1}$. The IMC solution of T_{n+1} is calculated in the usual way, and supersedes the Quasidiffusion estimate.

We next define the average temperature that depends on T_n and T_{n+1} and that may be used to evaluate the temperature-dependent data for the IMC solution.

5.1.3 An Average Interpolated Temperature

For sufficiently small time steps, the time-dependence of the temperature is approximately linear:

$$T(t) \approx T_n + \frac{T_{n+1} - T_n}{\Delta_t} t \,. \tag{5.28}$$

Then, assuming an opacity of the form

$$\sigma = \frac{\gamma}{T(t)^3} \,, \tag{5.29}$$

we look for a time-averaged σ given by:

$$\overline{\sigma} = \frac{1}{\Delta_t} \int_{t_n}^{t_{n+1}} \frac{\gamma}{T(t)^3} \, dt = \frac{\gamma}{T_*^3} \,, \tag{5.30}$$

where T_* is the properly averaged, time-dependent temperature at which to evaluate the opacities. Substituting Eq. (5.28) into Eq. (5.30) and carrying out this integral, we obtain:

$$\frac{1}{T_*^3} = \frac{(T_{n+1} + T_n)/2}{T_n^2 T_{n+1}^2} \,,$$

or

$$T_* = \left(\frac{T_n^2 T_{n+1}^2}{(T_{n+1} + T_n)/2} \right)^{1/3} \,. \tag{5.31}$$

Figure 5.1 depicts T_* as a function of the beginning and end of time step temperatures T_n and T_{n+1}. From it, we verify that T_* contains the proper limits when T_n and T_{n+1} are equal. We also see that T_* "favors" lower temperatures. This seems correct since the function $1/T(t)^3$ is weighted more heavily at lower temperatures. From another perspective, physically, the opacity is much greater at lower temperatures, therefore lower temperatures are more important during a time step.

Using the temperature defined by Eq. (5.31) to evaluate the opacities in an IMC calculation is more accurate than using T_n. In addition to the opacities, there are other temperature-dependent factors that appear in the IMC equations, specifically, $b_n(\nu)$, β_n, and f_n. Although these do not contain a temperature dependence of T^{-3},

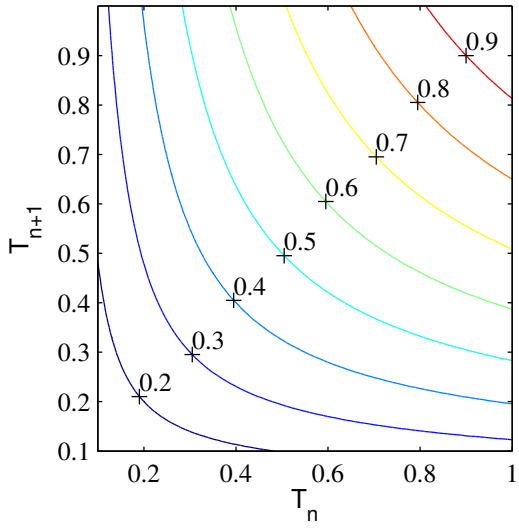

Figure 5.1: The average temperature T_* as a function of the beginning and end of time step temperatures T_n and T_{n+1}.

in this chapter, these will also be evaluated at the temperature T_*. One reason for doing this is consistency – if one attempts to use a different temperature to evaluate the normalized Planck function $b_n(\nu)$ and/or β_n, this would necessitate the introduction of a $\chi(\nu)$ emission spectrum that depends on more than one temperature [see Eq. (3.19a)]. This is possible to do, but inconvenient. Additionally, since the equation for $U_r(t)$ [Eq. (5.14b)] contains the product $\sigma_p\beta$, then under the usual assumption that c_v is constant,

$$\sigma_p\beta = \frac{\gamma}{T^3}\frac{4aT^3}{c_v} = \text{ constant}\,. \tag{5.32}$$

Thus, evaluating β and σ_p at the same temperature ensures that this product remains constant. Since the Fleck factor f contains this product, this also implies that $f_* = f_n$. However, as future work, alternative treatments of temperature-dependence of $b(\nu)$ and β should be considered. For instance, different average temperatures could be defined and independently used to evaluate the opacities, β, and the normalized Planck function. In this chapter, we will use T_* to evaluate all of the temperature-dependent problem data with the expectation that this should be an improvement over the use of T_n, and the acknowledgement that it is likely possible to further improve the IMC calculation by defining alternative time-averaged temperatures.

5.1.4 Iterative Refinement

The above procedure successfully produces time-discretized equations that may be solved to obtain an estimate of T_{n+1}. Since it is *much* less numerically expensive to perform this procedure than the corresponding IMC calculation, it may be worthwhile to employ the following modification. It is known that the Planck and Rosseland mean opacities are proportional to T^{-3}. Let us further assume that σ_I and σ_ρ contain this proportionality. If this is true, then instead of freezing the opacities to their known values at the beginning of the time step, a more accurate result may be obtained by using estimated opacities that have been averaged over the time step.

Let us define an iteration index i, and define "time-averaged" opacities by:

$$T_*^{(i)} = \left(\frac{T_n^2 (T_{n+1}^{(i)})^2}{(T_{n+1}^{(i)} + T_n)/2} \right)^{1/3} , \tag{5.33a}$$

$$\sigma_{\rho,*}^{(i)} = \sigma_{\rho,n} \left(\frac{T_n}{T_*^{(i)}} \right)^3 , \tag{5.33b}$$

$$\sigma_{I,*}^{(i)} = \sigma_{I,n} \left(\frac{T_n}{T_*^{(i)}} \right)^3 , \tag{5.33c}$$

$$\sigma_{p,*}^{(i)} = \sigma_{p,n} \left(\frac{T_n}{T_*^{(i)}} \right)^3 , \tag{5.33d}$$

and a time-averaged β by:

$$\beta_*^{(i)} = \beta_n \left(\frac{T_*^{(i)}}{T_n} \right)^3 , \tag{5.33e}$$

where the superscript (i) indicates evaluation at iterative index i. The quantities in Eqs. (5.33) are initialized at $i = 0$ by setting $T_*^{(i)} = T_n$, i.e.:

$$\sigma_{\rho,*}^{(0)} = \sigma_{\rho,n} , \tag{5.34a}$$

$$\sigma_{I,*}^{(0)} = \sigma_{I,n} , \tag{5.34b}$$

$$\sigma_{p,*}^{(0)} = \sigma_{p,n} , \tag{5.34c}$$

$$\beta_*^{(0)} = \beta_n . \tag{5.34d}$$

In other words, for $i = 0$, the time-averaged opacities are estimated using the known, explicit data.

Using these definitions, we rewrite Eqs. (5.25) with iteration index i as:

$$D_*^{(i)} = \frac{1}{\sigma_{\rho,*}^{(i)}}\,, \tag{5.35a}$$

$$\Sigma_*^{(i)} = \frac{1}{c\Delta_{t,n}} + (f\sigma_I)_*^{(i)}\,, \tag{5.35b}$$

$$S_*^{(i)} = (f\sigma_p)_*^{(i)} cU_{r,n} + \frac{1}{c\Delta_{t,n}} \langle I \rangle_n \,. \tag{5.35c}$$

Then Eq. (5.26a) may be rewritten using Eqs. (5.35) as:

$$-\frac{\partial}{\partial x} D_*^{(i)} \frac{\partial}{\partial x} E_n \langle I \rangle_{n+1} + \Sigma_*^{(i)} \langle I \rangle_{n+1} = S_*^{(i)}\,, \tag{5.36a}$$

for iteration index i, and its solution may be used to solve an iterative version of Eq. (5.26b):

$$U_{m,n+1}^{(i+1)} = U_{m,n} - (f\sigma_p)_*^{(i)} cU_{r,n} + (f\sigma_I)_*^{(i)} \langle I \rangle_{n+1} \,. \tag{5.36b}$$

Finally, inverting

$$U_{m,n+1}^{(i+1)} = \int_0^{T_{n+1}^{(i+1)}} c_v(T')\, dT' \tag{5.36c}$$

provides $T_{n+1}^{(i+1)}$, which may be used to update the quantities $D_*^{(i+1)}$, $\Sigma_*^{(i+1)}$ and $S_*^{(i+1)}$ for the next iteration. This process can be repeated until T_{n+1} has converged, and is not expected to require many iterations.

It should be noted that if the time steps are sufficiently large, then it is possible for Eq. (5.36b) to produce non-physical, negative values of $U_{m,n+1}$. Such behavior must be guarded against, either by using smaller time steps, by stopping the iterations before convergence has completed, or by ensuring that [from Eq. (5.36b):

$$U_{m,n} \geq \Delta_t f_* \sigma_{p,*} cU_{r,n}\,. \tag{5.37}$$

Since f is a monotonically decreasing function of Δ_t and

$$\lim_{\Delta_t \to \infty} \frac{\Delta_t}{1 + \beta_* \sigma_{p,*} c\Delta_t} = \frac{1}{\beta_* \sigma_{p,*} c}\,, \tag{5.38}$$

it is sufficient to satisfy

$$U_{m,n} \geq \frac{1}{\beta_* \sigma_{p,*} c} \sigma_{p,*} cU_{r,n} = \frac{1}{\beta_*} U_{r,n}\,, \tag{5.39}$$

or

$$\beta_* \geq \frac{U_{r,n}}{U_{m,n}} \,. \tag{5.40}$$

For the typical case in which c_v = constant, this may be written as:

$$\frac{4aT_*^4}{c_v} \geq \frac{aT_n^4}{c_v T_n} \,,$$
$$4T_*^3 \geq T_n^3 \,,$$

or

$$T_* \geq T_n \left(\frac{1}{4}\right)^{1/3} \approx 0.63 T_n \,. \tag{5.41}$$

For the purposes of numerical experiments, we have chosen to stop the iteration procedure in the event that T_* is found to violate Eq. (5.41), although an analytical result such as this may not be possible for arbitrary materials. Eq. (5.41) places a limit on the maximum cooling rate (note that this limit is implicit in the traditional form of the IMC equations). The general conclusion is that one should exercise caution if the temperature estimation scheme predicts temperatures that are substantially different from T_n, as this indicates that the desired time step is too large. Alternatively, this property of the temperature estimation algorithm could be used to adaptively reduce the size of the time step. For instance, if Eq. (5.41) is not satisfied, one could iteratively reduce the time step size and repeat the calculation until a suitable value of T_* is obtained. In current implementations of the IMC procedure that do not have access to this methodology, there is no way to determine if a proposed time step is too large until after the calculation has ended, after which it may be too difficult or cost-prohibitive to repeat the IMC calculation. Employing a Quasidiffusion calculation to estimate the maximum time step size before the IMC calculation is performed could be an inexpensive way to circumvent this difficulty.

The limit in Eq. (5.41) also applies directly to the IMC update equation. To see this, compare Eq. (5.36b) to Eq. (3.29b). Thus, both the Quasidiffusion and IMC equations contain a positivity restriction on T_*; one is not free to use arbitrary temperatures to evaluate the problem data. During the IMC calculation, we explicitly enforce the restriction in Eq. (5.41) – if the Quasidiffusion method produces a value of T_* that violates Eq. (5.41), then T_* is increased so that it satisfies Eq. (5.41).

Overall, this iteration procedure is *not* an essential feature of the temperature estimation method presented in this chapter, and should be viewed as an enhancement

designed to increase accuracy.

The final step to form a set of algebraic equations is to discretize Eqs. (5.36) in space.

5.1.5 Spatial Discretization

In this section we spatially-discretize Eqs. (5.36). The method we choose is a straightforward application of a finite volume method [53], but other schemes (like finite elements) could just as easily be considered [54]. We have chosen the finite volume approach because it is simple to derive and because it automatically conserves the unknowns averaged over each finite volume (spatial zone).

During each iteration on Eqs. (5.36) it is necessary to obtain an estimate of $\langle I \rangle_{n+1}$ in order to update the temperature at the end of the time step. Essentially the same equation is solved with different data. For simplicity, we shall drop the iteration index and temporal terms, and define the quantities:

$$\phi(x) = \langle I \rangle (x) \,, \tag{5.42a}$$

$$J(x) = -D(x) \frac{\partial}{\partial x} E(x) \phi(x) \,, \tag{5.42b}$$

to mean the frequency- and angle-averaged intensity and frequency-averaged first angular moment of I (sometimes called the "current"), respectively. This definition of J emerges from the approximation in Eq. (5.11). We would like to solve the following equation (representing a single iteration in the above procedure):

$$-\frac{\partial}{\partial x} D(x) \frac{\partial}{\partial x} E(x) \phi(x) + \Sigma(x) \phi(x) = S(x) \,, \tag{5.43}$$

subject to boundary conditions

$$\phi(0) + 2J(0) = 4 \int_{t_n}^{t_{n+1}} \int_0^{\infty} \int_0^1 \mu I^{\ell}(\mu, \nu, t) \, d\mu \, d\nu \, dt \,, \tag{5.44a}$$

and

$$\phi(X) - 2J(X) = 4 \int_{t_n}^{t_{n+1}} \int_0^{\infty} \int_{-1}^{\mu} |\mu| \, I^{r}(\mu, \nu, t) \, d\mu \, d\nu \, dt \,. \tag{5.44b}$$

To do this, we define a spatial zone with index k by $x_{k-1/2} \leq x \leq x_{k+1/2}$. The slab is discretized into a complete, disjoint set of zones with indices $k = 1, 2 \ldots K$. We also define $\Delta_{x,k} = x_{k+1/2} - x_{k-1/2}$, and define the notation that "zone-centered"

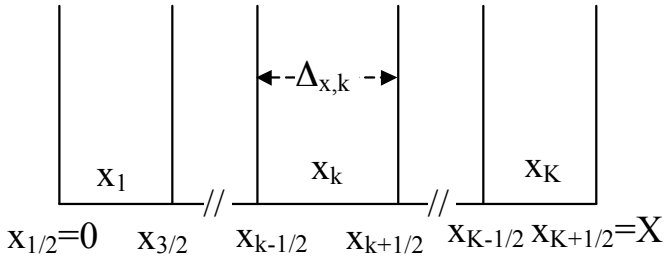

Figure 5.2: The zone-centered spatial discretization.

data is defined by the spatial average:

$$f_k \equiv \frac{1}{\Delta_{x,k}} \int_{x_{k-1/2}}^{x_{k+1/2}} f(x)\, dx\,, \tag{5.45}$$

and "node-centered" data by:

$$f_{k\pm1/2} = f(x_{k\pm1/2})\,. \tag{5.46}$$

Figure 5.2 is a graphical depiction of the zone-centered spatial discretization.

Next, we operate on Eq. (5.43) by the spatial averaging operator in Eq. (5.45) to obtain:

$$\frac{1}{\Delta_{x,k}} \left(J_{k+1/2} - J_{k-1/2}\right) + \Sigma_k \phi_k = S_k\,. \tag{5.47}$$

The term $\Sigma_k \phi_k$ is technically an approximation since Σ and ϕ are each dependent on x. However, the underlying data is already discretized into this form in order to solve the IMC equations, so it does not represent an additional approximation. We would like to eliminate the $k \pm 1/2$ terms in this equation to form a system that depends only on index k. To do this, we assume that a finite difference representation of the node-centered current $J_{k+1/2}$ is continuous between spatial cells k and $k+1$, or that:

$$J_{k+1/2} = -D_{k+1} \frac{E_{k+1}\phi_{k+1} - E_{k+1/2}\phi_{k+1/2}}{\Delta_{x,k+1}/2} = -D_k \frac{E_{k+1/2}\phi_{k+1/2} - E_k \phi_k}{\Delta_{x,k}/2}\,. \tag{5.48}$$

This system may be solved to eliminate $E_{k+1/2}\phi_{k+1/2}$ to find

$$J_{k+1/2} = -\left(\frac{D}{\Delta_x}\right)_{k+1/2} \left(E_{k+1}\phi_{k+1} - E_k \phi_k\right)\,, \tag{5.49}$$

where $(D/\Delta_x)_{k+1/2}$ is the harmonic average:

$$\left(\frac{D}{\Delta_x}\right)_{k+1/2} \equiv \frac{2\left(\frac{D_{k+1}}{\Delta_{x,k+1}}\right)\left(\frac{D_k}{\Delta_{x,k}}\right)}{\left(\frac{D_{k+1}}{\Delta_{k+1}}\right)+\left(\frac{D_k}{\Delta_k}\right)}\,. \tag{5.50}$$

Using Eq. (5.49) in Eq. (5.47), we obtain:

$$-\left(\frac{D}{\Delta_x}\right)_{k+1/2}(E_{k+1}\phi_{k+1}-E_k\phi_k)+\left(\frac{D}{\Delta_x}\right)_{k-1/2}(E_k\phi_k-E_{k-1}\phi_{k-1}) + \Delta_{x,k}\Sigma_k\phi_k = \Delta_{x,k}S_k\,. \tag{5.51}$$

Eq. (5.51) is the spatially-discretized Quasidiffusion equation that must be solved for each index $k = 2, \ldots K-1$ once per iteration. However, we must still derive the boundary conditions to obtain equations for the boundary zones $k = 1$ and $k = K$. Let us define the incoming partial current on the left boundary to be:

$$J^+_{1/2} = \frac{1}{\Delta_{t,n}}\int_{t_n}^{t_{n+1}}\int_0^\infty\int_0^1 \mu I^\ell(\mu,\nu,t)\,d\mu\,d\nu\,dt\,. \tag{5.52}$$

The continuity of current equation on the interior of zone 1 is:

$$J_{1/2} = -D_1\frac{E_1\phi_1 - E_{1/2}\phi_{1/2}}{\Delta_{x,1}/2}\,. \tag{5.53}$$

However, since we do not calculate the surface Eddington factor $E_{1/2}$, we assume that the diffusion boundary condition is sufficient. We recall from Chapter II that, in the diffusive limit, $E \to 1/3$, so that we shall use

$$J_{1/2} = -D_1\frac{E_1\phi_1 - \frac{1}{3}\phi_{1/2}}{\Delta_{x,1}/2} \tag{5.54}$$

instead. Next, Eq. (5.44a) may be solved for $\phi_{1/2}$:

$$\phi_{1/2} = 4J^+_{1/2} - 2J_{1/2}\,. \tag{5.55}$$

Substituting Eq. (5.55) into Eq. (5.54), we find:

$$J_{1/2} = -D_1\frac{E_1\phi_1 - \frac{1}{3}(4J^+_{1/2} - 2J_{1/2})}{\Delta_{x,1}/2}\,,$$

$$J_{1/2}\left(1+\frac{4D_1}{3\Delta_{x,1}}\right) = -2\frac{D_1}{\Delta_{x,1}}\left(E_1\phi_1 - \frac{4}{3}J^+_{1/2}\right) ,$$

$$J_{1/2} = -2D_1\frac{3E_1\phi_1 - 4J^+_{1/2}}{3\Delta_{x,1}+4D_1} . \tag{5.56a}$$

In the special case of a reflecting boundary, $J_{1/2} = 0$, which is considerably simpler to manage. Analogous equations may be used to find the current at the right boundary, $J_{K+1/2}$:

$$J_{K+1/2} = -2D_K\frac{3E_K\phi_K - 4J^+_{K+1/2}}{3\Delta_{x,K}+4D_K} . \tag{5.56b}$$

Combining these results with a modified form of Eq. (5.51) for $k = 1$ and $k = K$, we obtain the complete system of K equations:

$$-\left(\frac{D}{\Delta_x}\right)_{3/2}(E_2\phi_2 - E_1\phi_1) + 2D_1\frac{3E_1\phi_1 - 4J^+_{1/2}}{3\Delta_{x,1}+4D_1} + \Delta_{x,1}\Sigma_1\phi_1 = \Delta_{x,1}S_1 , \qquad \text{for } k = 1 , \tag{5.57a}$$

$$-\left(\frac{D}{\Delta_x}\right)_{k+1/2}(E_{k+1}\phi_{k+1} - E_k\phi_k) + \left(\frac{D}{\Delta_x}\right)_{k-1/2}(E_k\phi_k - E_{k-1}\phi_{k-1}) + \Delta_{x,k}\Sigma_k\phi_k = \Delta_{x,k}S_k , \qquad \text{for } k = 2, 3 \ldots K-1 , \tag{5.57b}$$

$$-2D_K\frac{3E_K\phi_K - 4J^+_{K+1/2}}{3\Delta_{x,K}+4D_K} + \left(\frac{D}{\Delta_x}\right)_{K-1/2}(E_K\phi_K - E_{K-1}\phi_{K-1}) + \Delta_{x,K}\Sigma_k\phi_k = \Delta_{x,K}S_K , \qquad \text{for } k = K . \tag{5.57c}$$

Eqs. (5.57) are a system of K equations that may be written in matrix-vector form. The resulting matrix is tridiagonal and diagonally dominant, thereby making the solution procedure a matter of forward and back substitution. In the limit of a completely diffusive problem, it is also symmetric.

To summarize this presentation, the temperature-estimation method consists of the following algorithm. We assume that at least one IMC calculation has been performed for the time step $t_{n-1} \le t \le t_n$, and that the quantities σ_I, σ_ρ, and E have been tallied for each spatial zone k. Then the procedure is:

1. Set the iteration index $i = 1$, and set $T^{(0)}_{n+1} = T_n$.

2. Set $T_{n+1}^{(i)} = T_{n+1}^{(i-1)}$.

3. For each spatial cell k, initialize the quantities in Eqs. (5.35).

4. Solve the system given by Eqs. (5.57) for $\phi = \langle I \rangle_{n+1}$.

5. For each spatial cell k, update $T_{n+1}^{(i+1)}$ according to Eq. (5.36b) and Eq. (5.36c).

6. If converged or iteration is not desired, stop iterating. If not, set $i \leftarrow i+1$ and begin again at step 2.

Once this process has been completed, T_* may be calculated using Eq. (5.31). Assuming that it does not violate Eq. (5.41), it may then be passed to the IMC calculation for evaluation of the temperature-dependent problem data for the upcoming time step $t_n \leq t \leq t_{n+1}$. For the first time step, one may choose either not to perform the algorithm (i.e., to only use traditional IMC), or to set $E = 1/3$, $\sigma_I = \sigma_p$, and $\sigma_r = \sigma_\rho$, and perform an ordinary diffusion calculation.

5.1.6 Gray Procedure

In the event that the opacities do not depend on frequency $[\sigma(\nu, T) = \sigma(T)]$, this procedure may be simplified. Assuming that the gray approximation is used (see discussion in Chapter II for details), then

$$\sigma_\rho(T) = \frac{\langle \mu^2 I \rangle}{\left\langle \frac{\mu^2}{\sigma(T)} I \right\rangle} = \sigma \frac{\langle \mu^2 I \rangle}{\langle \mu^2 I \rangle} = \sigma(T)\,, \tag{5.58a}$$

$$\sigma_I(T) = \frac{\langle \sigma(T) I \rangle}{\langle I \rangle} = \sigma(T) \frac{\langle I \rangle}{\langle I \rangle} = \sigma(T), \tag{5.58b}$$

$$E(x) = \frac{\langle \mu^2 I \rangle}{\langle I \rangle} = \frac{\int_{-1}^{1} \mu^2 I(\mu)\, d\mu}{\int_{-1}^{1} I(\mu)\, d\mu}\,. \tag{5.58c}$$

Thus, the specially-defined opacities reduce to the simpler, temperature-dependent opacity, and the Eddington factor no longer needs to be averaged over frequency. In other words, it is no longer necessary to explicitly tally σ_ρ or σ_I. These simplifications may be propagated into Eqs. (5.25) and the above procedure may still be used with no other modifications.

5.2 Stability Analysis

We next perform the 0-D stability analysis algorithm described in Chapter IV on Eqs. (5.26) to ensure that the temperature estimation scheme is numerically stable and to see whether it contains damped oscillations. We expect it to be stable due to the implicit treatment of the problem unknowns, but it is difficult to state *a priori* what the effects of the explicit treatment of the problem data are. Because the system is so similar in character to the IMC equations (it even contains a Fleck factor), one might conjecture that Eqs. (5.26) are also prone to damped oscillations, although we shall see that this is not the case.

We begin by assuming that $\sigma \propto T^{-3}$ and that c_v = constant. Since we have previously derived this form of the 0-D, gray, dimensionalized versions of the TRT equations, there is no need to explicitly carry out the first step of the algorithm. The equations are [from Eq. (4.9)]:

$$q\frac{\partial \phi}{\partial \tau} + \frac{1}{M^3}\phi = \frac{1}{M^3}R\,, \tag{5.59a}$$

with the material energy equation written exactly in either of the following two forms:

$$\frac{\partial M}{\partial \tau} + \frac{1}{M^3}R = \frac{1}{M^3}\phi, \tag{5.59b}$$

$$\frac{\partial R}{\partial \tau} + 4R = 4\phi\,. \tag{5.59c}$$

The second step is to apply the approximations that led to Eqs. (5.26). In gray, 0-D problems, there is no need to define any frequency-averaged data or Eddington factors. We begin by performing implicit time discretizations on Eqs. (5.59) for a time step $\tau_n \leq \tau \leq \tau_{n+1}$, assuming that the opacities are evaluated at time τ_n:

$$\frac{q}{\Delta_\tau}(\phi_{n+1} - \phi_n) + \frac{1}{M_n^3}\phi_{n+1} = \frac{1}{M_n^3}R_{n+1}\,, \tag{5.60a}$$

$$\frac{1}{\Delta_\tau}(M_{n+1} - M_n) + \frac{1}{M_n^3}R_{n+1} = \frac{1}{M_n^3}\phi_{n+1}, \tag{5.60b}$$

$$\frac{1}{\Delta_\tau}(R_{n+1} - R_n) + 4R_{n+1} = 4\phi_{n+1}\,. \tag{5.60c}$$

We solve Eq. (5.60c) for R_{n+1}:

$$\begin{aligned} R_{n+1} &= \frac{R_n}{1+4\Delta_\tau} + \frac{4\Delta_\tau}{1+4\Delta_\tau}\phi_{n+1}\,, \\ &= fR_n + (1-f)\phi_{n+1}\,, \end{aligned} \tag{5.61}$$

where f is defined in Eq. (4.19) (with $\alpha = 1$). We next eliminate R_{n+1} from the system by substituting Eq. (5.61) into Eq. (5.60a):

$$\begin{aligned} \frac{q}{\Delta_\tau}(\phi_{n+1}-\phi_n) + \frac{1}{M_n^3}\phi_{n+1} &= \frac{1}{M_n^3}\left(fR_n + (1-f)\phi_{n+1}\right)\,, \\ \left(\frac{q}{\Delta_\tau} + \frac{f}{M_n^3}\right)\phi_{n+1} &= \frac{fR_n}{M_n^3} + \frac{q}{\Delta_\tau}\phi_n\,, \end{aligned} \tag{5.62}$$

and Eq. (5.60b):

$$\begin{aligned} \frac{1}{\Delta_\tau}(M_{n+1}-M_n) + \frac{1}{M_n^3}\left(fR_n + (1-f)\phi_{n+1}\right) &= \frac{1}{M_n^3}\phi_{n+1}, \\ M_{n+1} &= M_n - f\Delta_\tau\frac{R_n}{M_n^3} + \frac{f\Delta_\tau}{M_n^3}\phi_{n+1}\,. \end{aligned} \tag{5.63}$$

Next, we solve Eq. (5.62) for ϕ_{n+1} and use the initial condition $R_n = M_n^4$ to eliminate the R_n and ϕ_{n+1} terms from Eq. (5.63):

$$M_{n+1} = M_n - f\Delta_\tau M_n + \frac{f\Delta_\tau}{M_n^3}\left[\frac{fM_n + \frac{q}{\Delta_\tau}\phi_n}{\frac{q}{\Delta_\tau} + \frac{f}{M_n^3}}\right]\,. \tag{5.64}$$

The third step is to use the conservation of energy to entirely eliminate ϕ from the system. At time τ_n, the conservation of energy produces

$$q\phi + M = q + 1\,, \quad \Rightarrow \phi_n = \frac{q+1-M_n}{q}\,. \tag{5.65}$$

Substituting Eq. (5.65) into Eq. (5.64) and rearranging, we obtain:

$$M_{n+1} = (1-f\Delta_\tau)M_n + f\Delta_\tau\left[\frac{f\Delta_\tau M_n + q + 1 - M_n}{qM_n^3 + f\Delta_\tau}\right]\,. \tag{5.66}$$

Eq. (5.66) is the exact solution of the scaled temperature at the end of the time step produced by the 0-D temperature estimation algorithm without iterations.

The fourth step is to employ a perturbation analysis. To do this, we set

$$M_n = 1 + \epsilon P_n \,, \tag{5.67a}$$

$$M_{n+1} = 1 + \epsilon P_{n+1} \,, \tag{5.67b}$$

where ϵ is a small parameter, and look for the relationship between the first-order perturbations P_{n+1} and P_n. Substitution of Eqs. (5.67) in Eq. (5.66) produces (to first order in ϵ):

$$1 + \epsilon P_{n+1} = (1 - f\Delta_\tau)(1 + \epsilon P_n) + f\Delta_\tau \left[\frac{q + 1 + (f\Delta_\tau - 1)(1 + \epsilon P_n)}{f\Delta_\tau + q(1 + 3\epsilon P_n)} \right] ,$$

$$\epsilon P_{n+1} = -f\Delta_\tau + (1 - f\Delta_\tau)\epsilon P_n + \frac{f\Delta_\tau}{f\Delta_\tau + q} \left[\frac{q + f\Delta_\tau + (f\Delta_\tau - 1)\epsilon P_n}{1 + \frac{3q}{f\Delta_\tau + q}\epsilon P_n} \right] ,$$

$$\epsilon P_{n+1} = -f\Delta_\tau + (1 - f\Delta_\tau)\epsilon P_n + f\Delta_\tau \left(1 + \frac{f\Delta_\tau - 1}{f\Delta_\tau + q}\epsilon P_n \right) \left(1 - \frac{3q}{f\Delta_\tau + q}\epsilon P_n \right) ,$$

$$\epsilon P_{n+1} = (1 - f\Delta_\tau)\epsilon P_n + \frac{f^2\Delta_\tau^2 - f\Delta_\tau}{f\Delta_\tau + q}\epsilon P_n - \frac{3qf\Delta_\tau}{f\Delta_\tau + q}\epsilon P_n \,,$$

$$P_{n+1} = -f\Delta_\tau P_n + f\Delta_\tau \frac{f\Delta_\tau - 1}{f\Delta_\tau + q} P_n - \frac{3qf\Delta_\tau}{f\Delta_\tau + q} P_n \,,$$

$$P_{n+1} = \frac{q + f\Delta_\tau - f^2\Delta_\tau^2 - qf\Delta_\tau + f^2\Delta_\tau^2 - f\Delta_\tau - 3qf\Delta_\tau}{f\Delta_\tau + q} P_n \,.$$

Simplifying, we identify the amplification factor for the 0-D, dimensionless temperature estimation algorithm as:

$$\rho = \frac{q(1 - 4f\Delta_\tau)}{q + f\Delta_\tau} \,. \tag{5.68}$$

The fifth and final step is to analyze Eq. (5.68) to assess the system's stability. We first prove that $\rho < 1$:

$$\frac{q(1 - 4f\Delta_\tau)}{q + f\Delta_\tau} < 1 \,,$$

$$-4qf\Delta_\tau < f\Delta_\tau \,. \tag{5.69}$$

Next, we show that $0 \leq \rho$:

$$0 < \frac{q(1 - 4f\Delta_\tau)}{q + f\Delta_\tau} \,,$$

$$0 < 1 - 4f\Delta_\tau \,,$$

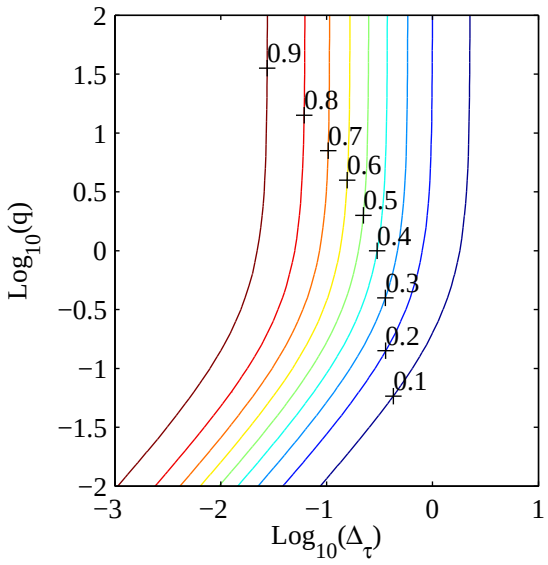

Figure 5.3: A contour plot of the amplification factor for the temperature estimation algorithm.

$$\begin{aligned} 4f\Delta_\tau &< 1\,, \\ \frac{4\Delta_\tau}{1+4\Delta_\tau} &< 1\,. \end{aligned} \tag{5.70}$$

This proves that $0 < \rho < 1$, indicating that the temperature-estimation algorithm is both unconditionally stable and cannot contain damped oscillations. Figure 5.3 is a contour plot of the amplification factor for the temperature estimation algorithm. Figure 5.3 further confirms that $0 < \rho < 1$, and illustrates how $\rho \to 0$ for large Δ_τ and $\rho \to 1$ for small Δ_τ, which is the correct behavior.

We do not expect the use of iteration in the temperature estimation algorithm (to obtain a more accurate temperature T_* at which to evaluate the opacities) to adversely affect its stability characteristics.

5.3 Numerical Results

In this section we consider three test cases to exercise the temperature estimation algorithm. The first is a nonlinear, 0-D problem that has initial conditions away from equilibrium. For this case we numerically determine the temporal order of accuracy for IMC equations with data evaluated at T_n, T_*, and T_{n+1} by comparing their solutions to a fine grid solution.

The second and third cases are Marshak waves for gray and frequency-dependent

problems respectively. In these experiments we consider whether using the temperature estimation algorithm to evaluate the opacities and the normalized Planck function improves the numerical accuracy of the wavefront location.

We also define a nomenclature to delineate the variations of the IMC method that we shall consider in this section. The three principal methods shall be referred to as:

- IMC: A traditional implementation of the IMC equations, with temperature-dependent problem data evaluated at T_n.
- IMC-T_*: An implementation of the IMC equations in which the temperature-dependent problem data (σ and β, also $b(\nu)$ in frequency-dependent problems) are evaluated at the time-average temperature T_* generated by the deterministic Quasidiffusion equations.
- IMC-T_{n+1}: An implementation of the IMC equations in which the temperature-dependent problem data (σ and β, also $b(\nu)$ in frequency-dependent problems) are evaluated at the time-average temperature T_{n+1} generated by the deterministic Quasidiffusion equations.

A further variation of the IMC-T_* and IMC-T_{n+1} methods is the inclusion of iteration in the Quasidiffusion equations. We delineate this feature explicitly when it is applicable.

5.3.1 Temporal Order of Accuracy

To numerically assess the temporal order of accuracy, we consider a sample 0-D problem that employs the dimensionless, gray, nonlinear TRT equations defined in Eqs. (4.87). For this problem, we assume that $\sigma = T^{-3}$, $a = c = 1$, and $q = 0.14$, which implies that $c_v \approx 7.14$. The temperature is set to an initial condition of 0.1, and the initial intensity ϕ is 7.428. The problem is solved using a variable number of time steps with an ending time fixed at $t = 1$, at which point the fine-mesh temperature solution is 0.96 [the temperature is 96% converged to its specified equilibrium condition].

Because this is a gray, 0-D problem, the temperature solutions of Eqs. (4.87) and the Quasidiffusive temperature estimation equations [Eqs. (5.26)] are exactly obtainable over a single time step. To avoid the introduction of Monte Carlo statistical errors into the accuracy studies, we numerically implemented the exact temperature

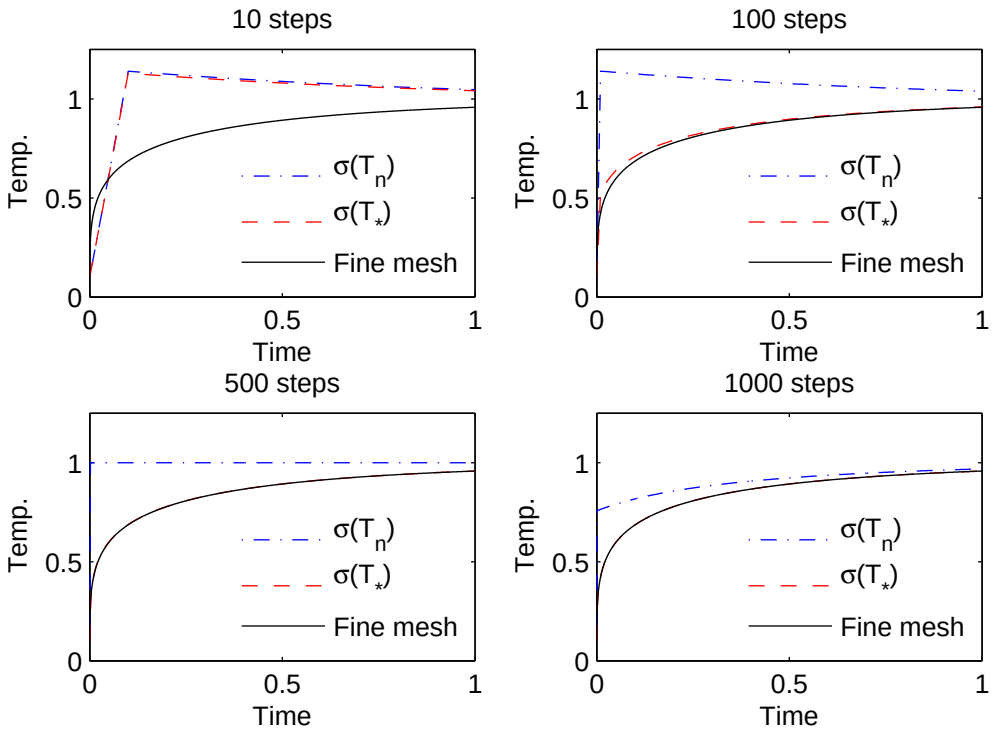

Figure 5.4: The time-dependent temperatures for IMC methods that that use data evaluated at T_n (blue) and at T_* (red) for 10, 100, 500, and 1000 time steps.

solutions of Eqs. (4.87) and a 0-D version of Eqs. (5.26); we did not use a Monte Carlo procedure.

Figure 5.4 depicts the time-dependent temperatures for the IMC-T_* and traditional IMC methods using a variable number of time steps. Iteration on the estimate of T_* was not considered. From Figure 5.4, we determine that if 10 time steps are used, then both solutions overshoot the equilibrium condition and then begin monotonic decay. If 100 time steps are used, then the IMC solution that uses data at T_n continues to overshoot the solution, but the IMC-T_* solution nicely approximates the fine-grid solution. Even if as many as 1000 steps are used, the traditional IMC solution continues to overshoot the equilibrium solution, while the IMC-T_* solution becomes indiscernible from the fine-grid solution. This overshooting in the traditional IMC equations is an undesirable characteristic that is discussed in [30], but the use of T_* appears to ameliorate this issue.

Next, we define the root mean square error of the time-dependent temperature

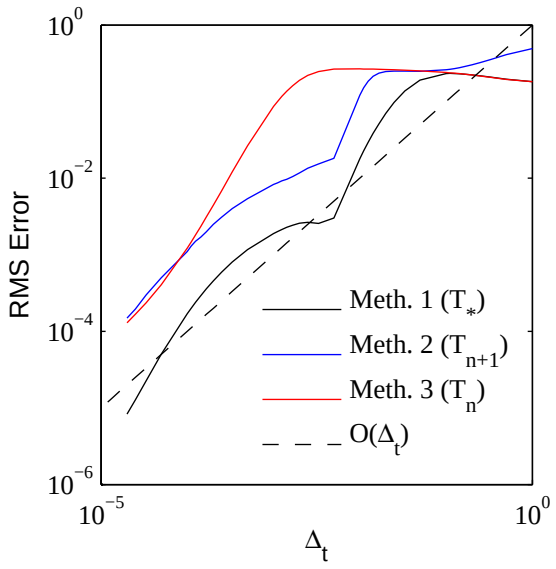

Figure 5.5: The numerically-calculated order of temporal error for the (1) IMC-T_*, (2) IMC-T_{n+1}, and (3) traditional IMC temperature solutions.

solutions by:

$$\text{RMS error} = \sqrt{\frac{1}{N}\sum_{n=1}^{N}\left(T_n - T_{\text{fine},n}\right)^2}\,, \tag{5.71}$$

where T_n is provided by an IMC calculation and $T_{\text{fine},n}$ is provided by an IMC calculation using an extremely fine grid[2].

In Figure 5.5, we plot the RMS error of the (1) IMC-T_*, (2) IMC-T_{n+1}, and (3) traditional IMC methods. From this figure, we determine that each method has (on average) $O(\Delta_t)$ accuracy, as expected. Also, the use of T_* to evaluate the problem data is *much* more accurate than the other methods for almost any time step value. For coarse time steps, all of the methods suffer from the overshooting issue. For the traditional IMC method, this overshooting tends to *increase* the RMS error as the number of time steps is increased to approximately 500; after this, further increases reduce the error. This behavior can be confirmed in Figure 5.4.

5.3.2 Gray Marshak Waves

In Chapter IV we considered a series of gray Marshak wave problems in order to test the predictive capability of the linear stability theory. For these problems, we

[2]For this problem, we used 10^7 time steps. To compare T_n and $T_{\text{fine},n}$, we interpolated on the values in $T_{\text{fine},n}$ when necessary. Further refinement of the fine-mesh does not affect the results presented here.

found that if sufficiently large time steps or sufficiently small spatial zones are used, then the temperature solution can violate the maximum principle. We also saw that when the maximum principle is violated [when the material temperature is greater than the boundary condition], the corresponding numerical wave speed is too slow.

In this section we revisit that gray Marshak wave problem, but here we evaluate the opacities using T_* and T_{n+1} generated from the new Quasidiffusion algorithm, with and without iteration. In each of these problem simulations, for the first time step, a fully diffusive calculation is used [$E = 1/3$]. Also, we note that it is not necessary to create special opacity tallies since the problem is gray; only the zone-averaged, instantaneous Eddington factors are tallied during the IMC calculation.

This problem is described by setting $q = 0.14$, $\sigma = T^{-3}$, and the initial temperature to 0.1. The specific heat is set to the constant value 7.14. We impose an isotropic right boundary condition equal to the initial temperature and an isotropic left boundary condition at a unit temperature. We consider a slab that is 4 cm wide. This implies that the slab is initially 4,000 mean free paths thick, but only 4 mean free paths thick once equilibrium is reached. We track the wavefront up to $\Delta_\tau = 40$ mean free times to emission. The spatial grid and time step sizes are varied, and each problem is solved using a Monte Carlo algorithm.

For convenience of comparisons, we briefly re-present the "traditional IMC" results that were provided in Chapter IV in Tables 5.1 and 5.2 and Figure 5.6. Table 5.1 provides the maximum temperatures of the Marshak wave over variable values of Δ_τ and Δ_x at the fixed time $\tau = 8$ mean free times for emission. From this table we concluded in Chapter IV that the IMC solution is sufficiently accurate roughly when Eq. (4.72) is satisfied, or when

$$\Delta_\tau \leq 5\Delta_x \,. \tag{5.72}$$

A similar conclusion may be found from Table 5.2, which depicts the estimated wave location over variable values of Δ_τ and Δ_x. For illustration purposes, the temperature profiles that correspond to the second column of Table 5.1 are graphically presented in Figure 5.6(a), and the third row is depicted in Figure 5.6(b). In each of these figures we can see the worsening violations of the maximum principle that result from increasing Δ_τ or decreasing Δ_x.

For our first test of the Quasidiffusion temperature estimation algorithm, we consider evaluating the opacities and β at temperature T_* defined in Eq. (5.31) (the IMC-T_* method) without the use of iterative refinement. Aside from this change, all other problem parameters are the same as before.

Table 5.1: Maximum temperatures in Marshak wave at $\tau = 8$ using "traditional" IMC. Bold values indicate violation of the maximum principle.

$\Delta_\tau \backslash \Delta_x$	0.025	0.05	0.1	0.2
0.10	0.953	0.951	0.947	0.937
0.25	**2.551**	0.949	0.946	0.939
0.50	**5.383**	**2.159**	0.946	0.938
1.00	**8.541**	**4.175**	**1.756**	0.937
2.00	**12.412**	**6.233**	**3.122**	**1.386**

Table 5.2: Estimated wavefront location at $\tau = 38$ using "traditional" IMC.

$\Delta_\tau \backslash \Delta_x$	0.025	0.05	0.1	0.2
0.10	3.688	3.675	3.75	3.7
0.25	3.438	3.675	3.65	3.7
0.50	1.887	3.425	3.65	3.7
1.00	0.938	1.875	3.35	3.5
2.00	0.463	0.925	1.85	3.3

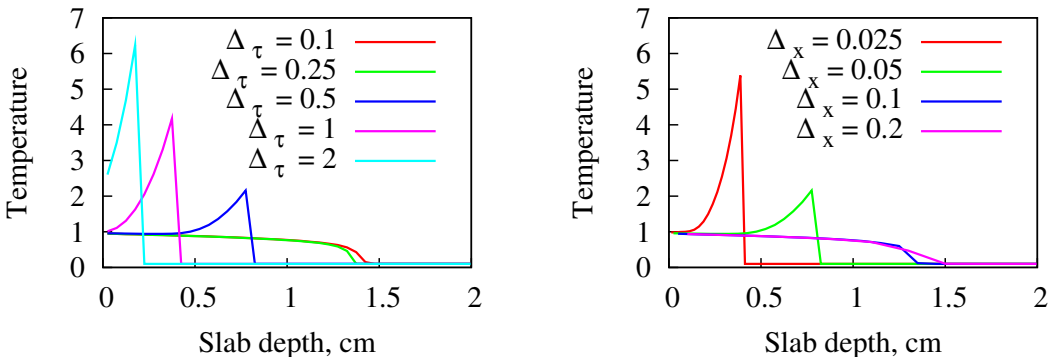

(a) Δ_x fixed at 0.05 cm.

(b) Δ_τ fixed at 0.5

Figure 5.6: Temperature profiles at $\tau = 8$ for a Marshak wave problem in which (a) the time step is varied and (b) the spatial grid size is varied using "traditional" IMC.

Figure 5.7 depicts the time-dependent temperature profiles produced by the IMC-T_* method (solid) and by the Quasidiffusion method (dashed) at four different time steps when $\Delta_x = 0.05$ cm and $\Delta_\tau = 1$ mean free time for emission. For instance, at $\tau = 10$, the red, dashed temperature profile is the estimate of T_{10} obtained by the Quasidiffusion calculation over $9 \leq \tau \leq 10$, whereas the red, solid profile is the IMC-T_* solution of T_{10} that is obtained with temperature-dependent problem data evaluated at T_* (generated from the Quasidiffusion calculation). The estimate produced by the deterministic Quasidiffusion method compares very well with the much more detailed IMC-T_* solution.

Additionally, from Table 5.1, we may safely say that $\Delta_x = 0.05$ cm and $\Delta_\tau = 1$ is a problematic choice of grid parameters; the maximum temperature obtained by the traditional IMC method is over 4 times the boundary temperature at $\tau = 8$. By contrast, in Figure 5.7, we see that the maximum temperature for the IMC-T_* method is below 1.25, and the maximum for the Quasidiffusion method is below 1.6. These values still violate the maximum principle, but to a lesser degree. Also, the wave locations appear to be reasonably accurate [compare with Figure 4.19]. These two metrics will be discussed in more depth shortly; the last characteristic we point out is the introduction of spatial oscillations behind the wavefront. As we shall further demonstrate, this appears to be the mechanism by which using T_* to evaluate the problem data can produce a much more accurate estimate of the wavefront location than the traditional use of T_n. We note that for less problematic grid choices (smaller Δ_τ and larger Δ_x), the spatial oscillations diminish, and the temperature profiles of the IMC-T_* and Quasidiffusion methods can become nearly identical.

From this point forward, all of the reported temperature values will refer to those produced by the Monte Carlo transport calculation, not the intermediate temperature produced by the Quasidiffusion calculation for data evaluation.

Table 5.3 depicts the maximum temperatures of the Marshak wave over variable values of Δ_τ and Δ_x for the IMC-T_* method without iteration. In this table we observe that (i) the number of entries for which the maximum principle is violated (in bold) has diminished and (ii) these entries are much less in magnitude then their corresponding values in Table 5.1, for which the problem data were evaluated at T_n. For instance, the worst violation in Table 5.1 is 12.4; this occurs for the largest time step and smallest spatial grid size. The corresponding entry in Table 5.3 is only 5.5, which is a 56% reduction.

Figure 5.8(a) depicts the temperature profiles at $\tau = 8$ for the second column of Table 5.3, for which Δ_x is fixed at 0.05 cm and Δ_τ is varied. There are two

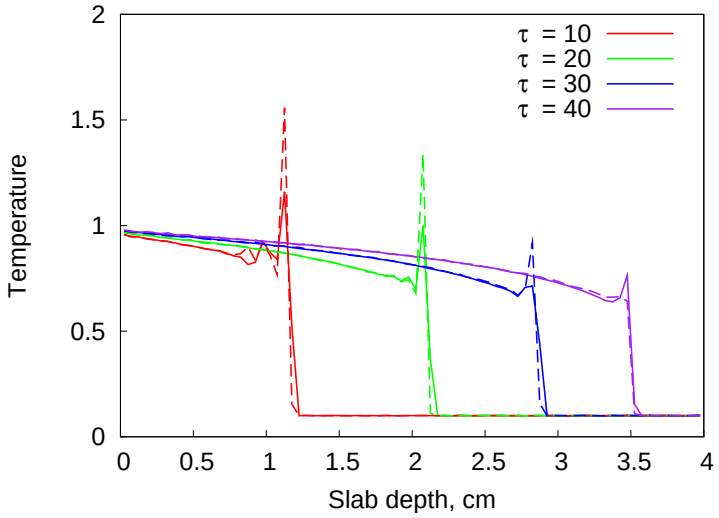

Figure 5.7: Time-dependent temperature profiles for a Marshak wave problem in which $\Delta_\tau = 1.0$ and $\Delta_x = 0.05$. Solid lines refer to the IMC-T_* solution, while dashed lines refer to the estimate produced by the Quasidiffusion method.

Table 5.3: Maximum values in temperature at $\tau = 8$ using the IMC-T_* method (without iteration). Bold values indicate violation of the maximum principle.

$\Delta_\tau \backslash \Delta_x$	0.025	0.05	0.1	0.2
0.10	0.953	0.951	0.945	0.937
0.25	0.953	0.949	0.947	0.938
0.50	**1.083**	0.949	0.944	0.937
1.00	**2.778**	**1.763**	**1.207**	0.936
2.00	**5.533**	**2.108**	**1.959**	**1.351**

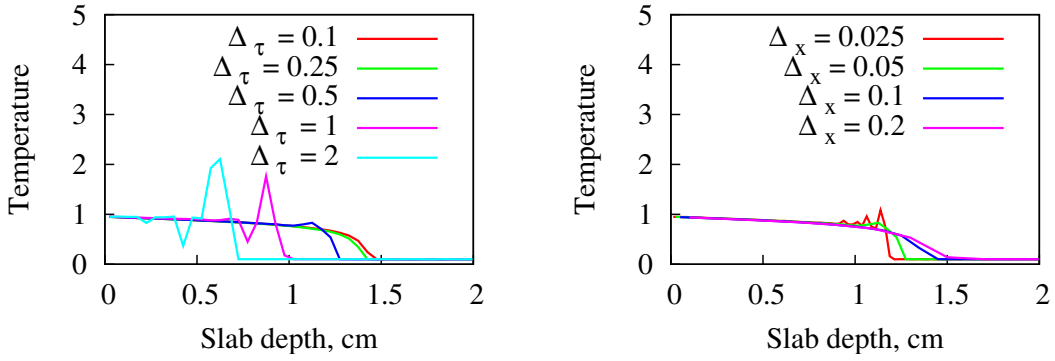

(a) Δ_x fixed at 0.05 cm.

(b) Δ_τ fixed at 0.5

Figure 5.8: Temperature profiles at $\tau = 8$ for a Marshak wave problem in which (a) the time step is varied and (b) the spatial grid size is varied for the IMC-T_* method (without iteration).

essential differences between this figure and Figure 5.6(a). The first is that when the maximum principle is violated, its magnitude is reduced, and it is followed by a spatial oscillation in the temperature *below* the boundary temperature. Instead of a single, large spike in the temperature at the wavefront, the use of T_* to evaluate the opacities appears to "smooth out" the peak at the expense of the introduction of a spatial oscillation whose magnitude increases with increasing Δ_τ. The second difference between the two figures is that even when the maximum principle is violated, the wave location is much more accurate.

Next we consider fixing Δ_τ and varying Δ_x. For the traditional IMC method, we observe from Table 5.1 that once the maximum principle is violated, the temperature essentially doubles when the spatial grid size is halved [trace along any of the bottom rows from right to left]. For the IMC-T_* temperature solutions, we see from Table 5.3 that this doubling no longer occurs; the spatial grid effect is weaker. Correspondingly, in Figure 5.8(b), the wave location remains fairly accurate over the entire range of Δ_x when Δ_τ is fixed. The wave locations in Figure 5.6(b) are much worse. From this we conclude that when T_* is used to evaluate the opacities, the violation of the maximum principle is much less sensitive to the spatial grid size than it is to the temporal grid size. This may be because the spatial oscillations in Figure 5.8(b) are more "spread out" and lower in magnitude since more spatial zones are available. In Table 5.4 we see how significant the use of T_* is for an estimate of the wavefront late in the calculation ($\tau = 38$). For instance, in the worst case of Table 5.2, the wavefront is estimated to be at location 0.463 cm. In Table 5.4, the corresponding entry is 2.388 cm, which is much closer to the correct value of 3.712 cm.

Table 5.4: Estimated wavefront location at $\tau = 38$ using the IMC-T_* method (without iteration)

$\Delta_\tau \backslash \Delta_x$	0.025	0.05	0.1	0.2
0.10	3.712	3.725	3.75	3.7
0.25	3.688	3.675	3.75	3.7
0.50	3.587	3.625	3.65	3.7
1.00	3.263	3.375	3.55	3.7
2.00	2.388	2.775	2.85	3.3

Table 5.5: Maximum values in temperature at $\tau = 8$ using opacities evaluated at T_* (with iteration). Bold values indicate violation of the maximum principle.

$\Delta_\tau \backslash \Delta_x$	0.025	0.05	0.1	0.2
0.10	0.951	0.949	0.944	0.937
0.25	0.950	0.948	0.947	0.938
0.50	**1.235**	0.951	0.944	0.936
1.00	**2.341**	**1.700**	**1.201**	0.936
2.00	**3.515**	**2.742**	**1.902**	**1.345**

So far, these results indicate that the use of T_* to evaluate the problem data can significantly improve the estimate of the wavefront location in Marshak wave problems, at the expense of introducing some spatial oscillation into the temperature profile. We next consider the effect of iteration in the Quasidiffusion algorithm.

Table 5.5 depicts the maximum temperatures of the Marshak wave over variable values of Δ_τ and Δ_x for an IMC-T_* method that uses iteration to improve the estimate of T_*. The overall effect of including iteration appears to be small – in some cases it reduces the maximum and in others it increases [compare Tables 5.3 and 5.5]. The difference between the estimated wave locations at $\tau = 38$ can be observed by comparing Tables 5.4 and 5.6. The inclusion of iteration changes only two values between these two tables; iteration improves their accuracy. In Figure 5.9(a), we see that varying the temporal grid does not affect the wavefront location at $\tau = 8$, but it does affect the maximum. The inclusion of iteration lessens the spatial oscillation effects, but the resulting maximum temperature can be slightly higher. The same behavior may be observed when one fixes the time step and varies the spatial grid size; this may be seen in Figure 5.9(b).

We conclude from these data that the use of iteration for this problem provides only marginal improvement for the temperature results. The spatial oscillations are slightly reduced, but this can be at the expense of a slightly higher maximum

Table 5.6: Estimated wavefront location at $\tau = 38$ using opacities evaluated at T_* (with iteration)

$\Delta_\tau \backslash \Delta_x$	0.025	0.05	0.1	0.2
0.10	3.712	3.725	3.75	3.7
0.25	3.688	3.675	3.75	3.7
0.50	3.587	3.625	3.65	3.7
1.00	3.263	3.375	3.55	3.7
2.00	2.487	2.775	2.95	3.3

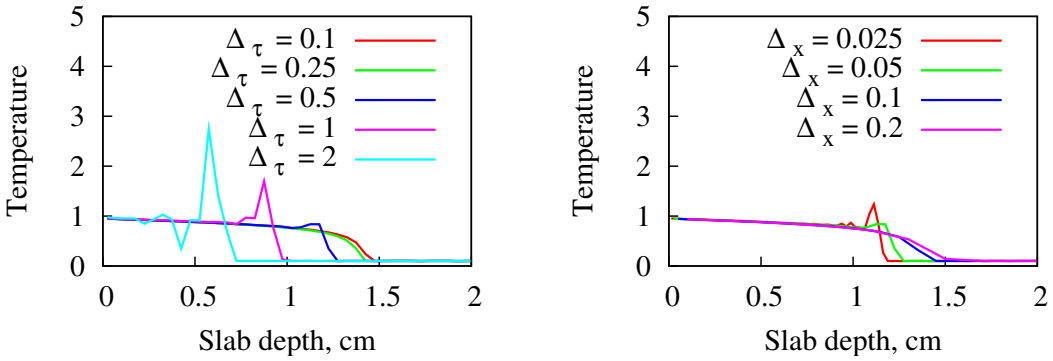

(a) Δ_x fixed at 0.05 cm.

(b) Δ_τ fixed at 0.5

Figure 5.9: Temperature profiles at $\tau = 8$ for a Marshak wave problem in which (a) the time step is varied and (b) the spatial grid size is varied with opacities evaluated at T_* (with iteration).

Table 5.7: Maximum values in temperature at $\tau = 8$ using opacities evaluated at T_{n+1} (without iteration). Bold values indicate violation of the maximum principle.

$\Delta_\tau \backslash \Delta_x$	0.025	0.05	0.1	0.2
0.10	0.949	0.951	0.944	0.937
0.25	0.951	0.950	0.946	0.936
0.50	**2.645**	0.946	0.943	0.936
1.00	**6.668**	**3.078**	0.973	0.934
2.00	**12.504**	**4.845**	**2.604**	**1.543**

temperature. However, the added computational cost of performing the iterations is essentially negligible compared to the cost of the IMC calculation, so we shall continue to use it for future problems.

Next, we consider the effects of evaluating the problem data (σ and β) at the "fully implicit" temperature T_{n+1}, without iteration. We do this because it is sometimes thought that treating everything as implicitly as possible is the most accurate and/or stable approach. Table 5.7 depicts the maximum temperatures of the Marshak wave obtained from the IMC-T_{n+1} method at $\tau = 8$ over variable temporal and spatial grid sizes. Comparing this table to 5.1, we see that almost the entire diagonal has become more accurate; these entries no longer violates the maximum principle. However, once the maximum principle *is* violated for the entries in Table 5.7, their magnitude is comparable to the entries in Table 5.1 [compare the worst cases: 12.412 vs. 12.504]. By contrast, in the IMC-T_* methods, the maximum temperatures are much less [see either of Tables 5.3 or 5.5].

Table 5.8 depicts the estimate of the wavefront location at $\tau = 38$ for the IMC-T_{n+1} method. These are also much more accurate than the traditional method of evaluating the problem data at T_n [compare with Table 5.2]. They are generally comparable to using T_* to evaluate the problem data. We note that for the borderline cases in which the use of T_n would begin to violate the maximum principle, the use of T_{n+1} is more accurate than T_* [compare the diagonals of Table 5.3 and Table 5.7]. However, for the more problematic choices of Δ_x and Δ_t in the lower left corner of the table, the use of T_{n+1} is less accurate than T_*, indicating that the IMC-T_{n+1} method degrades in accuracy more rapidly.

The nature of the degradation can be clearly seen in Figure 5.10(a) and Figure 5.10(b), in which the temperature profiles are shown at $\tau = 8$ for fixed Δ_x and a fixed Δ_τ, respectively. In these figures we observe that, although the wave locations

Table 5.8: Estimated wavefront location at $\tau = 38$ using opacities evaluated at T_{n+1} (without iteration)

$\Delta_\tau \backslash \Delta_x$	0.025	0.05	0.1	0.2
0.10	3.712	3.725	3.75	3.7
0.25	3.712	3.725	3.75	3.7
0.50	3.587	3.675	3.75	3.7
1.00	3.112	3.425	3.65	3.7
2.00	2.188	2.675	3.25	3.3

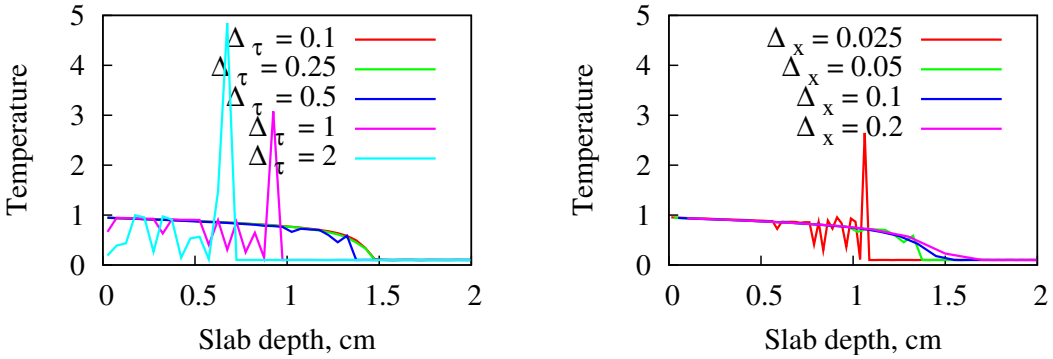

(a) Δ_x fixed at 0.05 cm.

(b) Δ_τ fixed at 0.5

Figure 5.10: Temperature profiles at $\tau = 8$ for a Marshak wave problem in which (a) the time step is varied and (b) the spatial grid size is varied with opacities evaluated at T_{n+1} (without iteration).

are much more accurate than using T_n, this can come at the expense of significant spatial oscillations for the problematic grid sizes.

From this we conclude that the IMC-T_{n+1} method is much more accurate than traditional IMC. It is also comparable to the IMC-T_* method in the following way. For borderline cases in which traditional IMC just violates the maximum principle, the IMC-T_{n+1} method is superior; it produces more accurate estimates of the wavefront without violating the maximum principle. However, for non-borderline cases, the IMC-T_{n+1} method produces a much larger temperature than the IMC-T_* method and introduces more significant spatial oscillations into the problem – the IMC-T_* method degrades more gradually.

For completeness, we also present results for the IMC-T_{n+1} method with iterative refinement in the deterministic Quasidiffusion algorithm. Table 5.9 depicts the maximum temperatures in the Marshak wave at $\tau = 8$. It is essentially comparable to Table 5.7, except that the values in the first column that violate the maximum principle have reduced in magnitude, while most of the other values have increased.

Table 5.9: Maximum values in temperature at $\tau = 8$ using opacities evaluated at T_{n+1} (with iteration). Bold values indicate violation of the maximum principle.

$\Delta_\tau \backslash \Delta_x$	0.025	0.05	0.1	0.2
0.10	0.954	0.952	0.946	0.938
0.25	0.950	0.948	0.946	0.937
0.50	**1.464**	0.948	0.943	0.937
1.00	**4.810**	**3.202**	**1.011**	0.934
2.00	**11.370**	**6.029**	**2.656**	**1.535**

Table 5.10: Estimated wavefront location at $\tau = 38$ using opacities evaluated at T_{n+1} (with iteration)

$\Delta_\tau \backslash \Delta_x$	0.025	0.05	0.1	0.2
0.10	3.712	3.725	3.75	3.9
0.25	3.712	3.725	3.75	3.7
0.50	3.612	3.675	3.75	3.7
1.00	3.138	3.375	3.65	3.7
2.00	2.188	2.625	3.25	3.3

Similar changes are seen in Table 5.10, the estimate of the wavefront location; two entries in the first column have become more accurate, and two in the second column are less accurate. There are also slight differences between Figures 5.10(a) and 5.11(a), for which the Marshak wave is depicted at $\tau = 8$ with variable Δ_τ with Δ_x held fixed. Primarily, the two worst cases in this figure have slightly slower wave speeds when iteration is employed. A greater difference occurs between Figures 5.10(b) and 5.11(b), for which the spatial grid size is varied. In these figures, the worst case [smallest Δ_x], has a lower maximum with more "spread out" spatial oscillations behind the wavefront. This indicates that the use of iteration for these problems improves their performance with respect to the reduction of the spatial grid size, although the improvement is not as good as was seen for the IMC-T_* method.

In this section we have seen that the IMC-T_* and IMC-T_{n+1} methods can produce much more accurate temperature profiles than the traditional IMC method. We also judge that the IMC-T_* method is the superior choice to IMC-T_{n+1} since IMC-T_* solutions degrade more gracefully for problematic spatial and temporal grid sizes. Both approaches can introduce spatial oscillations behind the Marshak wave, but these can become more severe when T_{n+1} is used. Finally, the use of iteration in the Quasidiffusion temperature estimation algorithm generally provides a marginal

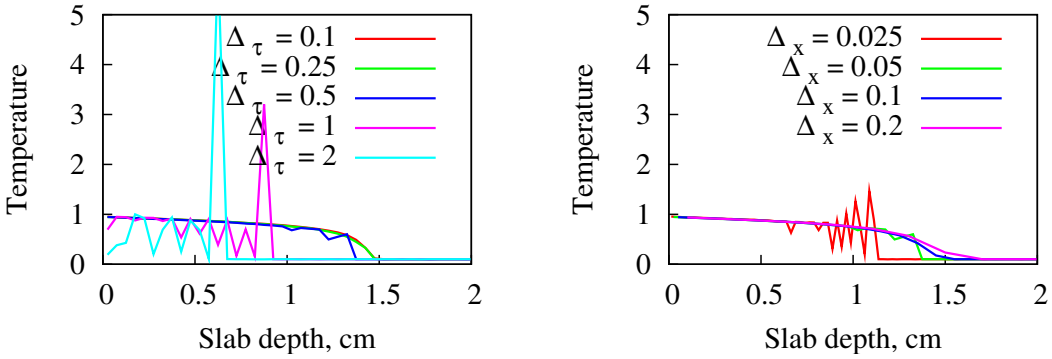

(a) Δ_x fixed at 0.05 cm.

(b) Δ_τ fixed at 0.5

Figure 5.11: Temperature profiles at $\tau = 8$ for a Marshak wave problem in which (a) the time step is varied and (b) the spatial grid size is varied with opacities evaluated at T_{n+1} (with iteration).

increase in problem accuracy.

Next, we consider a Marshak wave problem that incorporates frequency-dependence.

5.3.3 Frequency-dependent Marshak Waves

We next consider a frequency-dependent Marshak wave problem. Besides the inclusion of frequency dependence, this problem further departs from the gray Marshak wave problem in that we consider the original (unscaled) TRT equations. That is, for this problem, $c \approx 300$ cm/sh [recall 1 sh $= 10^{-8}$ s] and $a = 0.01372$ jk/cm^3-keV^4. By comparison, in the gray problem, we set $c = a = 1$.

The opacities and specific heat are chosen in an attempt to replicate a similarly-shaped Marshak wave as was observed for the gray Marshak wave problem. The initial condition is an equilibrium state with $T = 0.01$ keV. At $t = 0$, the left side of the slab is subjected to an isotropic burst of radiation maintained for $t > 0$ at temperature $T = 1$ keV. Because of this two order-of-magnitude difference in the boundary and initial temperatures, this may be expected to be a relatively difficult Marshak wave problem. The right boundary temperature is set to the constant, initial temperature. The slab size is 4 cm thick. The opacity coefficient [γ in Eq. (2.7)] is set to 200. The Planck mean opacity is therefore $30.8T^{-3}$ which means, at equilibrium ($T = 1$), the slab is 123.2 Planck mean free paths thick, whereas at the initial condition $T = 0.01$, it is 123.2 $\times 10^6$ Planck mean free paths thick. The specific heat is set to 0.1 jk/keV-cc. We consider temperature solutions up to 1 sh. In each of the below problems, the spatial grid size Δ_x is set to 0.2 cm.

These problems were computationally simulated by implementing a parallel Monte

Carlo algorithm on a homogeneous, distributed memory cluster of 3.4 GhZ machines, each with 2 Gigabytes of memory. The parallel implementation is necessary because of the memory requirements and/or long runtimes required to achieve acceptable statistics in frequency-dependent Marshak wave problems. The parallel message passing is handled through MPI [55], and random numbers are generated independently (but repeatably) on the different machines via the Scalable Parallel Random Number Generator (SPRNG) library [56]. Each of the frequency-dependent cases in this and the following chapters was performed by requesting 20 nodes of the 105-node `reserv` Linux cluster in the Nuclear Engineering division of Argonne National Laboratory. Only the Monte Carlo part of the algorithm is treated in parallel; all other tasks (input, output, and deterministic estimates) are replicated in serial on each processor. The Monte Carlo algorithm is not dynamically load-balanced as, by experiment, this was not found to be necessary if a sufficient number of particles are simulated during the time step. Each problem was simulated using 100,000 particles/jk. To estimate relative errors and calculate figures of merit, each problem was independently simulated 50 times; the relative errors were then calculated using the sample error. All timing results refer to the sums of the computational times (not wall-clock times) reported by each processor.

For the first case, we set Δ_t to 0.001 sh. Figure 5.12 depicts the IMC-T_* temperatures (solid) and the deterministically-calculated Quasidiffusion temperature solutions that supported the IMC-T_* calculation at times $t = 0.3$, 0.6, and 0.9 sh. Regarding the general shape of the Marshak wave, we observe that there are no violations of the maximum principle in either of the numerical solutions; the temperature wave simply forms and travels rightward. We remark that for this choice of grid parameters ($\Delta_t = 0.001$ and $\Delta_x = 0.2$ cm), the IMC and IMC-T_* methods produce essentially the same temperature profiles throughout the problem; in comparison plots (not provided), the two solutions were visually indistinguishable.

The more notable feature of Figure 5.12 is the "noise" in the Quasidiffusion solutions. Although the fundamental shapes of the Quasidiffusion temperature profiles are generally correct, there is some variation about the more accurate transport solution. Investigation has revealed that this noise is primarily due to the Monte Carlo estimator for σ_ρ. This estimator includes the factor $1/\sigma(\nu)$ [see Eq. (5.13)]; when a high-frequency particle contributes to the tally (corresponding to an exponentially small opacity), this factor can become very large. These relatively rare "spikes" in the tally can significantly increase the variance in the Monte Carlo estimator of σ_ρ, which introduces noise into the Quasidiffusion temperature estimate. It is possible to

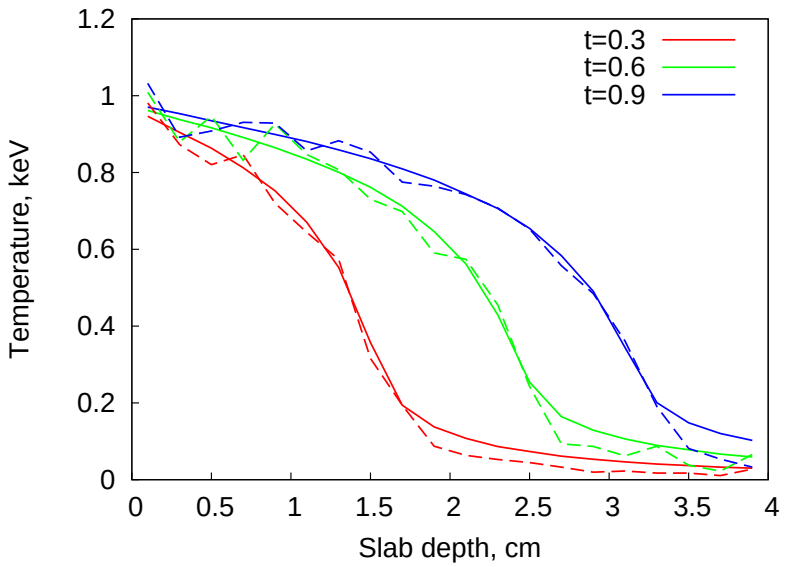

Figure 5.12: Temperature profiles at $t = 0.3$, 0.6 sh, and 0.9 sh for a frequency-dependent Marshak wave problem with $\Delta_t = 0.001$ sh. Solid lines refer to the IMC-T_* solution, while dashed lines refer to the deterministic Quasidiffusion estimate of the temperature that supported the IMC-T_* calculation for the same time step.

consider modifications to this tally that eliminate some of this noise at the possible expense of accuracy. For instance, we could consider "filtering" the high-frequency contributions from the denominator of the tally by using a cut-off frequency. This could be done using the following modification to the definition of σ_ρ:

$$\sigma'_\rho = \frac{\left\langle \frac{\sigma(\nu)}{\epsilon+\sigma(\nu)} \mu^2 I \right\rangle}{\left\langle \frac{\mu^2}{\epsilon+\sigma(\nu)} I \right\rangle}. \tag{5.73}$$

with ϵ set to be some small quantity. This has the following effect. When ν is small, $\sigma(\nu)$ is typically large. In this case, the numerator and denominator essentially reduce to the original form of σ_ρ seen in Eq. (5.13). When ν is large, $\sigma(\nu)$ can become exponentially small. When this occurs in the calculation, the numerator of this expression reduces to a small quantity since:

$$\frac{\sigma(\nu)}{\epsilon + \sigma(\nu)} \approx \frac{\sigma(\nu)}{\epsilon},$$

and the denominator can no longer become exponentially large; it is limited according

to:

$$\frac{1}{\epsilon + \sigma(\nu)} \approx \frac{1}{\epsilon}\,.$$

The magnitude of these rare spikes in the denominator of σ'_ρ is therefore limited to $1/\epsilon$ in this approach.

Alternatively, numerical tests have indicated that simply using σ_I in place of σ_ρ in the Quasidiffusion equations can produce reasonably accurate temperature solutions that do not contain as much noise. Such a replacement has a weak theoretical foundation, but it indicates that there is at least one way to reduce the noise in the Quasidiffusion solution observed in Figure 5.12.

Besides the noise in Figure 5.12, we also observe that the Quasidiffusion estimate of the temperature solution in the region ahead of the wavefront is somewhat poor. However, poor temperature estimates in the region ahead of the wavefront are acceptable so long as the numerical wave speed is not adversely affected (in this case, it is not). The degradation in accuracy in this region is likely because relatively few Monte Carlo particles are able to transport from the left boundary to the region ahead of the wavefront in order to contribute to the tallies. In our implementation of IMC-T_* method, there is a switch that replaces the tallied versions of σ_I and σ_ρ with analytically-calculated Planck (σ_p) and Rosseland (σ_r) means, respectively, whenever the number of particles that contribute to these tallies is below a certain threshold. We recall that when $I \approx B$, these limits should be reasonably accurate.

Despite the relative inaccuracy of the Quasidiffusion method in the region ahead of the wavefront and the noise in the temperature solution, the IMC and IMC-T_* methods are in excellent agreement. This implies that the IMC-T_* temperature solution is relatively insensitive to perturbations in the temperatures at which the problem data are evaluated – it is not necessary to achieve high accuracy in the deterministic calculation.

We next consider the differences in computational efficiency between the IMC-T_* and IMC methods, the first measure of which is the net CPU-time required to simulate the problem. For this problem, the IMC method required 74.4 CPU-hours and the IMC-T_* method required 97 hours, which is a 30% increase over the IMC method. We remark that the required time for the deterministic part of the total solution is essentially negligible (it takes few computational resources to perform forward and backward substitution for a tridiagonal matrix that is the size of the number of elements in the spatial grid), so the difference must be due to another effect – the Monte Carlo particle tracking. Before we investigate this further, we

first consider the differences between the IMC-T_* and IMC Figures of Merit (FOMs), which are a better indicator of the relative performance of Monte Carlo methods than the CPU-time. The FOM is defined by:

$$FOM(x,t) = \frac{1}{R(x,t)^2 t_{\text{cpu}}} \,. \tag{5.74}$$

Here, R is the relative error in the estimate of the solution at position x and time t, and t_{cpu} is the total calculation time required to generate the solution at time t. The FOM includes a combination of the relative error *and* the computational time because the desired properties of a highly efficient Monte Carlo method are small errors in relatively little time. In steady-state neutron transport problems, the relative error R in an estimate of the scalar intensity (scalar flux) is calculated "on the fly" using a single simulation. Since the problems we consider are time-dependent, a bias is introduced into the calculation that prevents the straightforward application of the neutron transport methodology to these problems. It may be possible to account for this bias, although we do not investigate that here. Instead, to calculate the relative error R in the FOM, we have performed 50 independent simulations of the entire problem, stored the results, and calculated the sample statistical error.

Figure 5.13 depicts a semilog plot of the temperature-FOMs for the IMC and IMC-T_* methods at $t = 0.9$ sh. This figure indicates that despite the 30% difference in the computational times, the overall differences in the FOMS are minor.

The relatively minor differences in the FOMs do not elucidate the discrepancy in the computation times for the IMC and IMC-T_* methods. To do this, we turn to the Monte Carlo particle collision density. To calculate the numerical Monte Carlo particle collision density, we increment a density tally by one – regardless of the particle's energy-weight – whenever it collides.

Figure 5.14 depicts a semilog plot of the Monte Carlo particle collision densities at $t = 0.9$ sh. The principal difference between the IMC and IMC-T_* method occurs at the leading edge of the wavefront, where the IMC-T_* method has a relatively larger number density. The increase in Monte Carlo collision densities for the IMC-T_* method for this region is due to differences in the temperatures at which the problem data are evaluated in this region between the IMC and IMC-T_* methods (even though the IMC and IMC-T_* temperature solutions are virtually indistinguishable, the deterministic Quasidiffusion temperature solution differs; see Figure 5.12). Specifically, the Quasidiffusion temperature solution in the region ahead of the wavefront is lower than the actual IMC temperature solution. Because T_* is lower, the

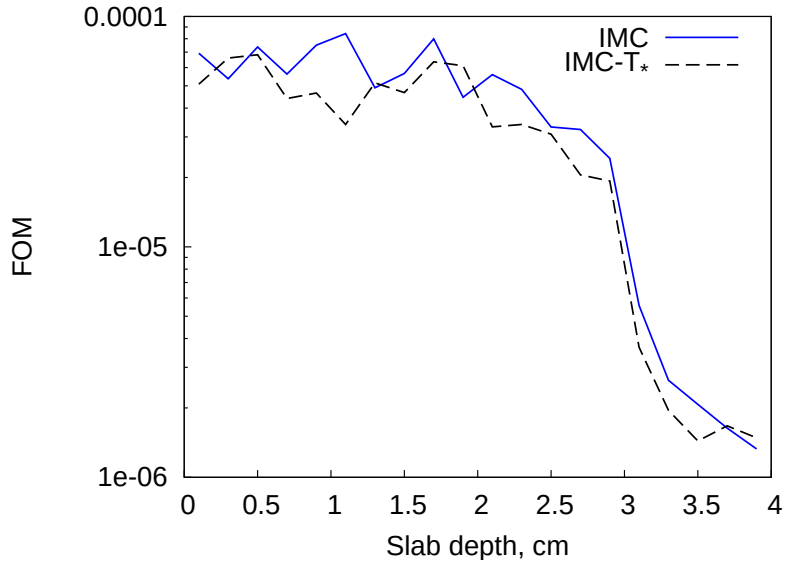

Figure 5.13: Temperature-FOMs for the IMC and IMC-T_* method at $t = 0.9$ sh for a frequency-dependent Marshak wave problem with $\Delta_t = 0.001$ sh.

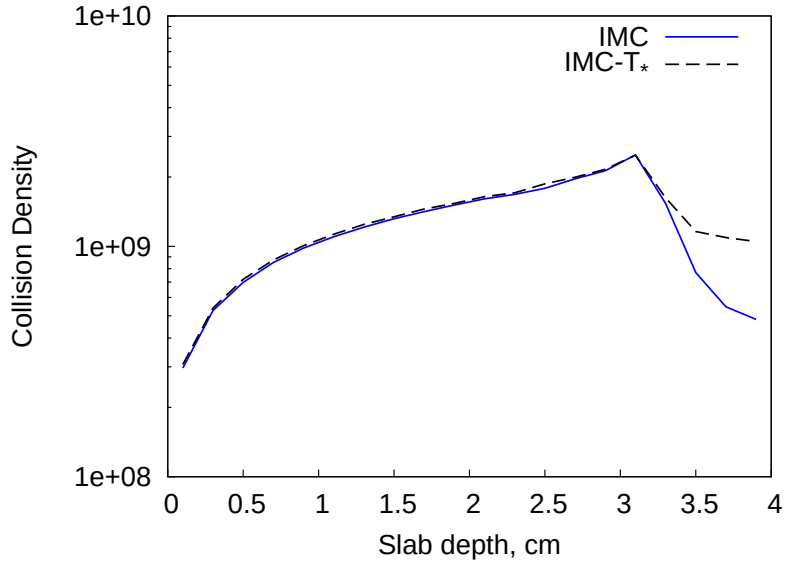

Figure 5.14: Monte Carlo particle collision densities for the IMC and IMC-T_* methods at $t = 0.9$ sh for a frequency-dependent Marshak wave problem with $\Delta_t = 0.001$ sh.

opacities appear more optically thick for this region in the IMC-T_* method than in the IMC method. This increases the number of collisions for an IMC-T_* particle in this region as compared to an IMC particle, as may be observed in Figure 5.14. Although this difference in opacity-evaluation temperatures does not substantially affect the final IMC-T_* temperature solution, it increases the time required to compute the IMC-T_* solution relative to the IMC solution. In Chapter VII we discuss a weight window technique that is based upon the scalar intensity solution generated by the deterministic Quasidiffusion calculation. There, we demonstrate that a simple modification to this weight window technique can suppress the Monte Carlo particle density and decrease the required calculation time by about an order of magnitude. The decrease in the Monte Carlo particle density in this region corresponds to a substantial decrease in the collision density. We also discuss other characteristics of the Monte Carlo particle density for the IMC calculation in much greater detail; the important characteristic here is the difference in collision densities in the region ahead of the wavefront.

We also consider a more difficult variation of the above frequency-dependent Marshak wave problem by setting $\Delta_t = 0.02$ sh: an increase of Δ_t by a factor of 20. The larger time step is more difficult from a numerical perspective in that fewer particles will reach the census, which implies that there will be fewer contributions to the "snapshot" tallies of the intensity, Eddington factor E, and average opacities σ_I and σ_ρ. In Figure 5.15, the IMC-T_* (solid) and the deterministically-calculated Quasidiffusion temperature solutions (dashed) that supported the IMC-T_* calculation at times $t = 0.3$, 0.6, and 0.9 sh. The traditional IMC temperatures are not explicitly provided in Figure 5.15, but we remark that the IMC and IMC-T_* temperature solutions are virtually indistinguishable.

In Figure 5.15, the IMC-T_* temperature solutions do not violate the maximum principle, despite the 20-fold increase in the time step size. The essential feature in Figure 5.15 is again the noise in the Quasidiffusion temperature solution; here, it is larger than that seen in Figure 5.12, for which $\Delta_t = 0.001$. This indicates that for longer time steps, it may be advisable to tally the factors required by the Quasidiffusion calculation throughout the time step rather than only at the census. A combination of the time-average and snapshot tallies might also be considered, with their relative contributions weighted by the inverse of their statistical sample error.

The required time for the IMC and IMC-T_* methods for this problem was 59.4 CPU-hours and 73.7 hours respectively; the IMC-T_* method requires 24% more time.

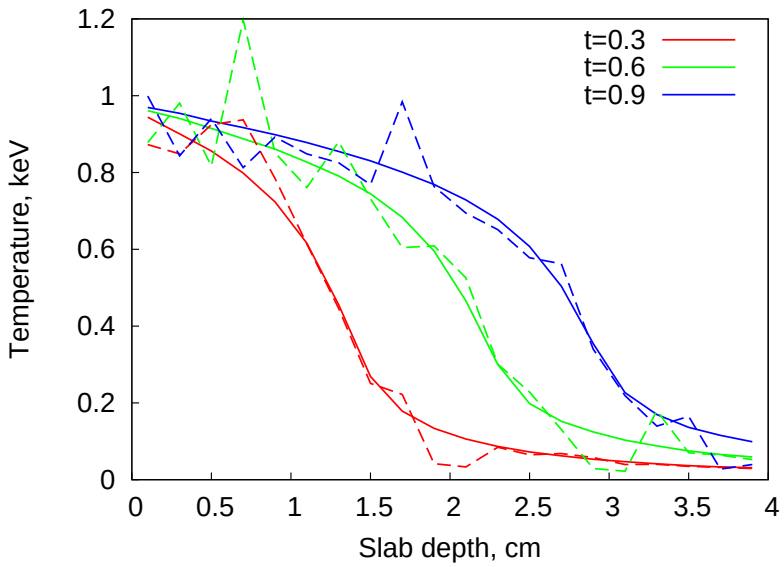

Figure 5.15: Temperature profiles at $t = 0.3$, 0.6 sh, and 0.9 sh for a frequency-dependent Marshak wave problem with $\Delta_t = 0.02$ sh. Solid lines refer to the IMC-T_* solution, while dashed lines refer to the deterministic Quasidiffusion estimate of the temperature that supported the IMC-T_* calculation for the same time step.

This discrepancy is due to the same reasons as were discussed above for a time step size of $\Delta_t = 0.001$ sh. We report that the FOMs for the IMC and IMC-T_* methods were again comparable, and that the CPU-time discrepancy is again due to an increase in the Monte Carlo particle collision density in the region ahead of the wavefront.

Due to time and resource constraints, it was not possible to consider further frequency-dependent problems. As future work, further studies of the temporal and spatial grid sizes should be performed. Specifically, we would like to verify that the IMC-T_* solution can produce more accurate answers than the IMC method when the grid sizes are chosen such that the IMC method violates the maximum principle in frequency-dependent problems. We would also like to investigate alternative ways to suppress the noise in the estimate of σ_ρ.

5.4 Summary

In this chapter we have presented a new method to estimate the end-of-time-step temperature T_{n+1}. We motivated its use by describing how, historically, Monte Carlo methods have essentially been limited to using data evaluated at the known beginning

of the time step temperature T_n. This introduces an unavoidable $O(\Delta_t)$ error into the calculations. By contrast, deterministic methods frequently incorporate iteration to estimate the temperature at which the normalized Planckian is evaluated.

Beginning from the 1-D, frequency-dependent form of the TRT equations, we derived new deterministic, gray, Quasidiffusion equations. In these equations we defined a new frequency-averaged Eddington factor E, and two new angle- and frequency-averaged opacities, σ_I and σ_ρ. These opacities limit to the Planck and Rosseland means respectively when the intensity I limits to the Planckian B. The gray Quasidiffusion equations are *much* easier to to solve than the original, frequency-dependent transport equation, and they should remain reasonably accurate since they exploit data generated from the transport solution during the previous time step. We then applied temporal and a finite-volume based deterministic scheme to solve them, with or without iteration on the temperature-dependent problem data. We also derived a time-average temperature T_* in Eq. (5.31).

This deterministic, Quasidiffusion method is intended to be used in tandem with a higher-order transport calculation in the following manner. During a time step $t_{n-1} \leq t \leq t_n$, a frequency-dependent transport calculation such as IMC is carried out. Throughout the calculation, the quantities E, σ_I, and σ_ρ are tallied. These data are then provided to the new Quasidiffusion method, which uses them to estimate the temperature solution over the upcoming time step $t_n \leq t \leq t_{n+1}$. The average temperature T_* is generated and passed to the frequency-dependent transport algorithm, which then uses it to evaluate the temperature-dependent problem data. The transport algorithm then produces solutions over the same time step $t_n \leq t \leq t_{n+1}$ using the more accurate problem data; these solutions supersede the Quasidiffusion solutions.

We also developed an iteration scheme for the Quasidiffusion equations under the assumption that σ_I and σ_ρ have T^{-3} proportionality. This iteration scheme is intended to further improve the estimate of T_*, but is not a fundamental feature of the temperature estimation method.

We derived positivity conditions on the temperature update equation for the method. We found that when iteration is used, there is an upper limit on the cooling rate to ensure positivity [see Eq. (5.41)]. The same limit exists for the IMC equations with $\alpha = 1$, and it was commented that one cannot use arbitrary temperatures to evaluate the temperature-dependent data in an IMC calculation. We noted that if the temperature estimation method indicates that the temperature decreases more rapidly than the numerically allowed limit, this is a strong indication that the desired

time step size is too large. We then motivated the use of the deterministic Quasidiffusion equation as an adaptive technique to limit the maximum time step size in a transport calculation.

We analyzed the stability characteristics of a dimensionless form of the 0-D, gray Quasidiffusion equations. These equations are unconditionally stable and should only exhibit monotonic convergence. This is likely because the time-discretization incorporated a fully-implicit treatment of the problem unknowns.

We numerically tested the temperature estimation algorithm on a gray, 0-D, nonlinear problem to estimate its order of accuracy. In this problem, the initial temperature is below the equilibrium temperature of 1, and the initial scalar intensity is above its equilibrium value. For sufficiently small time steps, we demonstrated how the IMC solution initially overshoots the equilibrium temperature. However, if IMC is used with its data evaluated at T_* (generated from the deterministic Quasidiffusion algorithm), then the overshooting is remedied much more rapidly when the time step size is reduced. This translates into an (on-average) $O(\Delta_t)$ methodology that is much more accurate than the traditional approach.

We numerically tested the temperature estimation algorithm on a gray Marshak wave problem. For these problems, we demonstrated that numerical complications arise in the traditional IMC procedure when the time step is sufficiently large or when the spatial grid size is sufficiently small. These complications are well-described by the maximum of the temperature wave, which can be larger than the boundary condition (indicating a violation of the maximum principle), and a correspondingly slow numerical wave speed. For these problems, we examined the temperature solutions generated by an IMC procedure using data evaluated at T_n, T_* without iteration, T_* with iteration, T_{n+1} without iteration, and T_{n+1} with iteration [we considered using T_{n+1} since it is sometimes thought that the most implicit treatment of the problem data should be superior]. In general, we found that the traditional approach of using T_n to evaluate the temperature data produces the worst violations of the maximum principle and slowest numerical wave speeds. Using T_* or T_{n+1} to evaluate the temperature-dependent problem data (i) lessens the violation of the maximum principle at the expense of introducing relatively small spatial oscillations behind the temperature wave, and (ii) significantly improves the accuracy of the wavefront location. Of these two approaches, we concluded that T_* is superior, since the magnitude of the spatial oscillations is less sensitive to the spatial and temporal grid size, even though using T_{n+1} is slightly more accurate in borderline values of the grid sizes. We also found that the use of iteration tends to marginally improve the temperature

estimation method at little cost relative to the IMC calculation.

We also numerically tested the temperature estimation method on a frequency-dependent Marshak wave problem in which the boundary and initial temperatures differ by two orders of magnitude. For each of the time step sizes we considered, the IMC and IMC-T_* temperature solutions were in good agreement. In no case did the traditional IMC method violate the maximum principle, so it was not possible to directly test the hypothesis (verified for gray Marshak wave problems) that the IMC-T_* method should ameliorate those effects. We observed that the most straightforward Monte Carlo estimator of σ_ρ can introduce noise in the Quasidiffusion temperature solution, and that the Quasidiffusion temperature can be inaccurate in regions ahead of the wavefront. However, this did not translate into inaccuracies in the IMC-T_* temperature solutions. As future work, alternate tally schemes for the frequency- and angle-averaged opacities should be considered that reduce the variance in σ_ρ. These could include "filtering" the high frequency data from the denominator of the estimator for σ_ρ and/or combining time-average and snapshot tallies using a weighting procedure that incorporates their statistical errors. Alternatively, one might consider performing more than one deterministic calculation per Monte Carlo time step if the time step is so long that the census may be expected to be relatively empty. We also observed the IMC-T_* calculation can take up to 30% longer than the corresponding IMC calculation, although this did not have a significant impact on the temperature-FOM. The reason for this discrepancy is due to an increase in the Monte Carlo particle collision density in the region just ahead of the wavefront for the IMC-T_* method relative to the IMC method. We note that in Chapter VII, we discuss a weight window technique that is based upon the deterministic Quasidiffusion method presented here that more than makes up for this discrepancy in the CPU-times.

One of the limitations of the method considered in this chapter is that we did not define different average temperatures for the temperature-dependent problem data; we used the same average temperature to evaluate *all* of the problem data in the IMC calculation [σ, β, and $b(\nu, T)$]. Since β and b differ from σ in their temperature-dependence, it would be beneficial to investigate the introduction of separately defined average temperatures for these data. Alternatively, one could consider evaluating these data with a time-dependent temperature that is continuous throughout the time step. For example, the temperature could be based upon a linear fit of T_n and the deterministically-estimated value of T_{n+1}. Additionally, the Quasidiffusion equations we derived are not flux-limited. It may be possible to

derive equations that are flux-limited, or to derive an appropriate flux-limiter. Finally, the Quasidiffusion equations were derived and tested only for 1-D problems, although generalization to 2- or 3-D problems should be straightforward. Each of these limitations are areas for future work, yet none of them should be overly difficult.

We did not investigate the the estimate of T_{n+1} as a means to limit or adaptively estimate the size of the time step. We also did not test the Quasidiffusion method in conjunction with a higher-order deterministic transport method, where it might be used to accelerate the convergence of the temperature or to improve accuracy. Each of these scenarios are relatively straightforward applications of the method derived in this chapter, but are also left to future work.

In conclusion, the deterministic Quasidiffusion method presented in this chapter is a promising first step. The gray numerical results obtained by using T_* to evaluate the temperature-dependent data in IMC indicate a marked improvement over traditional IMC, and there are several reasons suggesting that further improvement could be obtained. Application of the method to deterministic transport and as an adaptive means of time-step selection may produce further advances.

Chapter VI

A Time-Dependent Fleck Factor

In previous chapters we asserted that the most dubious approximation that takes place during the derivation of the IMC equations occurs when the time-average unknowns $\overline{U_r}$ and $\overline{I}$ are replaced by their "instantaneous" counterparts $U_r(t)$ and $I(t)$ [see Eqs. (3.16) or (4.21)]. The resulting expression for $U_r(t)$ is only correct in a time-average sense; in particular, it is not exact at the beginning of the time step $t = t_n$. In this chapter, we replace this step by a different, more accurate approximation that preserves the character of the IMC equations at the minor expense of adding a new, *time-dependent* Fleck factor. We refer to this as the IMC-TDF approach (Implicit Monte Carlo with a Time-Dependent Fleck factor). This approach also avoids the introduction of the user-defined parameter α.

Historically, most enhancements to the IMC method have focused on reducing its computational effort. Fleck and Canfield proposed a modification of the Monte Carlo transport process in the optically thick problem regions that emerge when large time steps are used [25]. This modification may be computationally employed for any particle in any region of the problem, provided that certain criteria are met concerning the size of a spatial zone and the expected number of collisions that must occur for the particle to exit the zone. When these criteria are satisfied, this method essentially replaces a transport random walk in these regions – under which a great many collisions take place – with a diffusion random walk, which requires fewer collisions and corresponding computational resources. A related modification was proposed by Densmore et. al., in which optically-thick problem regions are selected before the calculation is begun [26]. Instead of employing a particle-based diffusive random walk in these regions, a Monte Carlo interpretation of the discrete diffusion equation is provided for them. Thus, the problem is decomposed into discrete diffusion and transport regions, and particles are transported according to the diffusive

physics presented in [26] or the usual IMC physics presented in Chapter III depending on their location, with interface conditions also given in [26]. Both of these methods have been demonstrated to substantially decrease the computation time and/or memory requirements of IMC problems at little expense to accuracy, provided that the parameters that "turn on" these modifications are properly chosen. Also, Gentile has proposed the more involved modification of applying an IMC methodology to an equation for the difference between the radiation intensity and its equilibrium solution, which is termed the difference formulation [57]. This method is advantageous when the problem contains regions that are near equilibrium, as it does not "waste" computational effort by reproducing the equilibrium solution in those regions. It should also introduce none of the "extra" approximations with regard to the above methods that exploit some form of diffusion theory. However, Smedley-Stevenson has found that the difference formulation may be fundamentally incompatible with traditional IMC because of the statistical noise that can be introduced from negative particle weights [58]. Another commonly-employed modification is to "comb" the census particles at the end of the time step in order to limit their population [59]. This technique essentially removes some of the census particles at random and reallocates the energy-weights to the surviving particles. The net computational effect is that fewer particles are followed during the subsequent time step, which reduces the computational time and memory requirements.

The approach taken in this chapter departs from these earlier attempts to improve the IMC method in that it focuses primarily on improving the *accuracy* of the IMC equations instead of enhancing its computational efficiency. This new approach may likely be used in tandem with several of the above approaches, although we do not investigate that here. Alternatively, one could abandon the IMC equations altogether and use other proposed linearizations of the TRT equations (see, for instance, [23], [22], and [24]). However, our intent is to retain the fundamental form of the IMC equations in order to keep the required modifications to existing computational algorithms as simple as possible. We consider the 1-D form of the nonlinear, frequency-dependent TRT equations, but extension to the full 3-D problem would be trivial.

We begin by deriving the IMC-TDF equations, which we argue are a more accurate approximation than that made in by Fleck and Cummings in [21]. The IMC-TDF equations contain no user-defined parameters. We then show that for small time steps, the time-average of the time-dependent Fleck factor limits to the traditional Fleck factor with $\alpha = 0.5$, and for large time steps the average time-dependent Fleck

factor limits to the traditional Fleck factor with $\alpha = 1$. Thus, an implementation of the time-average of the time-dependent Fleck factor (which we discuss, but do not numerically test) can be interpreted as an adaptive choice of α. We show that the differences between the computational implementation of the IMC and the IMC-TDF equations are relatively minor. However, these minor implementation differences lead to increased computational costs relative to a traditional IMC calculation.

We analyze the IMC-TDF equations using the 0-D stability analysis presented in Chapter IV of this thesis to show that the IMC-TDF and traditional IMC equations have similar stability properties, and we derive the monotonicity conditions for the IMC-TDF equations. We show that an alternative form of the time-dependent Fleck factor can surprisingly lead to only a conditionally stable system.

We numerically test the IMC-TDF equations by using two gray, 0-D problems to assess its order of accuracy. These tests verify that the IMC-TDF equations are more accurate than the traditional IMC equations. For a linear problem, we demonstrate that the IMC-TDF equations are second-order accurate in Δ_t. For a nonlinear problem, the equations remain first-order accurate (as they must). Additionally, we demonstrate that solving the IMC-TDF equations using the temperature estimation algorithm presented in Chapter V provides significant gains in accuracy.

We also test the system on a series of gray Marshak wave problems, and we demonstrate that the IMC-TDF equations produce solutions that do not violate the maximum principle to the same extent that the traditional IMC equations do for equivalent choices of spatial and temporal grids. We show that for sufficiently small time steps, the relative costs of the IMC and IMC-TDF solutions are comparable. For larger time steps, the cost of the IMC-TDF equations can become prohibitive relative to the IMC equations. Similar effects are observed for a smaller set of frequency-dependent Marshak wave problems. We propose a simple modification the IMC-TDF equations to remedy their increased cost for large time steps relative to the IMC method.

In addition to differences in the total computation time, we also discuss the differences in efficiency between using a time-dependent or traditionally-defined Fleck factor. Because the IMC-TDF equations introduce additional computations during the calculation, they take longer to compute. We compare the efficiency of the IMC and IMC-TDF by comparing the differences in CPU times t_{cpu}, and by using the Figure of Merit (FOM), where

$$FOM(x,t) = \frac{1}{R(x,t)^2 t_{\text{cpu}}}\,. \tag{6.1}$$

Here, R is the relative error in the estimate of the solution at position x and time t, and t_{cpu} is the total calculation time required to generate the solution at time t. The FOM includes a combination of the relative error *and* the computational time because the desired properties of a highly efficient Monte Carlo method are small errors in relatively little time. Thus, Monte Carlo methods that consistently produce relatively large FOMs are superior. In numerical tests, we demonstrate that the temperature-FOMs for the IMC-TDF method are comparable to the IMC method unless large time steps are employed, in which case the IMC method can become superior. Again, the simple modification to the IMC-TDF equations that we suggest should reconcile the decrease in efficiency for large time steps.

We also note that the IMC-TDF equations should not be expected to affect the statistical variance (and relative statistical errors) of the Monte Carlo process; the IMC-TDF equations are designed only to improve the accuracy of the mean solution. Later, we confirm this by using FOM and CPU-time comparisons between the IMC and IMC-TDF methods.

6.1 IMC Equations with a Time-Dependent Fleck Factor

We begin from the 1-D, nonlinear, frequency-dependent TRT equations. The radiation intensity equation is:

$$\frac{1}{c}\frac{\partial I}{\partial t} + \mu\frac{\partial I}{\partial x} + \sigma_a I = \frac{1}{2}\sigma_a bcU_r + \frac{Q}{2}\,, \tag{6.2a}$$

with the radiation energy density equation:

$$\frac{1}{\beta}\frac{\partial U_r}{\partial t} + \sigma_p cU_r = \iint \sigma_a I \; d\mu' d\nu'\,, \tag{6.2b}$$

or the (equivalent) material energy density equation:

$$\frac{\partial U_m}{\partial t} + \sigma_p cU_r = \iint \sigma_a I \; d\mu' d\nu'\,. \tag{6.2c}$$

The quantities $b(\nu)$ and β were previously defined in Eqs. (3.2a) and (3.2b), and the double integral integrates over all frequencies and angles.

The first step is identical to the presented in Chapter III for the traditional IMC method. We "freeze" the opacities and β at the initial time t_n, which destroys the equivalency of Eqs. (6.2b) and (6.2c). We remark that one may also choose to use

the temperature T_* suggested in Chapter V of this thesis. This produces the system:

$$\frac{1}{c}\frac{\partial I}{\partial t} + \mu\frac{\partial I}{\partial x} + \sigma_{a,n} I = \frac{1}{2}\sigma_{a,n} bc U_r + \frac{Q}{2}\,, \tag{6.3a}$$

$$\frac{1}{\beta_n}\frac{\partial U_r}{\partial t} + \sigma_{p,n} c U_r = \iint \sigma_{a,n} I \; d\mu' d\nu'\,, \tag{6.3b}$$

$$\frac{\partial U_m}{\partial t} + \sigma_{p,n} c U_r = \iint \sigma_{a,n} I \; d\mu' d\nu'\,. \tag{6.3c}$$

Here, we depart from the Fleck and Cummings approach, which is to introduce the user-defined parameter α. Instead, we solve Eq. (6.3b) for $U_r(t)$ by using an integrating factor:

$$\frac{\partial}{\partial t} U_r(t) e^{\beta_n \sigma_{p,n} c(t-t_n)} = e^{\beta_n \sigma_{p,n} c(t-t_n)} \beta_n \iint \sigma_{a,n} I(t) \; d\mu' d\nu'\,,$$

$$U_r(t) e^{\beta_n \sigma_{p,n} c(t-t_n)} - U_{r,n} = \int_{t_n}^{t} e^{\beta_n \sigma_{p,n} c(t'-t_n)} \beta_n \iint \sigma_{a,n} I(t') \; d\mu' \, d\nu' \, dt'\,.$$

So far, this expression contains no additional approximations[1]. Here we approximate the time integral by treating the unknown intensity "implicitly":

$$\begin{aligned} U_r(t) e^{\beta_n \sigma_{p,n} c(t-t_n)} &\approx U_{r,n} + \int_{t_n}^{t} e^{\beta_n \sigma_{p,n} c(t'-t_n)} \beta_n \iint \sigma_{a,n} I(t) \; d\mu' \, d\nu' \, dt'\,, \\ &= U_{r,n} + \frac{1}{\sigma_{p,n} c}\left(e^{\beta_n \sigma_{p,n} c(t'-t_n)} - 1\right) \iint \sigma_{a,n} I(t) \; d\mu' \, d\nu'\,. \end{aligned}$$

Solving for $U_r(t)$, we obtain:

$$U_r(t) = U_{r,n} e^{-\beta_n \sigma_{p,n} c(t-t_n)} + \frac{1}{\sigma_{p,n} c}\left(1 - e^{-\beta_n \sigma_{p,n} c(t'-t_n)}\right) \iint \sigma_{a,n} I(t) \; d\mu' \, d\nu'\,. \tag{6.4}$$

Next, we define a new time-dependent Fleck factor $f_n(t)$ as:

$$f_n(t) = e^{-\beta_n \sigma_{p,n} c(t-t_n)}\,, \tag{6.5}$$

and we rewrite Eq. (6.4) using Eq. (6.5) as:

$$U_r(t) = U_{r,n} f_n(t) + \frac{1 - f_n(t)}{\sigma_{p,n} c} \iint \sigma_{a,n} I(t) \; d\mu' \, d\nu'\,. \tag{6.6}$$

Eq. (6.6) has the same form as the approximation used in the derivation of the IMC

[1] This is actually the final form employed in the Carter-Forest method [23].

equations [see Eq. (3.16)], but the Fleck factor in Eq. (6.6) is time-dependent. Additionally, Eq. (6.6) should be more accurate – it is exact at $t = t_n$, whereas Eq. (3.16) is not. This and other ramifications of the introduction of Eq. (6.5) will be discussed further; for now, we continue by introducing Eq. (6.6) into Eqs. (6.3a) and (6.3c). Substitution into Eq. (6.3a) yields:

$$\frac{1}{c}\frac{\partial I}{\partial t} + \mu\frac{\partial I}{\partial x} + \sigma_{a,n} I = \frac{1}{2}\sigma_{a,n} bc \left(U_{r,n} f_n(t) + \frac{1 - f_n(t)}{\sigma_{p,n} c} \iint \sigma_{a,n} I(t)\, d\mu'\, d\nu' \right) + \frac{Q}{2}\,. \tag{6.7}$$

Next, we define time-dependent versions of the effective absorption and scattering opacities [see Eqs. (3.18)]:

$$\sigma_{ea,n}(t) = f_n(t)\sigma_{a,n}\,, \tag{6.8a}$$

$$\sigma_{es,n}(t) = [1 - f_n(t)]\sigma_{a,n}\,. \tag{6.8b}$$

We remark that the effective scattering ratio $1-f_n(t)$ is still independent of frequency, but is now time-dependent, and that we also still have

$$\sigma_{a,n} = \sigma_{es,n}(t) + \sigma_{ea,n}(t)\,. \tag{6.9}$$

Introducing Eqs. (6.8) and the frequency spectrum $\chi_n(\nu)$ defined in Eq. (3.19a) into Eq. (6.7), we obtain an IMC radiation equation with a time-dependent Fleck factor [the first of the IMC-TDF equations]:

$$\frac{1}{c}\frac{\partial I}{\partial t} + \mu\frac{\partial I}{\partial x} + \sigma_{a,n} I = \frac{1}{2}\sigma_{ea,n}(t) b_n c U_{r,n} + \frac{1}{2}\chi_n \iint \sigma_{es,n}(t) I\, d\mu' d\nu' + \frac{Q}{2}\,. \tag{6.10}$$

Next we introduce the same approximations into Eq. (6.3c) to obtain the following equation for $U_{m,n+1}$:

$$\frac{\partial U_m}{\partial t} + f_n(t)\sigma_{p,n} c U_{r,n} = f_n(t) \iint \sigma_{a,n} I(t)\, d\mu' d\nu'\,. \tag{6.11}$$

Eq. (6.11) may then be integrated over the time step defined by $t_n \le t \le t_{n+1}$ with $\Delta_{t,n} = t_{n+1} - t_n$ to obtain the update equation for the material energy density [the second of the IMC-TDF equations]:

$$U_{m,n+1} - U_{m,n} + \sigma_{p,n} c U_{r,n} \int_{t_n}^{t_{n+1}} f_n(t) = \int_{t_n}^{t_{n+1}} \iint f_n(t)\sigma_{a,n} I(t)\, d\mu' d\nu' dt\,,$$

$$U_{m,n+1} = U_{m,n} - \frac{U_{r,n}}{\beta_n}\left(1 - e^{-\sigma_{p,n}\beta_n c\Delta_{t,n}}\right) + \int_{t_n}^{t_{n+1}} \iint f_n(t)\sigma_{a,n} I(t)\, d\mu' d\nu' dt\,. \quad (6.12)$$

Once $U_{m,n+1}$ is calculated, the temperature T_{n+1} can be updated as usual by solving:

$$U_{m,n+1} = \int_0^{T_{n+1}} c_v(T')\, dT'\,. \quad (6.13)$$

In the case of a perfect gas, this reduces to $T_{n+1} = U_{m,n+1}/c_v$.

We assert that none of the approximations introduced here violate the conservation of energy. This may be argued in general since we have already shown that the IMC method conserves energy, and this method uses fewer approximations. However, it is possible to demonstrate this more rigorously by revisiting the analysis that led to Eq. (3.28) and simply replacing the terms involving f_n with $f_n(t)$ where applicable.

To summarize, the IMC-TDF equations consist of the following radiation transport equation for I which is solved using a slightly-modified Monte Carlo process (to be discussed later):

$$\frac{1}{c}\frac{\partial I}{\partial t} + \mu\frac{\partial I}{\partial x} + \sigma_{a,n} I = \frac{1}{2}\sigma_{ea,n}(t) b_n c U_{r,n} + \frac{\chi_n}{2}\iint \sigma_{es,n}(t) I(t)\, d\mu' d\nu' + \frac{Q}{2}\,, \quad (6.14a)$$

and a material energy density update equation:

$$U_{m,n+1} = U_{m,n} - \frac{U_{r,n}}{\beta_n}\left(1 - e^{-\sigma_{p,n}\beta_n c\Delta_{t,n}}\right) + \int_{t_n}^{t_{n+1}} \iint f_n(t)\sigma_{a,n} I(t)\, d\mu' d\nu' dt\,, \quad (6.14b)$$

where $\sigma_{ea,n}(t)$, $\sigma_{es,n}$, and $\sigma_{a,n}$ are defined in Eqs. (6.8) and Eqs. (6.9), and $f_n(t)$ is defined in Eq. (6.5). The temperature T_{n+1} is calculated from:

$$U_{m,n+1} = \int_0^{T_{n+1}} c_v(T')\, dT'\,. \quad (6.14c)$$

The initial and boundary conditions are given by:

$$I(x,\mu,\nu,0) = I^i(x,\mu,\nu)\,, \quad (6.14d)$$

$$T(x,0) = T^i(x)\,, \quad (6.14e)$$

$$I(0,\mu,\nu,t) = I^\ell(\mu,\nu,t)\,, 0 < \mu \le 1\,, \quad (6.14f)$$

$$I(X,\mu,\nu,t) = I^r(\mu,\nu,t)\,, -1 \le \mu < 0\,. \quad (6.14g)$$

6.1.1 Discussion

There is only a minor difference between this derivation procedure and the derivation of the IMC equations presented previously in Chapter III. In the IMC derivation, the equation for $U_r(t)$ is time-averaged, α is introduced, and the time-average unknowns $\overline{U_r}$ and $\overline{I}$ are replaced with their instantaneous counterparts $U_r(t)$ and $I(t)$ [see Eq. (3.16)]. This results in an equation for $U_r(t)$ that is not exact at $t = t_n$, but that correctly reproduces the original time-average equation for $\overline{U_r}$. In the IMC-TDF equations, this procedure is circumvented by treating the time-integral of $I(t)$ "implicitly." The resulting equation for $U_r(t)$ [Eq. (6.6)] is exact at $t = t_n$ and should be more accurate for $t_n < t$.

Eqs. (6.14) are analogous to the IMC equations [Eqs. (3.29)] except for the introduction of the time-dependent Fleck factor $f_n(t)$ defined in Eq. (6.5). Therefore, we shall use our familiarity with the implementation details and characteristics of the IMC equations as a basis for discussion. The first thing to consider is how $f_n(t)$ compares to the usual f_n. To compare these two quantities directly, we employ the scaled time variable τ defined in Eq. (4.6). Then, we may more simply write the time-dependent terms as:

$$4(\tau - \tau_n) = \beta_n \sigma_{p,n} c (t - t_n) \,. \tag{6.15}$$

Here τ is the scaled time in mean free times for emission, as discussed in Chapter IV. Using Eq. (6.15) in Eq. (6.5), we write the scaled version of the time-dependent Fleck factor as

$$f_n(\tau) = e^{-4(\tau - \tau_n)} \,, \tag{6.16}$$

and the scaled version of the "traditional" Fleck factor as [see Eq. (4.19)]:

$$f = \frac{1}{1 + 4\alpha\Delta_\tau} \,. \tag{6.17}$$

We also derive the average value of $f_n(\tau)$ over the time step, which we denote by $\overline{f_n(\tau)}$. This is:

$$\overline{f_n(\tau)} = \frac{1}{\Delta_\tau} \int_{\tau_n}^{\tau_{n+1}} f_n(\tau)\, d\tau = \frac{1}{4\Delta_\tau} \left(1 - e^{-4\Delta_\tau}\right) \,. \tag{6.18}$$

In Figure 6.1, we plot Eqs. (6.16), (6.17), and (6.18) over a unit, scaled time step. As expected, $f_n(\tau)$ begins at unity and exponentially decays, passing through each

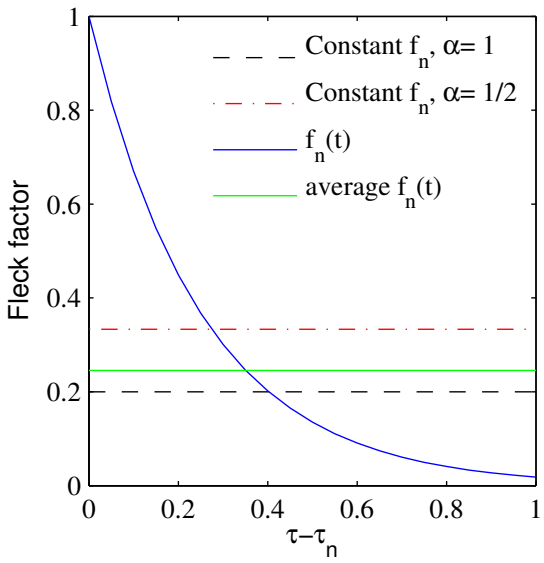

Figure 6.1: The time-dependent Fleck factor compared to the traditional Fleck factors during a time step.

of the constant valued Fleck factors by the end of the time step. We first consider what the time-average effect of this behavior is.

In Figure 6.1, the averaged time-dependent Fleck factor falls between the traditional Fleck factors evaluated with $\alpha = 0.5$ and $\alpha = 1$. If $\Delta_\tau \approx 0$, we find that:

$$\begin{aligned}\overline{f_n(\tau)} &= \frac{1}{4\Delta_\tau}\left[1-(1-4\Delta_\tau+8\Delta_\tau^2+O(\Delta_\tau^3))\right] , \\ &= \frac{1}{4\Delta_\tau}\left[4\Delta_\tau-8\Delta_\tau^2+O(\Delta_\tau^2)\right] ,\end{aligned}$$

$$\overline{f_n(\tau)} = 1-2\Delta_\tau+O(\Delta_\tau^2)\,. \tag{6.19a}$$

For the traditionally-defined, constant Fleck factor, this limit is:

$$\frac{1}{1+4\alpha\Delta_\tau} = 1-4\alpha\Delta_\tau+O(\Delta_\tau^2)\,. \tag{6.19b}$$

Thus, in the limit of *small* time steps, the average $f_n(\tau)$ behaves, to first order, like the traditional Fleck factor with $\alpha = 1/2$. This is advantageous since we already know that using $\alpha = 1/2$ for sufficiently small time steps is the most accurate choice.

For large time steps, the limiting values of the averaged time-dependent and

constant Fleck factors are:

$$\overline{f_n(\tau)} = \frac{1}{4\Delta_\tau} + O\left(e^{-4\Delta_\tau}\right) , \tag{6.20a}$$

$$\frac{1}{1+4\alpha\Delta_\tau} = \frac{1}{4\alpha\Delta_\tau} + O\left(\frac{1}{\Delta_\tau^2}\right) , \tag{6.20b}$$

so that, in the limit of *large* time steps, the average $f_n(\tau)$ behaves, to first order, like the traditional Fleck factor with $\alpha = 1$. This is again advantageous since we know that for large time steps, using $\alpha = 1$ in the traditional IMC approach is the "safest" choice (it minimizes the damped temporal oscillations that would otherwise occur from using $\alpha < 1$).

Together, Figure 6.1 and the limiting conditions in Eqs. (6.19) and (6.20) suggest an alternative to using the IMC-TDF equations that could be used as a simple first step towards an true implementation of the IMC-TDF equations. Instead of using $f_n(\tau)$, its time average $\overline{f_n(\tau)}$ could be employed to select an adaptive value of α for the IMC equations. Setting the traditional IMC Fleck factor in Eq. (6.17) to equal $\overline{f_n(\tau)}$ in Eq. (6.18) produces the following equation for α:

$$\alpha = \frac{1}{1-e^{-4\Delta_\tau}} - \frac{1}{4\Delta_\tau} \tag{6.21}$$

Figure 6.2 depicts α as a function of Δ_τ. For small time steps, Eq. (6.21) produces $\alpha \approx 0.5$; as the time step size grows, it asymptotically approaches 1. We note that this approach would not be as accurate as using the time-dependent Fleck factor, but it would be trivial to implement, and it should be investigated as future work.

Because the time-average of the time-dependent Fleck factor is larger than the traditional Fleck factor with $\alpha = 1$, the source term involving $U_{r,n}$ in Eq. (6.14a) will emit more energy during a time step than the corresponding term in Eq. (3.29a). By contrast, if $\alpha = 1/2$ is used, the source term in Eq. (6.14a) will be smaller. This is likely a significant contributor to the stability characteristics of these equations. Since the traditional IMC equations have already been demonstrated to be unconditionally stable for $\alpha \geq 1/2$, we may also conjecture that the IMC-TDF method will be so. It is not obvious, however, what the effects of using a time-dependent Fleck factor will be with regard to damped temporal oscillations. Later, we shall perform the 0-D stability analysis described in Chapter IV to investigate this question.

Because the time-average of the time-dependent Fleck factor limits to the traditional Fleck factor with $\alpha = 1$ for large time steps, we conjecture that solutions of

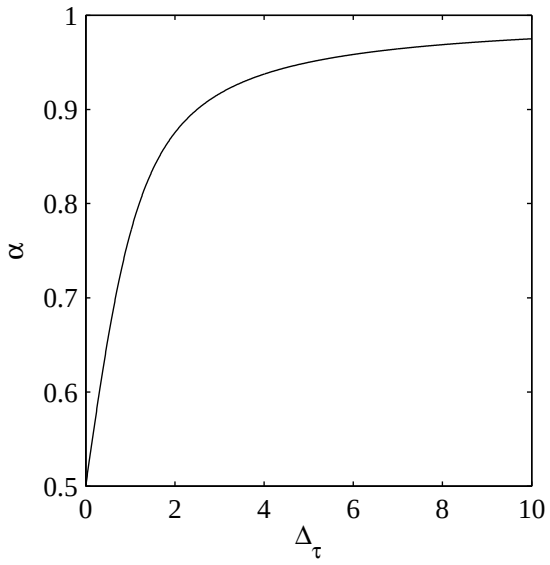

Figure 6.2: An adaptive value of α based on the relationship between the time-average of the time-dependent Fleck factor and the traditional Fleck factor.

Eqs. (6.14) should also violate the maximum principle if sufficiently large time steps are used [27]. It is unclear if the same limit on the time step found in [27] is applicable to Eqs. (6.14). Later, we numerically verify that the IMC-TDF equations can violate the maximum principle.

We next consider the time-dependent behavior of $f_n(\tau)$ shown in Figure 6.1. Recalling that the Fleck factor is the probability of an effective absorption, the exponential decay in $f_n(\tau)$ means that the overall probability of effective absorptions is *much* higher at the beginning of the time step than at the end. Particles born early in the time step are therefore much more likely to become absorbed into the material. On the other hand, $f_n(\tau)$ also appears on the right side of Eq. (6.14a) in the radiation source term that includes $U_{r,n}$. This implies that particle emission times due to this term are weighted to occur near the beginning of the time step. By contrast, the corresponding term in the traditional IMC equations [see Eq. (3.29a)] is time-independent, and the corresponding particle emission times are uniform over the time step. One may argue directly from Eq. (6.4) that using an exponential distribution of the source particles due to the estimate of $U_r(t)$ should be more accurate than a time-independent source; using a time-independent source will overestimate the contribution of this term late in the time step. The overall effect of using $f_n(t)$ is that (i) Monte Carlo particles are much more likely to be born from the $U_{r,n}$ term near the beginning of the time step and (ii) these Monte Carlo particles are also

more likely to undergo effective absorptions near the beginning of the time step, and effective scatters near the end. For large time steps, the dominance of the effective scattering can lead to a radiation equation that is highly diffusive for the end of the time step. Under these conditions, it would likely be advantageous to incorporate one of the diffusive modifications to reduce the computational cost discussed in [25] or [26], although we do not consider that here.

We would like to determine the positivity conditions on Eq. (6.14b) in a manner analogous to that performed in Chapter III. Since all of the terms in Eq. (6.14a) are positive, it does not permit negative solutions. Eq. (6.14b) is guaranteed to be positive when:

$$U_{m,n} - \frac{U_{r,n}}{\beta_n}\left(1 - e^{-\sigma_{p,n}\beta_n c\Delta_{t,n}}\right) > 0\,. \tag{6.22}$$

Using the definition of β from Eq. (3.2b), we write

$$\beta_n = \frac{4aT_n^3}{c_v(T_n)} = 4\frac{U_{r,n}}{c_v(T_n)T_n}\,, \tag{6.23}$$

which may be solved for $U_{r,n}$ to produce:

$$U_{r,n} = \frac{1}{4}\beta_n c_{v,n} T_n\,. \tag{6.24}$$

We therefore rewrite the inequality in Eq. (6.22) as:

$$U_{m,n} - \frac{1}{4}c_{v,n}T_n\left(1 - e^{-\sigma_{p,n}\beta_n c\Delta_{t,n}}\right) > 0\,. \tag{6.25}$$

Thus, the following condition is sufficient for positivity for all $\Delta_{t,n}$:

$$U_{m,n} - \frac{1}{4}c_{v,n}T_n > 0\,. \tag{6.26}$$

This is essentially the same limit as was found during the discussion of the traditional IMC equations in Section 3.2.1 but without α [see Eq. (3.35)]. There, we found that the form of the specific heat was an important contributor to the positivity of $U_{m,n+1}$. If the specific heat is of the form:

$$c_v(T) = vT^z\,, \tag{6.27}$$

where v is a constant and $z > 0$, then Eq. (6.26) becomes

$$v\frac{T_n^{z+1}}{z+1} > \frac{1}{4}vT_n^{z+1}\,,$$
$$1 > \frac{z+1}{4}\,. \tag{6.28}$$

Thus Eq. (6.14b) will produce positive solutions for all $\Delta_{t,n}$ so long as $z \leq 3$, which likely describes all physically meaningful materials. We conclude that using a time-dependent Fleck factor does not affect the positivity condition of the IMC equations (assuming $\alpha = 1$ is used in the traditional IMC method).

We have argued here that using the time-dependent Fleck factor should produce an unconditionally stable and more accurate method than the traditional approach. After a brief discussion on the specifics of the implementation differences between these methods, we shall address these assertions directly.

6.1.2 Implementation Differences

Since the average value of $f_n(t)$ differs from the traditionally defined f_n, the magnitude of the source energy due to the term containing $U_{r,n}$ may be expected to change for this method. The new source energy is given by:

$$\begin{aligned} E_R &= \int_{t_n}^{t_{n+1}} \int_0^X \int_0^\infty \int_{-1}^1 \frac{1}{2}\chi_n(\nu)cf_n(t)\sigma_{p,n}(x)U_{r,n}(x)\,d\mu\,d\nu\,dx\,dt\,, \\ &= \frac{1}{\beta_n}\left(1 - e^{\beta_n\sigma_{p,n}c\Delta_{t,n}}\right)\int_0^X U_{r,n}(x)\,dx\,. \end{aligned} \tag{6.29}$$

This result may compared with Eq. (3.51) for the traditional IMC equations. It is greater than that in Eq. (3.51) when $\alpha = 1$, and lesser when $\alpha = 0.5$.

Next, the emission time due to this source is no longer uniform. Instead, the pdf for the emission time is:

$$p(t)\,dt = \beta_n\sigma_{p,n}c\frac{e^{-\beta_n\sigma_{p,n}c(t-t_n)}}{1 - e^{-\beta_n\sigma_{p,n}c\Delta_{t,n}}}\,. \tag{6.30}$$

It is possible to write this directly since we have previously integrated $f_n(t)$ over the time step to obtain Eq. (6.14b). To sample from this pdf using a Uniform Random Variate ξ, we solve:

$$\xi = \int_{t_n}^t \beta_n\sigma_{p,n}c\frac{e^{-\beta_n\sigma_{p,n}c(t'-t_n)}}{1 - e^{-\beta_n\sigma_{p,n}c\Delta_{t,n}}}dt'\,,$$

$$\xi\left(1-e^{-\beta_n\sigma_{p,n}c\Delta_{t,n}}\right)=1-e^{-\beta_n\sigma_{p,n}c(t'-t_n)}\,,$$
$$-\beta_n\sigma_{p,n}c(t'-t_n)=\ln\left[1-\xi\left(1-e^{-\beta_n\sigma_{p,n}c\Delta_{t,n}}\right)\right]\,,$$
$$t=t_n-\frac{1}{\beta_n\sigma_{p,n}c}\ln\left[1-\xi\left(1-e^{-\beta_n\sigma_{p,n}c\Delta_{t,n}}\right)\right]\,. \tag{6.31}$$

Eq. (6.31) is the emission time of an IMC particle due to energy from E_R in Eq. (6.29). Using Eq. (6.31) will increase the cost of the computation relative to the traditional IMC method, as the traditional IMC method does not require the evaluation of a logarithm for this term.

Finally, the probability of an effective absorption becomes time-dependent. Instead of storing f_n at the beginning of the time step, it is necessary to evaluate the exponential in Eq. (6.5) upon each collision. This will also increase the computational cost of the calculation. These three changes are all that is required to convert an existing IMC code to one that employs a time-dependent Fleck factor.

We next consider the stability characteristics of Eqs. (6.14).

6.2 0-D Stability Analysis

We begin by assuming that $\sigma \propto T^{-3}$ and that c_v = constant. Since we have previously derived this form of the 0-D, gray, dimensionalized versions of the TRT equations, there is no need to explicitly carry out the first step of the algorithm. Assuming further that the opacities and β are evaluated at τ_n, the equations are [from Eq. (4.9)]:

$$q\frac{\partial\phi}{\partial\tau}+\frac{1}{M_n^3}\phi=\frac{1}{M_n^3}R\,, \tag{6.32a}$$

with the material energy equation written exactly in either of the following two forms:

$$\frac{\partial M}{\partial\tau}+\frac{1}{M_n^3}R=\frac{1}{M_n^3}\phi, \tag{6.32b}$$
$$\frac{\partial R}{\partial\tau}+4R=4\phi\,. \tag{6.32c}$$

The next step is to apply the approximations to obtain the IMC equations with a time-dependent Fleck factor. We have already frozen the temperature-dependent data at the beginning of the time step (although, without loss of generality, we could also evaluate them at an estimated temperature determined by the algorithm in

Chapter V). We next "solve" Eq. (6.32c) with an integrating factor:

$$R(\tau)e^{4(\tau-\tau_n)} - R_n = \int_{\tau_n}^{\tau} 4e^{4(\tau'-\tau_n)}\phi(\tau')\,d\tau'\,, \tag{6.33}$$

and again assume an "implicit" treatment of $\phi(\tau)$ [we replace $\phi(\tau')$ with $\phi(\tau)$]. This allows us to carry out the integral and obtain:

$$\begin{aligned} R(\tau)e^{4(\tau-\tau_n)} - R_n &\approx \left(e^{4(\tau-\tau_n)} - 1\right)\phi(\tau)\,, \\ R(\tau) &= R_n e^{-4(\tau-\tau_n)} + \left(1 - e^{-4(\tau-\tau_n)}\right)\phi(\tau)\,. \end{aligned} \tag{6.34}$$

We define a scaled version of the time-dependent Fleck factor as:

$$f(\tau) = e^{-4(\tau-\tau_n)}\,, \tag{6.35}$$

and write Eq. (6.34) as:

$$R(\tau) = R_n f(\tau) + [1 - f(\tau)]\,\phi(\tau)\,. \tag{6.36}$$

Introducing Eq. (6.36) into Eqs. (6.32a) and (6.32b), applying the initial condition $R_n = M_n^4$, and rearranging produces the dimensionless, 0-D IMC-TDF equations:

$$q\frac{d\phi}{d\tau} + \frac{f(\tau)}{M_n^3}\phi = f(\tau)M_n\,, \tag{6.37a}$$

$$\frac{dM}{d\tau} = \frac{f(\tau)}{M_n^3}\phi - f(\tau)M_n\,. \tag{6.37b}$$

For the third step of the analysis, we eliminate ϕ from Eq. (6.37b) by using the conservation of energy:

$$\phi = \frac{q + 1 - M}{q}\,. \tag{6.38}$$

This produces:

$$\begin{aligned} \frac{dM}{d\tau} + f(\tau)M_n &= \frac{f(\tau)}{M_n^3}\left(\frac{q+1-M}{q}\right)\,, \\ \frac{dM}{d\tau} + \frac{1}{qM_n^3}e^{-4(\tau-\tau_n)}M &= e^{-4(\tau-\tau_n)}\frac{1}{qM_n^3}\left((q+1) - qM_n^4\right)\,. \end{aligned} \tag{6.39}$$

Instead of presenting the derivation of the solution of Eq. (6.39), we simply write it

without proof as:

$$M(\tau) = q + 1 - qM_n^4 - \exp\left[-(1 - e^{-4(\tau-\tau_n)})/4qM_n^3\right](q + 1 - qM_n^4 - M_n)\,, \quad (6.40)$$

so that the solution at the end of a time step given by $\tau_n \leq \tau \leq \tau_{n+1}$ is

$$M_{n+1} = q + 1 - qM_n^4 - \exp\left[-(1 - e^{-4\Delta_\tau})/4qM_n^3\right](q + 1 - qM_n^4 - M_n)\,, \quad (6.41)$$

where $\Delta_\tau = \tau_{n+1} - \tau_n$. We have verified that Eq. (6.41) is the correct solution by substituting it back into Eq. (6.39) using mathematical software.

In the fourth step of the analysis, we perturb the scaled temperature about the specified equilibrium condition according to

$$M_n = 1 + \epsilon P_n\,, \quad (6.42)$$

where ϵ is a small parameter, and we look for a recursion relationship of the form $P_{n+1} = \rho P_n$. Noting that, to first order,

$$q + 1 - qM_n^4 = q + 1 - q(1 + 4\epsilon P_n) = 1 - 4q\epsilon P_n\,, \quad (6.43)$$

the introduction of Eq. (6.42) into Eq. (6.41) produces:

$$1 + \epsilon P_{n+1} = 1 - 4q\epsilon P_n + \exp\left[-(1 - e^{-4\Delta_\tau})/4q\right](1 + 4q)\epsilon P_n\,,$$
$$P_{n+1} = \left\{-4q + \exp\left[-(1 - e^{-4\Delta_\tau})/4q\right](1 + 4q)\right\} P_n\,,$$

and we recognize the amplification factor for this system as:

$$\rho(q, \Delta_\tau) = -4q + \exp\left[-(1 - e^{-4\Delta_\tau})/4q\right](1 + 4q)\,. \quad (6.44)$$

Our final task is to analyze Eq. (6.44) to assess its stability characteristics. First, it is trivial to show that $\rho < 1$, since:

$$-4q + \exp\left[-(1 - e^{-4\Delta_\tau})/4q\right](1 + 4q) < 1\,,$$
$$\exp\left[-(1 - e^{-4\Delta_\tau})/4q\right] < 1\,. \quad (6.45)$$

Thus, monotonically diverging solutions of Eq. (6.41) do not exist. Next, we examine whether oscillatory diverging solutions exist [$\rho < -1$]. If the following inequality is

true, they do not:

$$\begin{aligned} -1 &< -4q + \exp\left[-(1-e^{-4\Delta_\tau})/4q\right](1+4q)\,, \\ \frac{4q-1}{4q+1} &< \exp\left[-(1-e^{-4\Delta_\tau})/4q\right]\,. \end{aligned} \tag{6.46}$$

For $q < 1/4$, Eq. (6.46) is always satisfied since the left side is negative. If $q > 1/4$, then:

$$\begin{aligned} \ln\left(\frac{4q-1}{4q+1}\right) &< -(1-e^{-4\Delta_\tau})/4q\,, \\ -4q\ln\left(\frac{4q-1}{4q+1}\right) &> 1-e^{-4\Delta_\tau}\,. \end{aligned} \tag{6.47}$$

Since Eq. (6.47) is of the form

$$Q(q) > \Theta(\tau)\,, \tag{6.48}$$

we look for whether

$$\min_{1/4<q<\infty} Q(q) > \max_{0<\Delta_\tau<\infty} \Theta(\Delta_\tau)\,. \tag{6.49}$$

Now, $Q(q)$ is a monotonically decreasing function that has the following limit:

$$\lim_{q\to\infty} Q(q) = \lim_{q\to\infty} -4q\ln\left(\frac{4q-1}{4q+1}\right) = 2\,, \tag{6.50}$$

and $\Theta(\Delta_\tau)$ is a monotonically increasing function with the limit:

$$\lim_{\Delta_\tau\to\infty} \Theta(\Delta_\tau) = \lim_{\Delta_\tau\to\infty} 1-e^{-4\Delta_\tau} = 1\,. \tag{6.51}$$

Therefore, the inequality in Eq. (6.47) is satisfied if

$$2 > 1\,. \tag{6.52}$$

We therefore conclude that the use of the time-dependent Fleck factor defined in Eq. (6.5) produces an unconditionally stable system.

We next consider whether damped temporal oscillations are permitted [$-1 < \rho < 0$]. Figure 6.3 is a log-log plot of the amplification factor as a function of q and Δ_τ. From this figure we observe that $-1 < \rho \leq 0$ for large Δ_t and for $q \approx 0.1$. We conclude that damped oscillations can occur in the IMC-TDF equations. Also, comparing this figure to Figure 4.3, we observe that their magnitude and domain

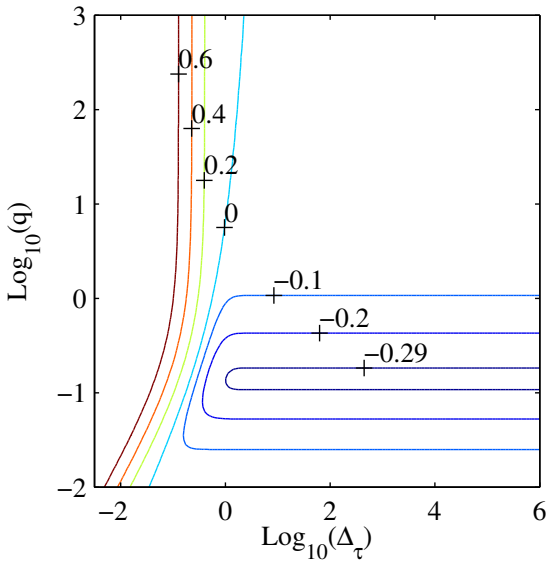

Figure 6.3: A contour plot of the amplification factor for an IMC method that employs a time-dependent Fleck factor.

of existence are comparable, although the monotonicity condition on the time step appears to be more restrictive. The absolute minimum amplification factor remains approximately -0.29, and it occurs for $q \approx 0.13$ and for sufficiently large Δ_τ.

Finally, we provide monotonicity conditions for the IMC-TDF equations. We expect temperature solutions to be monotonic when $0 < \rho$, or when:

$$\begin{aligned}
0 &< -4q + \exp\left[-(1-e^{-4\Delta_\tau})/4q\right](1+4q)\,, \\
\frac{4q}{1+4q} &< \exp\left[-(1-e^{-4\Delta_\tau})/4q\right]\,, \\
-4q\ln\left(\frac{4q}{1+4q}\right) &> 1-e^{-4\Delta_\tau}\,, \\
\ln\left[1+4q\ln\left(\frac{4q}{1+4q}\right)\right] &> -4\Delta_\tau\,, \\
\Delta_\tau &< -\frac{1}{4}\ln\left[1+4q\ln\left(\frac{4q}{1+4q}\right)\right]\,.
\end{aligned} \tag{6.53}$$

Eq. (6.53) is the monotonicity condition on Δ_τ for the IMC-TDF equations. In the unscaled time variable, the monotonicity condition is:

$$\sigma_0 c\Delta_t < -\frac{1}{4q}\ln\left[1+4q\ln\left(\frac{4q}{1+4q}\right)\right]\,. \tag{6.54}$$

Unfortunately, Eq. (6.54) limits to zero as q goes to infinity, implying that it is not

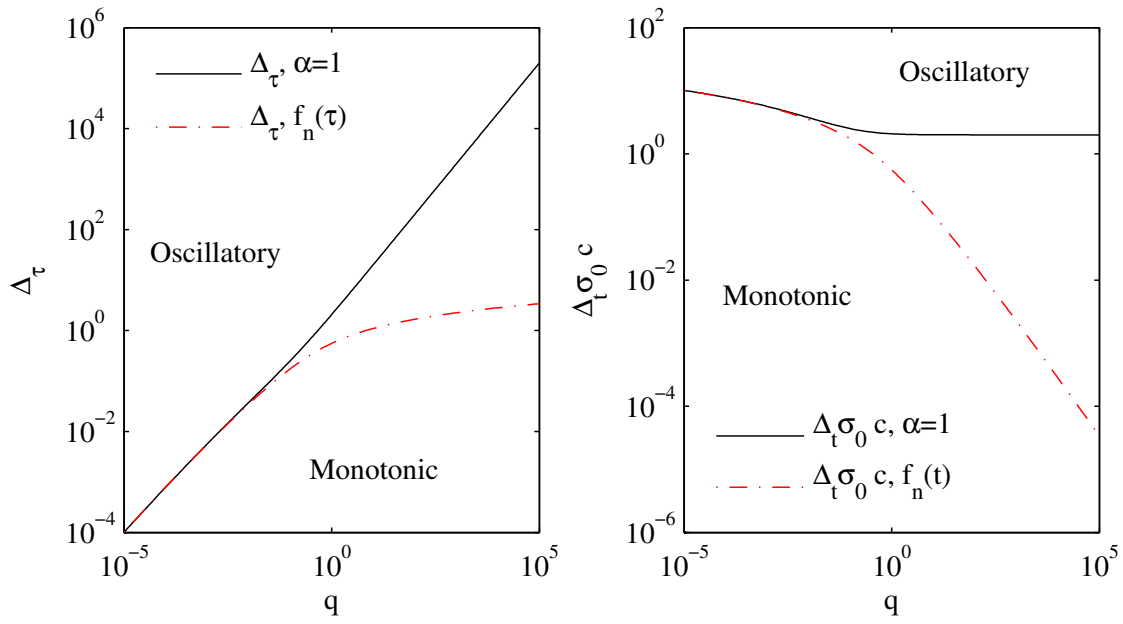

Figure 6.4: Monotonicity conditions on Δ_τ and $\Delta_t\sigma_0 c$ for the 0-D, nonlinear, gray IMC equations that employ a constant Fleck factor with $\alpha = 1$ and that use a time-dependent Fleck factor.

possible to find a single condition on Δ_t that ensures the temperature solution is monotonic for all q. While this is admittedly an argument against using a time-dependent Fleck factor, the global monotonicity condition on the IMC equations given by Eq. (4.69) is almost never met in practice, so it is likely not a strong enough argument to dismiss the use of $f_n(t)$. Figure 6.4 provides log-log plots of the monotonicity conditions given by Eq. (6.53) and Eq. (6.54). Comparing Figures 4.2 to 6.4, we see that the monotonicity conditions for the IMC-TDF equations are slightly less restrictive than those of traditional IMC with $\alpha = 1/2$.

6.2.1 An Alternative Time-dependent Fleck Factor, a Cautionary Tale

Here, we briefly discuss the numerical implications of choosing a simple, arguably compelling, alternative form of the time-dependent Fleck factor. This form has been previously proposed as an aside in [22]. However, we show that this form produces a system of equations that is only conditionally stable, indicating that further development may be ill-advised. The reader more concerned with the numerical results of the previously-defined Fleck factor may proceed to the next section.

It is possible to motivate a simpler, "rational" form of the time-dependent Fleck

factor. Instead of solving Eq. (6.32c) with an integrating factor, let us approximate by:

$$\frac{R(t) - R_n}{t - t_n} + 4R(t) \approx 4\phi(t)\,, \tag{6.55}$$

so that

$$R(t) = R_n \frac{1}{1 + 4(t - t_n)} + \frac{4(t - t_n)}{1 + 4(t - t_n)}\phi(t)\,. \tag{6.56}$$

Then, if we define a *rational* time-dependent Fleck factor by:

$$f_r(t) = \frac{1}{1 + 4(t - t_n)}\,. \tag{6.57}$$

we may write Eq. (6.55) in the form:

$$R(t) = f_r(t)R_n + [1 - f_r(t)]\phi(t)\,. \tag{6.58}$$

From this point, one may proceed as before to define an alternate form of the time-dependent IMC equations, using Eq. (6.57) instead of Eq. (6.35).

At first, this seems to be an appealing alternative to of Eq. (6.35). For one, Eq. (6.55) is still exact at $t = t_n$, which cannot be said of the traditional IMC equations. Also the use of Eq. (6.57) avoids the introduction and associated costs of exponential or logarithmic calculations in the Monte Carlo procedure. Furthermore, Eqs. (6.35) and (6.57) are related in the limit of small times since

$$\begin{aligned} e^{-4(\tau - \tau_n)} &= 1 - 4(\tau - \tau_n) + O((\tau - \tau_n)^2)\,, \\ &= \frac{1}{1 + 4(t - t_n)} + O((\tau - \tau_n)^2) = f_r(t) + O((\tau - \tau_n)^2)\,, \end{aligned} \tag{6.59}$$

so one would expect that the employment of Eq. (6.57) instead of Eq. (6.35) to lead to similar gains in accuracy. Also, equations with Eq. (6.57) should yield an effective scattering ratio which is always less than that of traditional IMC, which would lead to a reduction in the computational cost.

All of this seems positive until we perform a 0-D stability analysis of the resulting system. We do not provide the derivation details, but the analysis produces the following amplification factor ρ_r:

$$\rho_r = -4q + (1 + 4\Delta_\tau)^{-1/4q}(1 + 4q)\,. \tag{6.60}$$

From this point, one may show that $-1 < \rho_r$ if and only if:

$$\frac{e^2 - 1}{4} \approx 1.6 > \Delta_\tau \,. \tag{6.61}$$

Eq. (6.61) places a condition on the stability of the IMC equations with a Fleck factor defined by Eq. (6.57). If time steps are chosen that violate Eq. (6.61), the temperature solution will oscillate indefinitely. This is a good example of how the simplified stability analysis described in Chapter IV can be used to "weed out" potential time-discretizations of the TRT equations, and how the results of the analysis can be surprising.

6.3 Numerical Results

In this section, we numerically apply the IMC-TDF equations to a series of problems to assess its accuracy and its efficiency. We begin with the simplest possible problem: a 0-D, gray, linear problem that initially begins out of equilibrium. Such a problem is exactly solvable, so it is possible to compare the numerical solution to the exact solution to exactly calculate its order of error. We then consider a nonlinear version of the same problem, for which comparisons are made using a fine-grid solution.

A series of gray Marshak wave problems is considered in which the spatial and temporal grids are varied to determine whether the IMC-TDF equations are more accurate than the IMC equations when the time step is sufficiently large and/or the spatial grid size is sufficiently small. Under these conditions, we have previously shown in Chapters IV and V that the IMC temperature solutions can violate the maximum principle [the temperature solution may become greater than the boundary conditions.] We also investigate any increases in accuracy obtained by solving the IMC-TDF equations with temperature-dependent problem data evaluated at T_*, using the algorithm and definitions given in Chapter V.

We also implement the IMC-TDF equations a smaller set of frequency-dependent Marshak wave problems.

6.3.1 Temporal Accuracy in 0-D Problems

To numerically assess the temporal order of accuracy, we consider a 0-D sample problem that is described by the dimensionless, gray, linear TRT equations defined in Eqs. (4.87). For this problem, we assume that $\sigma = a = c = 1$ and $q = 0.14$, which

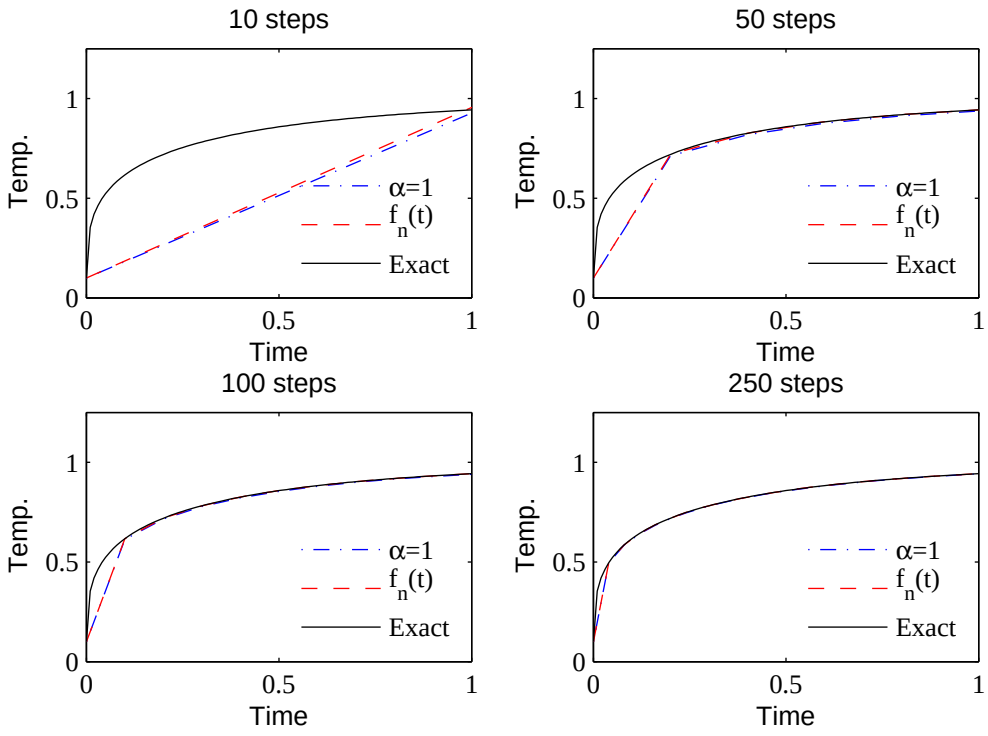

Figure 6.5: The time-dependent temperatures for a traditional IMC method with $\alpha = 1$ (blue) and an IMC method that uses $f_n(t)$ (red) on a linear problem for 10, 50, 100, and 250 time steps.

implies that $c_v \approx 7.14$. The temperature is set to an initial condition of 0.1, and the initial intensity ϕ is ≈ 2.79 [it is chosen to ensure that the equilibrium temperature is 1]. The problem is solved using a variable number of time steps with an ending time fixed at $t = 10$, at which point the fine-mesh temperature solution is 1.0. To obtain numerical solutions of the IMC and IMC-TDF equations, we calculated exact numerical solutions of Eqs. (3.29) and Eqs. (6.14) applied to this linear, 0-D problem; no Monte Carlo calculation was performed.

Figure 6.5 depicts the numerical temperatures solutions as a function of time for a variable number of time steps. We note that in Figure 6.5, the domain is restricted to $0 \leq t \leq 1$, which is not the final time in the problem. This is because both IMC methods somewhat rapidly reach the equilibrium condition; most of the variation in the results occurs for early times. From Figure 6.5 it is difficult to ascertain whether any advantage is gained from using the IMC-TDF equations. We observe that in linear problems, "overshooting" does not occur, and that the numerical solutions appear to approximate the exact solution as if they were performing a trapezoid-integral method.

Next, we again define the root mean square error of the time-dependent temperature solutions by:

$$\text{RMS error} = \sqrt{\frac{1}{N}\sum_{n=1}^{N}\left(T_n - T_{\text{exact},n}\right)^2}, \tag{6.62}$$

where T_n is provided by an IMC calculation, and $T_{\text{exact},n}$ is the exact solution.

In Figure 6.6, we plot the RMS error of IMC methods that use $\alpha = 1$, $\alpha = 0.5$, and $f_n(t)$ defined in Eq. (6.5). In this figure we clearly see the accuracy advantage of using the IMC-TDF equations; they are $O(\Delta_t^2)$. We also observe that the IMC equations with $\alpha = 0.5$ are $O(\Delta_t^2)$, as has been previously demonstrated numerically in [46] for a slightly more difficult problem. However, we remark that $\alpha = 0.5$ is rarely used in practice, since it is known that it can lead to difficulties regarding damped, temporal oscillations. As discussed previously, using the IMC-TDF equations may be viewed in a time-average sense as an automatic tuning of the user-parameter α. Thus, the IMC-TDF equations retain the second-order accuracy in the time step for linear problems without the necessity of manually changing α from its usually-employed value to a less conservative value.

Cheatham has demonstrated that it may be analytically shown that IMC equations with $\alpha = 0.5$ applied to a linear problem are $O(\Delta_t^2)$ [60]. Using Cheatham's method, it should be possible to analytically demonstrate each of these results for the IMC-TDF equations applied to linear problems. We note also that, by comparison, the Carter-Forest [23] and Ahrens-Larsen [22] methods are *exact* for this problem.

For linear, gray, 0-D problems, we have seen that the IMC-TDF equations are automatically second-order accurate in time. We next consider a nonlinear version of these problems.

The 0-D, gray, nonlinear problem we consider is identical to that presented in Chapter V. In this problem, we assume that $\sigma = T^{-3}$, $a = c = 1$, and $q = 0.14$, which implies that $c_v \approx 7.14$. The temperature is set to an initial condition of 0.1, and the initial intensity ϕ is 7.428. The problem is solved using a variable number of time steps with an an ending time fixed at $t = 1$, at which point the fine-mesh temperature solution is 0.96 [the temperature is 96% converged to its specified equilibrium condition].

Unfortunately, the accuracy gained for these problems is marginal. Figure 6.7 depicts the numerically estimated order of temporal error (calculated using Eq. (6.62) with T_{exact} replaced by a fine-mesh solution). In this figure, the IMC and IMC-TDF

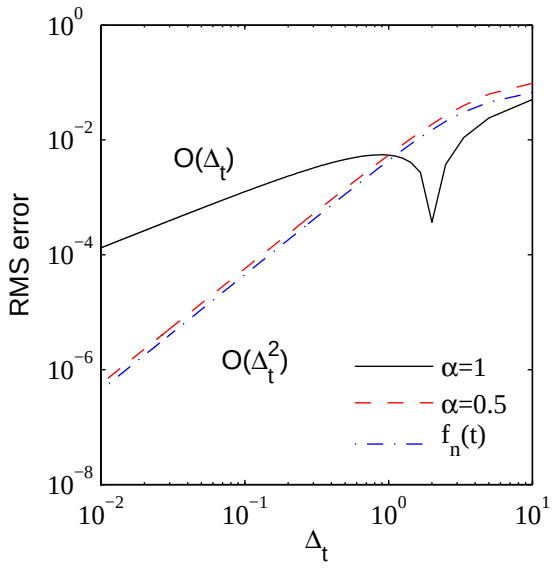

Figure 6.6: The numerically-calculated order of temporal error for a linear problem for traditional IMC with $\alpha = 1$ and $\alpha = 0.5$ and for IMC with the time-dependent Fleck factor $f_n(t)$.

methods (methods 1 and 2) are virtually indistinguishable. For comparison, we also provide the IMC solution with temperature-dependent problem data evaluated at T_* (method 3), as described in Chapter V. For this problem, we conclude that a better estimate of the temperature at which the problem data is evaluated has far more impact on the problem accuracy than does the introduction of a time-dependent Fleck factor.

Figure 6.8 depicts the time-dependent temperature profiles for IMC-TDF methods that use temperature-dependent problem data evaluated at T_n and at the average temperature T_*. The traditional IMC method is not shown since it is essentially identical to the IMC-TDF method for this problem. Figure 6.8 indicates that the IMC-TDF method is just as susceptible to overshooting problems as the IMC method. However, it is also just as receptive to improvement through the use of the temperature estimation algorithm described in Chapter V.

In this section we have demonstrated that the IMC-TDF equations may be expected to be more accurate than the IMC equations with $\alpha = 1$ for linear problems. We have also seen that little is gained by using the IMC-TDF equations on a 0-D nonlinear problem with respect to the order of accuracy and overshooting. We next consider a more realistic series of numerical tests: Marshak waves.

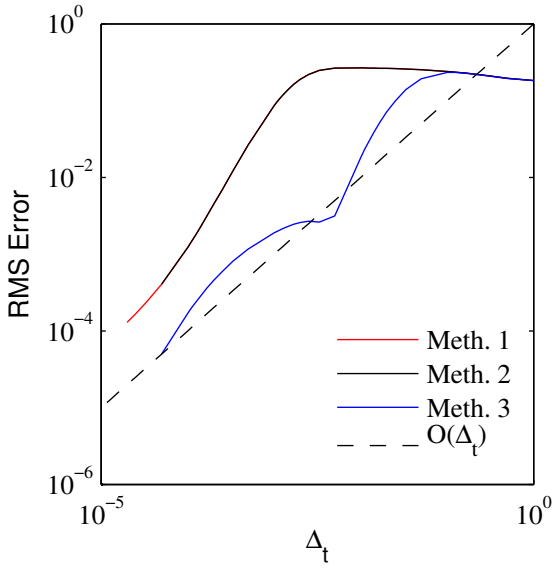

Figure 6.7: The numerically-calculated order of temporal error for (1) IMC-TDF with data evaluated at T_n, (2) traditional IMC with data evaluated at T_n, and (3) IMC-TDF with data evaluated at T_*.

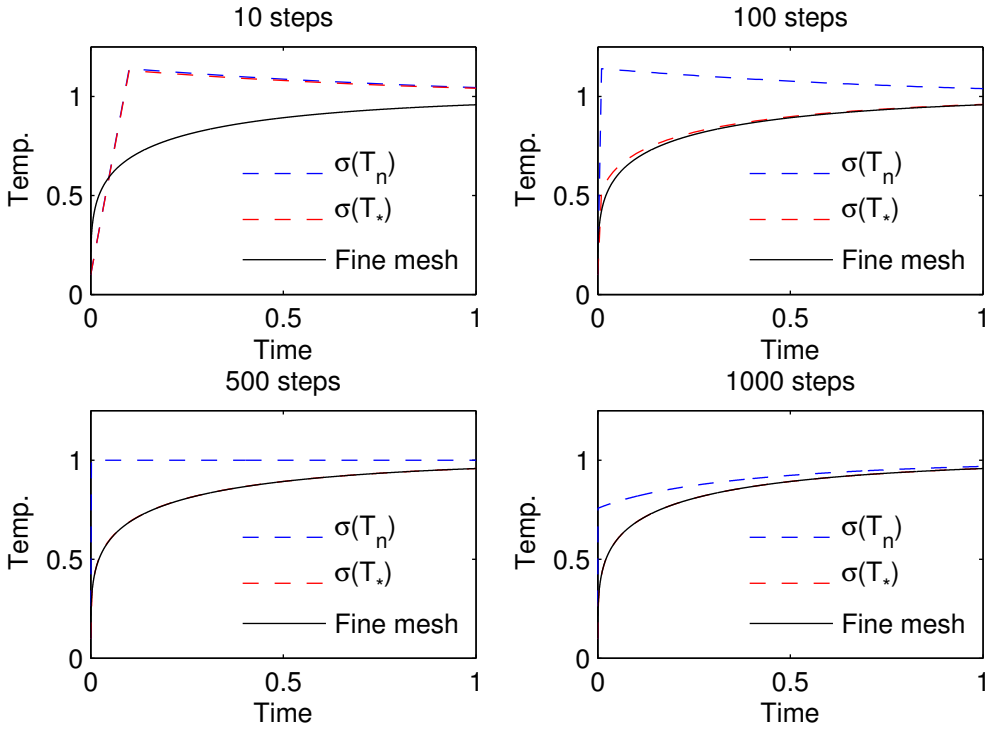

Figure 6.8: The time-dependent temperatures for IMC methods that use $f_n(t)$ with data evaluated at T_n (blue) and at T_* (red) on a nonlinear problem for 10, 100, 500, and 1000 time steps.

6.3.2 Gray Marshak Waves

In Chapters IV and V we considered a series of gray Marshak wave problems in order to test the predictive capability of the linear stability theory. For these problems, we found that if sufficiently large time steps or sufficiently small spatial zones are used, then the temperature solution can violate the maximum principle. We also saw that when the maximum principle is violated [when the material temperature is greater than the boundary condition], the corresponding numerical wave speed is too slow.

In this section we revisit those problems, but we employ the IMC-TDF equations to solve them. In each of these problem simulations, for the first time step, a fully diffusive calculation is used [$E = 1/3$]. Also, we note that it is not necessary to create special opacity tallies since the problem is gray; only the zone-averaged, instantaneous Eddington factors are tallied during the IMC calculation.

This problem is described by setting $q = 0.14$, $\sigma = T^{-3}$, and the initial temperature to 0.1. The specific heat is set to the constant value 7.14. We impose an isotropic right boundary condition equal to the initial temperature and an isotropic left boundary condition at a unit temperature. We consider a slab that is 4 cm wide. This implies that the slab is initially 4,000 mean free paths thick, but only 4 mean free paths thick once equilibrium is reached. We track the wavefront up to $\Delta_\tau = 40$ mean free times to emission. The spatial grid and time step sizes are varied, and each problem is solved using a Monte Carlo algorithm.

Copies of the numerical results for the "traditional" IMC method are provided in Chapters IV and V. Specifically, Table 5.1 provides the maximum temperatures of the Marshak wave over variable values of Δ_τ and Δ_x at the fixed time $\tau = 8$ mean free times for emission. Also, Table 5.2 depicts the estimate of the wave location when $\tau = 38$. These tables demonstrate that reducing the size of the spatial grid or increasing the size of the time step can lead to violations of the maximum principle and corresponding inaccuracies in the estimate of the wavefront location. The temperature profiles were also presented graphically for the second column and third row of Table 5.1 in Figures 5.6(a) and 5.6(b).

We next evaluate the employment of the IMC-TDF equations to solve this problem. Table 6.1 depicts the maximum temperatures obtained in the Marshak wave for various spatial and temporal grid sizes. In general, these represent a (non-marginal) improvement over the traditional IMC method. For instance, the worst case violation of the maximum principle in Table 5.1 [$\Delta_\tau = 2$, $\Delta_x = 0.025$] is 12.412; the

Table 6.1: Maximum values in temperature at $\tau = 8$ using the IMC-TDF method. Bold values indicate violation of the maximum principle.

$\Delta_\tau \backslash \Delta_x$	0.025	0.05	0.1	0.2
0.10	0.952	0.952	0.945	0.938
0.25	**2.762**	0.951	0.946	0.938
0.50	**5.865**	**2.290**	0.944	0.939
1.00	**8.435**	**3.998**	**1.560**	0.940
2.00	**7.622**	**4.461**	**2.122**	0.932

Table 6.2: Estimated wavefront location temperature at $\tau = 38$ for the IMC-TDF method.

$\Delta_\tau \backslash \Delta_x$	0.025	0.05	0.1	0.2
0.10	3.688	3.725	3.75	3.9
0.25	3.438	3.675	3.65	3.7
0.50	1.887	3.425	3.65	3.7
1.00	0.938	1.875	3.25	3.5
2.00	0.912	0.975	1.85	2.7

corresponding entry in Table 6.1 is 7.622. This is a 38% reduction. Additionally, the lower right table entry [$\Delta_\tau = 2$, $\Delta_x = 0.2$] no longer violates the maximum principle when the IMC-TDF equations are used [1.386 vs. 0.932]. These improvements in the maximum principle also translate into improved accuracy in the estimate of the wavefront when $\tau = 38$, provided in Table 6.2. For instance, in the worst case the traditional IMC method predicts that the wavefront is at location 0.463 cm, while the IMC-TDF equations predict 0.912 cm. We also observe generally that, while the spatial grid effect is still strong (halving the spatial grid size still approximately doubles the temperatures in violation of the maximum principle), the temporal grid effect is weaker. This is represented graphically in Figures 6.9(a) and 6.9(b), which depict the temperature profile at $\tau = 8$ for variable time step and grid sizes, respectively. These figures also demonstrate that the IMC-TDF equations produce temperature profiles that are similar in character to the IMC equations [see Figure 5.6]. That is, when the maximum principle is violated, no temporal or spatial oscillations are introduced; the temperature "piles up" at the wave front and moves too slowly.

We also consider the solution of the IMC-TDF equations together with the temperature-estimation method presented in Chapter V to evaluate the problem data at the average temperature T_* defined in Eq. (5.31). The maximum temperature data at $\tau = 8$ are provided in Table 6.3. The results shown in this table are the

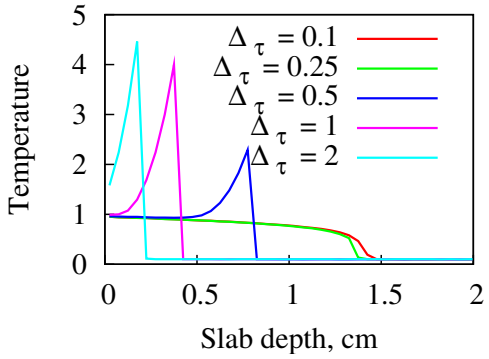

(a) Δ_x fixed at 0.05 cm.

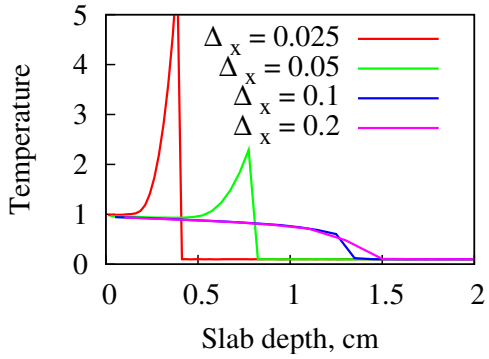

(b) Δ_τ fixed at 0.5

Figure 6.9: Temperature profiles at $\tau = 8$ for a Marshak wave problem using the IMC-TDF method in which (a) the time step is varied or (b) the spatial grid size is varied.

Table 6.3: Maximum values in temperature at $\tau = 8$ using opacities evaluated at T_* (with iteration). Bold values indicate violation of the maximum principle.

$\Delta_\tau \backslash \Delta_x$	0.025	0.05	0.1	0.2
0.10	0.957	0.950	0.945	0.937
0.25	0.951	0.950	0.945	0.936
0.50	**1.090**	0.949	0.944	0.937
1.00	**2.448**	**1.049**	**1.075**	0.937
2.00	**3.754**	**1.166**	0.948	0.933

most accurate for this problem of any presented in this thesis, including traditional IMC [Table 5.1], IMC with temperature-dependent data evaluated at T_* [Table 5.5], and the IMC-TDF equations with temperatures evaluated at T_n [Table 6.1]. This indicates that the enhancements presented thus far in Chapters V and VI are compatible. Interestingly, the maximum temperature when $\Delta_\tau = 2$ and Δ_x=0.1 cm does not violate the maximum principle, even though the entry for $\Delta_\tau = 1$ does. This is a spurious result due to a fortuitous temporal oscillation, which will be further discussed below. Table 6.4 depicts the estimate of the wavefront location for the IMC-TDF equations solved with temperature-dependent problem data evaluated at T_*. Its estimates are comparable to, but slightly worse than, the results obtained for the IMC equations using data evaluated at T_* [see Table 5.6]. Essentially, the bottom two rows of this table are all that is different, with most of the differences being relatively minor. The estimates are much better than those produced by the traditional IMC equations [Table 5.2] or the IMC-TDF equations using data at T_n [Table 6.2]. Figure 6.10(a) depicts the temperature profiles at $\tau = 8$ for variable

Table 6.4: Estimated wavefront location at $\tau = 38$ using the IMC-TDF method with opacities evaluated at T_* (with iteration)

$\Delta_\tau \backslash \Delta_x$	0.025	0.05	0.1	0.2
0.10	3.712	3.725	3.75	3.9
0.25	3.688	3.675	3.75	3.7
0.50	3.587	3.625	3.65	3.7
1.00	3.112	3.375	3.45	3.5
2.00	1.938	2.825	2.85	2.9

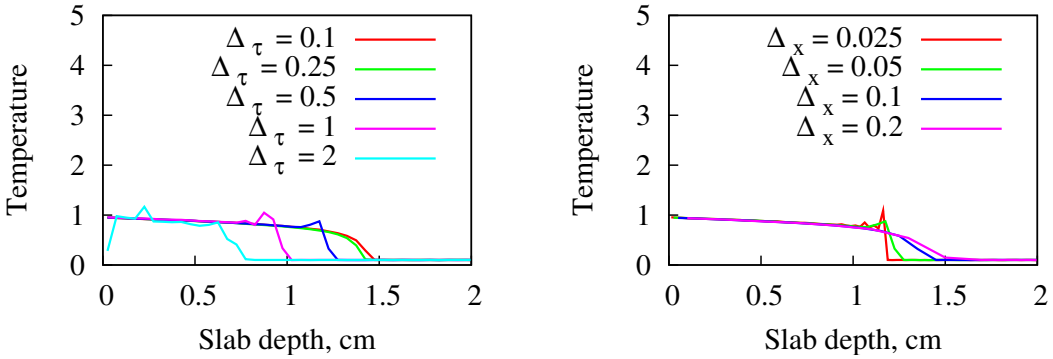

(a) Δ_x fixed at 0.05 cm.

(b) Δ_τ fixed at 0.5

Figure 6.10: Temperature profiles at $\tau = 8$ for a Marshak wave problem using a time-dependent Fleck factor in which (a) the time step is varied or (b) the spatial grid size is varied with opacities evaluated at T_* (with iteration).

values of Δ_τ with Δ_x fixed. This figure shows the somewhat remarkable suppression of the maximum principle violation that occurs for the IMC equations [Figure 5.6(a)] and for the IMC-TDF equations with data evaluated at T_n [Figure 6.9(a)]. However, we point out that for $\Delta_\tau = 2$ in this figure, the temperature is quite low near the left boundary. This is the result of a temporal oscillation – during the preceding time step, this temperature is too high. This damped temporal oscillation begins when the wavefront passes through this location, and gradually reduces in magnitude as the calculation proceeds. This behavior is indicative of the more stringent monotonicity condition in the IMC-TDF equations, although it is unlikely that the relatively simple enhancements presented in this thesis could completely resolve the inaccuracies that occur for this large a time step value. In Figure 6.10(b) we observe that the IMC-TDF equations with data evaluated at T_* also contain a weak spatial oscillation, comparable to that produced by the corresponding IMC equations [see Figure 5.9(b)].

We have demonstrated that the IMC-TDF equations generally produce more

Table 6.5: Comparison of computational times between IMC and IMC-TDF for a gray, nonlinear Marshak wave problem. The unit "h" indicates CPU-hours (not wall-clock time).

$\Delta_\tau \backslash \Delta_x$	0.025	0.2	Method
0.1	6.62 h	3.36 h	IMC
	6.83 h	3.30 h	IMC-TDF
	3.2%	-1.8%	% diff.
2.0	2.52 h	2.09 h	IMC
	2.80 h	2.57 h	IMC-TDF
	11.1%	23.0%	% diff.

accurate temperature solutions than the IMC equations under the same problem conditions. We next consider the differences in the computational cost between each of these approaches. The CPU times presented in this section represent those obtained from a serial implementation of the Monte Carlo algorithm on an Apple PowerMac consisting of dual 2.7 Ghz processors.

Table 6.5 provides the raw cpu-times in seconds for the corner entries of the above tables using the IMC ($\alpha = 1$) and IMC-TDF methods. We briefly remark that the general trend in both methods is for an increase in cost when the spatial grid size is reduced (this introduces more boundaries into the problem, at which the particles must intermittently pause), and when the time step size is decreased, which implies that more particles must be stopped and stored in the census.

In Table 6.5 we observe that the IMC-TDF method generally requires more time than the corresponding IMC calculation. This is expected because (i) the IMC-TDF method emits more energy from its $U_{r,n}$ term (which requires more particles) in any given time step, and (ii) the IMC-TDF method requires the calculation of logarithm and exponential functions that have no counterpart in the IMC method. For $\Delta_\tau = 0.1$, the differences in runtime are minor. However, when $\Delta_\tau = 0.2$, the differences are more significant (greater than 10%). This is likely because the time-dependent Fleck factor asymptotically approaches approaches 0 from the beginning to the end of the time step. When the time step size is extended this implies that a greater fraction of the time step (stretching back from the end of the time step) is more diffusive – and more costly to simulate – than that found in the IMC equations. We also observe that the worst case occurs for the largest *spatial* grid and time step sizes. It is not immediately apparent why this occurs.

While the CPU times t_{CPU} provide a measure of the increased cost, they do not

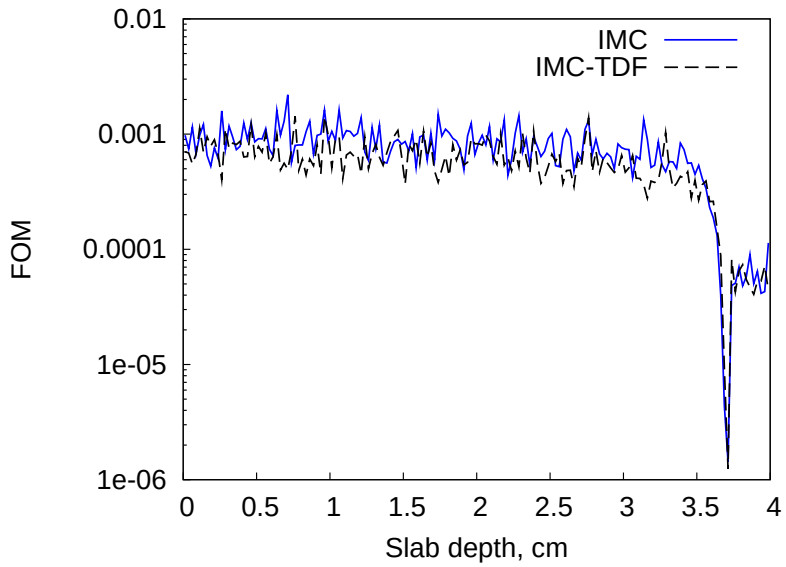

Figure 6.11: Temperature-FOM profile at $\tau = 38$ for a gray Marshak wave problem solved using the IMC and IMC-TDF methods with $\Delta_\tau = 0.1$ and $\Delta_x = 0.025$ cm.

incorporate the relative errors of the solutions. A fairer comparison of the methods requires the Figure of Merit (FOM), defined previously as Eq. (5.74) in Chapter V. In Chapter V we also discussed the differences between the calculation of the relative error R in steady-state neutronics problems and what is performed here for time-dependent TRT problems. Essentially, we calculate R using the sample mean of multiple (25 or more) independent simulations of the entire problem.

Figure 6.11 depicts the FOMs for the IMC and IMC-TDF equations at $\tau = 38$ for the most-refined choice of grid parameters, $\Delta_\tau = 0.1$ and $\Delta_x = 0.025$ cm. We note that the CPU time used to calculate the FOM in time-dependent problems is the elapsed computational time required to generate the solution at time τ beginning from the initial condition. This is in opposition to the use of a single CPU time for the entire problem or independent CPU times generated for each time step. The FOMs for these two methods are almost identical for this problem; neither method is obviously superior to the other from the standpoint of efficiency. From this figure, it does not appear that the IMC-TDF equations produce solutions with substantially different relative errors from the IMC equations. This implies that although the IMC-TDF equations may generally be expected to be more accurate than the IMC equations, the statistical variance in the two solution procedures is comparable.

Figure 6.12 depicts the FOMs for the IMC and IMC-TDF equations at $\tau = 38$ for the coarsest choice of parameters, $\Delta_\tau = 2$ and $\Delta_x = 0.2$ cm. In this figure, the FOM

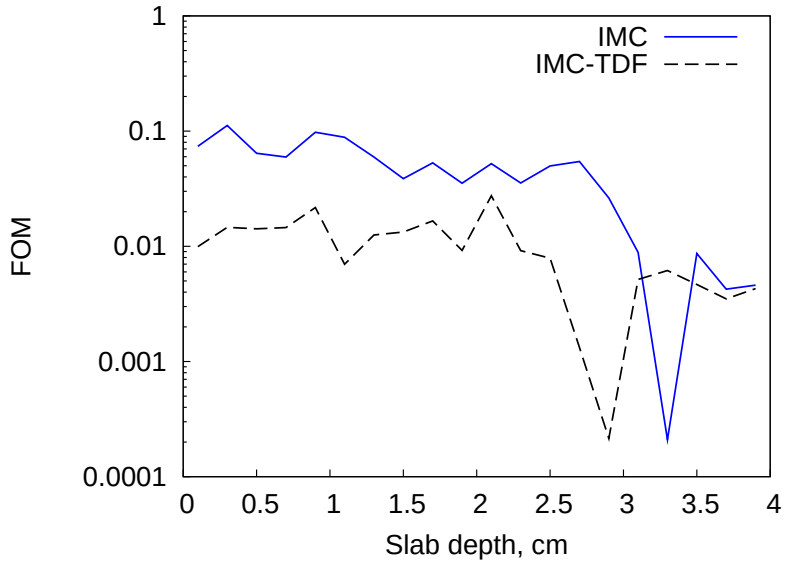

Figure 6.12: Temperature-FOM profile at $\tau = 38$ for a gray Marshak wave problem solved using the IMC and IMC-TDF methods with $\Delta_\tau = 2$ and $\Delta_x = 0.2$ cm.

for the IMC method tends to be greater than the IMC-TDF method, indicating that IMC is the superior method for this choice of grid parameters. We recall from Table 6.5 that this choice of grid parameters produced the greatest discrepancy between the CPU times required for the IMC and IMC-TDF methods. Also, the "spikes" that occur in this figure indicate approximately where the wavefronts are located. A comparison of the estimate of the wave locations using Tables 4.4 and 6.2 also verifies that the IMC equations provide a more accurate estimate of the wavefront location for the coarser spatial grid size.

We have seen that the IMC-TDF temperature solutions of the gray Marshak wave problems are generally more accurate than the IMC solutions from the standpoint of a reduction in the violation of the maximum principle and better estimates of the wavefront location. However, this comes at the cost of increased computational run-times. If the time step size is sufficiently small, the increase in cost can be negligible. As the time step size increases, however, the IMC-TDF method requires relatively greater amounts of time than a corresponding IMC calculation. Additionally, coarsening the grid size appears to increase the cost of the IMC-TDF calculation and worsen the accuracy of the IMC-TDF solutions. It does not appear that the IMC-TDF method produces solutions that are lower in variance than corresponding IMC solutions. Later, we propose a simple modification to the IMC-TDF equations that should improve its performance for large time steps.

6.3.3 Frequency-Dependent Marshak Waves

We next consider the frequency-dependent Marshak wave problem, previously defined in Chapter V. We recall that, besides the inclusion of frequency dependence, this problem further departs from the gray Marshak wave problem in that we consider the original (unscaled) TRT equations. That is, for this problem, $c \approx 300$ cm/sh [recall 1 sh $= 10^{-8}$ s] and $a = 0.01372$ jk/cm^3-keV^4. By comparison, in the gray problem, we set $c = a = 1$.

The initial condition is an equilibrium state with a Planckian frequency distribution at $T = 0.01$ keV. At $t = 0$, the left side of the slab is subjected to an isotropic burst of radiation at a Planckian temperature $T = 1$ keV. The right boundary temperature is set to the constant, initial temperature. The slab size is 4 cm thick. The opacity coefficient [γ in Eq. (2.7)] is set to 200. The Planck mean opacity is therefore $30.8T^{-3}$ which means, at equilibrium ($T = 1$), the slab is 123.2 Planck mean free paths thick, whereas at the initial condition $T = 0.01$, it is 123.2 $\times 10^6$ Planck mean free paths thick. The specific heat is set to 0.1 jk/keV-cc. We consider temperature solutions up to 1 sh. In each of the below problems, the spatial grid size Δ_x is set to 0.2 cm.

As in Chapter V, the frequency-dependent problems were computationally simulated by implementing a parallel Monte Carlo algorithm on a homogeneous, distributed memory cluster of 3.4 GhZ machines, each with 2 Gigabytes of memory. Each of the problems was performed by requesting 20 nodes of the 105-node `reserv` Linux cluster in the Nuclear Engineering division of Argonne National Laboratory Each problem was simulated using 100,000 particles/jk. To estimate relative errors and calculate figures of merit, each problem was independently simulated 50 times; the relative errors were then calculated using the sample error. All timing results refer to the sums of the computational times (not wall-clock times) reported by each processor.

For the first case, we set Δ_t to 0.001 sh. Figure 6.13 depicts the IMC (solid) and IMC-TDF temperature solutions at times of 0.3, 0.6, and 0.9 sh. For this choice of spatial and temporal grids, no difficulty emerges with regard to the maximum principle; the temperature wave forms and travels rightward. The temperature solutions of the IMC and IMC-TDF methods agree well.

The total time required for the IMC solution is 74.4 CPU-hours. The total time required for the IMC-TDF simulation is 12.8 % less at 64.9 CPU-hours. This result is somewhat unexpected, as we have indicated previously that the IMC-TDF method

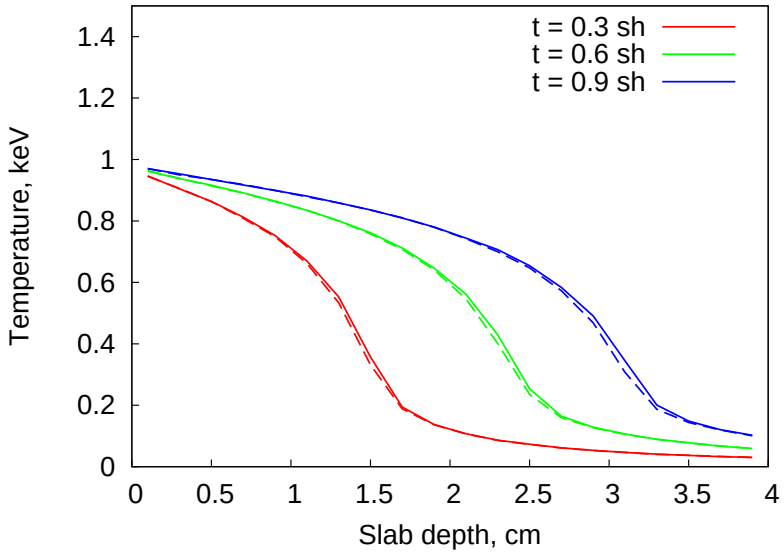

Figure 6.13: Temperature profiles for a frequency-dependent Marshak wave problem solved using the IMC (solid) and IMC-TDF (dashed) methods.

requires additional calculations relative to the IMC method. The reduction could perhaps be due to the small time step employed. We recall that early in the time step, the relative contribution of effective absorptions is dominant [see Figure 6.1]. It is possible that for small time steps, this leads to a net reduction in the required computation time relative to the IMC method. We will return to a discussion of the computation time when we consider the effects of increasing the time step size.

Figure 6.14 depicts a semilog plot of the temperature-FOMs for the IMC and IMC-TDF methods at $t = 0.9$ sh. These FOMS indicate that the temperature-FOMs of the IMC and IMC-TDF methods are comparable for this problem and choice of grid parameters.

We next consider increasing Δ_t by a factor of 20 to 0.02 sh. We note that this is a relatively large time step size for this problem. The effect of this change on the CPU-time comparison is dramatic – the total time required by the IMC method is 59.4 hours, whereas the IMC-TDF method required 501.6 hours. That is, the IMC-TDF method takes approximately 8.4 times longer than the IMC method. Figure 6.15 indicates the effect this has on the temperature-FOM at $t = 0.9$ sh – the IMC method is about two orders of magnitude superior to the IMC-TDF method.

Figure 6.16 provides a semilog plot of the cumulative CPU-time required to simulate each of the frequency-dependent Marshak wave problems as a function of the time step. This figure reveals that the majority of the CPU-time is spent during

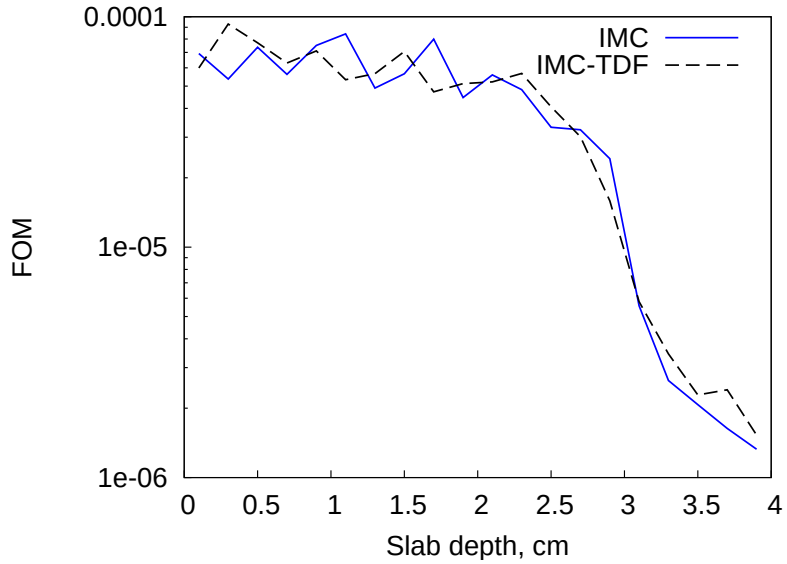

Figure 6.14: Temperature-FOM profiles at $t = 0.9$ sh for a frequency-dependent Marshak wave problem solved using the IMC and IMC-TDF methods.

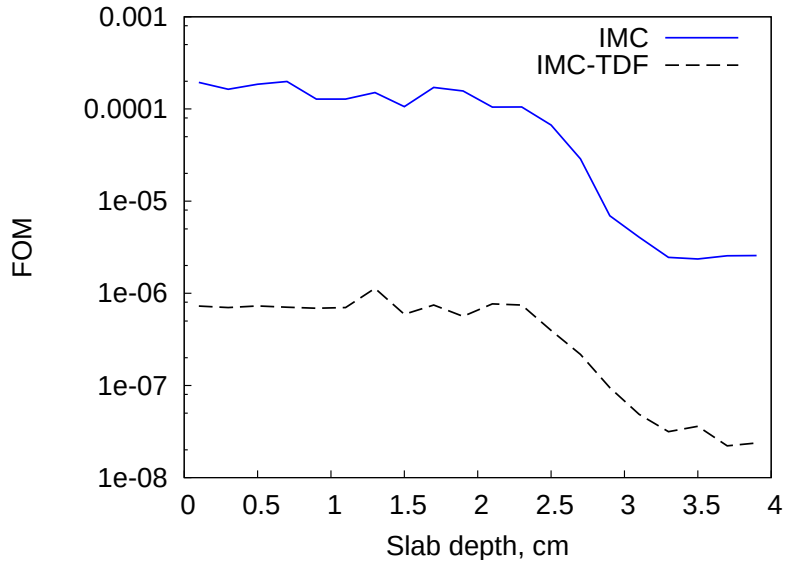

Figure 6.15: Temperature-FOM profiles at $t = 0.9$ sh for a frequency-dependent Marshak wave problem solved using the IMC and IMC-TDF methods.

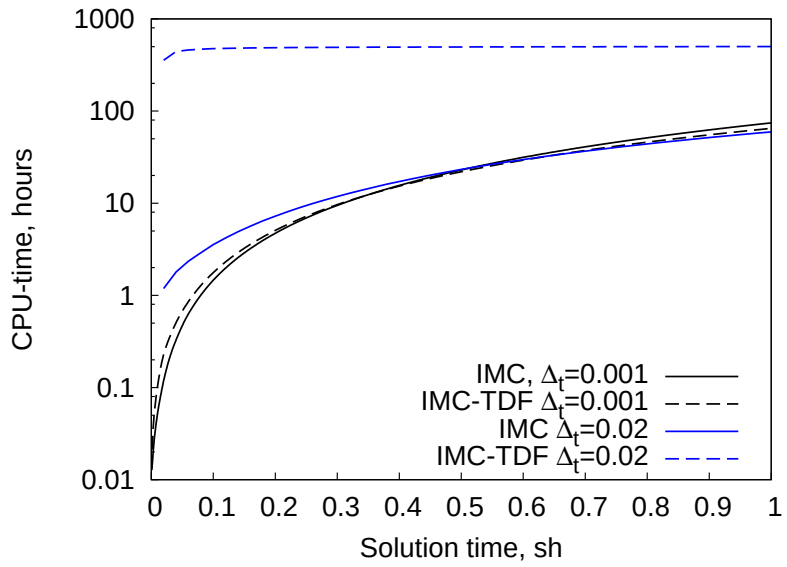

Figure 6.16: Cumulative CPU-times required to generate solutions at each time step using the IMC (solid) and IMC-TDF (dashed) methods with $\Delta_t = 0.001$ sh (black) and $\Delta_t = 0.02$ sh (blue).

the early time steps when most of the problem spatial domain is in near-equilibrium (this is the motivation for the difference formulation discussed in [57]). Increases in time step size enhance this effect. For the IMC-TDF method with $\Delta_t = 0.02$ sh, nearly all the of CPU-time is spent in the first time step. During the first time step, all Monte Carlo particles transport through the relatively cold, thick cells. When the IMC-TDF method is employed for large time steps, the effective scattering ratio can be large for the majority of the time step. Together, these factors indicate that the IMC-TDF method will require a much larger number of effective scatter events, which leads to the increase in the CPU-time.

We have demonstrated that the IMC-TDF method can be more accurate for gray Marshak wave problems and produce comparable solutions to IMC for an example frequency-dependent problem. We have also shown that the FOMs for the IMC and IMC-TDF methods compare well so long as the time step does not become too large. When the time step does become large, the IMC-TDF method can take much longer to simulate than the IMC method. Additionally, this large increase in cost is not balanced by a corresponding increase in accuracy, as both the IMC and IMC-TDF equations become inaccurate for large time steps.

As future work, it may be possible to remedy this problem by using a modified time-dependent Fleck factor in which the effective scattering ratio is limited to the value used in the IMC equations with $\alpha = 1$. To illustrate this we will use the

dimensionless time variable τ. We propose the following modification to $f_n(\tau)$:

$$f_n'(\tau) = \begin{cases} e^{-4(\tau-\tau_n)} & \tau_n \le \tau \le \tau_* \\ \frac{1}{1+4\Delta_\tau} & \tau_* < \tau \le \tau_{n+1} \end{cases}, \quad \tau_* = \tau_n + 0.5\ln(1+4\Delta_\tau)\,. \tag{6.63}$$

Thus, for $\tau \le \tau_*$, the time-dependent Fleck factor in Eq. (6.16) is used; for $\tau_* < \tau$, the "traditional", constant Fleck factor in Eq. (6.17) is used, and τ_* is chosen such that the two Fleck factors are equal. If the Fleck factor defined by Eq. (6.63) is used instead of Eq. (6.16), then the effective scattering ratio is limited by the traditional value used in Eq. (6.17). This modified time-dependent Fleck factor is designed to increase the accuracy of the IMC equations without significant increases in the required computational time. The implementation changes for the modified IMC-TDF equations would be slightly more complicated than the IMC-TDF equations, but not overly burdensome. For instance, the time-distribution of the source particles due to the $U_{r,n}$ term would no longer be purely exponential; it would be exponential for $\tau \le \tau_*$ and uniform for $\tau_* \le \tau$. Although we are unable to investigate this modified IMC-TDF method, we anticipate that it should retain the increase in accuracy for small time steps without corresponding increases in computational cost for large time steps. Since we have shown that the IMC and the IMC-TDF equations are unconditionally stable, we expect this modified approach to also be stable, although the 0-D stability analysis presented in Chapter IV should be performed before further development.

6.4 Summary

In this chapter we have presented an alternative, more accurate derivation of the IMC equations that leads to equations containing a time-dependent Fleck factor $f_n(t)$: the IMC-TDF equations. Our derivation avoids the dubious approximation that occurs in [21] when time-average unknowns are replaced by "instantaneous" unknowns, and it eliminates the user-defined parameter α. The IMC-TDF equations retain the fundamental form of the IMC equations, so few changes would be necessary to modify existing computational algorithms for the IMC equations.

We began by deriving the IMC-TDF equations from the 1-D form of the TRT equations. The essential departure from the derivation of the IMC equations occurs when the approximate equation for $U_r(t)$ is generated. In the IMC derivation, the equation for $U_r(t)$ is time-averaged, α is introduced, and the time-average un-

knowns $\overline{U_r}$ and $\overline{I}$ are replaced with their instantaneous counterparts $U_r(t)$ and $I(t)$ [see Eq. (3.16)]. This results in an equation for $U_r(t)$ that is not exact at $t = t_n$, though it correctly reproduces the original time-average equation for $\overline{U_r}$. In the IMC-TDF equations, this procedure is circumvented by treating the time-integral of $I(t)$ "implicitly." The resulting equation for $U_r(t)$ is exact at $t = t_n$.

The time-dependent Fleck factor $f_n(t)$ in the IMC-TDF equations does not contain any user-defined parameters. We discussed (but did not numerically investigate) how the time-average of this Fleck factor, $\overline{f_n(t)}$, could be employed to define an adaptive value of the user-defined parameter α in the IMC equations. For small time steps, $\overline{f_n(t)}$ limits to the traditional Fleck factor f_n with $\alpha = 0.5$. For large time steps, it limits to f_n with $\alpha = 1$. The adaptive value of α can therefore be obtained by setting $\overline{f_n(t)} = f_n$ and solving for α [see Eq. (6.21)]. As future work, and as a transition to the introduction of a fully time-dependent Fleck factor, one could consider using the adaptive value of α defined in Eq. (6.21) in the IMC method.

We also discussed how the time-dependence of $f_n(t)$ affects the particle transport throughout the time step. One of the effects is that particles due to $U_{r,n}$ are introduced throughout the time step according to an exponential distribution function. This behavior better approximates the underlying problem physics than the IMC equations, which employ a uniform distribution throughout the time step. Another effect is that particles are more likely to undergo effective absorptions at the beginning of the time step and more effective scatters at the end of the time step, because the effective scattering ratio is very small at the beginning of the time step but increases during the time step. For large time steps, this leads to a system of equations that is highly diffusive at the end of the long time step. As future work, it would likely be advantageous to incorporate one of the diffusive modifications to reduce the computational cost discussed in [25] or [26], or to investigate the modification to the IMC-TDF method proposed in Eq. (6.63).

Using the 0-D stability analysis algorithm provided in Chapter IV, we proved that the IMC-TDF equations are unconditionally stable. They are also slightly more susceptible to damped temporal oscillations in that smaller time steps are required to preclude them. We derived monotonicity conditions for the IMC-TDF equations. They are slightly weaker than the IMC equations with $\alpha = 0.5$, but stronger than the IMC equations with $\alpha = 1$. It is not possible to find a monotonicity condition for the IMC-TDF equations that holds for all values of β and σ as was shown in Chapter IV for the IMC equations. This arguably limits the viability of the IMC-TDF equations, although the "global" monotonicity condition for the IMC equations

(which stipulates that time steps must be smaller than two mean free times between particle collisions) is too restrictive to be met in practice.

We discussed the three algorithmic changes necessary to convert an existing IMC algorithm to one that solves the IMC-TDF equations. Although the differences are minor from an implementation standpoint, they will generally lead to increased computational costs. For small- to average-size time steps, the differences can be minor. For sufficiently large time steps, the differences can be substantial. We note that the IMC equations have been adapted for deterministic methods. Although the implementation changes between Monte Carlo algorithms that solve the IMC and IMC-TDF equations are minor, modifications to a deterministic method for the IMC equations are not straightforward. Therefore, the enhancements to IMC developed in this chapter for Monte Carlo algorithms would be problematic to implement in a deterministic algorithm.

We numerically tested the accuracy of the IMC-TDF equations by considering linear and nonlinear gray, 0-D problems. For the linear problem, we demonstrated that the IMC-TDF equations are second-order accurate in Δ_t. This matches the order of accuracy in the IMC equations with $\alpha = 0.5$, although this value of α is almost never used in computational implementations of the IMC equations due to inaccuracies that appear when Δ_t is sufficiently large. For the nonlinear problem, little gains in accuracy were observed, and the IMC-TDF equations were found to be just as susceptible to overshooting as the IMC equations. However, when the IMC-TDF equations are combined with the temperature-estimation algorithm described in Chapter V, large gains in accuracy occur, indicating that a better treatment of the temperature-dependent problem data is a much more important effect than the employment of $f_n(t)$.

We considered Monte Carlo solutions of the IMC-TDF equations applied to a gray, nonlinear, Marshak wave problem. For these problems, we demonstrated that the IMC-TDF equations do not violate the maximum principle to the same extent that the IMC equations do on corresponding problems. This leads to more accurate estimates of the wavefront location. We also considered a combination of the IMC-TDF equations with the temperature estimation algorithm presented in Chapter V. This combination of approaches led to a substantial suppression in the maximum principle violation that occurs in the corresponding IMC temperature solutions. We compared the relative computational costs of four IMC-TDF calculations to corresponding IMC calculations and noted that the general trend is that the IMC-TDF calculations require more CPU-time. This is anticipated because (i) the IMC-TDF

method emits more energy from its $U_{r,n}$ term (which requires more particles) in any given time step, (ii) the IMC-TDF method requires the calculation of logarithm and exponential functions that have no counterpart in the IMC method. We reported that increasing the size of the time step – and in one case, the spatial grid size – increases the relative cost of an IMC-TDF calculation. Comparisons of the temperature-FOM essentially reflected the differences in calculation time; the IMC-TDF equations did not exhibit significant reductions in relative error to compensate for their increased cost in the worst case of the coarsest choices of grid parameters.

We also considered a frequency-dependent Marshak wave problem. Due to time and resource constraints, we could not fully examine the effects of varying the spatial and temporal grid sizes for this problem. We saw that using $\Delta_t = 0.001$ sh in the IMC and IMC-TDF methods produced temperature profiles in agreement and comparable temperature-FOMs. However, a calculation that employed $\Delta_\tau = 0.02$ sh led to an 8-fold increase in the CPU time for the IMC-TDF equations relative to the IMC equations. The majority of calculation time for the IMC-TDF method with this relatively large time step size occurs during the first time step, in which a large number of effective scatter events must be simulated. To remedy this, we proposed the use of a modified IMC-TDF method. The modified IMC-TDF method contains a time-dependent Fleck factor that combines the IMC-TDF and IMC Fleck factors so that the effective scattering ratio of the modified Fleck factor is limited by the effective scattering ratio of the traditional IMC Fleck factor [see Eq. (6.63)]. This should produce a method that is more accurate than the IMC method without the associated increase in cost for large time step sizes, although we were not able to numerically test this hypothesis.

To summarize the future work recommended in this chapter, the numerical results should be extended to multi-dimensional problems, and parametric studies of the spatial and temporal sizes should be performed. For instance, we demonstrated that for small time step sizes in gray and frequency-dependent Marshak wave problems, the IMC-TDF equations can require less CPU-time than the IMC equations. Further reductions in the time step size should also be investigated. Additionally, the computational performance of the IMC-TDF equations could likely be enhanced by the diffusive approximations described in [25] and [26]. As a transition to the introduction of a fully time-dependent Fleck factor, one could consider replacing f_n in the IMC equations with $\overline{f_n(t)}$ defined by the IMC-TDF equations, or using Eq. (6.21) to implement an adaptive α in the traditional IMC method. We also proposed a modified time-dependent Fleck factor in Eq. (6.63) that is a combination of the IMC-

TDF and IMC Fleck factors. This modified IMC-TDF approach should improve the accuracy of the IMC equations for small time steps while preventing the substantial increase in computation time that occurs if the desired time step is large and the problem contains optically-thick spatial regions.

Chapter VII

A Global Weight Window

In the introduction to Chapter VI, we discussed that the efficiency of IMC calculations has been improved by using the diffusion approximation [25] [26]. In these methods, a modification of the particle transport process in the IMC algorithm is made in order to obtain the desired increase in efficiency. These modifications require additional approximations to the IMC equations. If the parameters that "turn on" these approximations are properly chosen, then the IMC calculation proceeds more rapidly without a substantial degradation in accuracy. In particular, the method due to Fleck and Canfield [25] is commonly used. Another enhancement technique requires recasting the TRT equations using a difference formulation [57] [58]. The IMC approximations are then applied to a radiation equation for the additive correction to the problem's equilibrium condition. This relatively new technique has been demonstrated to be more efficient in problems that contain regions that are near equilibrium. However, Smedley-Stevenson has found that the difference formulation may be fundamentally incompatible with traditional IMC because of the statistical noise that can be introduced from negative particle weights [58].

By contrast, variance reduction techniques for Monte Carlo problems are well-known to increase the efficiency in the solution estimate without a required modification to or approximation of the underlying equations. Variance reduction techniques should also be compatible with the diffusion-approximation methods in [25] and [26]. However, the employment of "standard" Monte Carlo variance reduction techniques described at the end of Chapter III (Russian roulette, particle splitting, and weight windows) has not, until recently [16], been a practical choice for TRT problems. This is due to a distinction that must be made between Monte Carlo problems that are *local* in nature, in which the solution is desired in a relatively small portion of phase space, and problems that are *global*, in which solutions must be obtained throughout

phase space.

Variance reduction techniques for local problems exploit the locality of the solution phase space to increase the efficiency of each history. If we consider a source-detector problem, then the detector and the regions containing the flight paths of particles that are most likely to journey to the detector are important, whereas regions far removed from these flight paths are not. The variance in the detector response may be reduced by ensuring that Monte Carlo particles follow these flight paths with a high probability, but without biasing the mean of the solution. Typically, this is achieved by employing a weight window method as described in Chapter III. However, determining the proper average weight throughout the problem phase-space requires much trial-and-error and an experienced, patient code user to adjust the parameters to an acceptable level. We note that it is sometimes possible to automatically and dynamically adjust these parameters during the Monte Carlo calculation [14]. If the problem is "simple enough" to determine a proper weight window by trial-and-error or by an adaptive Monte Carlo process, then its solutions should generally contain less variance and require shorter computational times. However, if the weight window is chosen poorly, the variance could become worse and/or the computational time could increase.

The choice of a proper average particle weight therefore becomes the "categorical imperative" for Monte Carlo variance reduction techniques. It has been shown that the "important" regions of a source-detector problem are proportional to the inverse of the adjoint solution, in which the detector region is employed as an adjoint source term [15]. Hybrid deterministic-Monte Carlo approaches exploit this fact by employing a deterministic calculation to obtain a global estimate of the adjoint solution, and then setting the inverse of the adjoint solution as the center of a weight window in a Monte Carlo calculation. It is not necessary to obtain a highly accurate adjoint solution, but generally, more accurate deterministic solutions yield more efficient Monte Carlo calculations.

Unfortunately, the use of an adjoint solution is not directly applicable to global Monte Carlo problems. Recently, Cooper and Larsen have demonstrated that the weight window for global problems should be proportional to the *forward* solution [16] [17]. As we shall demonstrate, choosing the weight window in this way implies that the Monte Carlo particle number density should be more spatially uniform than the corresponding neutron (or photon) number density, which may contain large gradients. This more equal redistribution of Monte Carlo particles throughout the problem's phase space reduces the statistical errors in the usually problematic

low-neutron (or photon) density regions. Using this approach, Cooper was able to numerically obtain figures of merit (FOMs) in 2-D steady-state neutron transport problems that are much higher than corresponding Monte Carlo calculations that used absorption weighting only. In his thesis, Cooper also examined the application of the forward weight window scheme to a 1-D, gray, nonlinear TRT problem, with mixed success. In this chapter, we develop a weight window for nonlinear gray and frequency-dependent problems. However, the method presented in this chapter contains a primary difference in character from that presented in Cooper's research for the following reasons.

Cooper did not consider energy (or frequency) dependent problems in his thesis, but it is implicated that the weight windows for such problems be energy or frequency dependent, according to the forward solution of the multigroup radiation equation.[1] We shall discuss this in greater detail later; for now we assert that choosing weight windows in this way gives each energy (or frequency) group in the Monte Carlo problem roughly equally-distributed Monte Carlo particle densities. Although this procedure should lead to more uniform statistics in every energy group, it does not reflect the physical importance of the underlying problem, and for problems with a large number of energy groups, it can lead to a hugely expensive calculation in which all energy groups, even the ones that are relatively unimportant, receive the same degree of computational effort. For example, a recent task at Oak Ridge National Laboratory required a global Monte Carlo solution of an entire reactor building to estimate the neutron dose (energy absorbed) [61]. Peplow reportedly attempted a multigroup application of Cooper's method, but we found the required calculation times to be prohibitively long. This is likely because each neutron energy group is *not* equally important with regard to the contributed dose. Peplow remedied this problem through an interesting combination of the adjoint *and* forward solutions of deterministic transport problems, which we do not consider in this thesis.

Instead of using frequency-dependent weight windows that give all particle frequencies equal importance, in this chapter we consider the use of a frequency-averaged (gray), forward weight window generated from the Quasidiffusion procedure in Chapter V [Eq. (5.14a)]. This implies that the Monte Carlo particle number density will therefore have (in the limit of an infinite number of particles) the same frequency distribution as the underlying radiation intensity. We have learned that

[1] Technically, a further adjustment must be made for neutron transport problems – the weight window should actually be made proportional to ψ/v, where v is the neutron speed and ψ is the angular flux, equal to v times the neutron number density.

Terry Adams of Los Alamos National Laboratory has employed some form of this procedure to solve time- and energy-dependent, multidimensional neutron transport problems with reported success [51]. However, because his results are unpublished, the specifics of his approach are unclear.

We also note that a competing hybrid method has been proposed by Wollaber and Larsen (and by Becker, Wollaber, and Larsen) for global radiation transport problems that may be applicable to TRT problems [62] [63]. In this "correcton" method, a deterministic procedure is used to generate an estimate of the forward scalar intensity, and a Monte Carlo procedure is used to solve an equation for the multiplicative correction to the estimated intensity. This method was considered in detail during the course of this research. It was found to be very successful for a series of 1-D gray, linear and nonlinear TRT problems, but it did not perform adequately on frequency-dependent problems. For this reason and due to time constraints, we decided not to pursue this method further. However, Becker is continuing to develop the method for steady-state, energy-dependent neutron transport problems.

We begin this chapter by motivating the use of a frequency-averaged, forward solution of the TRT radiation equation. In his thesis, Cooper provides a similar, but more heuristic motivation [17]. Our motivation is based upon the Monte Carlo number density $M(x, \mu, \nu, t, w)$ defined in Chapter III, in which w is the particle energy-weight. Using M, we compare the differences between using a global weight window that is centered about the exact forward solution throughout all of phase space (x, μ, ν, t) and a weight window that is centered about a frequency- and angularly-collapsed version of phase space (x, t). We then describe the basic algorithm we use for generating a weight window center $w_c(x)$. Essentially, the algorithm capitalizes on the frequency- and angle-averaged scalar intensity solution $\langle I \rangle_{n+1}$ produced by the deterministic Quasidiffusion algorithm in Chapter V. In that Chapter, $\langle I \rangle_{n+1}$ was calculated solely to generate an estimate of the temperature T_{n+1}; afterwards, it was discarded. Here, we re-employ it by setting $w_c(x) = \langle I \rangle_{n+1}$. After $w_c(x)$ is calculated, a weight-window IMC algorithm is performed over the time step $t_n \leq t \leq t_{n+1}$ to generate new solutions of T_{n+1} and I_{n+1} that supersede the solutions obtained by the deterministic Quasidiffusion method.

In his thesis, Cooper also presented a deterministic Quasidiffusion calculation to estimate the forward intensity [17]. However, he limited his analysis to 1-D, nonlinear, gray problems. The Quasidiffusion equations he generated are superior for gray problems in that they are automatically flux-limited, but they are not easily extendable to frequency-dependent problems.

We also discuss an enhancement that modifies the weight window for Marshak wave problems. At any time, a 1-D Marshak wave problem can be roughly divided into three spatial regions: the regions behind, in the vicinity of, and ahead of the wavefront. Accurate solutions are desired in the regions behind and in the vicinity of the wavefront, but regions ahead of the wavefront – where the solution is typically near equilibrium – are relatively unimportant. The enhancement we propose modifies the weight window generated by the deterministic calculation to prevent excessive particle tracking and its associated increase in computation time in regions ahead of the wavefront. Cooper discussed a related modification in his thesis [17], but later, after difficulties were encountered, he remarked that it was likely "too crude."

After motivating the use of this weight window, we numerically test the procedure on a series of gray and frequency-dependent Marshak wave problems. We compare the FOMs and computation times between the IMC method and its enhancement using weight windows. We also compare a combination of the temperature estimation technique presented in Chapters V with the global weight window technique defined here, as they are algorithmically compatible. We examine the Monte Carlo particle densities to assess the claims that using a weight window defined by a forward calculation should more uniformally spatially distribute the Monte Carlo particles.

To be clear, the following is a list of the essential distinctions between the hybrid global weight window discussed in Cooper's thesis and the method presented here.

1. Frequency (energy) dependence is not considered in Cooper's thesis.

2. Cooper's discussion of the forward weight window requires the use of a multigroup deterministic calculation and subsequently-defined multigroup weight windows. Our weight window is based upon the frequency-averaged, forward scalar intensity.

3. Cooper employs an adaptive updating technique that recalculates the weight windows based upon incremental improvements in the statistical properties of the Monte Carlo estimate of the Eddington factors. This is implemented by periodically pausing the Monte Carlo calculation and re-running the deterministic calculation. This process is essential in steady-state problems, but likely not as important in TRT problems where the solution of the previous time step usually provides an adequate estimate of the Eddington factors. Cooper also reported that this process can produce statistical instabilities in the IMC calculation. By contrast, we do not consider adaptively updating the Eddington factors or

frequency-averaged opacities; during each time step, the deterministic method and IMC method occur exactly once, and in order.

4. Cooper's gray Quasidiffusion equations are derived so that they are automatically flux-limited. Unfortunately, his derivation of the Quasidiffusion equation for gray problems cannot easily be extended to frequency-dependent problems while preserving their flux-limiting property. By contrast, our Quasidiffusion equation (derived in Chapter V is based upon an accurate treatment of the frequency-averaged TRT equations, although it is not flux-limited.

5. It is not clear that Cooper addressed the issue of energy conservation when Russian rouletting is used. Our implementation of Russian roulette, discussed in Chapter III, rigorously conserves energy.

6. Cooper proposed an enhancement, or modification to the weight window to prevent excessive particle splitting ahead of the wavefront. The method we propose is more sophisticated, although likely suboptimal. For instance, Cooper's modification to the weight window is "binary" in space: it turns on or off whenever a certain condition is met. Our modification is spatially continuous.

7. The Marshak wave problems that we consider are more difficult than those considered in Cooper's thesis, as ours contain larger differences between the boundary and initial temperatures and are more optically-thick. Also, Cooper's numerically-obtained FOMs represented relatively marginal improvements over the IMC method. Our numerically-obtained FOMs are typically an order of magnitude superior to the IMC method.

We note that the use of a global weight window should not affect the stability characteristics of the IMC method. We also note that the use of a weight window affects only the variance, and not the mean, of the problem solution, in the limit of an infinite number of particle histories.

7.1 A Global Weight Window

In his thesis, Cooper argued that the center of a weight window for a global particle transport problem should be obtained using an estimate of the the forward solution [17]. We begin our discussion by revisiting that assertion and putting it upon a more solid foundation using the notation defined in Eq. (3.43). The intensity

I is related to the Monte Carlo number density M by:

$$I(x,\mu,\nu,t) = \int_0^\infty cwM(x,\mu,\nu,t,w)\,dw\,, \tag{7.1}$$

where w is the *energy-weight* of the Monte Carlo particle, as discussed in Chapter III. Cooper's claim is that in a "perfect" global Monte Carlo procedure, the center of the weight window should be proportional to the forward solution I. For a very thin weight window, this corresponds to stipulating that M be of the form:

$$M(x,\mu,\nu,t,w) = \hat{M}(x,\mu,\nu,t)\delta\left(cw - I(x,\mu,\nu,t)\right)\,, \tag{7.2}$$

where $\hat{M}$ is (for now) an unknown Monte Carlo particle density that is independent of the energy-weight. We note the constant of proportionality c is the speed of light for this argument, but in a "real" Monte Carlo algorithm, this must be modified to account for the actual number of particles used to represent a unit of the radiation energy. Substituting Eq. (7.2) in Eq. (7.1), we may solve for $\hat{M}$:

$$\begin{aligned} I(x,\mu,\nu,t) &= \int_0^\infty cw\hat{M}(x,\mu,\nu,t)\delta\left(cw - I(x,\mu,\nu,t)\right)\,dw\,, \\ I(x,\mu,\nu,t) &= I(x,\mu,\nu,t)\hat{M}(x,\mu,\nu,t)\,, \\ \hat{M}(x,\mu,\nu,t) &= 1\,. \end{aligned} \tag{7.3}$$

This demonstrates that setting the center of an "infinitely thin" weight window to be exactly proportional to the forward solution produces a Monte Carlo particle density that is *independent* of space, time, angle, and frequency. In other words, this hypothetical Monte Carlo algorithm will uniformly distribute Monte Carlo particles throughout all phase space. This is advantageous if the solution is desired throughout all regions of phase space, as would be assumed from the moniker "global problem".

Often, despite the use of the term "global", this behavior is not what is desired. For instance, in TRT problems, an accurate temperature solution may be of more interest than an accurate intensity solution over all possible frequencies. Thus, although the method defined by Eq. (7.2) represents the correct starting point, it is reasonable to relax the requirement that *all* portions of phase space be equally populated. Additionally, the mechanics of implementing an angle and frequency-dependent weight window can be complicated, as they can introduce "extra" calculations into the problem that are not necessary if adequate resolution in angle and frequency is not desired. Therefore, instead of defining a weight window based upon

Eq. (7.2), we propose the following modification:

$$M(x,\mu,\nu,t,w) = \hat{M}(x,\mu,\nu,t)\delta\left(cw - \langle I\rangle(x,t)\right)\,, \tag{7.4}$$

where we have used the angle bracket notation (as in Chapter V) to indicate integration over all directions $[\mu]$ and frequencies $[\nu]$ and $\hat{M}$ is again to-be-determined. The difference between the weight window center in Eq. (7.2) and Eq. (7.4) is the exclusion of angle- and frequency- dependence. Substitution of Eq. (7.4) into Eq. (7.1) gives:

$$\begin{aligned} I(x,\mu,\nu,t) &= \int_0^\infty cw\hat{M}(x,\mu,\nu,t)\delta\left(cw - \langle I\rangle(x,t)\right)\,dw\,, \\ I(x,\mu,\nu,t) &= \langle I\rangle(x,t)\hat{M}(x,\mu,\nu,t)\,, \\ \hat{M}(x,\mu,\nu,t) &= \frac{I(x,\mu,\nu,t)}{\langle I\rangle(x,t)}\,. \end{aligned} \tag{7.5}$$

If we integrate Eq. (7.5) over all angles and frequencies, we obtain:

$$\langle\hat{M}\rangle(x,t) = 1\,. \tag{7.6}$$

Thus, the Monte Carlo particle density from this modified weight window center is *not* uniform over all phase space; it is only uniform over position and time. Furthermore, Eq. (7.5) says that the frequency-angle distribution of M should be proportional to the frequency-angle distribution of I. This implies that using a weight window center defined in Eq. (7.4) produces a scheme in which the importance of the frequency and angle distributions of the Monte Carlo particles is exactly matched to that of the physical problem ("physically important" photon frequencies match the "numerically important" Monte Carlo particle frequencies). For the following reasons, this treatment should be superior to assuming that each frequency is equally important, as is assumed if Eq. (7.2) is used to set the weight windows.

First, an estimate of the center of the weight window generally must be made available to the Monte Carlo algorithm prior to the calculation. If that estimate contains full phase-space dependence, then it is just as difficult to generate the estimate as it is to perform the Monte Carlo calculation; a full transport solution is necessary. By contrast, excluding the angle and frequency variables from phase space as in Eq. (7.4) simplifies and reduces the cost of the weight window calculation. Also, even if a weight window such as Eq. (7.2) could be made available to the Monte Carlo calculation, it would be costly to implement. For instance, when

an effective scatter event occurs in the IMC calculation, a photon changes its frequency. If the photon emerges from an effective scatter at a frequency for which the the weight window center defined in Eq. (7.2) is relatively low then it must be split. Since the frequency-dependence of the Planck function, for instance, varies by several orders of magnitude, then the required amount of splitting could become excessive if the difference between the entering and emerging frequencies is sufficiently large. Additionally, although angle-dependent weight windows have been demonstrated to be successful [17] [63], they can be difficult to extend to problems that contain anisotropic scattering (we do not consider such problems in this thesis, but more general TRT problems do contain anisotropic scattering). Finally, even if these implementational issues of using Eq. (7.2) could be overcome, a uniform distribution of Monte Carlo particles in all frequencies is still undesirable. According to the frequency-dependence of the absorption opacity, certain frequencies are actually more important than others with respect to their contribution to the temperature solution. Thus, an equal distribution of particles among all frequencies would "waste" time following particles in relatively unimportant frequencies.

7.1.1 The Global Weight Window Algorithm

In Chapter V, we discussed a temperature estimation algorithm that involves the solution of frequency-averaged (gray) Quasidiffusion equation as an intermediate step to obtain an estimate of the temperature at the end of the upcoming time step T_{n+1}. We then numerically demonstrated that using a properly time-averaged temperature T_* to evaluate the problem data in a subsequent IMC calculation over the same time step produces a much more accurate solution. However, after generating T_*, we discarded the gray, scalar intensity information generated by the solution of the Quasidiffusion equation – in Chapter V, this information was solely a means to obtain the temperature estimate.

Instead of discarding the gray scalar intensity $\langle I \rangle_{n+1}$, we propose using it to set the center of the weight window $w_c(x)$. This weight window center is of the form depicted in Eq. (7.4); the only difference is that the scalar intensity generated from the temperature estimation algorithm is approximate. This is permissible so long as the weight window center is sufficiently accurate to capture the spatial and temporal variation of the IMC intensity solution, and the width of the weight window is large enough to accommodate any errors. Generally, more accurate weight window centers should produce more efficient Monte Carlo solutions.

To be more clear, the "temperature estimation" algorithm described in Chapter

V is modified in the following way. During a time step $t_{n-1} \leq t \leq t_n$, a frequency-dependent IMC calculation is performed. Throughout the calculation, the quantities σ_I, σ_ρ, and E [defined in Eqs. (5.5) (5.13) and (5.12)] are averaged over frequency and angle. These data are then provided to the Quasidiffusion method, which uses them to estimate $\langle I \rangle_{n+1}$ (and, if desired, T_{n+1} and the time-average temperature T_*) for the upcoming time step $t_n \leq t \leq t_{n+1}$. The estimate of the gray, scalar intensity solution $\langle I \rangle_{n+1}$ is then used as the center of a weight window $w_c(x)$ for an IMC calculation over the same time step $t_n \leq t \leq t_{n+1}$. The IMC solution of I_{n+1} (and T_{n+1}) then supersedes the solution produced by the Quasidiffusion method.

In Chapter V, we discussed the Quasidiffusion method in detail. There, we applied a Quasidiffusion approximation to the TRT equations [Eqs. (5.14)], performed an implicit time-discretization [Eqs. (5.26)], defined an iteration procedure to improve their accuracy [Eqs. (5.36)], and provided a finite volume spatial discretization [Eqs. (5.57)]. The solution procedure of the Quasidiffusion equations for a general time step $t_n \leq t \leq t_{n+1}$ is summarized in the following algorithm.

1. Set the iteration index $i = 1$, and set $T_{n+1}^{(0)} = T_n$.
2. Set $T_{n+1}^{(i)} = T_{n+1}^{(i-1)}$.
3. For each spatial cell k, initialize the quantities in Eqs. (5.35).
4. Solve the system given by Eqs. (5.57) for $\phi = \langle I \rangle_{n+1}$.
5. For each spatial cell k, update $T_{n+1}^{(i+1)}$ according to Eq. (5.36b) and Eq. (5.36c).
6. If converged or iteration is not desired, stop iterating. If not, set $i \leftarrow i+1$ and begin again at step 2.
7. Provide $\langle I \rangle_{n+1}$ to the IMC calculation to be set as $w_c(x)$, the center of a weight window. Optionally, provide T_* [generated from the latest iteration of Eqs. (5.33)] to improve the evaluation of the temperature-dependent problem data, although this is not fundamental to the weight window algorithm.

The user has the flexibility of specifying the width of the weight window about $w_c(x)$, depending upon their confidence in the estimate of the forward solution generated by the Quasidiffusion approximation. In Chapter V, we discussed some of the deficiencies in the approximation. One deficiency of the Quasidiffusion equation given as Eq. (5.14) is that it is not flux-limited. Another is that it must use "old" estimates of the Eddington factors (although Cooper discusses a way of adaptively updating

them during the IMC calculation, which we do not consider). The net result is that, in general, if a given TRT problem and desired time step size is expected to produce relatively inaccurate estimates of the forward intensity, then the weight window width may be increased accordingly.

We remark on a particularity of our implementation of the weight window in the IMC algorithm. As described in Chapter V, the Quasidiffusion algorithm does not produce a continuous spatial representation of $\langle I \rangle_{n+1}(x)$; it generates zone-averaged data. In our implementation, we have chosen to fit the zone-averaged data to a continuous spatial representation of the form:

$$w_c(x) = \alpha_k e^{\beta_k x}, \quad x_{k-1/2} \leq x \leq x_{k+1/2}, \tag{7.7}$$

where α_k and β_k are zone-dependent parameters chosen to satisfy continuity conditions in the gray scalar intensity $\langle I \rangle_{n+1}$ at the zone boundaries[2]. Thus, although the Quasidiffusion estimate is spatially discontinuous, the weight window employed in the IMC equations is continuous. This detail is not fundamental to the hybrid global weight-window concept; spatially discontinuous or alternative functional forms of the intensity could also be considered. However, an exponential spatial distribution should be relatively accurate in a Marshak wave problem, and the employment of a spatially-continuous weight window should be less sensitive to changes in the grid size.

To implement the weight window in the IMC calculation, we introduce an extra *variance reduction particle weight* w_{VR} – separate from the energy-weight – that is used only for variance reduction purposes (splitting and Russian roulette). In Chapter III, we discussed how each particle receives roughly the same amount of energy-weight upon its birth. This quantity varies depending upon a user-controlled parameter that dictates the desired number of particles per unit of radiation energy. By contrast, at particle birth, the particle variance reduction weight w_{VR} is set equal to $w_c(x)$ generated from the functional fit of the forward solution of the deterministic algorithm. After particle birth, the particle's energy weight and variance reduction weight are proportional for the remainder of the calculation. For instance, if absorption weighting is used, then both the particle variance reduction and energy weights are reduced by the scattering ratio upon a collision event. When the variance reduction weight w_{VR} exceeds the upper weight window, then it is split, and

[2]The zone-averaged solution data are linearly interpolated to approximate nodal (zone-boundary) data. Equations for α_k and β_k are then solved using the nodal data.

both particle weights (w and w_{VR}) are reduced accordingly. All of the other particle properties (location, direction, frequency, etc.) remain unchanged. When w_{VR} falls below the lower weight window, then the Russian roulette mechanism described at the end of Chapter III is employed to either "kill" the particle or increase both particle weights such that the variance reduction weight is near the center of the weight window $w_c(x)$. We recall from Chapter III that the Russian roulette mechanism rigorously conserves energy in the following way. Whenever a particle is "killed", its energy-weight is allocated to spatially-dependent energy bank (this occurs relatively frequently). Later, if a particle survives the Russian roulette (this occurs relatively rarely), it is only permitted to draw upon the energy that exists in the bank. This implies that particles may briefly exist in the simulation such that w_{VR} is below the lower weight window, but this is necessary to ensure energy conservation.

For a generic TRT problem in which accurate solutions are sought throughout the entire spatial domain, this method should be expected to increase the efficiency of the IMC calculation (provided that the weight window width is properly chosen). However, certain TRT problems exist in which accurate solutions are *not* desired throughout the entire spatial domain of the problem. One example of this is Marshak wave problems, for regions ahead of the wavefront. We next discuss a modification to the weight window for Marshak wave problems that should produce more efficient solutions than either the traditional IMC method or the IMC method with the "default" weight window center $w_c(x) \approx \langle I \rangle_{n+1}(x)$.

7.1.2 A Modification for Marshak Waves

Marshak wave problems can be divided into three regions: (1) the region behind the wavefront, in which the spatial gradient of the temperature solution is small, (2) the region in the vicinity of the wavefront, in which the temperature solution varies rapidly, and (3) the region ahead of the wavefront, in which the gradient is small and the problem is generally in near-equilibrium at the initial temperature. Accurate temperature solutions are sought in regions 1 and 2, in which the temperature wave has already propagated through and is propagating, respectively. Ahead of the wavefront, in region 3, relatively unimportant problem physics is occurring, as this region is usually in near-equilibrium at the initial temperature of the problem (if the spatial boundary is vacuum, some cooling may occur, otherwise region 3 is relatively slowly being heated by high-frequency photons).

Using a weight window center $w_c(x) = \langle I \rangle_{n+1}(x)$ treats all of the spatial regions with equal importance, as may be seen in Eq. (7.6). This is undesirable, especially

when particles moving from the relatively high-density regions 1 or 2 reach region 3, where they would typically be forced to undergo computationally-intensive particle splitting. However, we can capitalize on this *a priori* knowledge of the TRT problem by modifying the weight window in advance to prevent the potential "waste" of computational resources in region 3.

We define $w_{\min}$ as the minimum weight window center to be used in the problem. For a Marshak wave problem, this usually corresponds to the initial problem temperature, in which case,

$$w_{\min} = acT_i^4 \,. \tag{7.8}$$

We would like to avoid excessive particle tracking (especially splitting) in spatial zones for which $w_c(x) \approx w_{\min}$, as these zones may usually assumed to be near equilibrium (in region 3). We therefore propose the following modification to the weight window generated from the above algorithm:

$$w_{\mathrm{m}}(x) = w_c(x) \left[1 + \left(\frac{1}{\epsilon} - 1 \right) e^{-(w_c(x) - w_{\min})/\epsilon} \right] . \tag{7.9}$$

We note that ϵ appears twice in Eq. (7.9). One could consider using different values in each location, but we did not. Figure 7.1 depicts the modified weight window center w_{m} as a function of w when $w_{\min}$ is set to 0.1 for $\epsilon = 0.05$, $\epsilon = 0.01$, and $\epsilon = 0.001$. The effect of decreasing ϵ is to make the modification more rapid as w approaches $w_{\min}$. We note that if ϵ is not sufficiently small, then the modified weight window may inadvertently "clip" weights that are relatively large compared to the minimum weight (as when $\epsilon = 0.05$ in Figure 7.1 – the logic imposes $w_{\mathrm{VR}} > 0.4$, which is 4 times the desired minimum weight). If ϵ is chosen to be very small, then the continuous function begins to approach a δ function at the lower weight cutoff, which essentially introduces a discontinuity. For our numerical problems, we set $\epsilon = 0.01$.

We next consider the spatial effects of using the modified weight window in Eq. (7.9). Figure 7.2 depicts modified weight windows $w_m(x)$ with $\epsilon = 0.05$, $\epsilon = 0.01$, and $\epsilon = 0.001$, and the unmodified weight window $w_c(x) = \langle I \rangle (x)$. The example unmodified weight window $w_c(x)$ was numerically generated by the deterministic Quasidiffusion solution in a gray, dimensionless Marshak wave problem with $\Delta_x = 0.025$ and $\Delta_\tau = 0.1$ at a time midway in the IMC calculation. For this problem, the initial scalar intensity – and $w_{\min}$ – are 0.0001. In Figure 7.2, each of the modified weight windows successfully raises the weight window center in the region ahead of the wave-

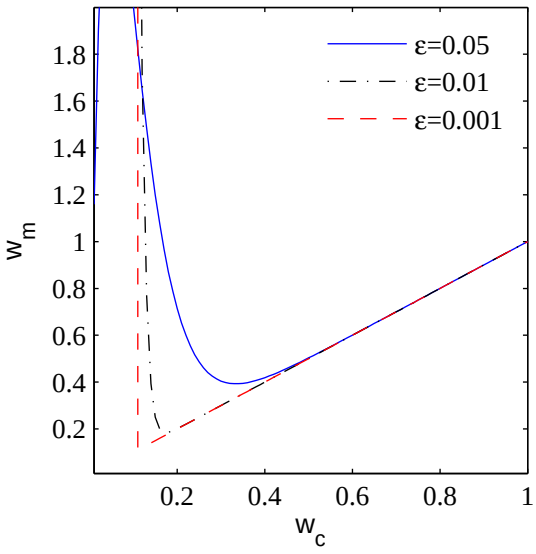

Figure 7.1: An example of the modified weight window center w_{m} as a function of the unmodified weight window center w_c for $\epsilon = 0.05$, 0.01, and 0.001. In this fictional example, the lowest desired weight for particle tracking is 0.1. This represents a single point in space.

front (region 3). This implies that there should be fewer Monte Carlo particles in region 3. Decreasing the value of ϵ increases the modified weight window throughout region 3. We also observe that decreasing the value of ϵ changes the rapidity with which the modified weight windows change in the vicinity of the wavefront (region 2). This is an important characteristic, as it affects the Monte Carlo particle density in region 2. For $\epsilon = 0.05$, $w_m(x)$ begins to increase somewhat early in region 2. This is undesirable, as it would decrease the amount of Monte Carlo particles there. When $\epsilon = 0.01$ (which is the value that we use in our numerical calculations), the weight window increase begins to occur at the leading edge of the wavefront. When $\epsilon = 0.001$, the weight window increase also occurs at the leading edge of the wavefront, but it is more dramatic in that it rapidly climbs to a value that is comparable to the weight window behind the wavefront (region 1). We note that none of the modified weight windows has a discernible effect in region 1.

We note that Cooper proposed a similar modification to the weight window in Marshak wave problems in his thesis [17]. His modification is to raise the *top* of the weight window to "infinity" (any value large enough to eliminate splitting) whenever the predicted temperature solution is less than 105% of the initial temperature:

$$T_{n+1}(x) \leq 1.05\, T(x,0)\,.$$

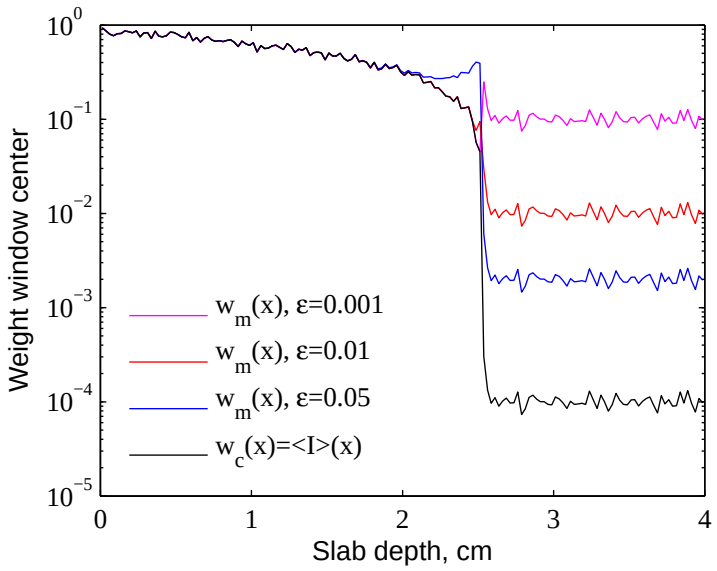

Figure 7.2: The unmodified weight window center $w_c(x) = \langle I \rangle (x)$ and modified weight window centers $w_m(x)$ for $\epsilon = 0.05$, 0.01, and 0.001 for an example Marshak wave problem with an initial scalar intensity of 0.0001.

Our proposed modification is different in that (i) it is a spatially-continuous modification, and (ii) the *center* of the weight window is adjusted. Therefore, our modification reduces the probability of particle splitting and increases the probability of Russian roulette in region 3, whereas Cooper's modification only eliminates splitting. Later in his thesis, Cooper remarked that his modification may be "too crude." [17] We believe that our proposed modification represents an advancement, but it is likely not optimal.

We remark that it may be possible to determine a nearly-optimal value of the weight window for Marshak wave problems, or for other generic global Monte Carlo problems. In Chapter III, we provided the IMC equations with a more rigorous Monte Carlo interpretation by introducing the particle energy-weight as an additional parameter [see Eqs. (3.45)]. In this chapter, we have discussed a modification to these equations by defining a global weight window, but we have not derived the associated modification to Eqs. (3.45). The introduction of Russian roulette and splitting in the IMC implementation corresponds to "extra", unaccounted-for particle sinks and sources in Eqs. (3.45). If some relatively simple assumptions are made regarding the computational cost of the particle tracking, then these modified equations could be deterministically solved (for sufficiently simple problems) to directly obtain an *a priori* estimate of the FOM. Such a procedure has been developed for variance reduction methods that employ the "exponential transform" with angular biasing

in frequency-independent, 1-D problems, but it does not account for weight window techniques [64] [65]. Using the Monte Carlo equations that contain the weight window terms, one could relatively rapidly determine the approximate effect of *any* proposed weight window on the FOM. Alternatively, one could analyze the equations to determine, for instance, when the expected number of particles that must be tracked will be greater than the number of particles introduced into the problem – a "criticality" condition. Such an event occurs if the upper weight window is set to sufficiently low. When this occurs, the number of split ("daughter") particles can rapidly exceed the computational memory resources. As future work, we would like to consider a derivation and solution of a version of Eqs. (3.45) that contains these additional terms that correspond to Russian roulette and splitting.

7.2 Numerical Results

In this section we numerically test the assertions of the previous section on a series of nonlinear Marshak wave problems. We consider both gray and frequency-dependent problems as well as "natural" and modified global weight windows.

As in previous chapters, we remark that the relative errors used to calculate the FOM are obtained by running multiple (25 or more) independent simulations of the problem and calculating the sample errors.

7.2.1 Gray Marshak Waves

In Chapters IV and V and VI, we considered a series of gray Marshak wave problems in order to assess the validity of the stability theory and the accuracy gained by the temperature estimation and IMC-TDF methods. The hybrid global weight window that we have proposed affects neither the stability characteristics nor the accuracy of the IMC method (except for the expected reduction in statistical variance). For the sake of consistent comparisons, we have chosen to test the global weight window method using a subset of the spatial and temporal grids employed for the same 1-D, gray, nonlinear Marshak wave problem.

This problem is described by setting $q = 0.14$, $\sigma = T^{-3}$, and the initial temperature to 0.1. The specific heat is set to the constant value 7.14. We impose an isotropic right boundary condition equal to the initial temperature and an isotropic left boundary condition at a unit temperature. We consider a slab that is 4 cm wide. This implies that the slab is initially 4,000 mean free paths thick, but only 4 mean free paths thick once equilibrium is reached. We track the wavefront up to $\Delta_\tau = 40$

mean free times to emission. The spatial grid and time step sizes are varied, and each problem is solved using a Monte Carlo algorithm.

Numerical results for the "traditional" IMC method are provided in Chapters IV and V. Specifically, Table 5.1 provides the maximum temperatures of the Marshak wave over variable values of Δ_τ and Δ_x at the fixed time $\tau = 8$ mean free times for emission. Also, Table 5.2 depicts the estimate of the wave location when $\tau = 38$. These tables demonstrate that reducing the size of the spatial grid or increasing the size of the time step can lead to violations of the maximum principle and corresponding inaccuracies in the estimate of the wavefront location. The temperature profiles were also presented graphically for the second column and third row of Table 5.1 in Figures 5.6(a) and 5.6(b).

In this section, we consider four permutations of the IMC method applied to this problem. To delineate the differences between these IMC methods, we introduce the following notation for the different methods:

- IMC: A traditional implementation of the IMC equations.
- IMC-WW: An application of the unmodified weight window $w_c(x)$ generated from the Quasidiffusion equation to the IMC equations.
- IMC-MWW: An application of the modified weight window $w_{\mathrm{m}}(x)$ scheme, in which information about the wavefront is used to suppress splitting ahead of the wavefront in the IMC solution.
- IMC-MWW-T_*: A combination of modified weight windows $w_{\mathrm{m}}(x)$ and the IMC-T_* method presented in Chapter V. This is a natural extension of both the IMC-MWW method and the IMC-T_* method, since it uses all of the information generated from the deterministic calculation.

Unless indicated otherwise, in each of the problems that use a weight window, the lower weight cutoff is set to 0.1 times the weight window center, and the upper weight cutoff is 10 times the weight window center. This is a relatively large, conservative window width.

Earlier, we claimed that the IMC-WW method should not affect the mean of the temperature solution. Here, we demonstrate that the global weight window method successfully reproduces the temperature distribution obtained by the traditional IMC method. Figure 7.3 depicts "snapshot" temperature profiles using a traditional IMC calculation (solid) and an IMC-WW calculation (dashed), in which $\Delta_x = 0.025$

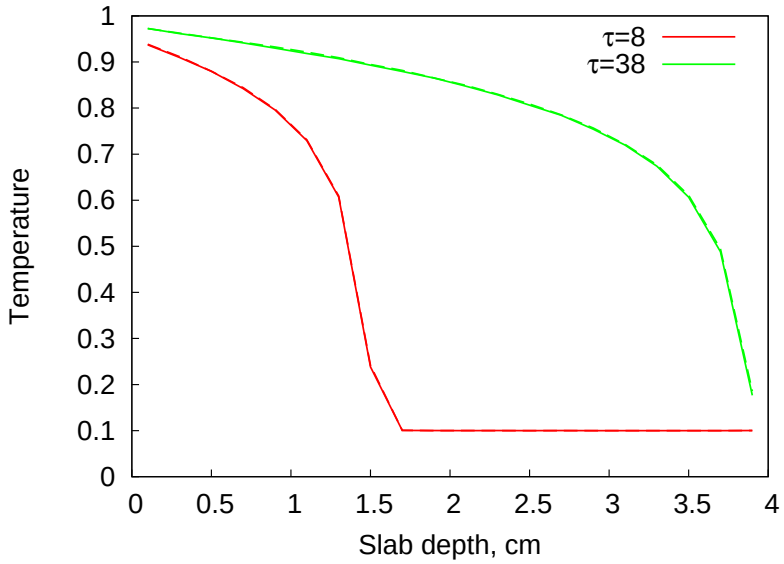

Figure 7.3: Temperature profiles at $\tau = 8$ and $\tau = 38$ for an IMC simulation (solid) and an IMC-WW simulation (dashed) [the results are nearly indistinguishable], with $\Delta_x = 0.025$ and $\Delta_t = 0.1$.

and $\Delta_\tau = 0.1$. As anticipated, the IMC and IMC-WW solutions agree; they are essentially indistinguishable.

We next consider the raw computation time required to obtain the solutions for a variable choice of spatial and temporal grid parameters. Table 7.1 depicts the consumed CPU-time in hours for each of the four methods. The CPU-times presented in Table 7.1 represent those obtained from a serial implementation of the Monte Carlo algorithm on an Apple PowerMac consisting of dual 2.7 Ghz processors. Each of the simulations used 10,000 particles per unit (dimensionless) energy, and 25 independent simulations were performed. We briefly remark that the general trend in all of the methods is for an increase in cost when the spatial grid size is reduced (this introduces more boundaries into the problem, at which the particles must intermittently pause), and when the time step size is decreased, which implies that more particles must be stopped and stored in the census.

Inspection of Table 7.1 reveals that using IMC with no weight window for this problem takes much longer (as much as 14 times for IMC-MWW when $\Delta_\tau = 2$, $\Delta_x = 0.025$) than any of the methods that employ a weight window. The IMC-WW and IMC-MWW methods require essentially the same amounts of time for this problem, which indicates that for this problem, the number of IMC particles that travel ahead of the wavefront (in region 3) must be small to begin with. This situation is more likely to occur in gray problems than in frequency-dependent problems, as

Table 7.1: Comparison of computational times between IMC, IMC-WW, IMC-MWW, and IMC-MWW-T_* for a gray, nonlinear Marshak wave problem. The unit "h" indicates CPU-hours (not wall-clock time).

$\Delta_\tau \backslash \Delta_x$	0.025	0.2	Method
0.1	6.61 h	3.35 h	IMC
	0.78 h	0.30 h	IMC-WW
	0.78 h	0.31 h	IMC-MWW
	0.78 h	0.30 h	IMC-MWW-T_*
2.0	2.53 h	2.09 h	IMC
	0.19 h	0.22 h	IMC-WW
	0.18 h	0.22 h	IMC-MWW
	0.64 h	0.21 h	IMC-MWW-T_*

each Monte Carlo particle "sees" the same opacity in gray problems, whereas high-frequency photons in frequency-dependent problems are much more likely to travel ahead of the wavefront. In all but the case for which $\Delta_\tau = 2$ and $\Delta_x = 0.025$, the IMC-MWW-T_* method requires the same amount of CPU-time as the other weight window methods. The exception occurs because using T_* to evaluate the opacities has a significant effect on the accuracy of the wavefront location – the wavefront in the IMC method is much too shallow. Because the IMC-MWW-T_* method produces a more penetrating (and more accurate) Marshak wave, it requires more computational effort; this should not be perceived as a disadvantage for this case.

The required computation time is an important, but not comprehensive indicator of the efficacy of the different Monte Carlo methods. A better indicator is the FOM, which includes a measure of the relative error. For instance, if the order-of-magnitude reduction in the CPU-times for the weight window methods correspond with larger increases in the relative error, then there would be no real advantage to using the weight window. Fortunately, this is not the case. Figure 7.4 depicts a semilog plot of the temperature-FOMs for each of these methods at $\tau = 38$. The IMC-MWW, IMC-MWW-T_*, and IMC-WW methods are all comparable, and roughly superior to the IMC method by an order of magnitude. This indicates that the spatially-dependent relative statistical errors in the temperature estimates produced by each of the methods is roughly equivalent; the reduction in CPU-time seen in Table 7.1 is the primary contributor to the differences in the temperature-FOMS. Throughout this thesis, we have primarily focused on the temperature solutions of Marshak wave problems, as opposed to radiation solutions. In this chapter, the relative error in the radiation solutions becomes more important, as the weight-window method is

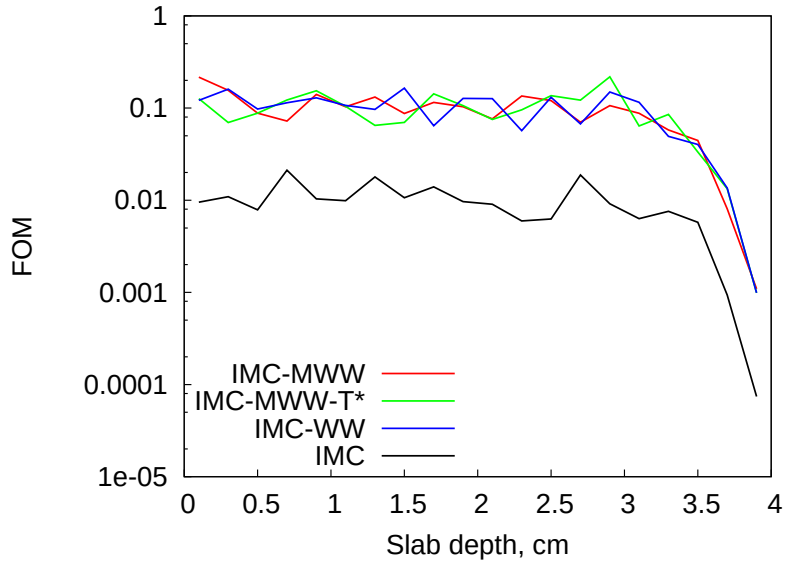

Figure 7.4: Temperature-FOM profile at $\tau = 38$ for a gray Marshak wave problem solved using the IMC, IMC-WW, IMC-MWW, and IMC-MWW-T_* methods with $\Delta_\tau = 0.1$ and $\Delta_x = 0.2$ cm.

primarily designed to minimize the variance of the intensity [see Eq. (7.4)]. The increased temperature-FOM observed in the weight window methods is essentially a byproduct of this effect.

The scalar intensity solution at $\tau = 8$ and $\tau = 38$ is plotted in Figure 7.5 for the IMC (solid) and IMC-WW (dashed) methods with $\Delta_x = 0.025$ and $\Delta_t = 0.1$. As in the temperature solution, the use of a weight window does not (and should not) affect the mean of the scalar intensity solution. We note that the larger spatial variation in the radiation wave is essentially due its approximately T^4 temperature "dependence" – small spatial variations in temperature correspond to relatively large variations in the intensity.

Figure 7.6 depicts a semilog plot of the radiation-FOMs for each of these methods at $\tau = 38$. As with the temperature-FOMS, the IMC-WW, IMC-MWW, and IMC-MWW-T_* methods are all comparable, and approximately an order of magnitude superior to the IMC method. The small jump in the FOM at the right side of the slab is due to the small, but nonzero amount of radiation that enters from the right boundary at the initial temperature.[3]

[3]In our implementation of the IMC method, we force the creation of Monte Carlo particles whenever a boundary or inhomogeneous source is present to ensure energy conservation. If the boundary temperature is small (as it is here), then these particles may have relatively smaller energy-weights, but they are still followed.

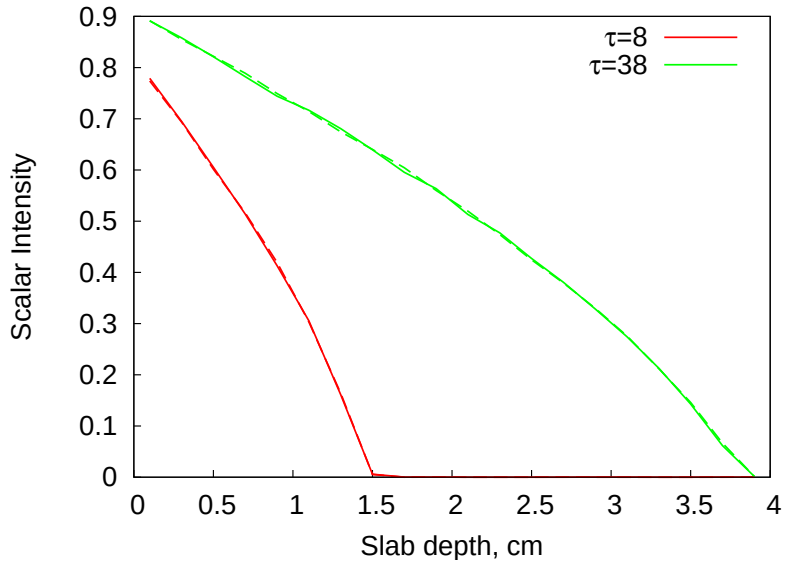

Figure 7.5: Scalar intensity profiles at $\tau = 8$ and $\tau = 38$ for an IMC simulation (solid) and an IMC-WW simulation (dashed) [the results are nearly indistinguishable], with $\Delta_x = 0.025$ and $\Delta_t = 0.1$.

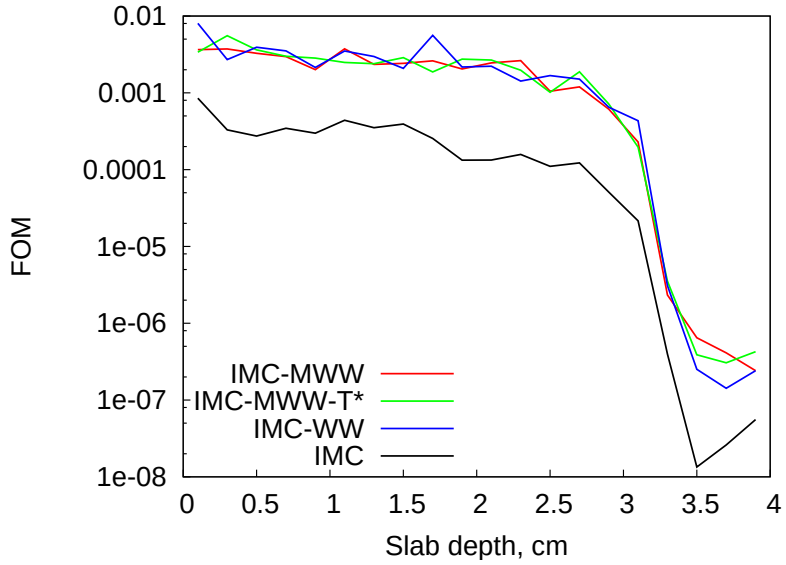

Figure 7.6: Radiation-FOM profile at $\tau = 38$ for a gray Marshak wave problem solved using the IMC, IMC-WW, IMC-MWW, and IMC-MWW-T_* methods with $\Delta_\tau = 0.1$ $\Delta_x = 0.2$ cm.

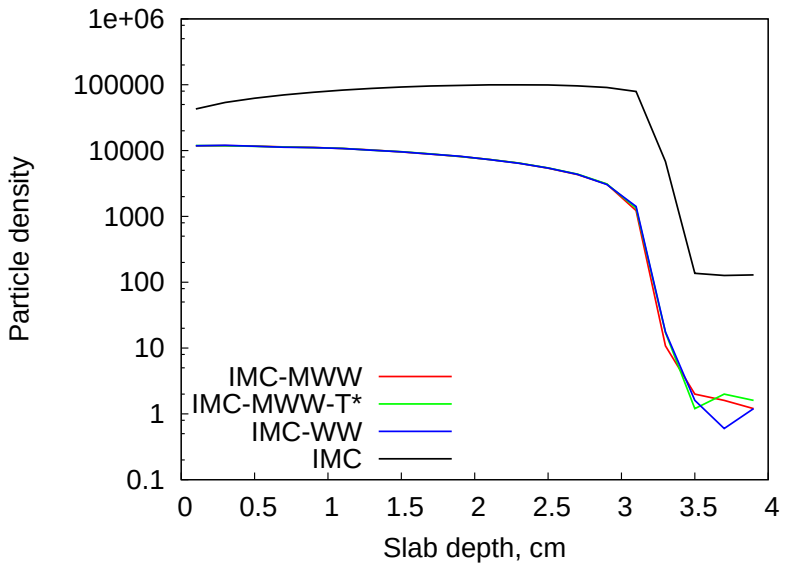

Figure 7.7: Monte Carlo particle density profiles at $\tau = 38$ for a gray Marshak wave problem solved using the IMC, IMC-WW, IMC-MWW, and IMC-MWW-T_* methods with $\Delta_\tau = 0.1$ $\Delta_x = 0.2$ cm.

We next consider one of the factors of the particle-tracking mechanics that could cause the order of magnitude difference in the temperature- and radiation-FOMs: the Monte Carlo particle density. To calculate the numerical Monte Carlo particle density, we increment a density tally by one – regardless of the particle's energy-weight – when it goes to the census at the end of the time step.

Figure 7.7 depicts a semilog plot of the numerically-obtained particle densities at $\tau = 38$ for the IMC, IMC-WW, IMC-MWW, and IMC-MWW-T_* methods with $\Delta_\tau = 0.1$ and $\Delta_x = 0.2$ cm. The IMC method generally contains a much larger number of particles in all regions of the problem than any of the weight window methods. This is because the IMC method does not have any mechanism of removing the low-weight particles[4], whereas the weight window methods employ Russian roulette. We also note that there is a peak in the particle density that occurs in the vicinity of the wavefront, whereas each of the other methods has a density profile that looks roughly like the temperature wave. The peak in the IMC particle density occurs because of

[4]In our implementation of IMC, this is not strictly true – there is an extremely small lower energy-weight cut-off (10^{-100}) below which particles are not followed. We remark that whatever cut-off is used, it must be low enough that it should not affect the problem solution. An alternative to using a cut-off is to "turn off" absorption weighting after a user-determined number of collisions or low-weight threshold is crossed. These approaches are more ad-hoc than Russian roulette but can improve the efficiency of the IMC method in region 3, potentially at the expense of accuracy in region 2.

the temperature-dependence of the opacities. In region 1, behind the wavefront, the opacities are relatively thin (approximately 1). In region 3, ahead of the wavefront, they are thick (approximately 1000). This means that particles spatially transport relatively freely until they reach region 2, the vicinity of the wavefront, where they undergo a large number of collisions. As they collide, their weights (energy-weight and w_{VR}) are reduced according to the effective scattering ratio. Thus, in region 2, a large number of low-weight particles "pile up" in the IMC method.

We also observe that near the left boundary in Figure 7.7, the IMC method has relatively fewer particles than in region 2, whereas the weight window methods have a more uniform spatial distribution throughout region 1. This more spatially-uniform behavior of the weight windows follows directly from Eq. (7.6), which says that weight windows based on the spatial dependence of the forward solution should have spatially-uniform Monte Carlo particle number densities. The mechanism by which this occurs in region 1 is likely particle splitting.

In region 3 of Figure 7.7, the IMC method has a larger number of particles than do any of the weight window methods. Each method introduces some number of particles into region 3 during the time step due to the nonzero $U_{r,n}$ term. However, without a lower weight window, there is no mechanism for the IMC method to remove the low-weight particles.The weight window methods, by contrast, use Russian roulette to reduce the photon population in region 3. This further demonstrates the value of the deterministic calculation, as it provides the crucial information to the Monte Carlo method that permits it to "know" the location of region 3 and not waste time following particles with low weights.

We conclude our discussion by noting that the IMC-WW and IMC-MWW methods are essentially comparable for this frequency-independent problem. The distinction in these two methods will become more important for the frequency-dependent problem, since for those problems high-frequency Monte Carlo particles are much more likely to transport ahead of the wavefront.

Altogether these results show that the global weight window successfully economizes the particle-tracking; it does not waste time following particles that are much lower than the average particle weight.

7.2.2 Frequency-Dependent Marshak Waves

We next consider using global weight windows on the frequency-dependent Marshak wave problem that we analyzed in Chapters V and VI. In this problem, $c \approx 300$ cm/sh (recall 1 sh $= 10^{-8}$ s), and $a = 0.01372$ jk/cm^3-keV^4 (by comparison, in

the gray problem, we set $c = a = 1$). The initial condition is an equilibrium state with $T = 0.01$ keV. At $t = 0$, the left side of the slab is subjected to an isotropic burst of radiation at temperature $T = 1$ keV. The right boundary temperature is set to the constant, initial temperature. The slab size is 4 cm thick. The opacity coefficient [γ in Eq. (2.7)] is set to 200. The Planck mean opacity is therefore $30.8T^{-3}$ which means, at equilibrium ($T = 1$), the slab is 123.2 Planck mean free paths thick, whereas at the initial condition $T = 0.01$, it is 123.2 $\times 10^6$ Planck mean free paths thick. The specific heat is set to 0.1 jk/keV-cc. We consider temperature solutions up to 1 sh. In each of the below problems, the spatial grid size Δ_x is set to 0.2 cm.

As in Chapters V and VI, the frequency-dependent problems were computationally simulated by implementing a parallel Monte Carlo algorithm on a homogeneous, distributed memory cluster of 3.4 GhZ machines, each with 2 Gigabytes of memory. Each of the problems was performed by requesting 20 nodes of the 105-node `reserv` Linux cluster in the Nuclear Engineering division of Argonne National Laboratory Each problem was simulated using 100,000 particles/jk. To estimate relative errors and calculate figures of merit, each problem was independently simulated 50 times; the relative errors were then calculated using the sample error. All timing results refer to the sums of the computational times (not wall-clock times) reported by each processor.

Using a time step of $\Delta_t = 0.001$ sh, the above-described frequency-dependent problem was simulated using the IMC, IMC-MWW, and IMC-MWW-T_* methods. For this problem, it was not possible to obtain solutions using the IMC-WW method (the method that uses an unmodified global weight window). When the IMC-WW method was attempted for this problem, the requested memory to follow the daughter particles due to particle splitting exceeded the available memory on the machines, despite their relatively large (2 GB per node) capacity. Even raising the upper weight window to $100w_c(x)$ did not remedy this. This demonstrates that weight windows generated for an assumed-global problem should not blindly be applied to a sufficiently difficult problem that is truly only semi-global in nature (i.e., the region ahead of the wavefront does not fundamentally affect the problem solution). For this problem at least, it is necessary to restrict the application of the weight window only to regions where the Marshak wave is expected to be. This also indicates the importance of developing a satisfactory logic system for modifying the weight window, which could be supported by the development and analysis of the previously discussed equation for the Monte Carlo particle density M that contains terms corresponding to particle splitting and rouletting.

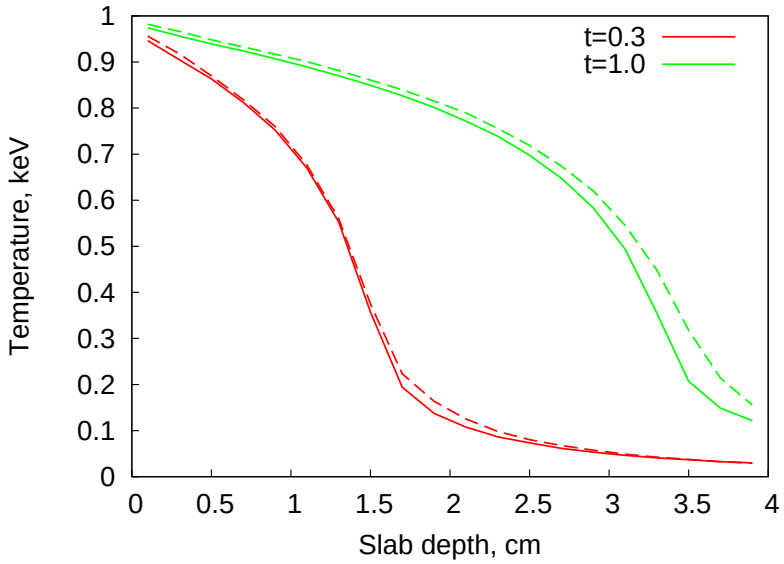

Figure 7.8: Temperature profiles at $t = 0.3$ sh and $t = 1$ sh for a frequency-dependent Marshak wave problem solved using the IMC (solid) and IMC-MWW (dashed) methods with $\Delta_t = 0.001$ sh.

The temperature profiles at $t = 0.3$ sh and $t = 1$ sh using the IMC (solid) and IMC-MWW (dashed) methods are depicted in Figure 7.8. The IMC and IMC-MWW profiles are in general agreement, but there is a discrepancy between them at the wavefront for $t = 1$ sh; the IMC-MWW solution is slightly ahead of the IMC solution. This could be due to an inaccuracy in the treatment of the Russian roulette process. We recall that for a Russian roulette particle to survive the rouletting process, it must draw upon the available energy in a zone-dependent bank into which particles that do not survive the process have their energy deposited. For a spatial zone that contains a large portion of the wavefront, this could lead to an unphysical conduction of the radiation. Particles might roulette and deposit energy into the left part of the zone, behind the wavefront, and then other particles might survive the rouletting procedure at the leading edge of the wavefront. Also, because the particle frequency information is not stored when its energy is deposited into the bank, this could ease the transport process for high-frequency particles – a high-frequency particle (which is more likely to be at the leading edge of the wavefront) could "use" the energy contributed into the bank by the low-energy particles (which are more likely to be behind the wavefront).

Alternatively, in our implementation of the Russian roulette method, the excess energy in the zone-dependent roulette energy banks is dumped into the material at the end of the time step to conserve energy. Typically this energy is small, but it

could potentially contribute to an unphysical heating of the material in the vicinity of the wavefront.

It is not clear to what extent the above-described effects may have contributed to the difference in the wavefront locations for the IMC and IMC-MWW methods at $t = 1$ sh in Figure 7.8. Both of these effects can be mitigated by using smaller grid sizes. We also note that a related form of the unphysical heat conduction problem has always existed in the IMC equations and has been addressed to some extent. Because the temperature is calculated using an integral over the spatial zone, in the most straightforward implementation of the IMC equations, the locations at which the particles deposit their energy is lost (this is the implementation that we employ). For spatial zones in the vicinity of the wavefront, this implies that although most of the energy may have been deposited in one side of the zone, during the subsequent time step the spatial locations of the heat-source particles are sampled uniformally. Alternatively, it is possible to keep a tally that determines not only the correct integrated temperature, but also a slope. Thus, the heat-source particle location may be sampled according to a linear spatial function. Such a fix could also be extended to the Russian roulette procedure, although we do not consider that here. It could also be modified to account for particle frequencies. For instance, relatively coarse frequency-dependent energy banks could be employed.

Table 7.2 depicts the computational time required by each of the methods to simulate the frequency-dependent problem. The IMC method requires approximately 30 times longer to simulate than the modified weight window methods, indicating that the modified weight window methods are much more efficient in particle tracking. We also report again that the unmodified weight window method (IMC-WW) did not complete due to memory issues. In Table 7.2, we also observe that the IMC-MWW-T_* method takes about 7% longer than the IMC-MWW method. In Chapter V, we reported that the IMC-T_* method takes approximately 30% longer than the IMC method. This indicates that the modified weight window (i) lessens the timing discrepancy between the IMC and IMC-T_* methods (from 30% to 7%), and (ii) more than compensates for the increase in required CPU-time observed in Chapter V (the IMC method takes about 30 times longer than the IMC-MWW-T_* method).

Figure 7.9 depicts the temperature-FOMs at $t = 0.9$ sh for the IMC, IMC-MWW, and IMC-MWW-T_* methods. In general, the weight window methods are at least an order of magnitude superior to the IMC method. Judging from the spatial variation in the solution and the data in Table 7.2, this difference appears to be mostly attributable to the differences in computation times. This is an exciting result, given

Table 7.2: Comparison of computational times between IMC, IMC-WW, IMC-MWW, and IMC-MWW-T_* for a frequency-dependent Marshak wave problem. The unit "h" indicates CPU-hours (not wall-clock time).

CPU-time, h	Method
74.4	IMC
2.40	IMC-MWW
2.57	IMC-MWW-T_*
Failed	IMC-WW

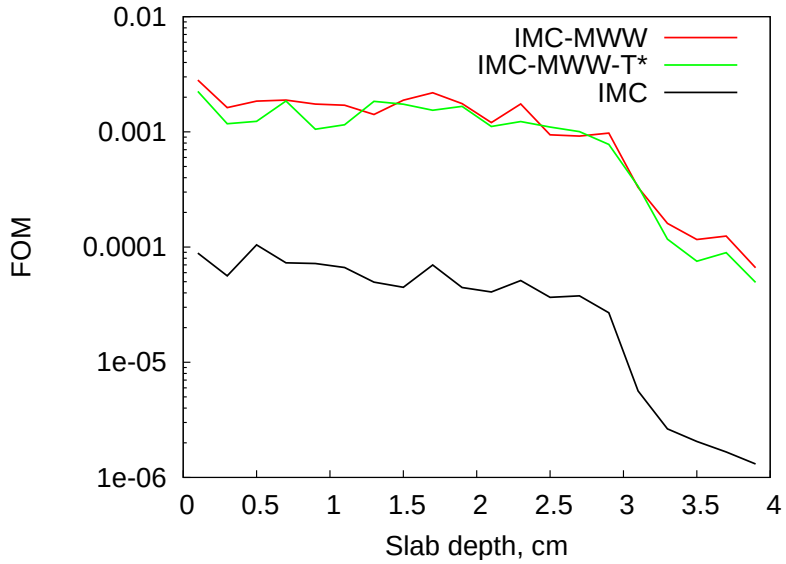

Figure 7.9: Temperature-FOM profile at $t = 0.9$ sh for a frequency-dependent Marshak wave problem solved using the IMC, IMC-MWW, and IMC-MWW-T_* methods with $\Delta_t = 0.001$.

that the problem is numerically difficult problem and the deterministic Quasidiffusion method and weight window modification logic are relatively simple. This strongly suggests that these already-impressive results could likely be further improved.

We next consider the scalar intensity solution, as it is this quantity for which the weight window is generated. Figure 7.10 provides a semilog plot of the gray, scalar intensities at $t = 0.3$ sh and $t = 1$ sh for the IMC (solid) and IMC-MWW (dashed) methods. We note that for $t = 0.3$ sh, the IMC intensity solution is larger than the IMC-MWW solution well ahead of the wavefront, although the solutions behind and in the vicinity of the wavefront agree well. This is acceptable since the IMC-MWW method is designed to limit particle tracking ahead of the wavefront, where the solution accuracy is relatively unimportant. However, for the $t = 1$ sh

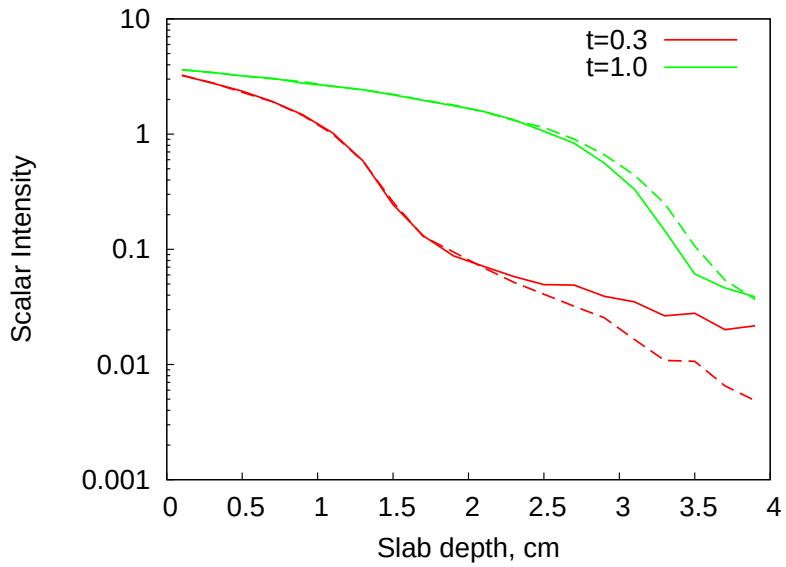

Figure 7.10: Scalar intensity profiles at $t = 0.3$ sh and $t = 1$ sh for a frequency-dependent Marshak wave problem solved using the IMC (solid) and IMC-MWW (dashed) methods with $\Delta_t = 0.001$ sh.

solutions, the IMC-MWW method predicts a wavefront that is slightly ahead of the IMC solution, as occurred in the temperature profiles (see Figure 7.8). This effect could be due to an unphysical conduction that emerges from the treatment of the Russian roulette process, as was discussed previously.

Figure 7.11 provides a semilog plot of the radiation-FOMS at $t = 0.9$ sh for the IMC, IMC-MWW, and IMC-MWW-T_* methods. As with the temperature-FOMS, the weight window methods are at least an order of magnitude improved over the traditional IMC solution. This should largely be due to the approximately 30-fold reduction in computational time depicted in Table 7.2. We again remark that this achievement could likely be further improved by further development in the deterministic method and weight window logic.

Next, we return to our assertion that the Monte Carlo particle densities should be more spatially uniform in the weight window methods. Figure 7.12 provides a semilog plot of the Monte Carlo particle number densities at $t = 0.9$ sh for the IMC, IMC-MWW, and IMC-MWW-T_* methods. As in the gray problems, the weight window methods have an advantage over the IMC method since there is less spatial variation in region 1 due to Eq. (7.6), less piling-up of low weight particles in region 2 due to Russian roulette, and fewer overall particles, also due to Russian roulette. There is less spatial variation in the Monte Carlo particle densities for the weight window methods, especially since Figure 7.12 employs a semilog scale. The reduction

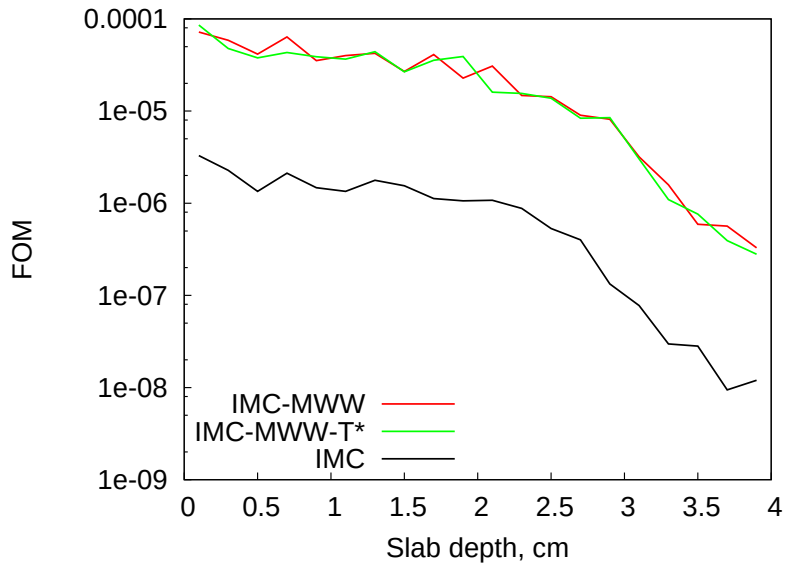

Figure 7.11: Radiation-FOM profiles at $t = 0.9$ sh for a frequency-dependent Marshak wave problem solved using the IMC, IMC-MWW, and IMC-MWW-T_* methods with $\Delta_t = 0.001$.

in spatial variation in the regions behind and in the vicinity of the wavefront can be directly explained by Eq. (7.6). Also, the difference between the IMC and IMC-MWW particle densities in region 3 is about an order of magnitude. We recall that for the modified weight window in Eq. (7.9) we have chosen $\epsilon = 0.01$ in our implementation of the IMC method, which corresponds to about a factor of 100 difference in the weight window center in Figure 7.2. Since our weight window extends for an order of magnitude about the weight window center (the upper cut-off is $10w_c(x)$; the lower cut-off is $0.1w_c(x)$), this, together with the fact that the unmodified weight window does not converge for this problem, is an indication that the modified weight window is working correctly.

7.3 Summary

In this chapter, we have considered the introduction of a global angle- and frequency-independent weight window. This weight window is based on the deterministic, gray, (forward) Quasidiffusion equations presented in Chapter V. Using this weight window in a global TRT calculation helps to automatically globally redistribute the particles throughout the spatial problem domain, decrease the required computational time, and increase the figures of merit in the temperature and radiation solutions.

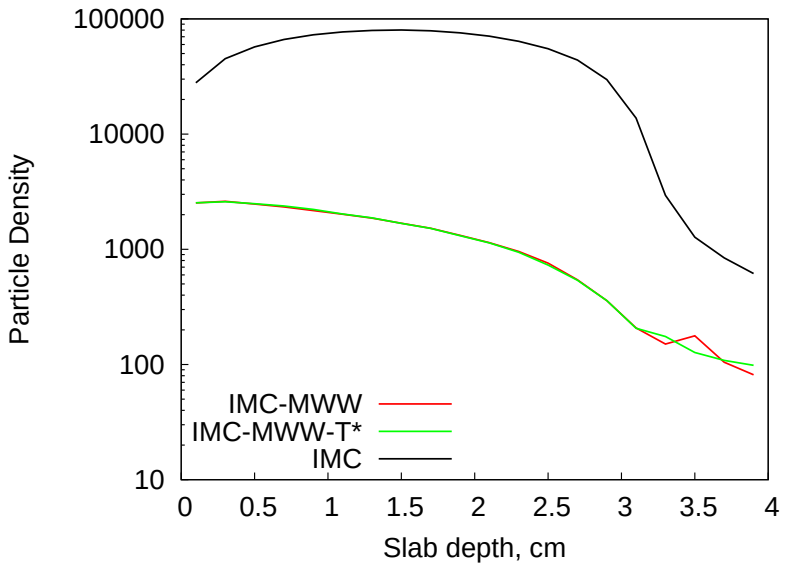

Figure 7.12: Monte Carlo particle densities at $t = 0.9$ sh for a frequency-dependent Marshak wave problem solved using the IMC, IMC-MWW, and IMC-MWW-T_* methods with $\Delta_t = 0.001$ sh.

We motivated the use of a forward weight window by using the Monte Carlo number density M defined in Chapter III. We showed that setting a weight window center to be proportional to the full forward problem solution implies a uniform Monte Carlo particle number density. We then argued that a superior solution for TRT problems is to set the weight window to be proportional to only the space-time elements of phase space (not frequency or angle).

We presented a global weight window algorithm that is based on the temperature-estimation algorithm provided in Chapter V. The primary modification is to employ the estimate of $\langle I \rangle_{n+1}$ generated by the deterministic method as the weight window center in a subsequent IMC calculation over the same time step.

We considered a modification of this weight window for Marshak wave problems. These problems are better described as "semi-global", since the region ahead of the wavefront is relatively unimportant. The modification is intended to prevent excessive particle tracking in the region ahead of the wavefront, which is in near-equilibrium at the initial temperature. The modification we propose is continuous in space, and it raises the center of the weight window to prevent particle splitting and promote rouletting in regions that are near the initial temperature. The modification could likely be further improved upon. We suggested modifying the IMC equations with weights [Eqs. (3.45)] to include terms that correspond to particle rouletting and splitting to assist the analysis of alternative modifications and the

general analysis of weight windows for variance reduction. In numerical tests for gray and frequency-dependent Marshak wave problems, we demonstrated that the modified weight window successfully decreases the spatial variation in the Monte Carlo particle number density in the region behind and in the vicinity of the wavefront. The weight window also reduces the overall number of particles, which implies that the weight window better economizes the Monte Carlo particle tracking.

We tested several weight window schemes against traditional IMC for several gray and frequency-dependent Marshak wave problems. In general, the FOMs obtained by the weight window methods were at least an order of magnitude superior to the traditional IMC methods, and required an order of magnitude less computational time to complete. We confirmed the assertion that the weight window better economizes the particle tracking by more uniformly distributing the Monte Carlo particles. We saw that for sufficiently difficult (frequency-dependent) Marshak wave problems, it is necessary to incorporate some logic in the weight window to preclude splitting in regions where the solution is assumed to be unimportant. Otherwise, the Monte Carlo solution can exceed the machine memory requirements, which can disallow completion of the problem. In the frequency-dependent Marshak wave problem, we observed that an unphysical conduction occurred late in the problem for the IMC-MWW method as compared with the IMC method. We believe that this is due to the energy-conserving Russian roulette mechanism. This may be remedied by introducing within-zone spatially- and/or frequency-dependent roulette-energy banks, similar to what has historically been proposed to prevent unphysical conduction in the heat source particles.

The global weight window algorithm defined and employed in this chapter is similar to a weight window proposed by Cooper [16] [17], but there are several key distinctions.

1. Frequency (energy) dependence is not considered in Cooper's thesis.

2. We better motivate the use the forward weight window and argue that it should *not* contain frequency dependence.

3. We do not adaptively update the Eddington factors by pausing the Monte Carlo calculation and resolving the deterministic method. Including this feature could be investigated as future work.

4. Cooper's gray Quasidiffusion equations are flux-limited. Ours are not, but they attempt to include an accurate representation of the frequency-dependent

problem physics that does not appear possible using Cooper's derivation.

5. Our weight window technique rigorously conserves energy.

6. Our modified weight window is more sophisticated (although probably still sub-optimal).

7. The numerical problems we consider are more difficult, and we obtain better FOM results.

As future work, we recommend further development of the deterministic Quasidiffusion method and the weight window modification for Marshak wave problems. Each of these areas stands to further advance the already-impressive FOM results shown in this chapter. The results in this chapter should also be extended to multidimensional problems, and further parametric studies should be performed with variations in the problem data and grid sizes. The use of Cooper's adaptive method of updating the Eddington factors (and, by extension, the frequency- and angle-averaged opacities) might also improve the weight window and temperature estimates. Finally, alternative Russian roulette mechanisms that contain within-zone spatially-dependent (and/or frequency-dependent) roulette-energy banks should be investigated.

Chapter VIII

Conclusions

The IMC method due to Fleck and Cummings [21] has historically been the dominant Monte Carlo approach to solving radiative transfer problems. In this thesis, we have scrutinized the IMC method in an attempt to better understand how it should be implemented, determine when it will produce unphysical temporal oscillations, enhance its accuracy, and improve the efficiency of solution. The following remarks concern the new material presented in this thesis.

In Chapter III we explicitly provided the 1-D IMC equations with a Monte Carlo interpretation by introducing energy-weight as an independent variable. We also discussed the difference between energy-weight and the concept of particle weight used in Monte Carlo neutron transport. Finally, we presented a Russian roulette variance reduction scheme that conserves energy, and we motivated the technique presented in Chapter VII to determine how it should be used.

In Chapter IV, we developed a linear stability theory for the IMC equations applied to a 1-D, gray, nonlinear problem. We did this by considering a dimensionless form of the 1-D, gray TRT equations, deriving the IMC approximation to these equations, and forming equations for first-order additive perturbations to a specified equilibrium condition. We then related the the magnitude of these perturbations at the beginning and end of the time step through an amplification factor ρ. To obtain ρ, we considered spatial solutions described by Fourier modes $e^{i\xi z}$ and found it necessary to assume that the radiation intensity is separable in space and angle. These assumptions limited the applicability of the stability theory to sufficiently small ξ (slowly-varying spatial oscillations) and sufficiently large time steps Δ_t. After finding ρ, we proved that the IMC equations are unconditionally stable ($|\rho| < 1$). The theory reveals the conditions under which the IMC equations produce damped, temporal oscillations ($-1 < \rho < 0$). We were then able to provide monotonicity

conditions for the solutions of the IMC equations, although they are likely too strong to be of practical use. Numerical tests confirmed that the linear stability theory is accurate when problems contain slowly-varying spatial modes and large time steps. These are also the conditions for which one should expect temporal oscillations to be greatest in magnitude.

Using this knowledge, we presented a simplified, 0-D version of the stability theory in algorithmic form. We used it to reproduce the limiting case $\xi = 0$ of the 1-D results, and we used it again on the IMC equations applied to a linear problem. From this, we reproduced the monotonicity condition on the IMC equations for a linear problem that are due to Mosher and Densmore in [31]. We further demonstrated that the character of the amplification factor is retained when IMC is applied to linear problems, which indicates that damped, temporal oscillations are a fundamental feature of the IMC equations (i.e., more accurate treatments of the temperature-dependent data in nonlinear problems do not substantially affect the stability characteristics of the IMC equations). The 0-D stability theory algorithm is used extensively throughout the later chapters and in Appendix A. It has proved to be a powerful tool in its simplicity and its ability to produce sometimes surprising results.

The stability theory was found to be an inadequate indicator of when the IMC equations applied to a Marshak wave problem would satisfy the maximum principle that the TRT equations satisfy, discussed in [27]. Using numerical experiments, we found that the conditions under which the maximum principle is satisfied are strongly linked to *both* the spatial and temporal grid sizes, much like a CFL condition (even though the IMC equations automatically satisfy the true CFL condition). This relationship should be further explored, as it may be possible to derive a stricter form of the CFL condition to determine when the IMC equations will satisfy the maximum principle. Additionally, it may be possible to extend the stability theory to frequency-dependent problems. Finally, we plan to comprehensively apply the stability theory to other time-discretizations of the TRT equations in a future publication, particularly those in [24], in which 5 different methods are considered and contrasted.

After considering the stability properties of the IMC equations, we turned our attention to accuracy-enhancing techniques. The first of these is the temperature estimation and evaluation algorithm presented in Chapter V. Recognizing that the temperature-dependent problem data in the IMC equations has traditionally been limited to evaluation at the beginning of the time step, we motivated the use of a more accurate temperature to evaluate these data. Starting from the 1-D form of the

TRT equations, we derived a system of gray, Quasidiffusion equations that contain frequency- and angle-averaged problem data generated from the IMC solution over the previous time step. We then discretized the equations over time and space to describe a sample deterministic procedure that may be used to solve them. The simplified Quasidiffusion equations are much more efficient to deterministically solve than the Monte Carlo solution of the IMC equations and should produce reasonably accurate solutions. We also derived a properly time-averaged temperature T_* at which the opacities are evaluated in the subsequent IMC calculation of the upcoming time step.

Overall, the temperature estimation algorithm proceeds in the following way. During a time step $t_{n-1} \leq t \leq t_n$, a frequency-dependent IMC calculation is carried out. Throughout the calculation, certain problem data are averaged over frequency and angle. These data are then provided to the new Quasidiffusion method to estimate the temperature T_{n+1} for the upcoming time step $t_n \leq t \leq t_{n+1}$. The average temperature T_* is generated and passed to the IMC method, which then uses it to evaluate the temperature-dependent problem data. The IMC equations are then used to produce solutions over the same time step $t_n \leq t \leq t_{n+1}$ using the more accurate problem data. The solution obtained by the IMC equations supersedes the solution produced by the deterministic Quasidiffusion equation. We refer to the IMC method that uses temperature-dependent problem data evaluated at T_* as the IMC-T_* method.

From numerical experiments, we found that the IMC-T_* method can produce much more accurate results than the traditional IMC method. For a nonlinear 0-D problem, we saw that the IMC-T_* method helps ameliorate the "overshooting" that can occur as an IMC solution attempts to reach an equilibrium condition, discussed in [30]. For a series of nonlinear, gray Marshak wave problems, we saw that the temperature estimation algorithm produces temperature solutions that reduce or eliminate violations of the maximum principle generated by the corresponding traditional IMC solution. In a frequency-dependent Marshak wave problem solved using two values of Δ_t, the IMC-T_* and IMC methods were found to produce nearly identical temperature solutions and comparable temperature-FOMs.

We observed that that IMC-T_* simulation can take slightly longer than the IMC simulation due to an increase in the Monte Carlo particle collision density in the region ahead of the wavefront. This increase in cost can be more than compensated for by employing a modification of the global weight window presented in Chapter VII. We also observed that the Monte Carlo estimator for the frequency- and angle-

averaged opacity σ_ρ can be noisy, which leads to statistical noise in the deterministic temperature solution of the Quasidiffusion equations. To ameliorate this, we proposed, but were not able to investigate, an alternative estimator that should remove some of the statistical noise.

The Quasidiffusion equations presented in Chapter V are not flux-limited; this limits their accuracy, although not to the same extent that would be expected had diffusion equations been used. As future work, it may be possible to derive equations that are flux limited or to introduce flux-limiters to these equations. We also implicated the use of different average temperatures for each of the temperature-dependent problem data [β, σ, and $b(\nu)$], although we observed that using T_* based upon the average value of σ alone produced substantial gains in accuracy. Alternatively, one could consider evaluating these data with a time-dependent temperature that is continuous throughout the time step. For example, the temperature could be based upon a linear fit of T_n and the deterministically-estimated value of T_{n+1}. We also motivated the use of the deterministic Quasidiffusion algorithm as a means to adaptively determine the correct time step size; for this the algorithm may be employed equally well by Monte Carlo or deterministic transport methodologies. To complete its analysis, the method should be extended to 2- or 3-D problems.

An alternative way to enhance the accuracy of the IMC equations is to remove one of the more dubious approximations that takes place during their derivation. This was the focus of Chapter VI. The removal of this approximation led to IMC equations that contain a time-dependent Fleck factor $f_n(t)$, which we refer to as the IMC-TDF equations. We argued and numerically demonstrated that the IMC-TDF equations should be more accurate than the IMC equations. We also discussed the implementation differences between the IMC and IMC-TDF equations and showed that they are minor. Using the time-average of the time-dependent Fleck factor, we proposed (but did not test) an adaptive value of the user-defined parameter α that could be used as a simple first step towards a full implementation of the IMC-TDF equations. We demonstrated that the IMC-TDF equations are unconditionally stable, but contain monotonicity conditions on the temperature solutions that are slightly worse than the IMC equations.

We tested the IMC-TDF equations on a linear 0-D TRT problem and showed that they are second-order accurate in Δ_t. For nonlinear problems, the IMC-TDF equations are first-order accurate in Δ_t due to the approximate treatment of the temperature-dependent problem data. We tested the IMC-TDF equations on several gray Marshak wave problems and found them to be more accurate than the IMC

solutions in most cases; the IMC-TDF equations produced temperatures solutions with decreases in the violation of the maximum principle and improvements in the estimate of the wavefront locations relative to the IMC solutions. We also numerically tested the IMC-TDF equations in conjunction with the IMC-T_* method proposed in Chapter V on a gray Marshak wave problem and found this combination to be more accurate than any of the individual IMC, IMC-TDF, and IMC-T_* methods. We considered timing studies of several gray Marshak wave problems, and we noted that the IMC-TDF and IMC methods require comparable amounts of CPU-time unless large time steps are used, in which case the IMC-TDF method required up to 23% more time. The FOMs obtained for these problems essentially reflected the difference in the required CPU-times. We compared the IMC and IMC-TDF methods for a frequency-dependent Marshak wave problem. We verified that the temperature solutions obtained by both approaches are comparable, and we saw that the IMC-TDF method can be slightly more efficient (13%) than the IMC calculation. However, when we increased the time step size by a factor of 20, the IMC-TDF method required 8 times more CPU-time than the IMC method.

Because the effective scattering ratio in the IMC-TDF equations is time dependent in that it asymptotically approaches 1 throughout the time step, the IMC-TDF equations can contain spatial regions that require more effective scattering collisions than do the IMC equations. This factor, coupled with a gain in the amount of radiation energy that must be simulated due to the $U_{r,n}$ term, can lead to a substantial increase in the cost of the IMC-TDF equations relative to the IMC equations. We proposed, but did not test, a modified version of the IMC-TDF equations that should limit the increase in computational cost in the IMC-TDF equations for relatively large time steps while preserving the accuracy enhancements observed for small time steps. Also, a combination of the IMC-TDF equations with one of the diffusion theory based enhancements to the IMC equations such as in [25] or [26] should also improve the overall calculational performance.

In Chapter VII, we proposed a frequency- and angle-independent global weight window for the Monte Carlo solution of the IMC equations. Cooper has previously considered a global weight window for the IMC equations [16] [17], and we discussed the differences between his and our approach at length in Chapter VII. Our weight window is centered upon the forward gray, scalar intensity solution produced by the same deterministic Quasidiffusion equations used in Chapter V. We argued that using our weight window should produce a Monte Carlo particle number density that is uniform in space and time but whose frequency- and angle-dependence match those

of the forward intensity solution (in the limit of an infinite number of histories). Using a frequency-independent weight window (i) precludes the need for a multigroup deterministic calculation, (ii) prevents particle splitting from group to group, and (iii) does not attempt to uniformally distribute the Monte Carlo particles throughout frequency space, which is arguably less efficient than allowing the particles to distribute according to the frequency-dependence of the problem. To implement the lower weight window, we used the Russian roulette algorithm discussed in Chapter III that rigorously conserves energy.

We proposed a simple modification to the weight window for use in Marshak wave problems. This modification is designed to limit the number of particles that are tracked in the region ahead of the wavefront by raising the weight window center in that location. We noted that this modification could likely be further improved upon, but in numerical tests, it was found to be adequate. We refer to the IMC method that uses a modified weight window as the IMC-MWW method.

We numerically tested the IMC-MWW method on gray and frequency-dependent Marshak wave problems, and demonstrated approximately an order-of-magnitude improvement in the FOMs. For the frequency-dependent Marshak wave problem, the modified weight window was necessary to obtain solutions – the unmodified weight window method was not able to complete due to computer memory restrictions. For this problem we also observed a discrepancy in the solution profiles late in the calculation between the IMC and IMC-MWW methods that may be due to an unphysical conduction that can occur in the Russian roulette mechanism. This problem can likely be mitigated by using existing techniques for the IMC method that concern a related unphysical conduction in the material temperature.

8.1 Coda

The IMC method has existed for over 35 years with only few modifications. The intent of this research was to better understand the IMC method and to provide it with several enhancements to improve its accuracy and efficiency, although much of our material can be applied to other time-discretizations of the TRT equations. As future work, each of these proposed enhancements requires further testing, and they each should be extended to 2- and 3-D. We remark that none of the enhancements discussed in Chapters V, VI, or VII is limited to 1-D. Essentially, each of the enhancements and analysis tools that we applied to the IMC equations represents a promising first step along several paths that can be taken to improve Monte Carlo

and deterministic simulations of TRT problems. The 0-D stability analysis that we developed should be a useful tool for any TRT methods developer, for instance. Also, the scope of the temperature estimation method that we proposed could be widened to include acceleration or accuracy enhancements in deterministic methods, as well as adaptive time step sizing for either Monte Carlo or deterministic methods. The IMC-TDF equations that we developed successfully increased the accuracy and efficiency for small- to average-size time steps, and the modification that we proposed should further improve its calculational efficiency. The global weight window that we presented can and should be applied to Monte Carlo methods other than IMC.

Two of our proposed enhancements – IMC-T_* and IMC-MWW – rely on a relatively inexpensive deterministic calculation that supports the Monte Carlo solution, and we demonstrate that this hybrid deterministic-Monte Carlo approach can substantially increase both the accuracy and efficiency of the overall solution. The emergence of hybrid methods is a relatively new phenomenon for global particle transport problems. We hope that our results are compelling enough to motivate additional research in this area, and that this will lead to increased collaboration between practitioners who work primarily with either deterministic or Monte Carlo methods.

Appendices

Appendix

A 0-D Stability Analysis of the Carter-Forest Equations

In 1973, two years after the Fleck and Cummings published their IMC paper, Carter and Forest presented an alternative time-discretization of the TRT equations in an unpublished technical report [23]. The derivation of the Carter-Forest (CF) method is much more straightforward, avoids the introduction of any user parameters, and should be more accurate than the IMC method. For instance, one can show that the CF time-discretization is exact for a linear problem, while the IMC method is $O(\Delta_t)$ when $\alpha = 1$ and $O(\Delta_t^2)$ for $\alpha = 0.5$ [46]. The CF method is more computationally expensive, as it requires the computation of logarithms that do not exist in the IMC method. In some regards, it is similar to the IMC-TDF method we discuss in Chapter VI. For instance, the emission time for the photons is exponentially distributed so that particles are more likely to be born near the beginning of the time step. Because of the added cost, and perhaps for other reasons that are less clear, the CF method has not received much attention since its introduction. Martin and Brown recently included the CF method in a paper contrasting it with four other time-discretizations, including IMC [24]. They also extended the CF method to nonanalog transport schemes and demonstrated it to be more accurate than IMC at a slightly increased computational cost [66]. However, no one has yet analyzed the CF method to determine its stability characteristics.

By contrast, another time-discretization due to Ahrens and Larsen has more recently been presented that shares many of the characteristics of the CF approach [22]. Its derivation is straightforward, it is exact for the linear problem, and it should be expected to be more accurate in general. It should also be slightly more expensive to implement than IMC. While the implementation details of the CF and Ahrens-Larsen methods differ, the final equations are remarkably similar. However, after

implementing and testing the Ahrens-Larsen method on a gray, nonlinear problem, we determined it to be numerically unstable. After developing the 0-D stability analysis presented in Chapter IV, we then proved it to be conditionally stable[1]. Because the Ahrens-Larsen and CF methods are so similar, we hypothesized that if one was unstable, then both were. Fortunately, that is not the case. In the next section, we perform the 0-D stability analysis algorithm presented in Chapter IV upon the CF method applied to a typical, nonlinear problem.

A.1 0-D Stability Analysis

The first step of the algorithm is to derive the dimensionless, 0-D form of the TRT equations applied to the problem of interest. For this, we choose the familiar, representative problem data in which $\sigma \propto T^{-3}$ and c_v = constant. Then, the dimensionless 0-D TRT equations are [from Eq. (4.73)]:

$$q\frac{d\phi}{d\tau} + \frac{1}{M^3}\phi = \frac{1}{M^3}R\,, \tag{A.1a}$$

with the material energy equation written exactly in either of the following two forms:

$$\frac{dM}{d\tau} + \frac{1}{M^3}R = \frac{1}{M^3}\phi, \tag{A.1b}$$

$$\frac{dR}{d\tau} + 4R = 4\phi\,. \tag{A.1c}$$

We next apply the Carter-Forest (CF) approximation to these equations. The central approximations are that the opacities and β are frozen[2] at t_n. These approximations have the following effects: Eq. (A.1a) and Eq. (A.1b) will have their coefficients replaced by:

$$\frac{1}{M^3} \approx \frac{1}{M_n^3}\,, \tag{A.2}$$

and $\beta \approx \beta_n$ implies that:

$$\frac{dR}{dM} = 4M^3 \approx 4M_n^3\,. \tag{A.3}$$

[1] We plan on reporting this in a future publication.

[2] In [23], a time-extrapolation procedure is discussed with an associated fitting procedure for the temperature-dependent problem data. Here we do not consider time-extrapolations, as we do not expect them to be employed in a modern implementation of the CF equations.

Then Eqs. (A.1) become:

$$q\frac{d\phi}{d\tau} + \frac{1}{M_n^3}\phi = \frac{1}{M_n^3}R\,, \tag{A.4a}$$

with

$$\frac{dR}{d\tau} + 4R = 4\phi\,, \tag{A.4b}$$

$$\frac{dM}{d\tau} + \frac{1}{M_n^3}R = \frac{1}{M_n^3}\phi\,, \tag{A.4c}$$

and we observe that the material energy equations are no longer identical – the equation for R contains no approximations, but the equations for ϕ and M do contain approximations that are consistent with the conservation of energy.

To perform the CF method upon this problem, Eq. (A.4b) is solved exactly for R and substituted into Eq. (A.4a). The resulting equation is then solved with a Monte Carlo procedure [in [23], see Eq. (14)], and Eq. (A.4c) is also interpreted in a Monte Carlo sense to tally the resulting temperature (as in Eq. (35) of [23]).[3] Note that *no* other approximations are made in the CF method. This is in stark contrast to the IMC derivation; it is at this point that the user-parameter α is introduced, the equation for $R(\tau)$ is averaged over a time step, and the resulting average data is replaced by instantaneous data [see Eq. (4.89)]. It is from this difference that we claim that the CF method should naturally be more accurate than the IMC method.

Our next step is to eliminate ϕ entirely via the conservation of energy, [see Eq. (4.75)]

$$\phi = \frac{1}{q}(q + 1 - M), \tag{A.5}$$

and write Eq. (A.4c) as:

$$\frac{dM}{d\tau} + \frac{1}{qM_n^3}M + \frac{1}{M_n^3}R = \frac{q+1}{qM_n^3}\,. \tag{A.6}$$

We may also eliminate R by integrating Eq. (A.3) using the initial condition $R_n = M_n^4$:

$$R(\tau) - R_n = 4M_n^3(M(\tau) - M_n)\,,$$

[3] It is not sufficient to solve Eq. (A.4a) and Eq. (A.4b) for $\phi(\tau)$ and $R(\tau)$, and to then use $M(\tau) = R(\tau)^{1/4}$, as this does not conserve energy – energy conservation requires that we use Eq. (A.4c) to calculate the new temperature. Therefore, ϕ and M are the central unknowns, while R's primary utility is to estimate the material radiation during the time step.

$$R(\tau) - M_n^4 = 4M_n^3 M(\tau) - 4M_n^4 \,,$$
$$R(\tau) = 4M_n^3 M(\tau) - 3M_n^4 \,. \tag{A.7}$$

Substituting this result into Eq. (A.6), we obtain:

$$\frac{dM}{d\tau} + \frac{1}{qM_n^3} M + \frac{1}{M_n^3}(4M_n^3 M - 3M_n^4) = \frac{q+1}{qM_n^3} \,,$$
$$\frac{dM}{d\tau} + \left(4 + \frac{1}{qM_n^3}\right) M = \frac{q+1}{qM_n^3} + 3M_n \,. \tag{A.8}$$

This ordinary differential equation may be solved with an integrating factor to obtain the following solution:

$$M(\tau) = \frac{3qM_n^4 + q + 1}{4qM_n^3 + 1} + \frac{M_n + qM_n^4 - q - 1}{4qM_n^3 + 1} e^{-(4+1/qM_n^3)\tau} \,. \tag{A.9}$$

Eq. (A.9) is the exact scaled-temperature solution of the CF method within a time step $\tau_n \leq \tau \leq \tau_{n+1}$.

Next, we examine a first-order perturbation in the initial condition such that:

$$M_n = 1 + \epsilon P_n \,,$$

and we look for a recursion relationship between P_n and P_{n+1}. It is useful to note that, to $O(\epsilon^2)$, we have the following identities:

$$\frac{1}{1 + 4qM_n^3} = \frac{1}{1 + 4q(1 + 3\epsilon P_n)} = \frac{1}{4q+1}\left(\frac{1}{1 + \epsilon\frac{12qP_n}{4q+1}}\right) = \frac{1}{4q+1}\left(1 - \epsilon\frac{12qP_n}{4q+1}\right) \,, \tag{A.10a}$$

and

$$M_n + qM_n^4 - q - 1 = 1 + \epsilon P_n + q(1 + 4\epsilon P_n) - (q+1) = \epsilon(4q+1)P_n \,, \tag{A.10b}$$

and

$$3qM_n^4 + q + 1 = 3q(1 + 4\epsilon P_n) + (q+1) = 4q + 1 + 12q\epsilon P_n \,. \tag{A.10c}$$

Using Eqs. (A.10) in Eq. (A.9), we obtain [to $O(\epsilon)$]:

$$1 + \epsilon P_{n+1} = \frac{4q + 1 + 12q\epsilon P_n}{4q+1}\left(1 - \epsilon\frac{12qP_n}{4q+1}\right) + \epsilon\frac{(4q+1)P_n}{4q+1} e^{-(4+1/q)\Delta_\tau} \,,$$
$$= 1 + \epsilon\frac{12qP_n}{4q+1} - \epsilon\frac{12qP_n}{4q+1} + \epsilon P_n e^{-(4+1/q)\Delta_\tau} \,,$$

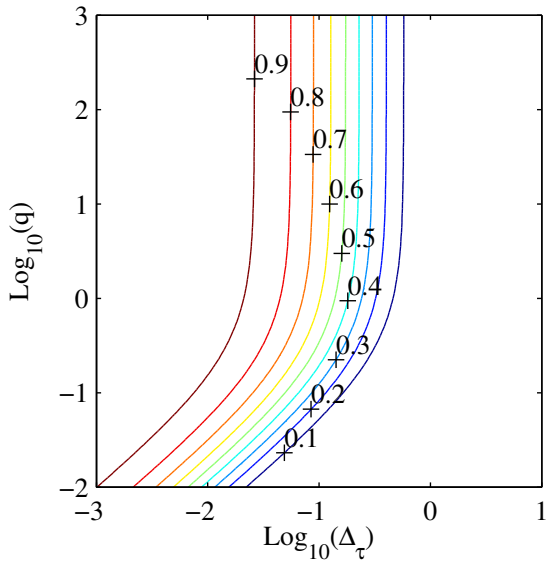

Figure A.1: A contour plot of the amplification factor for the Carter-Forest method applied to a 0-D, gray, nonlinear problem.

$$= 1 + \epsilon P_n e^{-(4+1/q)\Delta_\tau} \,. \tag{A.11}$$

Equating the terms that are $O(\epsilon)$, we find that:

$$P_{n+1} = e^{-(4+1/q)\Delta_\tau} P_n \,. \tag{A.12}$$

The amplification factor for the first-order perturbation is therefore given by:

$$\rho(q, \Delta_\tau) = e^{-(4+1/q)\Delta_\tau} \,. \tag{A.13}$$

The last step is to analyze ρ to determine its stability, but it should be clear that $0 < \rho < 1$. In other words, the CF method is unconditionally stable and should never exhibit oscillations for this nonlinear problem. Figure A.1 depicts the amplification factor over a logarithmic range of q and Δ_τ. It is very similar in character to the amplification factor obtained from the fully-implicit method used in the temperature-estimation algorithm [see Figure 5.3].

From this analysis, we conclude that the CF method remains a promising approach that deserves more consideration. It is clearly advantageous over IMC from the standpoints of accuracy and stability, and it has been reported that its required increase in computational cost is not prohibitive [66]. Additionally, it should be straightforward to apply the enhancements in Chapters V and VII to the CF method

to further improve its accuracy and efficiency.

A.1.1 A Brief Comparison of the CF and Ahrens-Larsen Methods

For the interested reader, we summarize the essential difference between the CF method and the Ahrens-Larsen (AL) method as follows. The fundamental difference is that in the CF method, the following approximation is made:

$$\beta = \frac{\partial U_r}{\partial U_m} \approx \beta_n, \tag{A.14}$$

and in the AL equations, the corresponding approximation is:

$$\eta = \frac{U_r}{U_m} \approx \eta_n. \tag{A.15}$$

For the gray, nonlinear problem that we have considered in this thesis, this implies that

$$\beta_n = \frac{4aT_n^3}{c_v} = 4\frac{U_{r,n}}{U_{m,n}}, \tag{A.16}$$

whereas, in the AL method,

$$\eta_n = \frac{U_{r,n}}{U_{m,n}}. \tag{A.17}$$

There are further differences that concern the implementation details of the AL equations; however, this factor of 4 difference between the relationship of $U_{r,n}$ and $U_{m,n}$ appears to be the fundamental contributor that makes the AL method only conditionally stable despite the unconditional stability of the CF method. Additionally, using a Monte Carlo implementation of the AL equations, we have numerically verified that the temperature solutions can exhibit undamped temporal oscillations. Again, we plan on reporting this in more detail in a future publication.

Bibliography

Bibliography

[1] Ludwig Boltzmann. "Weitere Studien über das Wärmegleichgewicht unter Gasmolekülen". *Wiener Berichte*, 66:275–370, 1872.

[2] E. E. Lewis and W. F. Miller Jr. *Computational Methods of Neutron Transport*. John Wiley & Sons, New York, 1984.

[3] M.S. Reed, M.L. Adams, and J.E. Morel. "Transport Error Estimates for Adaptive Refinement of Spatial Grids". *Transactions of the American Nuclear Society*, 95, 2006.

[4] J.I. Duo and Y.Y. Azmy. "Global Error Analysis of the Spatial Approximation in Discrete Ordinates Methods". *Transactions of the American Nuclear Society*, 92:723–4, 2005.

[5] Edward W. Larsen. "Asymptotic Diffusion Limit of Discretized Transport Problems". *Nuclear Science and Engineering*, 112(2):199–214, November 1992.

[6] Marvin L. Adams and Edward W. Larsen. "Fast Iterative Methods for Discrete-Ordinates Particle Transport Calculations". *Progress in Nuclear Energy*, 40(1):3–159, 2002.

[7] Edward W. Larsen and Jim E. Morel. *Nuclear Computational Science: A Century in Review, a Century Anew*, chapter "Advances in Discrete-Ordinates Methodology". To appear, Springer, 2008.

[8] J. Abhilash Chandy, David J. Glaze, and Steven H. Frankel. "Parallelizing the Discrete Ordinates Method (DOM) for Three-Dimensional Radiative Heat Transfer Calculations Using a Priority Queuing Technique". *Numerical Heat Transfer, Part B*, 52:33–49, 2007.

[9] Douglas F. Swesty. *Computational Methods in Transport*, chapter "The Solution of the Time-Dependent S_N Equations on Parallel Architectures", pages 469–486. Springer, 2004.

[10] J. Tal, R. Ben-Zvi, and A. Kribus. "A High-Efficiency Parallel Solution of the Radiative Transfer Equation". *Numerical Heat Transfer, Part B: Fundamentals*, 44(3):295 – 308, 2003.

[11] J. M. Hammersly and D. C. Handscomb. *Monte Carlo Methods*. John Wiley & Sons, New York, 1964.

[12] J. Spanier and E. M. Gelbard. *Monte Carlo Principles and Neutron Transport Problems*. Addison-Wesley, Reading, Massachusetts, 1969.

[13] M. H. Kalos and P. A. Whitlock. *Monte Carlo Methods, Volume I: Basics*. John Wiley & Sons, New York, 1986.

[14] Thomas E. Booth. "An Approximate Monte Carlo Adaptive Importance Sampling Method". *Nuclear Science and Engineering*, 138:96–103, 2001.

[15] Alireza Haghighat and John C. Wagner. "Monte Carlo Variance Reduction with Deterministic Importance Functions". *Progress in Nuclear Energy*, 42(1):25–53, 2003.

[16] Marc A. Cooper and Edward W. Larsen. "Automated Weight Windows for Global Monte Carlo Particle Transport Calculations". *Nuclear Science and Engineering*, 137(1):1–13, January 2001.

[17] Marc Cooper. *"An Automated Variance Reduction Method for Global Monte Carlo Neutral Particle Transport Problems"*. PhD thesis, The University of Michigan, 1999.

[18] T. N'kaoua. "Solution of the Nonlinear Radiative Transfer Equations by a Fully Implicit Matrix Monte Carlo Method Coupled with the Rosseland Diffusion Equation via Domain Decomposition". *SIAM J. Sci. Stat. Comp.*, 12:505, 1991.

[19] J.E. Morel, Todd A. Wareing, and Kenneth Smith. "A Linear-Discontinuous Spatial Differencing Scheme for S_n Radiative Transfer Calculations". *Journal of Computational Physics*, 128:445–462, 1996.

[20] Jim E. Morel and James S. Warsa. "An S_n Spatial Discretization Scheme for Tetrahedral Meshes". *Nuclear Science and Engineering*, 151:157–166, 2005.

[21] J. A. Fleck and J. D. Cummings. "An Implicit Monte Carlo Scheme for Calculating Time and Frequency Dependent Nonlinear Radiation Transport". *Journal of Computational Physics*, 8:313–342, 1971.

[22] Cory Ahrens and Edward Larsen. A "Semi-Analog" Monte Carlo Method for Grey Radiative Transfer Problems". In *Proc. ANS Topical Meeting, International Topical Meeting on Mathematics and Computation* , Salt Lake City, Utah, September 2001.

[23] L. L. Carter and C. A. Forest. "Nonlinear Radiation Transport Simulation with an Implicit Monte Carlo Method". Technical Report LA-5038, Los Alamos National Laboratory, 1973.

[24] William R. Martin and Forrest B. Brown. "Comparison of Monte Carlo Methods for Nonlinear Radiation Transport". In *Proc. ANS Topical Meeting, International Topical Meeting on Mathematics and Computation* , Salt Lake City, Utah, September 2001.

[25] J. A. Fleck, Jr. and E. H. Canfield. "A Random Walk Procedure for Improving the Computational Efficiency of the Implicit Monte Carlo Method for Nonlinear Radiation Transport". *Journal of Computational Physics*, 54:508–523, June 1984.

[26] Jeffery D. Densmore, Todd J. Urbatsch, Thomas M. Evans, and Michael W. Buksas. "A Hybrid Transport-Diffusion Method for Monte Carlo Radiative-Transfer Simulations". *J. Comput. Phys.*, 222(2):485–503, 2007.

[27] Edward W. Larsen and Bertrand Mercier. "Analysis of a Monte Carlo Method for Nonlinear Radiative Transfer". *J. Comput. Phys.*, 71(1):50–64, 1987.

[28] Jeffery D. Densmore and Edward W. Larsen. "Asymptotic Equilibrium Diffusion Analysis of Time-Dependent Monte Carlo Methods for Grey Radiative Transfer". *J. Comput. Phys.*, 199(1):175–204, 2004.

[29] W. Martin and F. Brown. "Error Modes in Implicit Monte Carlo". In *ANS Winter Meeting and Student Mini-Conference*, volume 85, pages 329 – 332, Reno, Nevada, Nov. 11-15, 2001. On CD-ROM, American Nuclear Society, LaGrange Park, IL (2001).

[30] N.A. Gentile. "A Comparison of Various Temporal Discretization Schemes for Infinite Media Radiation Transport, invited". *Trans. Am. Nucl. Soc. (USA)*, 97:544–546, 2007.

[31] Scott W. Mosher and Jeffery D. Densmore. "Stability and Monotonicity Conditions for Linear, Grey, 0-D Implicit Monte Carlo Calculations". In *ANS Winter Meeting and Nuclear Technology Expo*, volume 93, pages 520 – 522, Washington D.C., Nov. 13-17, 2005. On CD-ROM, American Nuclear Society, LaGrange Park, IL (2005).

[32] Bingjing Su and Gordon L. Olson. "Benchmark Results for the Non-Equilibrium Marshak Diffusion Problem". *Journal of Quantitative Spectroscopy and Radiative Transfer*, 56:337–351, 1996.

[33] John Castor. *Radiation Hydrodynamics*. Cambridge University Press, Cambridge, 2004.

[34] Gerald C. Pomraning. *The Equations of Radiation Hydrodynamics*. Dover Publications, Inc., Mineola, New York, 1973.

[35] James Gleick. *Chaos: Making a New Science*. Penguin Books, New York, NY, USA, 1987.

[36] Edward Larsen. "A Grey Transport Acceleration Method for Time-Dependent Radiative Transfer Problems". *Journal of Computational Physics*, 78:459–480, 1988.

[37] Tamas I. Gombosi. *Gaskinetic Theory*. Cambridge University Press, 1994.

[38] E. W. Larsen, G. C. Pomraning, and V. C. Badham. "Asymptotic Analysis of Radiative Transfer Problems". *Journal of Quantitative Spectroscopy and Radiative Transfer*, 29(4):285–310, 1983.

[39] G. C. Pomraning, A.K. Prinja, and I.R. Shokair. "On the Use of Mean Absorption Coefficients in the Presence of Strong Temperature Gradients". *Journal of Quantitative Spectroscopy and Radiative Transfer*, 26(3):199–213, 1981.

[40] V. Ya. Gol'din. "A Quasi-Diffusion Method of Solving the Kinetic Equation". *USSR Computational Mathematics and Physics*, 4:136–149, 1967.

[41] G. C. Pomraning. "The Non-Equilibrium Marshak Wave Problem". *Journal of Quantitative Spectroscopy and Radiative Transfer*, 21:249–261, 1979.

[42] Bingjing Su and Gordon L. Olson. "An Analytical Benchmark for Non-Equilibrium Radiative Transfer in an Isotropically Scattering Medium". *Annals of Nuclear Energy*, 24(13):1035–1055, 1997.

[43] Bingjing Su and Gordon L. Olson. "Non-grey Benchmark Results for Two Temperature Non-Equilibrium Radiative Transfer". *Journal of Quantitative Spectroscopy and Radiative Transfer*, 62:279–302, 1999.

[44] Edward W. Larsen and Jeffrey D. Densmore. "A Linearized Theory for Near-Equilibrium Thermal Radiative Transfer Problems". In *Nuclear Mathematical and Computational Sciences: A Century in Review, A Century Anew*, Gatlinburg, Tennessee, April 6-11 2003. On CD-ROM, American Nuclear Society, LaGrange Park, IL (2003).

[45] R. E. Alcouffe, B. A. Clark, and E. W. Larsen. *The Diffusion-Synthetic Acceleration of Transport Iterations, with Application to a Radiation Hydrodynamics Problem*, pages 73–111. Multiple time scales (A86-47618 23-64). Orlando, FL, Academic Press, Inc., 1985.

[46] Scott Mosher. "Exact Solution of a Nonlinear, Time-Dependent, Infinite-Medium, Grey Radiative Transfer Problem". In *ANS Winter Meeting and Nuclear Technology Expo*, volume 95, Albuquerque, New Mexico, November 12-16 2006. On CD-ROM, American Nuclear Society, LaGrange Park, IL (2006).

[47] Wikipedia contributors. "Exponential distribution – Wikipedia, The Free Encyclopedia." `http://en.wikipedia.org/w/index.php?title=Exponential_distribution&oldid=145395631`, July 2007.

[48] R. E. Marshak. "Effect of Radiation on Shock Wave Behavior". *Phys. Fluids*, 1:24–29, 1958.

[49] R. Courant, K.O. Friedrichs, and H. Lewy. "Über Die Partiellen Differenzengleichungen der Mathematischen Physik ". *Math. Ann.*, 100:32, 1928.

[50] K. W. Morton and D. F. Mayers. *Numerical Solution of Partial Differential Equations*. Cambridge University Press, Cambridge UK, 1994.

[51] Edward Larsen. personal communication.

[52] C. D. Levermore and G. C. Pomraning. "A Flux-Limited Diffusion Theory". *Astrophys. J.*, 248:321–334, 1981.

[53] H. K. Versteeg and W. Malalasekera. *An Introduction to Computational Fluid Dynamics: The Finite Volume Method*. Addison-Wesley, 1995.

[54] R. E. White. *An Introduction to the Finite Element Method with Applications to Nonlinear Problems*. Wiley, New York, 1985.

[55] Greg Burns, Raja Daoud, and James Vaigl. LAM: An Open Cluster Environment for MPI. In *Proceedings of Supercomputing Symposium*, pages 379–386, 1994.

[56] M. Mascagni and A. Srinivasan. "Algorithm 806: SPRNG: A Scalable Library for Pseudorandom Number Generation". *ACM Transactions on Mathematical Software*, 26:436–461, 2000.

[57] N.A. Gentile. "The Difference Formulation of Radiation Transport in Implicit Monte Carlo". *Trans. Am. Nucl. Soc. (USA)*, 95:871 – 2, 2006.

[58] Richard P. Smedley-Stevenson. "Improved Implicit Monte Carlo Schemes Based on the Difference Formulation". In *Joint International Topical Meeting on Mathematics and Computations and Supercomputing in Nuclear Applications, M & C + SNA 2007*, Monterey, CA, United States, 2007.

[59] Thomas E. Booth. "A Weight (Charge) Conserving Importance-Weighted Comb for Monte Carlo". Technical Report LA-UR-96-0051, Los Alamos National Laboratory, 1996.

[60] Jesse Cheatham. personal communication.

[61] Douglas E. Peplow and John C. Wagner. "Automated Variance Reduction for Scale Shielding Calculations". In *American Nuclear Society's 14th Biennial Topical Meeting of the Radiation Protection and Shielding Division*, pages 556 – 558, Carlsbad, NM, United States, 2006.

[62] Allan B. Wollaber and Edward W. Larsen. "A Hybrid Monte Carlo Deterministic Method for Global Deep Penetration Particle Transport Calculations". In *Proc. ANS Topical Meeting, International Topical Meeting on Mathematics and Compuation, Supercomputing, Reactor Physics, and Nuclear and Biological Applications*, Avignon, France, September 12-15 2005. On CD-ROM, American Nuclear Society, LaGrange Park, IL (2005).

[63] Troy L. Becker, Allan B. Wollaber, and Edward W. Larsen. "A Hybrid Monte Carlo Deterministic Method for Global Particle Transport Calculations". *Nuclear Science and Engineering*, 155:155–167, 2006.

[64] T. Ueki and E.W. Larsen. "Kinetic Theory for Nonanalog Monte Carlo Algorithms: Exponential Transform with Angular Biasing". *Nuclear Science and Engineering*, 130(3):269 – 291, 1998.

[65] T. Ueki and E.W. Larsen. "A Kinetic Theory for Nonanalog Monte Carlo Particle Transport Algorithms: Exponential Transform with Angular Biasing in Planar-Geometry Anisotropically Scattering Media". *J. Comput. Phys. (USA)*, 145(1):406 – 31, 1 Sept. 1998.

[66] W. Martin and F. Brown. "Improved Method for Implicit Monte Carlo". volume 86, pages 212–15, Hollywood, FL, USA, 2002.

Index